THE UNIVERSITY OF CHICAGO

SPIN QUBITS IN SILICON CARBIDE ELECTRONIC DEVICES

A DISSERTATION SUBMITTED TO
THE FACULTY OF THE DIVISION OF THE PHYSICAL SCIENCES
IN CANDIDACY FOR THE DEGREE OF
DOCTOR OF PHILOSOPHY

DEPARTMENT OF PHYSICS

BY
CHRISTOPHER PAUL ANDERSON

CHICAGO, ILLINOIS
JUNE 2020

For Lisa

Table of Contents

List of Figures

This thesis represents the motivations, results, and conclusions from the following works:

[1] Entanglement and control of single quantum memories in silicon carbide.
A. Bourassa*, **C. P. Anderson***, K. C. Miao, M. Onizhuk, H. Ma, A. Crook, H. Abe, J. Ul-Hassan, T. Ohshima, N. T. Son, G. Galli, D. D. Awschalom, *arXiv* 2005.07602 (2020)

[2] Developing silicon carbide for quantum spintronics. (*Perspectives Article*)
N. T. Son, **C. P. Anderson**, A. Bourassa, K. C. Miao, C. Babin, M. Widmann, M. Niethammer, J. Ul-Hassan, N. Morioka, I. G. Ivanov, F. Kaiser, J. Wrachtrup, D. D. Awschalom, *Applied Physics Letters* **116**, 190501 (2020)

[3] Purcell enhancement of a single silicon carbide color center with coherent spin control.
A. L. Crook, **C. P. Anderson**, K. C. Miao, A. Bourassa, H. Lee, S. L. Bayliss, D. O. Bracher, X. Zhang, H. Abe, T. Ohshima, E. L. Hu, D. D. Awschalom, *Nano Letters* (2020)

[4] Vanadium spin qubits as telecom quantum emitters in silicon carbide.
G. Wolfowicz, **C. P. Anderson**, B. Diler, O. G. Poluektov, F. J. Heremans, D. D. Awschalom, *Science Advances* **6**, 18 eaaz1192 (2020)

[5] Coherent control and high-fidelity readout of chromium ions in commercial silicon carbide.
B. Diler, S. J. Whiteley, **C. P. Anderson**, G. Wolfowicz, M. E. Wesson, E. S. Bielejec, F. J. Heremans, D. D. Awschalom, *npj Quantum Information* **6**, 1 (2020)

[6] Electrical and optical control of single spins integrated in scalable semiconductor devices.
C. P. Anderson*, A. Bourassa*, K. C. Miao, G. Wolfowicz, P. J. Mintun, A. L. Crook, H. Abe, J. Ul-Hassan, N. T. Son, T. Ohshima, D. D. Awschalom, *Science* **336**, 6470, 1225-1230 (2019)

[7] Electrically driven optical interferometry with spins in silicon carbide.
K. C. Miao, A. Bourassa, **C. P Anderson**, S. J. Whiteley, A. L. Crook, S. L. Bayliss, G. Wolfowicz, G. Thiering, P. Udvarhelyi, V. Ivády, H. Abe, T. Ohshima, A. Gali, D. D. Awschalom, *Science Advances* **5**, 11, eaay0527 (2019)

[8] Heterodyne detection of radio-frequency electric fields using point defects in silicon carbide.
G. Wolfowicz, **C. P. Anderson**, S. J. Whiteley, D. D. Awschalom, *Applied Physics Letters* **115**, 4, 043105 (2019)

[9] Spin–phonon interactions in silicon carbide addressed by Gaussian acoustics.
S. J. Whiteley*, G. Wolfowicz*, **C. P. Anderson**, A. Bourassa, H. Ma, M. Ye, G. Koolstra, K. J. Satzinger, M. V. Holt, F. J. Heremans, A. N. Cleland, D. I. Schuster, G. Galli, D. D. Awschalom, *Nature Physics* **15**, 5, 490-495 (2019)

[10] Strain annealing of SiC nanoparticles revealed through Bragg coherent diffraction imaging for quantum technologies.
S. O. Hruszkewycz, S. Maddali, **C. P. Anderson**, W. Cha, K. C. Miao, M. J. Highland, A. Ulvestad, D. D. Awschalom, F. J. Heremans, *Phys. Rev. Materials* **2**, 8, 086001 (2018)

[11] Optical charge state control of spin defects in 4H-SiC.
G. Wolfowicz, **C. P. Anderson**, A. L. Yeats, S. J. Whiteley, J. Niklas, O. G. Poluektov, F. J. Heremans, D. D. Awschalom, *Nature Communications* **8**, 1, 1-9 (2017)

[12] *In-situ* study of annealing-induced strain relaxation in diamond nanoparticles using Bragg coherent diffraction imaging.
S. O. Hruszkewycz, W. Cha, P. Andrich, **C. P. Anderson**, A. Ulvestad, R. Harder, P. H. Fuoss, D. D. Awschalom, F. J. Heremans, *APL Materials* **5**, 026105 (2017)

Acknowledgments

Maybe the most valuable discoveries were the friends we made along the way...

I'd first like to thank my advisor, David Awschalom, for providing guidance and support throughout my graduate career. In particular, David excels at developing a group culture and environment of exploration, creativity, and camaraderie. One of my earliest memories of David is his saying "I don't care how smart you are, if you're an asshole I don't want you in my group." This kind of mentality, along with him consistently "having my back" and being an outspoken advocate for me and the other members of his group has made my graduate years enjoyable and successful. I'd also like to thank the other members of my thesis committee: Shinsei Ryu, John Carlstrom, and David Schuster for their time and support.

When I came to the University of Chicago, I was David's first student after his move from the University of California, Santa Barbara. The newly formed Institute for Molecular Engineering (now the Pritzker School of Molecular Engineering) was not even accepting graduate students. I was involved in setting up our new labs, and saw the departure of the last of the 'Santa Barbarians'. Seeing this program grow, from the facilities to the impressive faculty expansion and the development of academic programs from the "ground up" has been an extremely enjoyable and educational experience. The University of Chicago now has one of the best quantum science and engineering programs in the world, and I am extremely grateful that I came to Chicago for my graduate career.

David Schuster has been an awesome advisor, mentor and friend ever since the beginning

of my graduate years. My first few projects in graduate school were in his group, ranging from 3D microwave cavities for masers and cQED with spins, to superconducting SAW devices. Although my research eventually deviated from the expertise of his group, I will always appreciate his deep understanding of quantum mechanics, his approachable personality, and his creativity.

Part of what has made graduate school so enjoyable is the colleagues from lab and my cohort in the physics program. From potlucks, parties, BBQs at the point, movies, dinners, and late nights doing homework, I have made great lifelong friends. Watching their careers grow and going through these formative years together has made an outsized impression on my life. In particular, I'd like to thank Thomas Vidabaek, Aaron Mowitz, Keiran Murphy, Gerwin Koolstra, Mary Burkey, Patrick Bryant, Nathan Schine, and Clai Owens.

My fellow lab-mates in the Awschalom group are an amazing group of people, and this thesis would be nothing without them. Science is a team sport. I've been 'Bagel', 'Crandy', 'CSPAN', 'Crispy' and 'Lab Mom' to all or some of you, and I'll miss you all. I'll always cherish the hours and hours of playing *Super Smash Brothers* and beer-league softball games. In particular, I worked very closely with Alexandre Bourassa, Gary Wolfowicz, Kevin Miao, Alex Crook and Sam Whiteley on the SiC effort.

Alex B. ('Bourassa') is an exceptional engineer, scientist, and friend. He (and others) essentially rebuilt the SiC efforts in our lab from the ground up. His technical understanding, physical intuition, and software skills have made him an invaluable asset to the lab. We worked very closely together on the major successes in this thesis, and none of it would have happened without him. A lot of good science was discussed on those '173' bus rides. Thanks for being so easy to work with.

Gary W. is the first postdoc I ever really worked with directly. He is impressively knowledgeable, and set off a large fraction of the work in this thesis with his ideas. He strikes the perfect balance between excitement and passion for science with realism (french pessimism). Gary is a great experimentalist and friend, and I have been fortunate to work with him on

many projects that were successes because of him.

Alex C. ('Crook') is the lifeblood of the Awschalom lab. His fabrication abilities, deep scientific thinking and willingness to ask the 'stupid questions' blend with his wonderful humor, niceness, and freakish athletic ability (a home-run hero) to make a one-of-a-kind coworker and friend.

Kevin M. has made unparalleled scientific, engineering, and technical advances for the SiC team. He is a powerhouse scientist who is willing to delve deeply into the physics and really understand how things work. Kevin is a very hard worker and most of the recent SiC advances would not have been possible without him.

Sam W. is one of the few people really passionate about materials science and fabrication. His development of new measurement techniques and devices for SiC came with great success and I was fortunate to be a part of those efforts. He and I were both 'joint' graduate students in David Schuster's lab, where we spent a lot of time developing mechanical resonators and measuring in the dilution fridge (& dreaming big dreams). Thanks for being a valuable friend, bartender, Tolkien aficionado, and movie-quote lover.

Joseph Heremans was the first person from the lab I ever met, and he took me under his wing in the early years. I'll always remember his role as (the original) 'Lab Mom' and all the time we spent setting up equipment, making CAD drawings, and our time in Jones. Abram Falk guided many of the younger students in the lab, and set me on my maser dreams. If only you knew how many times we opened the 'SiC Bible'[13] and that we named the lab fish 'Abram Jr.' to mourn you leaving us. David Christle (DC) and Paul Klimov (PVK) are legends in the land of SiC. Paul was an enigma who had a deep grasp of quantum and was great to talk science with. DC was a crazy man, whose social media postings, love for statistics, and unique taste in music drove many a conversation. The SiC dream you both helped start lives on. Look where 'putting a spin in a diode' got us! In my early years, I shared an optical table with Charlie De Las Casas whose consumption of energy drinks still impresses me today. I just want you to know *WIGS* is still going strong. Paolo Andrich was

a force of nature who brought a certain energy and pizzazz to the group. We miss you and your jaw hurting at lunchtime. I still don't know how you are so good at American fantasy sports leagues. I will always remember Konstanz. Will Koehl, the 'founding father' of spins in SiC was an institution in the group. His perspectives and ideas are still driving the major research thrusts in the lab. Chris Yale was also involved heavily in my formative years in the group, along with Brian ('Postdoc Power') Zhou with both of who I enjoyed many food truck runs and softball games.

For the younger crowd, Berk Diler was the first student to join after me. Berk's passion for hard sci-fi, coffee, and good food have made for plenty of fun discussions and excursions (div school?). From Mickey Mouse sounds to dad jokes, Peter Mintun brings an unparalleled vibrancy to the lab. Thanks for being (sadly) my only touchstone on modern hip-hop and rap (& swang). I'm glad I was CMOS compatible with you, and that we didn't get in that black taxi. Don't trust the Mojito Man. Paul Jerger is a thoughtful person and a great scientist who really thinks deeply about problems and keeps up to date with the latest and greatest work in the community. Sorry for firing you all those times. You're hired (chalk it up!). No one understands physics in the group like Masaya Fukami does. I'm glad I was able to be your 'rubber duck' all those times.

I'd also like to acknowledge the other members of the lab: Andrew Yeats, Erzebet Vincent (who was exceptionally helpful in editing this thesis), Joost van Bree, and Sam Bayliss for their companionship and support. The lab is in good hands with the newer members: Grant, Jonathan, Ben, Cyrus, Pratiti, Jacob, Joseph, and our new postdocs Yegishe and Leah. Joseph and Yegishe are the newest members working on SiC, who bring needed expertise and drive to new and existing projects. I'm excited to see where things will go.

I had the opportunity to mentor many great undergraduates in my time, notably Xu Xiao in the early years. Although the science dreams never came to fruition, your help was greatly appreciated. Later on, Elena Glen was an REU student before she came to Chicago for graduate school and became a member of the group. I remember very early on knowing

that she would be a great fit for the group with her awesome personality, independence, and scientific ability. The future of SiC is safe with you, and thanks for all your help. Hope Lee is an excellent undergraduate researcher who I also had the pleasure of working with, who has impressive fabrication and simulation skills.

Our group recently formed an offshoot at Argonne National Lab, where I was a guest graduate student. Nazar Delegan and Sean Sullivan are great and I'm excited to see where the research directions at Argonne go. I'd also like to thank the following administrators: Mary Pat McCullough, Brenda Thomas, Maria Jimenez, and the PNF staff: Peter Duda, Anna Mukhortova, Sally Wolcott, Mike Medina. At the MRSEC, I'd like to thank Justin Jureller and Qiti Guo for the their scientific and technical support over the years. Furthermore, I'd like to acknowledge our collaborators who provided materials and processing: N.T. Son and Takeshi Ohshima, and who provided theoretical guidance and work: Adam Gali, Meng Ye, Hosung Seo, Mykyta Onizhuk, He Ma, and Giulia Galli.

Finally, I'd like to thank my family. From an early age, the value of education and inquiry was instilled in me, along with a deep love of learning. I have been extremely fortunate (privileged) to be supported wholly through my academic trajectory. None of this would be possible without your love, guidance and encouragement.

My wife Lisa has been an incredible bedrock of stability, support, and love throughout the sometimes trying times of graduate school (such as having your samples thrown in the trash). She is an amazing partner in life, and is willing to put up with my 'Science Brain', long hours, and stress. This journey would have been much harder and much less successful without your emotional and academic backing. I love you.

Abstract

This thesis investigates the development of quantum technologies with spins in silicon carbide (SiC). In particular, SiC can host optically active defect spins which are key to developing solid-state quantum sensors, communications networks, and distributed quantum computation over long distances. The neutral divacancy (VV^0) is such a spin defect, which displays long coherence times and possesses a spin-photon interface for long-distance entanglement. Throughout this thesis, we leverage the distinct advantages that SiC has as a host material for quantum bits. Broadly, we describe how quantum states can be controlled, tuned, and enhanced through their integration into SiC mechanical, photonic and electrical devices.

Specifically, this thesis focuses on understanding and controlling the electrical environment of single qubits. Electrical and optical control of the charge state of defects is achieved in ensembles and is extended to single VV^0 that are isolated and manipulated in wafer scale commercial semiconductor p-i-n diodes. We find that through this integration an ideal, widely tunable, and spectrally narrow spin-photon entanglement interface is created. This pathway for eliminating spectral diffusion in doped semiconductor devices unlocks the possibility of efficient long distance quantum entanglement in the solid-state. This thesis further develops VV^0 for quantum technologies by extending the coherence times of this system and by demonstrating control and entanglement between electron and nuclear spins in SiC.

Combining the mature semiconductor industry for SiC semiconductor devices with coherent single spins with high-fidelity spin-photon interfaces provides an exciting avenue for scalable quantum technologies in the solid-state.

Chapter 1

Introduction and Perspectives on Classical and Quantum Technologies

One of the goals of this thesis is to provide reference and resource for both experts and non-experts in the field. As such, we will start with very broad strokes and build up to the context and applications for quantum science and technology that this thesis advances.

We start in **Chapters 1-3** with the basics of classical and quantum information technologies. **Chapters 4-7** cover spin defects in the solid-state, focusing on the VV^0 center in SiC studied in this thesis, alongside recent advances in transition metal centers. **Chapter 8** describes in detail the applications of these qubits to long distance entanglement, while **Chapters 9-10** briefly discusses the integration of VV^0 qubits into photonic and phononic devices. The major thrust of this thesis starts in **Chapter 11**, describing the linking of SiC electronics with quantum science, resulting in ideal spin-photon interfaces. **Chapter 12** illustrates the advances in understanding and imaging SiC and diamond nanoparticles. The final thrust of this thesis is represented in **Chapter 13**, which describes entanglement and control of the nuclear environment in SiC, creating viable quantum memories. This thesis culminates with **Chapter 14**, which summarizes the other (failed) research avenues during my graduate career.

1.1 What is 'Quantum'?

"*Take a huge step back*"

1.1.1 The Wonders of Classical Information Technologies

You are probably reading this thesis on a computer. If not, you are reading it on a piece of paper that was printed by one. Perhaps you are even reading this on a smartphone. You probably downloaded this thesis off the internet. Let's take a moment and appreciate what a feat this is. The flow of electrons being controlled through billions and billions of transistors, which are only nanometers in size. Gigabytes to terabytes (more bits than the number of stars in the Milky Way Galaxy) of data being stored in your device's memory, and information is reaching your eyes by encoding the information on this page onto millions and millions of individually controlled pixels. Imagine having to build all of that from scratch. Think broader: Supercomputers can simulate the stellar dynamics of entire galaxies, and a smartphone that you can buy for less than $100 can stream live video to someone on the other side of the world and can give you directions to your local supermarket using satellites in space. The internet is another wonder: a globally interconnected, distributed network of networks that drives the majority of communications and commerce worldwide. From virtual realities, artificial intelligence, to anything as simple as a microwave oven, it doesn't stop there. Take a moment to appreciate all the technology around you. Someone had to discover the physics, do the engineering, come up with the design, and physically build every device and piece of technology you use. There were thousands of people who made incremental improvements and had fun ideas that miraculously worked, people who lived and died. This is the course of human advancement. The goal of this thesis is along these lines- to work towards in my own small way to develop the equivalent 'quantum' technologies to these classical feats of human ingenuity.

The transistor, which forms the basis for most of our modern technology, was invented

in 1947 at Bell labs and was about the size of the palm of your hand. Before the transistor (a solid-state semiconductor device), rudimentary computers were built out of vacuum tube diodes (invented in 1904) which were the size of large light bulbs. Solid state transistors allowed for the rapid miniaturization and technological advancement that brought us to where we are today. Coined in 1965, Moore's law postulates that the number of transistors in a microprocessor doubles every two years. This exponential explosion has resulted in commercially available transistors only 7 nm large, where relevant features start to approach the size of single atoms. This presents an interesting problem: when will this explosion stop? are we at the limit? when do we need to think about quantum effects at these small scales?

The transistor is the most widely manufactured device is history, with over 13 sextillion units (10^{21}) sold[14]. The inventors of the transistor would have had no chance at guessing how far their invention has gone, and thought the transistor's application might be in hearing aids (the first commercial product using transistors in 1952). I imagine if you had asked the first scientists working on transistors, they would have been skeptical that it would be useful for anything at all, and would have told you how hard the problem was. Despite this, 1954 and 1955 had the first transistor-based radio and calculator. 1961 had IBM's first transistorized supercomputer, the IBM 7030 which operated at around 1 MFLOPS (Floating Operations Per Second) and took up a whole room[15]. Current smartphones can reach hundreds of GFLOPS and can fit in your pocket.

This is where we are today with quantum technologies: since the early 1990's we have built a kind of quantum equivalent of the transistor, and have basic quantum communications. But now we are developing these basic building blocks into real world technologies. We're in the "1950's" of quantum- we have rudimentary quantum technologies, and support from industry and large companies is growing. Even though we roughly know where the field is going, there's no way we could possibly fathom a whole new generation of information technologies (just look at 1950's science-fiction!). The most exciting part is that we don't know where this will all go.

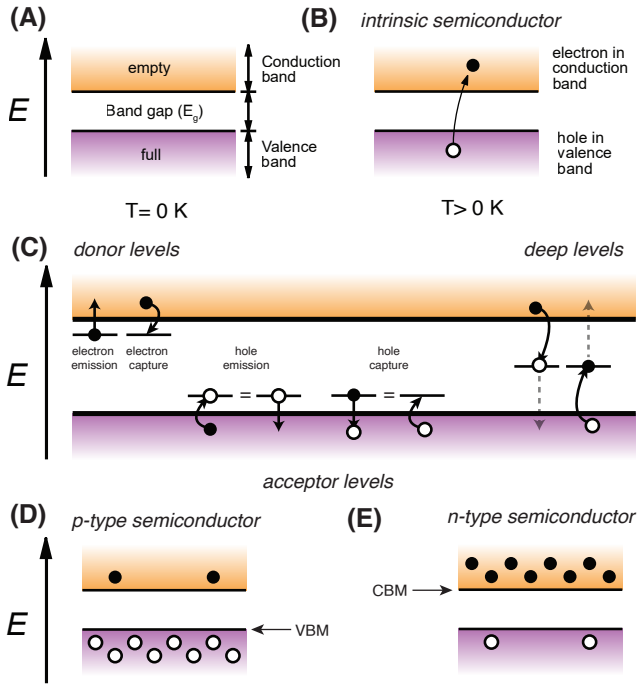

Figure 1.1: **Semiconductor physics.** **(A)** Band gap and full (valence) and empty (conduction) bands of a semiconductor. **(B)** At nonzero temperatures, electrons can be excited to the conduction band and leave behind a hole. **(C)** Available processes for electrons and holes. Deep levels have very low rates of thermal excitation, but can capture carriers effectively. **(D)** In a p-type semiconductor there are an excess of holes. **(E)** In a n-type semiconductor there are an excess of electrons. Adapted from [16].

1.1.2 Transistors and Semiconductors

Why are transistors the key success that led to modern technologies? The transistor is just a device that forms an electronic switch. An electrical voltage on one terminal controls the voltages and currents on another terminal. This can be used to form basic logical operations by wiring transistors together, where 'On' and 'Off' or '1' and '0' refer to the voltages or currents in the transistor. Classical information is 'binary' in that the constituent systems can only take one of two states (On/Off 1/0). Each one of these pieces of information, or 'bits', represents the 'On' or 'Off' states of a transistor. This 'digital' technology is easy to fabricate using transistors, diodes (one way switches for electrons) and other electronic components put together in billion dollar fabrication plants.

It's important to this thesis and to later sections to briefly go into how transistors work,

and why they are made of semiconductors. A semiconductor is a material that conducts electricity not quite like an electrical insulator nor like an electrical conductor. Importantly, by doping the material with different impurities, the electrical characteristics can be altered. An insulator has a large *band gap*, which is the energy difference between the electrons in a material that are bound tightly to the atomic cores and do not participate in electrical conduction (the *valence band: VB*), to electronic states that can move around the material and conduct electricity (the *conduction band: CB*) Fig. 1.1A. This large band gap prevents electrons from being thermally excited to the conduction band, resulting in high resistance and low conductivity (Fig. 1.1B). Metals, on the other hand, have small or nonexistent band gaps (and high conductivity), while semiconductors have small/moderate band gaps. In this thesis, we will focus on crystalline materials with regularly ordered atoms that can be described with band theory. Crystalline silicon, with a band gap of around 1.15 eV, is the quintessential semiconductor that makes modern technology work.

When doping a semiconductor, electronic states can be formed 'in' the band gap of the material by replacing atoms in the crystal lattice with an impurity species. Depending on the dopant, these impurities either contribute extra electrons ('donors') to the system or are deficient of electrons and suck them up from the crystal ('acceptors') creating a quasiparticle called a 'hole' which carries positive charge. A semiconductor region doped with acceptors has many holes and is called 'p' type, while a region doped with donors has more free electrons and called 'n' type (Fig. 1.1D). An undoped region is usually called 'intrinsic' or 'i' type (insulating). These states are usually close enough in energy to the valence or conduction band in energy to be thermally populated and depopulated (Fig. 1.1C). Upon applying electric fields and voltages to a semiconductor, free charges can drift and move. Dopants in a semiconductor can therefore have their associated charges moved spatially to different regions of a device. Similarly, carrier diffusion occurs where electrons and holes move towards areas of lower concentration. With drift and diffusion, depletion regions or 'space-charge' regions can form. These are spatial regions of a doped semiconductor where all

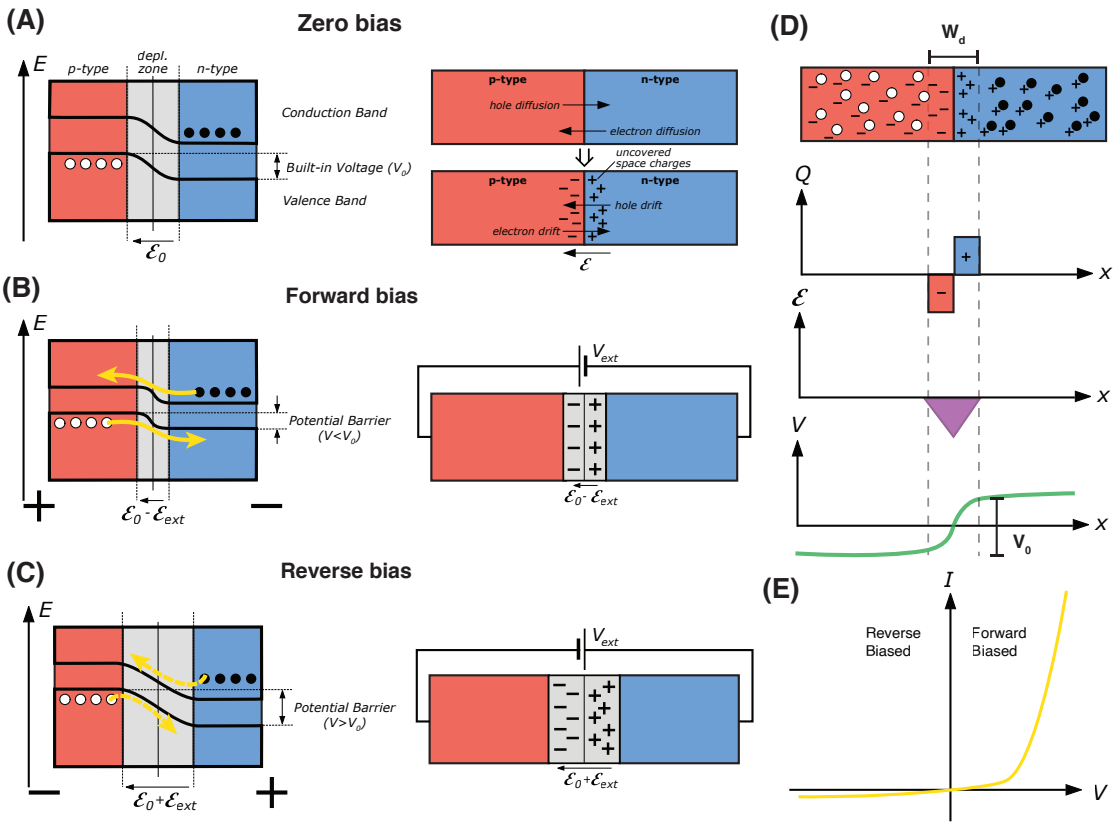

Figure 1.2: **pn diodes.** **(A)** no applied bias, drift and diffusion balance to create a space charge region and a built in potential. **(B)** Under forward bias, the potential height lowers and charges can flow while the space charge region shrinks. **(C)** Under reverse bias, the potential height increases and charges cannot flow while the space charge region grows. **(D)** Schematic of the donors and acceptors with their bound electrons and holes in a pn device. The depletion/space-charge region is devoid of carriers and has ionized donors and acceptors. The charge Q, the electric field ϵ and the voltage in this device is shown. **(E)** Schematic I-V characteristic of a pn diode showing the current rectification. Adapted from [16].

the donors (acceptors) are stripped of their electrons (holes) by redistributing the electrical charge in the system.

In the simplest semiconductor device, a p-n diode, a p-type region is placed in contact with a n-type region (Fig. 1.2). Diffusion of electrons and holes across the p-n interface creates ionized acceptors and donors of opposite charge, which then builds up an electric field across the interface. The directions of carrier drift and diffusion are opposing, such that an equilibrium is reached and a region completely devoid of free carriers is formed (a depletion region Fig. 1.2D). As covered in 4.2, defect or impurity states in the band gap are

isolated from the states of the crystal host resulting in a so called *semiconductor vacuum*. Depletion offers an extension of this, creating a true semiconductor and *charge vacuum*. This idea forms the basis of the results in 11.4[6]. Applying forward and reverse bias as shown in Fig. 1.2B and 1.2B show that electric fields can shrink and grow this depletion region.

Furthermore, under forward bias the applied field opposes the built-in field, reducing the energy barrier for conduction and driving current. Under reverse bias, the applied potential adds to the built-in field and blocks current from flowing. Reverse biased diodes therefore *add to the electric field in the depletion zone*, but *do not drive any current*. The current only flows one way and is *rectifying*, shown Fig. 1.2E. In a sense, charges are blocked from entering the depletion zone and any charges generated in the region get swept away to the zone barriers. Eventually, with high enough reverse bias *dielectric breakdown* occurs, which actually creates an *avalanche photodiode*. These results are easily extendable to p-i-n diodes which have similar physics for depletion and are described in 11.4 (Fig. 1.3C)

We can use these effects to make a solid state transistor by extending the results in the p-n diode. In particular, we will describe the MOSFET (Metal-Oxide-Semiconductor Field-Effect Transistor) which makes up 99.9% of all transistors. Furthermore, MOSFETs made of the semiconductor silicon carbide (SiC) form one of the major motivational technologies for the work in this thesis. The basic idea is that an electrical gate (where voltages are applied) can create a depleted area that has no charge carriers to conduct current (sometimes called the 'field-effect'), and by turning on/off the voltage conductivity is restored. Conversely, by applying sufficient gate voltage, an *accumulation layer* can form a conductive channel between source and drain. Shown in Fig. 1.3, the basic schematic of the MOSFET is a source and drain of either n or p-type, with an opposing p or n channel between them. Fig. 1.3 shows the basic principles of these effects in a MOS capacitor and one particular MOSFET geometry.

It is briefly worth describing the concept of the *Fermi level* that will be become important later. The Fermi level is a thermodynamic (read: equilibrium) concept that in the solid-state

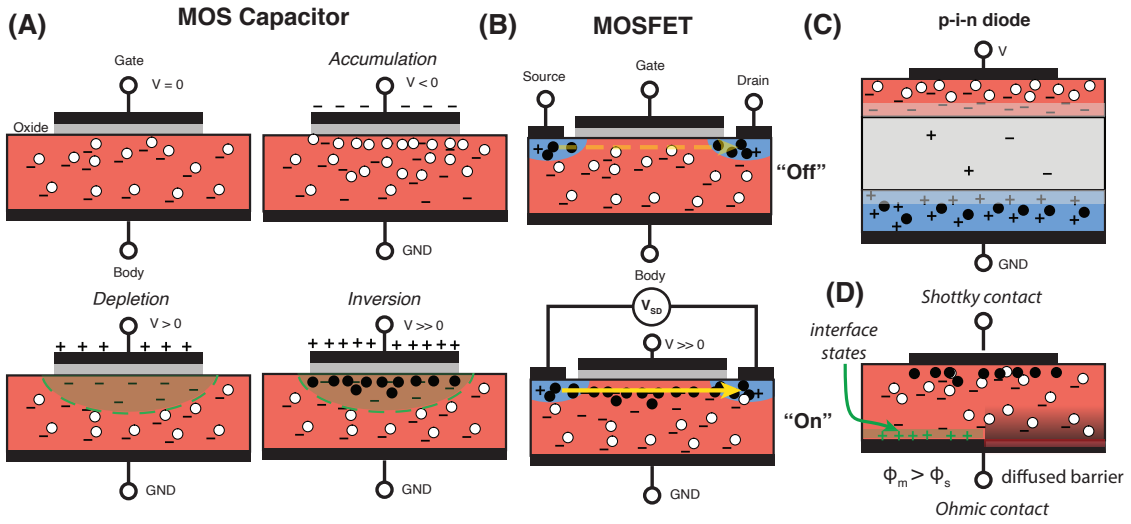

Figure 1.3: **Semiconductor devices that use depletion.(A)** A Metal-Oxide-Semiconductor (MOS) capacitor in accumulation, inversion and depletion. The depleted region is shown in green. **(B)** A MOSFET device (p-channel enhancement mode). Under zero gate voltage, no current can flow. With sufficient positive gate voltage a n-type conducting channel accumulated at the interface and current can flow from the n-type contacts (yellow arrow). **(C)** p-i-n diode schematic. The intrinsic region (grey) has very few donors and acceptor which are ionized. Forward and reverse bias shrink and grow the depletion region at the p-i and i-n interfaces. **(D)** Shottky and Ohmic contacts on a p-type semiconductor. At the Shottky contact, charges build up creating a space-charge region and rectifying barrier for conduction. At the Ohmic contact no charges built up but the Fermi level can be pinned by surface states. Diffusing the metal into the semiconductor eliminates surface-defect state Fermi level pinning.

context means: "if I were to put a level at this energy, it would have a 50/50 chance of being occupied in equilibrium" (Fig. 1.4C). The full probabilistic/thermodynamic distribution of occupation probabilities follows the *Fermi distribution*. Where this distribution is at 50/50 probability is the Fermi level. At high temperatures, the Fermi distribution is spread out such that states above the Fermi level have a nonzero probability of being occupied. At zero (low) temperatures, no states are filled above the Fermi level, and the Fermi level is the highest possible occupied state in equilibrium. In general, there can be separate Fermi levels for electrons and holes. Given that the Fermi level can tell us what states are filled and not filled, in a semiconductor with donors and acceptors, the Fermi level is a valuable construct for thinking about what charges are doing in the device (in equilibrium). That

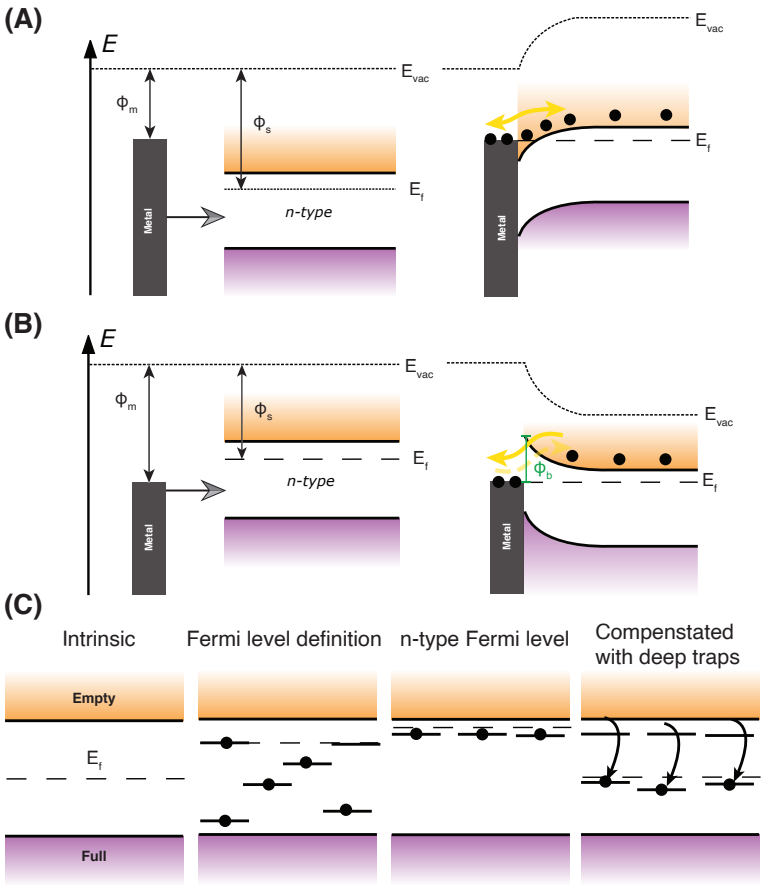

Figure 1.4: **Creating Ohmic contacts and understanding Fermi levels.(A)** Metal-semiconductor interfaces when $\phi_m < \phi_s$. In contact, the bands bend down when with a n-type semiconductor. The contact is Ohmic and current can flow from the metal Fermi sea to the conduction band. **(B)** Metal-semiconductor interfaces when $\phi_m > \phi_s$. In contact, the bands bend up when with a n-type semiconductor. The contact is rectifying (Shottky, non-Ohmic) and current can only flow from the semiconductor to the metal in the form of electrons. For p-type semiconductor contacts, the opposite requirements and trends apply. **(C)** Schematics of the Fermi level in a perfect intrinsic semiconductor. The Fermi level describes the filled levels in equilibrium. In an n-type material the Fermi level is near the CB. However, if many deep defects are introduced, the charges can become trapped in the middle of the bandgap, shifting the Fermi level.

being said, in many cases in this thesis and in device physics, the system is not in equilibrium. Laser excitation and ultralow temperatures cause deviations from equilibrium, along with electrically biasing a device. In these cases, a *quasi Fermi level* describes the new 50/50 point of level occupation in this non-equilibrium system, and can be different for electrons and holes.

To actually make good electrical contact to doped semiconductor layers to create devices, *Ohmic contacts* are needed. When put into physical contact, the Fermi level of a metal and the semiconductor must match (a flat line in energy). This is another way of saying that whatever space-charge regions and electric fields are formed at the semiconductor-metal interface, they must result in the equilibrium energies of electrons matching up. Unfortunately, these built up potentials can prevent currents form flowing. To understand the potentials at the interface, we consider the *work function* of electrons in a metal (ϕ_m) and in a semiconductor (ϕ_s) (defined in reference to the Fermi level, shown in Fig. 1.4). The work function is just the energy needed to remove an electron to infinity, whereby a global energy reference is defined. For an n-type semiconductor, if $\phi_m < \phi_s$, then the CB and VB of the semiconductor must *bend down* at the interface to maintain energy consistency at the vacuum level for a n-type semiconductor (Fig. 1.4A). The bands don't *physically* bend, the bending just represents an energy offset from the effect of the space-charge regions at the interface. In the case of $\phi_m < \phi_s$, this means that electrons can flow freely into the semiconductor. On the other hand, if $\phi_m > \phi_s$, then the bands *bend up* for a n-type semiconductor, creating an energy barrier that the electrons need to pass through of height $\phi_s - \phi_m$ shown in Fig. 1.4B. This is called a *Shottky contact*, and due to the space-charge region, this contact is rectifying much like a p-n diode (Fig. 1.2D) and only allows current to flow in one direction. SiC Shottky diodes are another electrical device that drives the motivations of the work in this thesis. On the other hand, Ohmic contacts are purely resistive and non-rectifying. For a p-type semiconductor, the conditions are flipped and $\phi_m > \phi_s$ gives Ohmic contact.

However, the actual interfacial chemistry of metals and semiconductors is complicated by surface states. By annealing the metal and the semiconductor together, the interface becomes blended with metal-semiconductor alloys. With the proper choice of annealing and metals, the blending eliminates the contact barrier and allows for Ohmic contact (Fig. 1.2D).

Bringing it all together, by fabricating dopants and gates on semiconductors we can create a device that flows current if a gate voltage is 'On' and flows no current when the gate

voltage is 'Off'. This is exactly the transistor described earlier. The patterning/fabrication of these devices uses a process called lithography and happens in a *clean room* (where I spent a good amount of time in graduate school), with lithography being just a fancy type of plastic stenciling. This stenciling at the nanoscale however, drives all of modern technology and is perhaps the most important way of making things unknown by the general public. In this thesis, we will mainly focus on simple p-i-n diodes, but MOSFETs and other more complicated devices and circuits present an exciting avenue towards scaling quantum technologies.

1.1.3 Bits and Qubits

We've described the technology behind the digital technology revolution. Gates on transistors being turned on and off, zeroes and ones. These 'bits' of information can be more than just electrical currents, though. For communication technologies, bits are encoded in photons (light). In some computer memories, bits are magnetic domains on a ferromagnet. Once you have some bits, you want to be able to do operations on them. Transistors and other devices, as described in 1.1.2, can perform logical operations. Representing information in binary, combined with simple Boolean logical operations like ANDs and ORs, can form adders, counters or other complicated computational functions.

What happens when we make things quantum? Quantum mechanics is just the set of rules that describes the universe at the smallest scales, from single atoms and electrons to particles of light. Everything obeys quantum mechanics, it's just that the spooky properties (see 1.2.3, and 1.2.4) of quantum only become apparent at the smallest scales, or at the single particle level ('quantized'). Taking transistors down to the single electron level turns into considering the presence or absence or single charges ('single electron transistors', SETs or charge qubits, see 3.4.3). Communications are taken down to single photons of light (see 3.4.5), and magnetic hard drives are shrunk from being giant domains of electron spins lined up in a ferromagnet and transition to working with single electron spins.

It turns out that single electron spins are a good place to start talking about quantum mechanics. Spin is an intrinsic property of particles that gives them angular momentum, much like a spinning top. However, spin does not describe actual spinning of the particle- it is a property just like charge or mass. Spin describes angular momentum and the magnetic moment of a system, such that the angular momentum is influenced by magnetic fields. Think of a bar magnet (which is weird, since a bar magnet is made of tiny spins all lined up): if you apply a magnetic field, the bar magnet wants to line up with the field (its low energy state). If it is anti-aligned, it has higher energy (unstable, it wants to flip around on you). This is how a single electron spin (or any other spin) behaves in a magnetic field. Furthermore, the bar magnet produces a magnetic field itself, much like a single spin will. There are two states, aligned and anti-aligned, with different energy. You could think about using these two possible states of an electron spin, sometimes called 'Up'(↑) or 'Down'(↓) (1 and 0), as your binary system for computation. However, life isn't that simple. Quantum mechanics, which describes the behavior of single particles, gives us new insight and ways to think about the states of systems. Not only can we make information technologies smaller by moving to single particles, we get exciting new functionalities as well! (see 1.2.3 and 1.2.4)

The basic equation describing quantum mechanics is the (time-independent) Schrödinger equation:

$$H\Psi = E\Psi \tag{1.1}$$

Where H is the Hamiltonian of the system, E is the energy and Ψ is the *wavefunction*. This equation is actually a linear algebra problem (or equivalently, a differential equation problem). H is a matrix (or an *operator*), E is a scalar and Ψ is a vector. The wavefunction represents the state of our quantum system, while H is a quantum analog to the Hamiltonian (related to the Lagrangian) in classical mechanics that describes the energies in a system. When solving this equation, as we know from linear algebra, we get eigenvalue and eigenvector solutions. In the Schrödinger equation, the eigenvalues are the energies of the 'states' that are the eigenvectors. Really, quantum mechanics is just a linear algebra problem with

our states as vectors and dynamics as matrices multiplying those vectors.

In the case of a single electron spin, the Hamiltonian is very simple:

$$H = g\mu_b B \cdot S = \gamma_e B \cdot S \tag{1.2}$$

Where μ_b is the Bohr magneton, the magnetic moment of an electron spin. And g is the electron g factor (described in section 5.3). γ_e is the *gyromagnetic ratio* of the electron spin. This looks very much like the dipole energy E of a classical electron spin $E = -\mu B \cdot S$ (with $\mu = -g\mu_b$), except that now S is a matrix, not a vector. S describes the spin of the electron, which for a spin $= \frac{1}{2}$ particle is described by a vector of *Pauli* matrices (up to a normalization factor):

$$\sigma_x = \begin{pmatrix} 0 & 1 \\ 1 & 0 \end{pmatrix} \qquad \sigma_y = \begin{pmatrix} 0 & -i \\ i & 0 \end{pmatrix} \qquad \sigma_z = \begin{pmatrix} 1 & 0 \\ 0 & -1 \end{pmatrix} \tag{1.3}$$

With $S = [a_x\sigma_x, a_y\sigma_y, a_z\sigma z]$. In a magnetic field oriented along the z-axis (completely arbitrary, though this choice of basis makes things nicer) the Hamiltonian with the proper normalization then looks like:

$$H = g\mu_b B_z \sigma_z/2 = \gamma_e B_z \sigma_z/2 \tag{1.4}$$

Which result in the eigenvectors:

$$\psi_{up} = |\uparrow\rangle = \begin{pmatrix} 1 \\ 0 \end{pmatrix} \qquad and \qquad \psi_{down} = |\downarrow\rangle = \begin{pmatrix} 0 \\ 1 \end{pmatrix} \tag{1.5}$$

Where we have introduced the beginnings of *Dirac notation* for the state *'Kets'*, $|\uparrow\rangle$ and $|\downarrow\rangle$. We can also get the eigenvalues for these eigenvectors:

$$E_\uparrow = g\mu_b B_z/2 \qquad and \qquad E_\downarrow = -g\mu_b B_z/2 \tag{1.6}$$

If we remember our understanding of bar magnets, we recognize that the dipole (μ) aligned with the 'upwards' B_z magnetic field is lower in energy than the dipole aligned against the field. This corresponds to the spin 'down' state with $\mu = -g\mu_b$ (for electrons). This is how we assigned 'up' and 'down' to these states. We then have recovered the classical energies for an electron spin pointing up (high energy) and down (low energy). The two energy levels of this system make an electron in a magnetic field a quintessential example of a quantum two level system (TLS). The eigenstates of this TLS are a little harder to understand.

If we go back to classical systems, the state of a bit can be either 0 or 1. However, we can also describe the state of a *probabilistic* classical system. We construct a vector containing the probabilities to have 0 (p_0) or 1 (p_1):

$$\begin{pmatrix} p_0 \\ p_1 \end{pmatrix} \tag{1.7}$$

This can be used to describe the following scenario: "after I flip this coin and cover it, it is either heads up or tails up with equal probability." Another way of representing this system is with a state vector $\left|P_{system}\right\rangle$:

$$\left|P_{system}\right\rangle = p_{heads}\left|heads\right\rangle + p_{tails}\left|tails\right\rangle = \frac{1}{2}\left|heads\right\rangle + \frac{1}{2}\left|tails\right\rangle = \begin{pmatrix} 0.5 \\ 0.5 \end{pmatrix} \tag{1.8}$$

Where here we have used $|heads\rangle \equiv \begin{pmatrix} 1 \\ 0 \end{pmatrix}$, $|tails\rangle \equiv \begin{pmatrix} 1 \\ 0 \end{pmatrix}$ to represent the outcomes of the coin flip. The probabilities for heads and tails must add to one (be normalized) and be positive (in general). For classical bits like a coin that can be in one of two states, Eq. 1.8 just represents our incomplete knowledge of the system before measurement (looking at the coin). However, the true 'state' of our system is really just $|heads\rangle$ *or* $|tails\rangle$. In formalizing

the state as a vector, we can see that certain computational operations can be generalized as matrices that act on this vector. This gives us the probabilities after an operation, even if we don't know what the input state is exactly. For example, the NOT gate:

$$NOT = \begin{pmatrix} 0 & 1 \\ 1 & 0 \end{pmatrix} \tag{1.9}$$

Additionally, multi (classical) bit states can be treated with a bigger vectors and multi-bit gates can have their "truth-tables" mapped just like the NOT gate above to a matrix form. Overall, treating our classical system as a *vector* allows us to make statements about probabilities, and how operations (which are matrices) act on those probabilities [17].

In quantum mechanics, the situation is very similar, but has important differences. Our choice to use 'kets' ($|ket\rangle$) in Eq. 1.8 was suggestive. Any arbitrary vector, or any arbitrary quantum state, can be described by a similar normalized vector. Since our eigenvectors in Eq. 1.4 form an orthonormal basis set, any arbitrary quantum state can be described in a similar manner to Eq. 1.8. Bringing our example to an electron spin with two eigenstates:

$$\Psi_{spin} = |spin\rangle = a_{\uparrow} |\uparrow\rangle + a_{\downarrow} |\downarrow\rangle \tag{1.10}$$

However, there is a very important difference. $a_{\uparrow}$ and $a_{\downarrow}$ no longer represent probabilities, but represent 'state amplitudes'. Our state vector needs to be normalized, which from linear algebra means that $|a_{\uparrow}|^2 + |a_{\downarrow}|^2 = 1$. Importantly, the state amplitudes can be negative or complex, and are not restricted to positive numbers ≤ 1. The only requirement is that the norm-square sum of amplitudes needs to add to one. This state (Eq. 1.10) represents the actual quantum state of our system, not just incomplete information as in the classical example. The link to the classical example gives us another insight: the norm-squared state amplitudes represent the *probabilities* of a certain outcome, if we were to make a measurement. The measurement process itself is a little tricky, but this is all we need to

know to understand how things are working.

Quantum systems that can be in one of two quantum states are the classical analog of systems that can make a bit. These quantum bits or *'qubits'* are not always in a definite state of being up or down, for example, but can be in an arbitrary state. This state doesn't represent our incomplete knowledge about the state of the system or its probabilities; it represents the wavefunction- the real quantum state of our particle. The wavefunction being an object that describes reality is part of the weirdness of quantum.

1.2 Qubits and Control

1.2.1 The Rotating Wave Approximation

The wavefunction can evolve in time, according to the (time-dependent) Schrödinger equation (Eq. 1.11), which is the equation of motion for the system.

$$H\Psi = i\hbar\frac{d}{dt}\Psi \tag{1.11}$$

Where $\hbar$ is the reduced Planck's constant. This equation can be easily solved if H is time-independent:

$$\Psi(t) = e^{-iHt/\hbar}\Psi(t=0) \tag{1.12}$$

For an electron spin with a field along the z-axis, as described above, we can manipulate the state by driving magnetic fields *perpendicular* to the spin's axis. To show this, we will assume the driving magnetic field is along the x direction. We can use the same Hamiltonian to understand our situation (Eq. 1.2). Expanded out, assuming our driving field is time dependent:

$$H(t) = H_0 + H_{drive}(t) = \gamma_e B_z \sigma_z/2 + \gamma_e B_x(t)\sigma_x/2 \tag{1.13}$$

Where H_0 is our undriven/unperturbed Hamiltonian. Assuming our manipulation tone is an oscillating wave with angular frequency ω, we can define:

$$B_x(t) = |B_x|(I\cos\omega t + Q\sin\omega t) \tag{1.14}$$

Which describes an arbitrary wave with variable phase. This decomposition of the drive, and the modulation of the parameters I and Q in time are called IQ decomposition and IQ modulation, respectively. We will see the importance of this in chapter 2. The IQ decomposition is normalized such that $|I|^2+|Q|^2= 1$.

There is some subtlety about time evolution. There are three possible 'pictures' for quantum mechanics, depending on if the state kets evolve in time, if the operators and observables evolve in time, or if both do. These are called the Heisenberg, Schrödinger and *'interaction'* pictures, respectively. These are mathematically equivalent ways of treating quantum mechanics, but have different definitions.

To start, let's look at time evolution Eq. 1.11 and use H_0, which is the bare Hamiltonian for an electron in a magnetic field without the oscillating components. The time evolution can be expanded in a Taylor series of the exponential (remember, H is a matrix). This looks like:

$$e^{-iHt/\hbar} = \mathbb{I} + -it/\hbar H + \frac{(-it/\hbar H)^2}{2} + \frac{(-it/\hbar H)^3}{6} + ... \tag{1.15}$$

Since

$$\sigma_z^n = \begin{cases} \mathbb{I}, & \text{if n is even} \\ \sigma_z, & \text{if n is odd} \end{cases} \tag{1.16}$$

Or equivalently, by realizing that any power of a diagonal matrix is just the power of the

matrix elements, the time evolution operator is:

$$\begin{pmatrix} 1 + -it/\hbar E_\uparrow + \frac{(-it/\hbar E_\uparrow)^2}{2} + ... & 0 \\ 0 & -(1 + -it/\hbar E_\uparrow) + \frac{(-it/\hbar E_\uparrow)^2}{2} + ...) \end{pmatrix} \tag{1.17}$$

$$= \begin{pmatrix} e^{-it/\hbar E_\uparrow} & 0 \\ 0 & e^{it/\hbar E_\uparrow} \end{pmatrix} = \begin{pmatrix} e^{-it/\hbar E_\uparrow} & 0 \\ 0 & e^{-it/\hbar E_\downarrow} \end{pmatrix} \tag{1.18}$$

Using the definitions for the energies in Eq. 1.6. For an initial state $|\Psi\rangle = a|\uparrow\rangle + b|\downarrow\rangle$, the time evolution operator Eq. 1.17 gives the state at a later time:

$$|\Psi(t)\rangle = ae^{-i\frac{E_\uparrow}{\hbar}t}|\uparrow\rangle + be^{-i\frac{E_\downarrow}{\hbar}t}|\downarrow\rangle \tag{1.19}$$

This is the Schrödinger picture where the kets evolve in time. In general, *eigenstates accumulate phase according to their energies*, where the frequency of oscillation is $E/\hbar$. This is related to the energy-frequency relation of quantum mechanics $E = \hbar\omega$, such that:

$$H_0 = \begin{pmatrix} E_\uparrow & 0 \\ 0 & E_\downarrow \end{pmatrix} = \hbar \begin{pmatrix} \omega_0/2 & 0 \\ 0 & -\omega_0/2 \end{pmatrix} = \hbar\omega_0\sigma_z/2 \tag{1.20}$$

$$|\Psi(t)\rangle = ae^{i\omega_0 t/2}|\uparrow\rangle + be^{-i\omega_0 t/2}|\downarrow\rangle \tag{1.21}$$

This same time evolution has a classical analog to spin precession in a magnetic field (Larmor precession). For quantum information however, we commonly want to make a transformation where the states we are talking about are stationary in time. An ideal bit shouldn't do anything when left alone.

In particular, we will operate in the interaction picture with the unperturbed qubit Hamiltonian H_0 and a perturbation H_{drive}. In the interaction picture, the state kets and

the Hamiltonian (H_I) are defined using a transformation $U(t)$ (moving to a different basis):

$$H(t) = H_0 + H_{drive}(t) \tag{1.22}$$

$$U(t) = e^{iH_0 t/\hbar} \tag{1.23}$$

$$H_I = U^\dagger H_{drive}(t) U \tag{1.24}$$

And importantly the new states in the interaction picture:

$$|\Psi_I(t)\rangle = U\,|\Psi(t)\rangle = a\,|\uparrow\rangle + b\,|\downarrow\rangle \tag{1.25}$$

Where by comparing to Eq. 1.19, we can see that the explicit time dependence has been removed. The time evolution happens on these states defined according to the perturbing Hamiltonian H_I. Just as in Eq. 1.12:

$$\Psi_I(t) = e^{-iH_I t/\hbar}\Psi_I(t=0) \tag{1.26}$$

Note that the Eq. 1.25 has the time dependence in the kets included in the definition of the new kets in the interaction picture. We've just applied a transformation that exactly undoes the evolution from the bare qubit Hamiltonian. Eq. 1.24 is a general way to find the new Hamiltonian after using a transformation U (from linear algebra). Another way of viewing this is that we are moving to a frame that rotates with the phase accumulation at the qubit frequency ω_0. This is the beginning of the *rotating wave approximation* (though here technically we are just moving into the interaction frame).

We already know what the matrix exponential of H_0 is, giving:

$$U(t) = e^{iH_0 t/\hbar} = \begin{pmatrix} e^{i\omega_0 t/2} & 0 \\ 0 & e^{-i\omega_0 t/2} \end{pmatrix} \tag{1.27}$$

Going through the matrix multiplication of Eq. 1.24 using Eq. 1.13 for our example of a spin, we end up with:

$$H_I = A \begin{pmatrix} 0 & e^{-i\omega_0 t} \\ e^{i\omega_0 t} & 0 \end{pmatrix} \tag{1.28}$$

Where:

$$A = \frac{\gamma_e}{2}|B_x|(I\cos(\omega t) + Q\sin(\omega t)) = A_0[I\frac{(e^{i\omega t} + e^{-i\omega t})}{2} + Q\frac{(e^{i\omega t} - e^{-i\omega t})}{2i}] \tag{1.29}$$

With $A_0 = \frac{\gamma_e}{2}|B_x|$. Multiplying the exponentials in Eq. 1.28 with the definitions in 1.29, we find (complex exponential) terms that rotate at $\omega + \omega_0$ and other terms which evolve at $\omega - \omega_0$. In the limit that the detuning $\Delta = \omega - \omega_0 \approx 0$, we have fast rotating terms at $\sim 2\omega$ and relatively slow ones. The major assumption of the rotating wave approximation is that *the rapidly oscillating terms average out to zero and do not contribute to the dynamics*. This is generally an extremely good assumption, as long as $\Delta << \omega$ and $A_0 << \omega$. As shown later, this second condition corresponds to the *Rabi* frequency needing to be smaller than the qubit frequency. Deviations from the validity of this approximation results in the so-called *Bloch-Siegert* shift.

Once we ignore the terms that rapidly rotate, and keep the other terms, we get:

$$H_{RWA,I} = A_0 \begin{pmatrix} 0 & \frac{1}{2}(Ie^{i\Delta t} - iQe^{i\Delta t}) \\ \frac{1}{2}(Ie^{-i\Delta t} + iQe^{-i\Delta t}) & 0 \end{pmatrix} \tag{1.30}$$

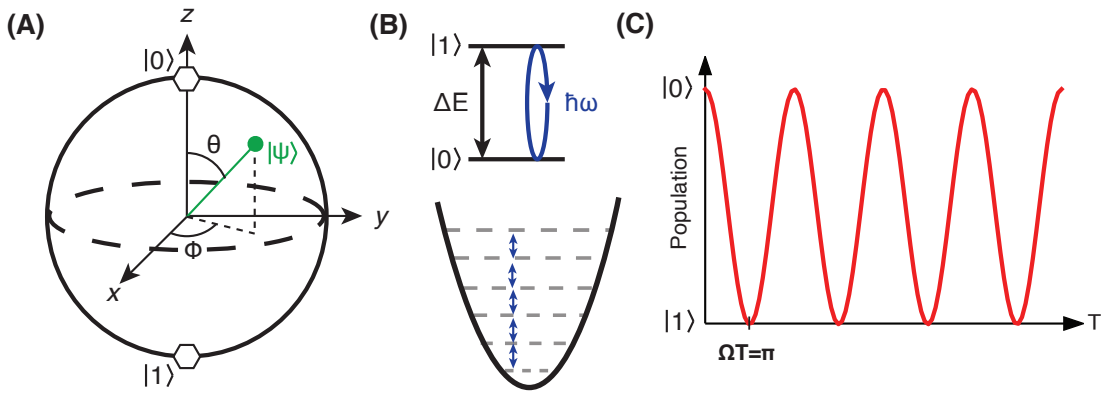

Figure 1.5: **Bloch spheres, quantum objects and dynamics. (A)** The Bloch sphere. **(B)** TLS are qubits with well-defined energy splitting ΔE which can be driven and manipulated. Harmonic systems have equally spaced levels that cannot be individually addressed.**(C)** Rabi oscillations of a qubit prepared in $|0\rangle$.

In the limit that we can assume we are on resonance, $\Delta = 0$, and:

$$H_{RWA,I} = A_0 \begin{pmatrix} 0 & \frac{(I-iQ)}{2} \\ \frac{(I+iQ)}{2} & 0 \end{pmatrix} \tag{1.31}$$

Noting the definitions in Eq. 1.3, we can rewrite:

$$H_{RWA,I} = A_0 I \sigma_x/2 + A_0 Q \sigma_y/2 \tag{1.32}$$

For which we define the *Rabi frequency* $\Omega = \gamma_e |B_x|/(2\hbar) = A_0/\hbar$, such that:

$$\frac{H_{RWA,I}}{\hbar} = \Omega I \sigma_x/2 + \Omega Q \sigma_y/2 \tag{1.33}$$

This is a great result. In the same way that σ_z gives phase accumulation which is a 'z-rotation' (precession), σ_x and σ_y give x and y rotations of our qubit state. By controlling I and Q (the phase of our driving magnetic field) we can perform arbitrary x and y rotations of varying angles. The time dependence/oscillating nature of our drive is also gone, and our rotating wave Hamiltonian is constant in time. The axes x and y here in the rotating frame

are arbitrary, and are picked out by either being 'in-phase' (I) or 'out-of-phase' (Q) with the frame rotating with the spin (or qubit). How can we think about these angles? Why are we referring to the Pauli terms as rotations? What do these rotations do? This is covered in the next section, 1.2.2.

Technically, the rotating frame and the interaction frame are different, with one rotating with the qubit and one rotating with the drive. On resonance, there are no differences. However, with a small detuning in the rotating frame there is an additional Hamiltonian term $\frac{\Delta}{2}\sigma_z$ that corresponds to unwanted extra phase accumulations of our states. The exact treatment for nonzero detunings is not explored here. However, it's easy to think about decomposing a $\frac{\omega_0}{2}\sigma_z$ term in the original Hamiltonian to be $\frac{\omega}{2}\sigma_z + \frac{\Delta}{2}\sigma_z$ such that the extra $\frac{\Delta}{2}\sigma_z$ term becomes part of the perturbing Hamiltonian (H_{drive}). Applying the transformation U to this term to this term results in no change, such that in H_I there is an additional $\frac{\Delta}{2}\sigma_z$ term in the frame that rotates with ω.

Furthermore, we can note that in the interaction picture, the only terms in the Hamiltonian are Pauli matrices multiplied by the Rabi rate. This means that if we diagonalize, the energy splittings between our new eigenstates will be the Rabi frequency. If we diagonalize Eq. 1.22 fully, we will see extra moving of the states according to the Rabi rate. This is related to the AC Stark and Autler-Townes splitting of qubit and multi-level quantum systems, but we don't need many details of this for the purposes of this thesis.

1.2.2 The Bloch Sphere

To understand, let's think about an arbitrary quantum state of a two level system. We know that our state is a vector that can have complex values, and that the norm-squared amplitudes need to add to one (normalized vector). We can write any state with these constraints as:

$$|\Psi\rangle = \cos(\theta/2)\,|0\rangle + e^{i\phi}\sin(\theta/2)\,|1\rangle \tag{1.34}$$

Where $|\downarrow\rangle = |0\rangle$ and $|\uparrow\rangle = |1\rangle$, relates the general treatment of a qubit with two states in analogy to classical binary logic to the spin example. If we define $|Z\rangle = |0\rangle$, $|-Z\rangle = |1\rangle$, $|X\rangle = \frac{|0\rangle+|1\rangle}{\sqrt{2}}$, $|-X\rangle = \frac{|0\rangle-|1\rangle}{\sqrt{2}}$, $|Y\rangle = \frac{|0\rangle+i|1\rangle}{\sqrt{2}}$, $|-Y\rangle = \frac{|0\rangle-i|1\rangle}{\sqrt{2}}$, we see that this representation relates to spherical coordinates of a unit sphere that looks like Fig. 1.2.2A. The coordinate system here is a little odd, since $|0\rangle$ and $|1\rangle$ are along the same axis, but are orthogonal states (in the *Hilbert space*, the mathematical space where the state vectors live). The relation to spherical coordinates can be done by relating the coordinates in regular polar coordinates $\cos(\theta)\hat{z} + e^{i\phi}\sin(\theta)\hat{x}$ to this weird basis where $|0\rangle$ and $|1\rangle$ should be orthogonal ($\pi/2$, not π), and the polar angle will be half ($\theta/2$ instead of θ).

Here's the connection: the Hamiltonian terms that look like σ_x and σ_y are rotations of the qubit state about the x and y axis *on the Bloch sphere*. For example, let's say we initialize our qubit into $|0\rangle$ and apply our manipulation tone on our spin in phase (I=1).

$$\frac{H_{RWA}}{\hbar} = \omega_0\sigma_z/2 + \Omega\sigma_x/2 \tag{1.35}$$

$$\frac{H_{RWA,I}}{\hbar} = \Omega\sigma_x/2 \tag{1.36}$$

$$|\Psi_I(t)\rangle = e^{-iH_{Drive,I}t}\,|0\rangle = e^{-i\Omega\sigma_x t/2}\,|0\rangle \tag{1.37}$$

Using:

$$\sigma_x^n = \begin{cases} \mathbb{I}, & \text{if n is even} \\ \sigma_x, & \text{if n is odd} \end{cases} \tag{1.38}$$

We can expand our time evolution operator acting on $|0\rangle$ which simplifies:

$$\begin{gathered}|\Psi(t)\rangle = e^{-i\Omega\sigma_x/2t}\,|0\rangle = \\ \begin{pmatrix} 1+\frac{(-it\Omega/2)^2}{2}+\frac{(-it\Omega/2)^4}{4!}+... & (-it\Omega/2)+\frac{(-it\Omega/2)^3}{3!}+... \\ (-it\Omega/2)+\frac{(-it\Omega/2)^3}{3!}+... & 1+\frac{(-it\Omega/2)^2}{2}+\frac{(-it\Omega/2)^4}{4!}+...) \end{pmatrix}|0\rangle \\ = \begin{pmatrix} 1+\frac{-(t\Omega/2)^2}{2}+\frac{(t\Omega/2)^4}{4!}+... & -i(t\Omega/2)+\frac{i(t\Omega/2)^3}{3!}+... \\ -i(t\Omega/2)+\frac{i(t\Omega/2)^3}{3!}+... & 1+\frac{-(t\Omega/2)^2}{2}+\frac{(t\Omega/2)^4}{4!}+...) \end{pmatrix}|0\rangle \end{gathered} \tag{1.39}$$

We note that the expansions of $\sin(x) = x - x^3/3! + x^5/5! + ...$ and $\cos(x) = 1 - x^2/2! + x^4/4! + ...$, such that our time evolution operator is just:

$$|\Psi(t)\rangle = \begin{pmatrix} \cos(\Omega/2t) & -i\sin(\Omega/2t) \\ -i\sin(\Omega/2t) & \cos(\Omega/2t) \end{pmatrix}|0\rangle = \begin{pmatrix} \cos(\Omega/2t) & -i\sin(\Omega/2t) \\ -i\sin(\Omega/2t) & \cos(\Omega/2t) \end{pmatrix}\begin{pmatrix} 1 \\ 0 \end{pmatrix} \tag{1.40}$$

This matrix is just the rotation matrix about the x-axis. Thus:

$$|\Psi(t)\rangle = \cos(\Omega/2t)\,|0\rangle - i\sin(\Omega/2t)\,|1\rangle \tag{1.41}$$

$$R_x(\theta) = \begin{pmatrix} \cos(\theta/2) & -i\sin(\theta/2) \\ -i\sin(\theta/2) & \cos(\theta/2) \end{pmatrix} \tag{1.42}$$

Note that a rotation of θ has $\theta/2$'s in the sines and cosines. In general, for any rotation on the Bloch sphere about axis $\hat{n}$ (a vector on the Bloch sphere) and of angle θ, the rotation evolution is just $e^{-i\theta\hat{n}\cdot\sigma}$, where σ is the vector of Pauli matrices. Using an analogy to Euler's formula $e^{i\theta} = \cos(\theta) + i\sin(\theta)$, it can be shown that any rotation will just be $\cos(\theta) + i\hat{n}\cdot\sigma\sin(\theta)$. In other words, with both I and Q control on our drive, we have two independent axes of rotation (x and y) and can access any part of the Bloch sphere through qubit rotations. We then have universal control of our single quantum bit using oscillating field driven dipole

transitions.

For our example, if we look at Eq. 1.41, at time $t = \frac{\pi}{\Omega}$ our state is $|\Psi\rangle = |1\rangle$ and the term inside the cosine and sines are $\pi/2$, but the rotation matrix Eq. 1.42 is for an 'angle' of π. If we turn off our drive at this point, we will have flipped the spin from $|0\rangle$ to $|1\rangle$ and done a 'π' pulse which corresponds to a NOT gate. Turning our drive on for only half that time takes us to the state $|\Psi\rangle = \frac{|0\rangle - i|1\rangle}{\sqrt{2}}$, which is on the 'equator' of the Bloch sphere (Fig. 1.2.2) and is a (right-handed) rotation *about* the x-axis of '$\pi/2$' onto the '-y'-axis and corresponds to the commonly-used *Hadamard gate*. Leaving the drive on continuously, we will rotate around the Bloch sphere and oscillate between $|0\rangle$ and $|1\rangle$. This is called a *Rabi Oscillation*, shown in Fig. 1.2.2C. In general, a Rabi oscillation experiment involves polarizing the qubit, then applying a drive pulse of varying length (t), and reading out the population in one of the eigenstates in which we will see oscillations of the qubit. The treatment of this section is universal to two level systems and shows how to drive single qubit gates, which we can achieve by pulsing drive tones with different phases on resonance with our TLS.

1.2.3 Superposition

Backing things up a bit, what does the state $|\Psi\rangle = \frac{|0\rangle + |1\rangle}{\sqrt{2}}$ *mean*, for example? This state is in a *superposition*. As discussed in 1.1.3, it represents a definite state of our qubit, but upon measurement we can only make *probabilistic* statements about the outcome. In the context of the example of a single spin, such a state represents the spin both pointing up and pointing down *at the same time*. Superposition states describe the indefinite quantum state of being in two discrete possibilities at the same time. The often cited example of this effect is Schrödinger's cat, which emphasizes how bizarre these states can truly be. This is one of the major properties of quantum mechanics that quantum technologies try to leverage.

In particular, let's move onto *multi-qubit* states. In the same way that many bits of information can be represented as a series of ones and zeros, the states of many qubits can be described. If we remember, the state of one qubit is just a vector with dimension of

the number of possible states. For one qubit, this is either 0 or 1. For two qubits, we have the possibilities 0_A0_B, 0_A1_B, 1_A0_B, and 1_A1_B or 4 possible states of the measurement outcomes (with the first qubit labelled A, and the second qubit labelled B). The quantum state of this two particle system is then a 4 element vector. For three qubits there are 2^3 possible qubit state combinations that describe our full quantum state. We can easily see that with large qubit number (N), this number grows like 2^N such that the state vector is huge. We established in section 1.2.2 that single qubit operations like flipping spins and creating superpositions are possible. These operations are the direct analogs of single bit operations like NOTs. However, the power in classical computing is in logical operations that take multiple bits as the input and gives multi-bit outputs corresponding to Boolean operations like ANDs and ORs, for example. These are the operations that the transistors in section 1.1.2 provide. The quantum equivalent to these operations are *two-qubit* (or *multi-qubit*) operations. These operations are possible in many qubit candidates, but in general are much harder than single qubit operations.

A simple (if slightly inaccurate) comparison to classical computing is that of a circuit that does a computation on a given input (0_A0_B, for example), and gives an output. To see what the result of the computation is for another input (such as 1_A0_B) instead, we have to run through the whole calculation again. For large numbers of bits, we can see that to test all the possibilities we need to run 2^N times. However, in quantum information we can prepare a large superposition state that has amplitudes in all the different possibilities. Running through the *quantum circuit*, this state has equivalently 'run the computation' on all the possibilities at the same time (parallelization). It's easy to see how with clever choices of the types of superpositions, combined with one and two qubit gates and measurements that we can read out state amplitudes that correspond to useful quantities. This description gives a flavor for the power of superposition, but many subtleties are swept under the rug.

1.2.4 Entanglement

The other major property that quantum technologies leverage is *entanglement*. Let's look at the state:

$$|\Psi\rangle = \frac{|0_A 0_B\rangle + |1_A 1_B\rangle}{\sqrt{2}} \tag{1.43}$$

This is one of the 2 qubit superposition states we discussed in 1.2.3. What this state means is that when measuring, either both qubits are 0's, or both are 1's, and there is no amplitude of them being in any other configuration. We can create such a state with one and two-qubit operations, and look at results from single qubit measurements. For example, the classic entangling/two-qubit gate (operator) is a CNOT. Just as in classical logic, a $C_A NOT_B$ is a gate that is a NOT ($|0\rangle \rightarrow |1\rangle$,$|1\rangle \rightarrow |0\rangle$, or just a π pulse) that only happens when qubit A is in state $|1\rangle$, and nothing happens when A is in state $|0\rangle$. In matrix form:

$$U_{CNOT} = \begin{array}{c} \\ 0_A 0_B \\ 0_A 1_B \\ 1_A 0_B \\ 1_A 1_B \end{array} \begin{array}{c} \begin{array}{cccc} 0_A 0_B & 0_A 1_B & 1_A 0_B & 1_A 1_B \end{array} \\ \begin{bmatrix} 1 & 0 & 0 & 0 \\ 0 & 1 & 0 & 0 \\ 0 & 0 & 0 & 1 \\ 0 & 0 & 1 & 0 \end{bmatrix} \end{array} \tag{1.44}$$

Applying this gate to an initial state $|\Psi\rangle$ that is just a combination of states we can easily make with single qubit rotations/initialization:

$$|\Psi\rangle = \frac{|0_A\rangle + |1_A\rangle}{\sqrt{2}} \otimes |0_B\rangle = \frac{|0_A 0_B\rangle + |1_A 0_B\rangle}{\sqrt{2}} \tag{1.45}$$

$$U_{CNOT}\,|\Psi\rangle = \frac{|0_A 0_B\rangle + |1_A 1_B\rangle}{\sqrt{2}} \tag{1.46}$$

Which is the state in Eq. 1.43. One way for creating this gate is to have two qubits that are strongly coupled (see chapter 2). For example, if I have an electron spin A dipole-dipole

coupled to a nuclear spin B, then my Hamiltonian is:

$$H = \gamma_e B_z \cdot S_{z,A} + \gamma_n B_z \cdot S_{z,B} + g\ S_{z,A} \cdot S_{z,B} \tag{1.47}$$

Where we have assumed that the coupling strength 'g' is the dipole-dipole energy (more generally the *hyperfine* coupling, see chapter 13), and that the magnetic field is along z and that the axis between the spin is perpendicular to z. This energy is analogous to two bar magnets wanting to line up opposite to each other. Since this is a two-qubit system, our state vector has 4 amplitudes and the Hamiltonian can be written explicitly with both qubits in mind:

$$H = \gamma_e B_z \cdot S_{z,A} \otimes \mathbb{I}_B + \gamma_n B_z \cdot S_{z,B} \otimes \mathbb{I}_A + g \cdot S_{z,A} \otimes \mathbb{I}_B \cdot S_{z,B} \otimes \mathbb{I}_A \tag{1.48}$$

Where '$\mathbb{I}$' is the identity and '$\otimes$' is the outer product. For reference, an easy way to find the new $4x4$ matrices for this system is to take the 'Kronecker product' of the single qubit matrices (using *Mathematica*, for example). You can also use it to find a multiqubit state vector from the single qubit states as in Eq. 1.45. Multiplying out all the matrices and defining $\gamma B_z \cdot S_z = \omega \sigma_z / 2$:

$$\frac{1}{2}\begin{bmatrix} \omega_A + \omega_B + 2g & 0 & 0 & 0 \\ 0 & -\omega_A + \omega_B - 2g & 0 & 0 \\ 0 & 0 & \omega_A - \omega_B - 2g & 0 \\ 0 & 0 & 0 & -\omega_A - \omega_B + 2g \end{bmatrix} \tag{1.49}$$

Since the Larmor/qubit frequency of the electron is much greater than that of the nuclear spin (since the magnetic moment of a nuclear spin is small), we can simplify:

$$\frac{1}{2}\begin{bmatrix} \omega_A + 2g & 0 & 0 & 0 \\ 0 & -\omega_A - 2g & 0 & 0 \\ 0 & 0 & \omega_A - 2g & 0 \\ 0 & 0 & 0 & -\omega_A + 2g \end{bmatrix} \tag{1.50}$$

The assumption that $\omega_A >> \omega_B$ is not necessary, but does simplify the analysis here. Since all the elements are already diagonal, these elements are just the energies of our eigenstates. Drawing this out we see the energy structure in Fig. 2.1B.

Essentially, the coupling term 'g' splits our electron spin's energy levels into two (the *hyperfine* splitting). If g is larger than the linewidth of our electron and nuclear spin transitions, then a drive tone can be tuned into resonance with two of these lines. Specifically, we can see that driving $|0_A 0_B\rangle \leftrightarrow |1_A 0_B\rangle$ and $|1_A 1_B\rangle \leftrightarrow |0_A 1_B\rangle$ have distinct energies depending on qubit B's state. This drive is then *conditional* on the nuclear spin (qubit). On the other hand, $|0_A 0_B\rangle \leftrightarrow |1_A 1_B\rangle$ and $|0_A 1_B\rangle \leftrightarrow |1_A 0_B\rangle$ have the same energy. This drive is *unconditional* in that it is on resonance no matter if qubit B is in 0 or 1. In the two qubit system, our drive couples the same way as in 1.2.2 and we can perform π pulses on these transitions (a fun exercise to prove to yourself).

In particular, if we perform a π pulse on $|1_A 0_B\rangle \leftrightarrow |0_A 0_B\rangle$ we map:

$$\begin{aligned} |0_A 0_B\rangle &\rightarrow |1_A 0_B\rangle \\ |0_A 1_B\rangle &\rightarrow |0_A 1_B\rangle \\ |1_A 1_B\rangle &\rightarrow |1_A 1_B\rangle \\ |1_A 0_B\rangle &\rightarrow |0_A 0_B\rangle \end{aligned} \tag{1.51}$$

this is the operator:

$$\begin{bmatrix} 1 & 0 & 0 & 0 \\ 0 & 1 & 0 & 0 \\ 0 & 0 & 0 & 1 \\ 0 & 0 & 1 & 0 \end{bmatrix} = U_{CNOT} \tag{1.52}$$

Which is exactly the CNOT from Eq. 1.44. Additionally, we can perform a π pulse on $|0_A 0_B\rangle \leftrightarrow |1_A 1_B\rangle$ and $|0_A 1_B\rangle \leftrightarrow |1_A 0_B\rangle$ (which are degenerate). This is just an unconditional rotation of both qubits:

$$\frac{1}{2}\begin{bmatrix} 0 & 0 & 0 & 1 \\ 0 & 0 & 1 & 0 \\ 0 & 1 & 0 & 0 \\ 1 & 0 & 0 & 0 \end{bmatrix} = \sigma_{x,A} \otimes \sigma_{x,B} \tag{1.53}$$

The fact that we can decompose this operator (separable) also demonstrates why it is an unconditional gate (only two single qubit gates). The CNOT in Eq. 1.52 cannot be decomposed in this way. The point of this exercise is to illustrate how coupling systems together allows for an energy splitting which can be used to drive *conditional* gates which form the basis of two-qubit gates such as the CNOT. In particular, the energy splitting needs to be large enough to have the lines resolved. Details and further considerations are mentioned in chapter 2.

We have to remember that this (Eq. 1.46) is the state of two qubits, physically separate and distinct objects. If we generate this state, and put both qubits in separate black boxes, if we open one box and see "qubit A is in state $|0\rangle$"- then, without even opening the box with qubit B inside we *already know its state* to be $|0\rangle$. The results of measuring will always be random (50%: 0, 50%: 1), but will be perfectly correlated. Importantly, we can physically separate black box A and black box B such that the result that we measure for qubit A *would have to be communicated faster than the speed of light* in order to change the

outcome for qubit B (if we measure it immediately after qubit A). Another way of saying this is that quantum mechanics and entanglement say that the universe is *inherently non-local*, meaning that quantum correlations fly in the face of Einstein's relativity. Sometimes this is referred to as 'spooky action at a distance' and is illustrated in the seminal *EPR* (Einstein-Podolsky-Rosen) paper[18]. Proofs of this involve violating *Bell's inequalities or 'Bell tests'* which eliminates 'hidden' classical correlations (at a distance). These inequalities eliminate the possibility that classically correlated pairs of particles are generated (such as equal production of either $|00\rangle$ or $|11\rangle$, but not Eq. 1.46) by measuring the qubits in different ways and looking at the statistics. For example, if I rotate both qubit A and B by $\pi/2$ then for the entangled state is transformed:

$$\begin{aligned} \frac{|0_A 0_B\rangle + |1_A 1_B\rangle}{\sqrt{2}} \implies & (|0_A\rangle + |1_A\rangle)(|0_B\rangle + |1_B\rangle) + (|0_A\rangle - |1_A\rangle)(|0_B\rangle - |1_B\rangle) \\ & = \frac{|0_A\rangle|0_B\rangle + |1_A\rangle|1_B\rangle}{\sqrt{2}} \end{aligned} \tag{1.54}$$

Such that upon measurement, we still see that the correlations are preserved. But if we had classically correlated states and applied the same pulse:

$$\begin{aligned} |0_A 0_B\rangle\,, 50\%, \quad |1_A 1_B\rangle\,, 50\% \implies & \\ |0_A 0_B\rangle + |0_A 1_B\rangle + |1_A 0_B\rangle + |1_A 1_B\rangle\,,\ 50\% & \\ |0_A 0_B\rangle - |0_A 1_B\rangle - |1_A 0_B\rangle + |1_A 1_B\rangle\,,\ 50\% & \end{aligned} \tag{1.55}$$

Then there's a chance we measure $|0_A 1_B\rangle$ or $|1_A 0_B\rangle$. The conclusion is that the measurement outcomes are different between classical and quantum correlations. This is ironclad unless our qubit knows what we're doing, and sends a classical signal to the other qubit to flip it appropriately. Separating the two qubits such that they would have to communicate faster than the speed of light while maintaining these correlations shows the non-locality of nature. Thus, by measuring the entangled qubits in different basis directions and comparing the correlations, one can then compare to the *Bell* or *CHSH* inequalities to prove that

quantum mechanics is incompatible with these 'local hidden variable' theories. This is one of most exciting aspects of quantum mechanics that quantum technologies try to leverage. Furthermore, using entanglement we can 'teleport' the quantum state of a particle from one location to another or use *superdense coding* and perform other quantum oddities.

Entanglement describes the quantum correlations of qubit states that can occur after two-qubit operations. With many qubits, we can create large entangled states that have exotic properties. In a full quantum analog of a computer, superpositions and entanglement arising from these gates give rise to new abilities for quantum information.

1.2.5 Quantum Circuits and Algorithms

Using two qubit (such as CNOTs) and single qubit operations, many quantum algorithms have been developed that could be run on a *quantum computer*, a device with full initialization, control and readout of many fully-connected qubits. These algorithms and other quantum processes for many qubits are commonly framed in quantum circuit diagrams which are inspired by classical circuit diagrams. Importantly, many of these algorithms outperform their classical counterparts on specific problems with important examples being *Grover's*[19] and *Shor's*[20] algorithms, which can search unstructured databases and factor large numbers in 'polynomial' time. As the number of bits (or qubits) gets larger, classical algorithms get exponentially harder- so the ability to solve many problems in polynomial time constitutes an *exponential speedup* of quantum computers compared to classical computers. Importantly, RSA encryption which forms the basis of most technology today relies on the exponential 'hardness' of factoring large numbers such that a large enough 'key' would take a supercomputer many years to crack (see chapter 8). Computer and quantum scientists are constantly coming up with new algorithms that can outperform classical computing.

1.2.6 The Density Matrix

Arguably, a more natural way to think about quantum mechanics is to think about an object called the *density matrix* that has an even closer analogy to the classical probabilities example in 1.1.3.

$$\rho = \sum_j p_j \left|\psi_j\right\rangle \left\langle\psi_j\right| \tag{1.56}$$

Where $\langle\psi|$ is called a *'Bra'* and is the row vector equivalent of the column state vectors as in Eq. 1.5 and p_j is the classical probability to be in state j (such that the sum of the p_j's add to one, and p_j is real and non-negative). Multiplying the row and column vectors means that this object is a square matrix. Eigenstates correspond to 'on-diagonal' elements of this matrix, while 'coherences' (or superpositions) make the off diagonal elements nonzero. The density matrix formalism is a completely general treatment of quantum mechanics but also can treat so-called 'mixed' states that describe probabilistic mixtures of of the quantum states (starting in classical 50:50 mixtures such as Eq. 1.55 or in thermal equilibrium, for example). In reality, to measure superpositions and entangled states we can only really measure *statistics* on measurement results, and the density matrix treats the statistics/ensembles of measurements easily. The density matrix can evolve in time, and linear algebra manipulations of it can represent the measurement process or give the results of measurements in a particular basis. For mixed states/ensembles of measurements, the density matrix can be used to find the *Bloch vector* of our qubit which is a vector on the Bloch sphere, but does not need to be of unit length. Due to decoherence and depolarization, the Bloch vector can shrink to zero length. In general, the density matrix is a powerful tool for treating quantum systems (especially with losses, decoherence and measurement). Particularly, testing that multi-qubit states are actually entangled sometimes involves tests of the density matrix of the two qubit system (such as the PPT test, see chapter 13). That being said, all the details and applications of the density matrix are not as relevant to the bulk of the work in this thesis and we will mostly use the state ket notation of quantum.

Chapter 2

Decoherence, Lifetimes and Linewidths

The problem with dealing with any quantum system is that the things that make it look quantum (*superposition* and *entanglement*), are quite fragile. Just as with classical waves, coherence refers to consistent phases over time and space. Coherent light from a laser, for example, can display interference fringes because the light can have a definite phase and constructively and destructively *interfere*. *Decoherence* is the unwanted scrambling of the amplitudes and phases of our quantum system, usually by the qubit's 'environment'. For most quantum systems, holding onto the 'quantum-ness' for long periods of time is referred to having a long 'coherence time'. There are a few basic relevant metrics we will go through here. Many of these processes are understandable through a density matrix picture, but I will keep things simple. In particular, we can describe how these measurements are done in terms of the control described in 1.1.3.

2.1 T_1

T_1 is an energy relaxation time, and is not directly related to coherences. It is the state lifetime of your qubit (Fig. 2.1A). This could be the radiative lifetime of an optical transition,

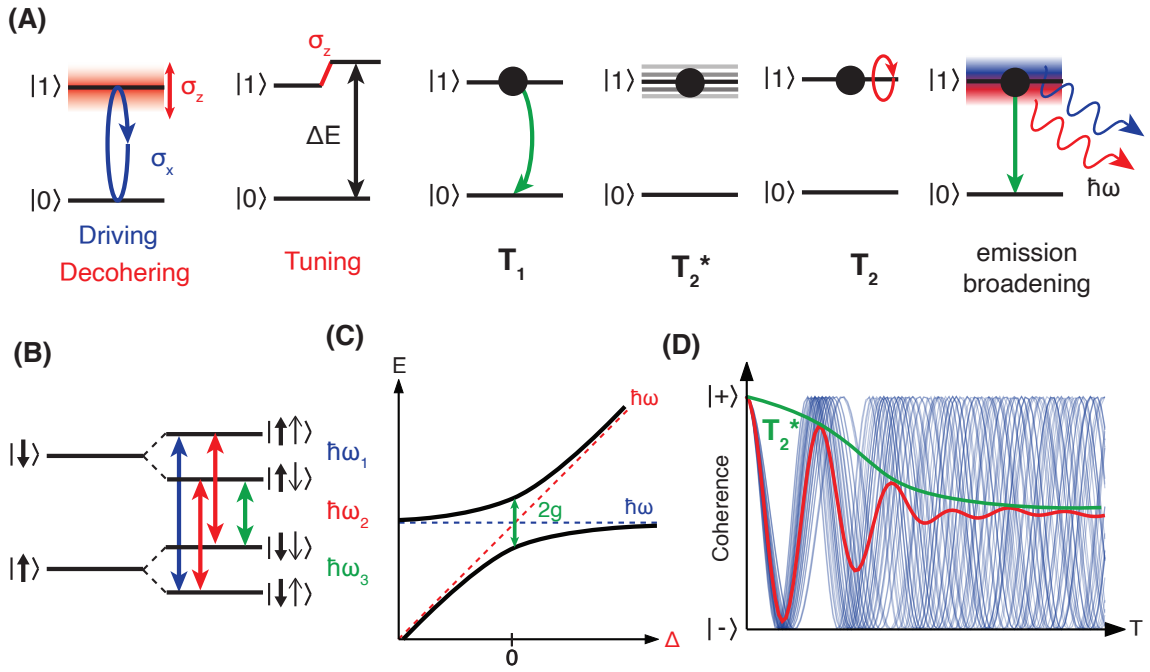

Figure 2.1: **Decoherence, tuning and coupling.(A)** (left to right) Different terms/dipoles of the qubit allow for either driving and manipulation, and for the shifting and decoherence of the states. However, the term that decoheres is also a term that can be used for tuning the energies of quantum states. In general, a 'bit' flip like error can occur when the qubit flips or transfers population erroneously, the timescale where this happens is called T_1. Under many experimental instances, the qubit frequency can be in one of many locations (grey lines). The result of this is a decay in the lifetime of superposition states T_2^*. Under a refocusing pulse, T_2 decay is only limited by dynamic noise (red arrow) during the experiment. TLS can have T_1 decay happen radiatively, emitting a photon at $E = \hbar\omega$. However, the linewith and coherence of the TLS causes a spectral uncertainty and broadening in the emitted photon. **(B)** Schematic of an electron spin (thick arrow) coupling to nuclear spin (thin arrow). The resulting Hamiltonian has 4 levels with three possible transitions. **(C)** Anticrossing from coupling qubit 1 at frequency 1 (blue) with qubit 2 (red) by varying the frequency detuning. The splitting $2g$ corresponds to the coupling strength. **(D)** Illustrative T_2^* decay (red, with a set detuning) from averaging many experimental instances with slightly detuned frequencies (blue).

or the lifetime of a spin ground state. For example, if I prepared a spin in $|\uparrow\rangle$ (its high energy state) T_1 would be the time it takes to decay into an equal mixture of $|\downarrow\rangle$ and $|\uparrow\rangle$. Starting in $|0\rangle$, the probability of being in $|0\rangle$ when measuring after a variable time delay t is $P_0(t)$ and decays according to:

$$P_0(t) = \frac{(e^{-t/T_1} + 1)}{2} P_0(t = 0) \tag{2.1}$$

That's to say, if I ran the experiment many many times I would see a random loss of my state (such as a spin flip) with characteristic time T_1 manifested as an average decay of population according to Eq. 2.1 (remember, all I measure are 0's and 1's). Depending on the system, T_1 isn't the time to go into an equilibrium mixture but into the qubit's ground state (such as at low temperatures, or in optical emission). Thermally induced relaxation, population loss (your qubit flies away) and noise resonant with the qubit transition frequency can all drive T_1 processes. Importantly, we can't control this decay: it happens randomly and destroys any superpositions and entanglement you may have prepared. Another way of thinking about T_1 is the environment driving a random Rabi oscillation/spin flip that you didn't want.

In a T_1 experiment, we usually polarize into $|0\rangle$. We then wait time t and (at least for the systems investigated in this thesis) measure the population in $|0\rangle$. To measure the population in $|1\rangle$, on the other hand, we can perform a π pulse right before measuring such that we map the amplitude of $|1\rangle$ onto $|0\rangle$. Given that drifts and other issues can happen as this time is swept, and to gain full contrast in the signal, we use a differential measurement. In the differential measurement of T_1, we compare the decay with and without the final π pulse over many experiments. The two measurements reach equal probability at long times, which means that the state decays to a 50:50 mixture of $|0\rangle$ and $|1\rangle$ (a thermal mixture at our temperatures).

2.2 T_2^*

T_1 is the lifetime of our system prepared into one of its eigenstates. T_2^* is the lifetime of a superposition of our qubit (on the equator of a Bloch sphere), and thus is a direct measure of coherence and is sometimes referred to as the *'dephasing'* time. Any effect on the phases in the superposition and any unwanted rotations on the Bloch sphere will mean that when we come to measure, the state will be *in a different place than we expect.* If I run an experiment

many, many times with each iteration having slightly different extra rotations and phases, and compare to the state I expect (measure the superposition), then the 'projection' of my true state to my expected state will decay as I let the system be kicked around:

$$P_{superposition}(t) = e^{-t/T_2^*} P_{superposition}(t=0) \tag{2.2}$$

In practice, we start by preparing in $|0\rangle$. From 1.1.3 we prepare a superposition on the equator of the Bloch sphere using a $\frac{\pi}{2}$ pulse. For this pulse we can pick I=1 ($\frac{\pi}{2}_x$) or Q=1 ($\frac{\pi}{2}_y$) which once again is arbitrary (and just needs to be consistent with later choices of pulses). We let this superposition evolve for time t, and then perform a differential measurement by either performing a $-\frac{\pi}{2}$ (either I=-1 or Q=-1) which maps the original coherence back onto $|0\rangle$, or by doing another $+\frac{\pi}{2}$ pulse which maps onto $|1\rangle$. Once again, this is to maximize measurement contrast.

If we remember our discussion of the interaction picture/rotating frame, it was mentioned that in the case of small detuning Δ from the frame we want to rotate in, there results a $\Delta\sigma_z/2$ term in the Hamiltonian. In the Schrödinger picture, we already know that states accumulate phases according to their energies/frequencies (from a σ_z term). It's not surprising then that small deviations in what we expect for qubit energies gives this extra rotation term, as mentioned in section 1.2.1.

What this means is that with small *unwanted* shifts in the qubit energy (and thus detuning), there is a different amount of z phase accumulation. The upshot is that if our frequency is slightly off, a state on the equator of the Bloch sphere such as $\frac{|0\rangle+|1\rangle}{\sqrt{2}}$ will rotate about the z axis on the equator *differently than we expect* (at the 'speed' of the detuning). Interestingly, if my environment induced detuning is fairly static, if I wait time $t = 2\pi/\Delta$ then the state will be fully recovered (and actually just oscillates in time). The problem is not the detuning, but that the detuning is random and uncontrolled. Imagine that each time I run an experiment, I get an oscillation at the frequency of the detuning which is random.

Averaging a bunch of waves with different frequencies will result in a decay in time (see Fig. 2.1D), which is the cause of Eq. 2.2. The detuning for each experiment can also change in time (non-static) within each experiment, and further shortens coherences. Usually, for a T_2^* measurement, a small amount of known detuning will be added which adds oscillations to the envelope decay of the coherence and makes fitting easy.

T_2^* represents our phase coherence of a superposition in time. Since T_2^* makes a statement on the sum of all possible detunings of our qubit, it is inherently linked to the resonance *linewidth* Γ (in frequency) of our qubit. Generally, $T_2^* = 1/(\pi\Gamma)$ depending on the lineshape and the noise timescale. Measuring T_2^* is called performing a *Ramsey*[21] measurement where the oscillations above are called Ramsey oscillations or fringes and can be used in sensing. A narrow qubit spectrum means oscillations with little damping. If a specified detuning is set, one can set a delay time to measure small shifts in the resulting oscillation. By setting the time delay to a position of maximum slope in the fringes/oscillations, boosted sensitivity can be achieved to an external degree of freedom[22]. A longer T_2^* means smaller and smaller DC shifts can be measured. Furthermore, the linewidth of a qubit (related to T_2^*) determines how well it is resolved from other objects spectrally. This has implications later in performing conditional gates and in achieving 'strong coupling'. In general, T_2^* takes into account *inhomogeneous broadening* which can happen if a single qubit is wiggling around in energy experiment to experiment, *or* if there are many qubits with differing resonance frequencies (an *ensemble* of qubits) resulting in a broadened distribution that are all measured at the same time.

2.3 T_2

The great thing about quantum science is that issues of two level systems and coherence were worked out by the electron spin resonance and NMR community a long time ago. We're just catching up. It turns out a clever trick for extending coherence is to perform a

spin-echo. In the limit that the noise is quasi-static (the induced detuning in each experiment is constant), after preparing a superposition as described above, we can correct for unwanted phase accumulation of this coherence. If we let the qubit in state:

$$|\Psi(0)\rangle = \frac{|0\rangle + |1\rangle}{\sqrt{2}} \tag{2.3}$$

accumulate spurious phase as $\Delta\sigma_z/2$ for time $t/2$, we get:

$$|\Psi(t/2)\rangle = \frac{e^{-i\Delta t/4}\,|0\rangle + e^{i\Delta t/4}\,|1\rangle}{\sqrt{2}} \tag{2.4}$$

If we then perform a π pulse that flips the qubit to the other side of the Bloch sphere we get:

$$|\Psi(t/2)\rangle = \frac{e^{i\Delta t/4}\,|0\rangle + e^{-i\Delta t/4}\,|1\rangle}{\sqrt{2}} \tag{2.5}$$

Which just swapped the phase factors on $|0\rangle$ and $|1\rangle$. Evolving under the same detuning for time $t/2$ again:

$$|\Psi(t/2)\rangle = \frac{e^{i\Delta t/4}e^{-i\Delta t/4}\,|0\rangle + e^{-i\Delta t/4}e^{i\Delta t/4}\,|1\rangle}{\sqrt{2}} = \frac{|0\rangle + |1\rangle}{\sqrt{2}} = |\Psi(0)\rangle \tag{2.6}$$

Which is just the state we started with! This technique is called a *Hahn echo*[23]. Importantly, the idea is that if we wait the same time between the 'refocusing' π pulse and the measurement as we do between the start of coherence evolution and the π pulse, the coherence 'echoes' back and gets recovered. We can also see that we don't need to know what Δ is for each experimental instance. As long as it is quasi-static, the π pulse in the very middle of the evolution time completely rephases our state. The measurement proceeds in the exact same way as in Ramsey, but there is no detuning and a π pulse is put in the middle of the evolution time. A Hahn echo eliminates static noise, but cannot correct for detuning that changes faster than the order of t. When T_2 is measured, a decay will be observed that corresponds to higher frequency components of the noise. A single pulse Hahn echo T_2

time is a fairly universal benchmark for how coherent a quantum system is (the "coherence time").

2.4 Dynamical Decoupling

Luckily, the problem of non-static noise was also addressed by the spin resonance community. If we apply multiple π pulses, as long as the noise is roughly constant between the pulses we can effectively rephase the coherence. So instead of breaking up our coherence evolution into two segments with $t/2$, we can break it up into many small segments with $t/(N+1)$ using N π pulses. This is called 'Dynamical Decoupling' and in particular is called a CPMG sequence (named after Meiboom and Gill [24] improved on the original sequence of Carr and Purcell [25]). In this scheme, we are only sensitive to noise faster than the $t/(N+1)$ timescale. We can see then that with large pulse number we can rapidly echo the qubit and are sensitive to only faster and faster noise. Most noise sources are stronger with lower frequency, so having larger pulse number can dramatically enhance the coherence time. The extension of this is something called continuous dynamical decoupling which constantly drives the qubit and dresses the states while rephasing rapidly (rapidly moving between two different sides of the Bloch sphere).

There are many types of dynamical decoupling that use different pulses and phases with different spacings, that are designed to efficiently rephase coherence for different kinds of pulse errors and noise sources. In particular, later in this thesis we will use the XY-8 sequence which alternates between X(I) and Y(Q) quadrature π pulses in the CPMG sequence and corrects for imperfect pulse calibration.

Importantly, with a choice of the pulses and their separation, the measurement of coherence becomes sensitive to different frequency components of noise. In general, each pulse sequence can be Fourier-transformed into frequency space and constitutes a *filter function* that determines what part of a noise spectral density $S(\omega)$ the qubit is sensitive to. Ramsey,

Hahn and higher pulse number sequences each have their own filter functions that sample a global noise spectral density. As the pulse timing is swept, this filter function moves and can cause non-exponential decays depending on the shape of $S(\omega)$. Interestingly, at high pulse number the filter function approaches a delta function and can be used to transform the decay of coherence in time directly to a measured $S(\omega)$ using the *spectral decomposition* technique [26].

If the noise is oscillating with a certain frequency and I want it to couple to my qubit, I can choose the pulse spacing to constructively add the phases, and if I want to become insensitive to it, I can pick timing that exactly cancels the phase accumulation between consecutive pulses. The ability to drastically enhance coherence while maintain sensing capabilities is a major advantage. In particular, dynamical decoupling allows for drastic improvements for AC sensing. Similarly, certain arbitrary single and two-qubit controls can still be performed even while maintaining dynamical decoupling, though there are certainly added complexities ([27], for example). Further details of this will be described later in chapter 13.

2.5 Clock and ZEFOZ Transitions

Another way to increase coherence is to design the energy spectrum of the qubit. If I have an environmental degree of freedom (magnetic fields, electric fields, strain, etc.) whose strength is characterized by δ, a qubit energy spectrum that is designed to be 'flat' with respect to this perturbation will have increased coherence. The idea is to make a system such that perturbations do not wiggle the energies/frequencies around, which was the cause of decoherence in the first place. Sometimes these are are called ZEFOZ (Zero First Order Zeeman) points in the spin literature or 'clock-like' transitions which arises from the atomic clock community (these are the transitions which are extremely stable). In general, the energy spectrum isn't perfectly flat, so the goal is to engineer the dispersion such that the

first order derivative of the energy with respect to δ is zero (hence: ZEFOZ). These sorts of systems are investigated in chapter 13 and have resulted in some of the longest coherence times ever measured[28].

2.6 A Comment on Dipoles

A more general way to think about the effects in this section is that there are two type of dipoles: longitudinal and transverse. Dipoles are just terms in the Hamiltonian that look like $\delta_i d_i \sigma_i$ with some perturbing field δ and 'dipole moment' d that relates the perturbation to terms in the qubit's Hamiltonian. If our qubit is in the σ_z basis, we need to use σ_x and σ_y terms to drive qubit rotations (see 1.1.3) which are *transverse* to the qubit's quantization axis. However, from the discussion in this chapter, we know that there are also terms that change the frequency/energy of our qubit such that we get extra uncontrolled σ_z (*longitudinal*) terms that cause decoherence. In the example of a spin, we have the Hamiltonian in Eq. 1.2, and note that the same dipole moment $g\mu_B = \gamma_e$ is multiplying the σ_x, σ_y and σ_z terms. This means that although we can drive rotations of our qubit with transverse magnetic fields, it is still just as sensitive to longitudinal/on-axis magnetic field noise that causes decoherence (see Fig. 2.1A). A more ideal scenario is one where the transverse dipole is large and the longitudinal dipole is small. However, this also means that tuning the qubit's energy is suppressed ("nature never lets you win"). Some qubit systems can be designed and engineered along these lines to have the right sorts of dipoles to make them controllable, but stable systems. This theme will be covered in other chapters as well.

2.7 Limits of Coherences and Linewidths

T_1 can actually limit the T_2 time. Our discussion above about coherence doesn't take into account population loss or T_1 relaxation. If T_1 is really short, it's fairly straightforward to understand that any superposition would also decay as well. It turns out that a superpo-

sition state only has to decay 'half as far' compared to a polarized state to become fully mixed/decayed, such that:

$$T_2 < 2T_1 \tag{2.7}$$

This means that the ultimate limit for coherence time is T_1 decay. In general, even if we employ dynamical decoupling as described above, the ultimate limiting factor will always we T_1, our qubit's lifetime.

We also must consider the Heisenberg uncertainty limit such that a state with a lifetime $T_1 = \tau$ (such as an excited state/radiative lifetime) will result in a natural linewidth. Using the time-energy uncertainty principle from quantum mechanics:

$$\Delta E \Delta t \leq \hbar/2 \tag{2.8}$$

We can say that if the state has a lifetime τ, then τ sets the uncertainty in time. Additionally, we can relate the Lorentzian linewidth Γ (the Full Width Half Maximum: FWHM) to the energy uncertainty:

$$\Delta E \approx h\Gamma/2 \tag{2.9}$$

The factor of two here roughly comes from the fact the Γ describes the decay of population (Ψ^2) while the ΔE comes from the Fourier transform of the decay of the wavefunction/phases (Ψ) to get the lineshape, which means we have to take a square root of the exponential lifetime, reducing the effective power of the exponent of the decay by a factor of two (rigorous derivations can be found in [29]). Combining the two and seeing what the limit of Eq. 2.8 is, we find:

$$h\frac{\Gamma}{2}\tau = \frac{h}{2\pi}\frac{1}{2} \tag{2.10}$$

$$\Gamma = \frac{1}{2\pi\tau} \tag{2.11}$$

Alternatively, looking at the limit of Eq. 2.7, if we use the relation in section 2.2 re-

lating linewdith (assumed there to be Lorenztian) to T_2^*, but assume that T_2^* has no static inhomogenous broadening and is at the T_2 limit:

$$T_2 = 1/(\pi\Gamma) \tag{2.12}$$

$$T_2 = 2T_1 \tag{2.13}$$

$$\Gamma = \frac{1}{2\pi T_1} \tag{2.14}$$

Which is the same result as Eq. 2.11. A qubit with a Lorentzian linewidth that is completely determined by these considerations (no inhomogenous broadening) is called *lifetime limited* and is critical for understanding section 11.4. A good qubit will usually have very long T_1 and will have T_2 limited by other noise sources first. On the other hand, coherence from short-lived optical excited states is 'as good as it can be' when it's at the T_1/lifetime limit.

2.8 Other Considerations

In general, when coupling to other qubits or degrees of freedom, narrow lines allow measurement and control of small interaction strengths (coupling). If two quantum objects are coupled with strength g (single particle coupling strength) which is like a Rabi frequency for a two-qubit interaction (or a qubit-harmonic system interaction), then in order to resolve that coupling in spectroscopy, we need the coupling induced splitting (an example for nuclear spins is given in section 1.2.4) to be larger than the linewidths of our individual systems (κ and γ) :

$$g > \kappa, \gamma \tag{2.15}$$

Which is called being in *strong coupling*. Being in strong coupling means that an interaction strength of two systems is larger than the damping rate of each individual system. Unfortunately the term is often overused; a set of coupled classical pendulums can have 'strong

coupling'. When two pendulums have the same resonance frequency but are coupled, they don't swing separately, but gain *shared oscillation* modes that have different energies. As two (classical or quantum) systems are brought into near-resonance, the shared spectrum of the system hybridizes and displays an *anticrossing* (see Fig. 2.1C). This can be described by the *Jaynes-Cummings* Hamiltonian[30] which generally treats a qubit coupled to a harmonic mode of a cavity. Additionally, there is also an anticrossing as a function of detuning in the interaction frame with the 'coupling strength' being the Rabi frequency. When the system is driven harder, the eigenstates in this frame split more. Rabi oscillations occur when the drive-induced splitting is larger than the linewidth.

Strong coupling is useful when dealing with qubits and single particles, and determines if two-qubit operations can happen without losing the coherences first. A related metric is *high-cooperativity* ($C > 1$) where:

$$C = \frac{4g^2}{\kappa\gamma} \tag{2.16}$$

Which is a more general condition for being able to see nice 'quantum' effects between two systems (cooling, swapping states, entangling, etc.) and forms a single number metric for strong coupling. In general we can see, however, that having narrow lines and small κ and γ are very important.

It may be pedantic, but conditional two-qubit (entangling) gates can be created in two rough possible ways in the context of section 1.2. Given that the system is strongly coupled:

1. Define the 'H_0' to include the qubit-qubit coupling. Use the energy splitting from the coupling between the qubits to resolve levels. These levels can be driven with an external perturbation selectively to perform two-qubit gates. The rotation terms are turned on and off by turning on and off the drive.

2. Use the interaction frame which does *not* include the coupling 'g' (bare qubits). Then, find a way to modulate g in time to turn the interaction on and off to perform gates.

In terms of the physics, these two methods are very similar but have different strategies

in experiment. Both of them require strong-coupling/strong-driving. Similarly, depending on the form of the interaction, one may have to perform single-qubit gates (such as a $\pi/2$ pulse) that create superpositions (moving into a different basis) in order to create the desired interaction. In a sense, single-qubit operations can turn the right sorts of interaction terms on and off (in the correct basis). This idea is used in chapter 13 to form gates despite an 'always-on' interaction. Finally, one can beat the linewidth limit for a two-qubit interaction by performing dynamical decoupling and extending the effective limit from T_2^* to T_1, as alluded to earlier. An example of this is in performing two-qubit gates with 'weakly coupled' nuclear spins in chapter 13. Strong coupling of two electron spins generally requires placement and individual control of the electrons at the nanometer scale, which is a challenge. Importantly, entanglement can also be created for systems where direct coupling/two-qubit gates (with high-fidelity) like these are infeasible. This is covered in detail in chapter 8.

Chapter 3

Realizations of Quantum Technologies

Now that we have gone over what qubits are and the interesting properties they can display, what can they be used for real-life applications? There are three major branches of quantum technologies that have been proposed and developed, each leveraging different advantages and giving new opportunities. In particular, as will be discussed in 3.4, the systems that this thesis focuses on (spin defects in the solid-state) have had proof of principle demonstrations in all three branches. However, quantum sensing and quantum communications are where spins in SiC show the most promise.

3.1 Quantum Computers

Quantum computers are perhaps the most well known quantum technology. A large part of the motivation and context behind quantum computers is given in the previous sections. More examples of applications for quantum computers beyond those in 1.2.5 are machine learning, quantum AI, quantum simulation, and quantum annealing. In particular, Feynman's quote: "*Nature isn't classical, dammit, and if you want to make a simulation of nature, you'd better make it quantum*", illustrates the motivation for quantum simulation. Simulations of complex molecules and materials, for example, use approximations because classical computers can't handle the entire quantum state of these systems. Quantum annealers (such

as D-Wave), on the other hand, make use of quantum superposition and tunneling to search through energy landscapes faster than classical techniques. However, quantum computers will not make your smartphone or desktop faster! They only perform certain problems better than their classical counterparts.

There are many major companies in the race for quantum computers including Google, IBM, Intel, Honeywell, Amazon and others including smaller companies and start-ups, and the competition is certainly growing. The major issues are in scaling to large qubit numbers while keeping errors in check (and correcting for them), connectivity, coherence times, control, and calibration, among others. A metric often thrown around is 'quantum supremacy'[31], which is the point where a quantum machine performs a task that is not possible to perform on any classical machine. Claims of quantum supremacy have been made and disputed, along with arguments about the proper metrics to aim for in performance. That being said, quantum computers (based on superconducting technology, see 3.4) are at the forefront and are being developed commercially. These systems have real prototype computers doing calculations right now. The solid-state spin systems focused on in this thesis have shown very basic error correction and compiled quantum algorithms, and have local many-qubit nodes. However, they lack the ability to scale and connect to the qubit numbers needed for useful computations (though there are some ideas for distributed and photon-based quantum computing).

3.2 Quantum Sensors

Quantum things are (usually) small. As such, exquisite control and readout of these states provides a window into the (nanoscale) environment of the qubit. Furthermore, as we saw in chapter 2, quantum states like superposition have phases that are extremely sensitive to perturbations. Accumulating these phases and translating them into variations in the amplitudes for qubit readout allows for very good sensing capabilities. In particular, qubits usually

have narrow transitions and are highly coherent which allow small changes to be detected. Sometimes it is said "a bad qubit is a good sensor", which is in part true- and illustrates the need for a qubit to couple well enough to the sensed degree of freedom, while dealing with reduced coherence. The applications of quantum sensing are wide-ranging, from nanoscale NMR of single molecules, biosensing, probing condensed matter phenomena, dark matter detection, to tests of quantum gravity. In a sense, an MRI scan is a rudimentary quantum sensing technology that performs electron spin manipulation and measures relaxation and coherences of the hydrogen spins in your body (which are sensitive to their environment). The definition of what actually is a quantum sensor is quite broad.

Quantum sensors don't (always) require thousands of qubits, error correction or fancy algorithms. As such, there are many near-term technologies and companies invested (with many start-ups). Some important examples are superconducting SQUID detectors/magnetometers, scanning single spin tips, Josephson Parametric Amplifiers, and Quantum LIDAR/RADAR among many others. Atomic clocks, which forms the precise reference for time used across the world and are the basis for modern GPS, are also a quantum technology which could be put in this category. Related to this thesis, single spins in the solid state are excellent quantum sensors and have been used as gyroscopes and as nanoscale sensors of temperature, strain, electrical and magnetic fields- even in living organisms. That being said, spins are predominantly *magnetic moments* and really excel at magnetometry.

3.3 Quantum Communications and Networks

Quantum communications, a quantum internet, and quantum networks are the major applications that drives the work in this thesis. As alluded to in 1.1.3, taking classical communications to 'the quantum level' gives some interesting properties. In classical communications, an eavesdropper can tap off a tiny fraction of your communications signal and listen in. However, in quantum communications we can use the fact that observing quantum states changes

them. Because the signals can be encoded in single photons, and that there is a 'no cloning' theorem in quantum mechanics that prevents making copies of quantum states, that means that if an eavesdropper listens in, it will destroy the quantum state and we can even detect the act of eavesdropping. The result is that quantum communications can be used to create a provably-secure 'key' (see further discussion in chapter 8) for encryption that is secured by the fundamental laws of physics. Interestingly, quantum provides a 'double-edged sword' for security. Quantum computers as discussed above can break the encryption we all use today, but on the other hand, quantum communications provides us a way to ensure information security ('unhackable' communication). Such quantum key distribution schemes are widely used today and have had some traction with commercial systems like secure banking, a quantum video-chat, etc. Some major companies are also getting into developing quantum key distribution systems. These quantum communication channels are commonly achieved using telecommunications fibers which offer low signal loss around 1550 nm of light (the telecom C-band). This is the same technology that transports 90% of international data and spans across the globe (just think how big the 'telecom' industry is). Quantum communications can also be achieved with free space optics. Entangled particles have even been sent from a 'quantum satellite' hundreds of kilometers above the earth to two telescope based ground stations[32].

However, demonstrations to date are based on either bright single photon sources or attenuated lasers, and importantly on spontaneous parametric downconversion (SPDC). SPDC uses a crystal with a large $\chi^{(2)}$ nonlinearity to take one photon to produce two photons at different output angles/wavelengths with entangled polarization states (whether the light is vertically or horizontally polarized, etc). Interestingly, your qubit can even be whether your photon arrives 'early' or 'late' to some detector. These are called *time-bin qubits*.

These methods have allowed for major advances, but lack one key component: a quantum memory. Entangled particles can be distributed to different stations, where the entanglement can be verified by measurement. However, the distributed entanglement cannot be stored

without a memory. As will be described in 8.3, holding onto entanglement is necessary to send quantum states over long distances and to generate entanglement over many nodes. If you want a 'quantum internet' or the ability to have distributed quantum computing, you need memories. For example, if I needed to send a photon from Chicago to New York, then my memory at each station needs to hold onto its quantum state for over ~ 5 ms. For many qubit candidates this is extremely long. Systems that have interfaces to photons but have a long-lived quantum memories are then ideal candidates. The system developed in this thesis is one such candidate.

3.4 Candidate Systems

A full list of all candidate quantum systems would be infeasible, but the following are the major thrusts for the community and help put into context the relative disadvantages and advantages of the systems developed in this thesis. There are two main sorts of quantum objects: two level systems, and *harmonic oscillators* (Fig. 1.2.2B). Two level systems (TLS) constitute the discussions in the previous sections. A harmonic systems is any degree of freedom that looks like a classical harmonic oscillator, and can be anything from a mass on a spring to an optical cavity or a LC resonator from electronics. Harmonic systems do not have two isolated energy levels, but have an infinite number (sometimes called a *ladder*) of equally spaced states. If I prepare both a TLS and a harmonic system in their ground state, and apply a drive (such as in section 1.2.1), for the TLS we will get Rabi oscillations, but for the harmonic system the energy to go from $|0\rangle$ to $|1\rangle$ is the same as the energy to go from $|1\rangle$ to $|2\rangle$. Instead of qubit control and Rabi, we instead continuously excite the system to some high excited state and have no precise control where we are. The candidates covered here sometime have more than two levels, but as long as two levels can be isolated in energy and the system is *not* harmonic, things are fine. Most candidate systems have very good single qubit control, but the major differences in maturity is in two-qubit gates and scaling,

with other differences being operation temperature and initialization and readout schemes.

In general, systems for quantum computation and communication need to meet *Divencenzo's criteria*[33]. For computing we need:

- A scalable physical system with a well-characterized qubit
- The ability to initialize the state of the qubits
- Long decoherence times
- A universal set of quantum gates
- A qubit-specific measurement capability

For quantum communications we need:

- The ability to interconvert *stationary* and *flying* qubits
- The ability to faithfully transmit flying qubits between locations

Where flying qubits are commonly photons and the stationary qubits are the TLS/quantum memories.

3.4.1 Superconducting Circuits

As discussed above, a LC resonator can be a quantum object but cannot be a qubit. However, if we can add enough *anharmonicity* to the circuit, then the levels are no longer equally spaced and by tuning our manipulation tone we can selectively drive only two of the levels at a time. It turns out that in superconducting physics, a *Josephson Junction*, which is just a small insulating region between two superconductors, does just this. Combined with the extremely low losses in superconductors, these systems are exciting candidates for quantum computing. Unfortunately, superconductivity usually only appears at cryogenic temperatures. Additionally, to prepare the qubit state we have to cool the system down

such that only the ground state is thermally populated. In the GHz regime where superconducting qubits operate, this means we need to operate in dilution refrigerators which are special instruments that can reach 10's of mK. This makes the inside of such a cryostat 'the coldest place' in the known universe. Superconducting circuits utilize the field of quantum electrodynamics (cQED) to readout (dispersive shifts on a readout resonator) and store single microwave photons. The GHz operation with electronics and microwaves makes this system very appealing, along with the ability to fabricate any superconducting device you may want using traditional lithography techniques. This means that superconducting circuits are a 'bottom up' approach: you build a quantum object nature didn't give you. This also means that two-qubit gates and connectivity can be wired from the ground up. In particular, one can construct 'tunable couplers' that can modulate qubit-qubit coupling and make two qubit gates (see 2.8).

Superconducting systems have been used as single photon detectors, can search for dark matter, and form the basis for SQUID loops that are exceptional magnetometers. For computing, superconducting system have been scaled up to over 50 qubits with very good gate fidelities and proof-of concept error correction. Superconducting systems are perhaps the most popular qubit candidate for computing, but have drawbacks in terms of cryogenic limitations and in terms of wiring up computers together. Since everything is in the microwave domain and cold, there is no way to get anything quantum out of your dilution refrigerator (room temperature is *full* of thermal microwave photons that destroy your information).

3.4.2 Neutral Atoms and Ions

Atoms are nature's best qubit. Every atom is exactly the same as every other atom. The AMO subfield of physics (Atomic, Molecular and Optical) is perhaps the first to really think about using and observing the weirdness of quantum mechanics. Atoms have narrow, selective transitions with long coherences and control realized by lasers. As mentioned in 3.2, because of this, atoms can be great sensors and used as universal time reference. Laser cooling

and optical pumping can cool the atoms and initialize them into a particular quantum state. In order to annoy everyone in the field, I have combined the discussion on neutral atoms and ions. Ions are just ionized atoms that have a net charge, this means that with appropriate electrostatic gates one can confine the atoms in space. Gates between atoms are realized by using the Coulomb interaction of these ions as they occupy different *motional* states of the trap with a gate called the *Molmer-Sörenson gate*[34] that can realize arbitrary two qubit operations[35]. Neutral atoms are neutral and are confined with laser trapping techniques, while gates can be realized through long range *Rydberg* excitations of the atoms. Atoms don't require cryostats (though some are starting to adopt them for better vacuum performance), but require extremely stable laser systems and ultra high vacuum (UHV). Atoms and ions can have ground state spin and hyperfine states that can have long coherence times, as well.

Small-scale (11+ qubits) but high fidelity quantum processors are available for trapped ions that can do basic quantum simulation and computing. Scaling ions up to many tens to hundreds of qubits is a huge technical challenge. Scaling beyond that as necessary for a full-scale quantum computer would require many small scale computers wired up using atom-photon interfaces[36], or on-chip reconfigurable traps[37]. Along these lines, the first quantum repeater protocols (see [38]) were actually proposed using atomic clouds using the high-fidelity atom-photon interface and techniques from QED. Recent advances and demonstrations are still being made [39]. Single ion remote entanglement is still an active area of research today [40, 41], but suffers from UV wavelengths incompatible with long-distance transmission.

3.4.3 Quantum Dots

As mentioned in previous sections, an electron spin is a quintessential qubit. But how does one get a single electron to play with? By taking electronics to the single electron level, we can either grow materials that form a *quantum well* that traps electrons and forms particle-in-a-box type states (hence 'dot'), or we can confine electrons using gates and band

engineering borrowed from classical electronics ('gate defined'). There are many types and materials that make quantum dots, but there are two major categories. One type operates in a dilution fridge, and is based on the spin states of single or multiple trapped charges. Qubit preparation and readout occur through spin dependent tunneling using 'single electron transistors' (which are extremely good sensors of charge), relating back to 1.1.2. Manipulation occurs through magnetic driving or through sloshing the electrons back and forth next to a micromagnet (electrically driving a time-varying magnetic field). Such devices made of isotopically purified silicon and silicon/germanium devices leverage the expertise from silicon nano-fabrication and display exceptional coherences and control. Scaling these systems to many qubits, however, remains a huge technical challenge. Additionally, these qubits are not optically active and cannot link to flying qubits.

The second kind of quantum dots are optically active. They have higher excited state orbitals in the dot. A related technology is quantum dot TV's that are actually on the market right now! These dots (usually 'self-assembled') are grown in crystals/semiconductors of materials containing Ga, As, In, for example and essentially form 'particle-in-a-box' states for electrons (confined to the dot). These emitters are extremely good single photon sources (which can even be engineered to be close to the telecom band) and can be manipulated with lasers or microwaves. Quantum dots can even be used as the gain medium in creating solid-state lasers. Readout and polarization can be achieved by borrowing techniques from AMO physics. Electrically-driven single photon emission, single-shot readout and nanophotonic integration with strong coupling have all been achieved. The major downside is that the interface to flying qubits is degraded through fluctuating electrical noise, since the qubit is not in a vacuum but in a real solid-state material. There have been recent advances on this front, and the work in this thesis is broadly applicable to alleviating this issue (chapter 11). QD's have recently been used to distribute entanglement over long distances [42, 43]. However, the materials that have good optically active quantum dots have *extremely poor* spin coherence properties due to the abundance of magnetic noise from nuclear spins, which

limits their applicability for quantum communications (discussion in the introduction of [44]). By the time the single photon (flying qubit) from the dot gets anywhere, the associated spin (stationary qubit) is long decohered. Despite this, commercial quantum dot quantum devices are being sold today (mostly as single photon sources for QKD: see section 3.3).

3.4.4 Impurity Electron Spins

Once of the original proposals for a physical realization of a quantum computer is the *Kane quantum computer* from 1998[45]. The proposal relies on electrons bound to impurities in a semiconductor (silicon) such as the donor phosphorus (see 1.1.2). Importantly, an impurity in a semiconductor lattice can trap electron or hole spins and localize them without the need for gates or growth. At low temperatures where the impurity states are isolated from the bands and the qubits are thermally polarized, these states are stable and can be manipulated with microwaves. Furthermore, the phosphorus atom contains a nuclear spin. Nuclear spins serve as exceptional quantum memories because their gyromangetic ratio is around one thousand time smaller than the electron, and because the nuclear spin is confined to the core of the atom. This makes nuclear spins extremely insensitive and a very long-lived qubit[46] (but slow to control,"nature never lets you win"). Related to this, controlling and understanding nuclear spins for SiC qubits is the topic of chapter 13. The electronic wave function can be electrically tuned[47] and driven[48], shifting the qubit frequencies such that gates can be implemented with a global microwave drive and nanoscale gating of individual qubits. Borrowing from the semiconductor field effect physics 1.1.2, another gate can draw the electron wavefunctions of two adjacent qubits to overlap under a gate and implement a two qubit operation. Qubit readout is similar to quantum dots using a spin-dependent tunneling (sometimes called *spin-to-charge conversion*). With isotopic purification of silicon to reduce stray nuclear noise, and with recent advances in placing individual phosphorus atoms on an atom-by-atom basis, the Kane proposal is still alive today (with most work done in Australia). The time difference between the original proposal to today shows how

hard of a physics and engineering challenge building quantum technologies is. There are other impurity systems being investigated such as bismuth in silicon, for example. Arguably, systems like the divacancy in silicon carbide, the NV^- center in diamond, and rare earths in oxides are 'impurity electron spins', but they will be described separately in chapter 4 as they have an added feature of an optical interface.

3.4.5 Other Quantum Objects

As mentioned at the beginning of this section, there are two major kinds of objects: two level systems and harmonic oscillators. The qubit candidates outlined above are all two-level systems (or contain one). However, many useful quantum systems are harmonic oscillators. For example, while photon polarization can be a qubit with only two states, photons are a harmonic system in terms of their occupation (photons make up a field and in a particular mode, the occupation can be thought of as harmonic with the photon energy). There is even a large community implementing quantum computations using *photons only* (linear optics quantum computing). To display quantum properties, harmonic systems usually need to be in or near their ground state. Luckily for optical photons, the energy is high enough that there are no thermal photons to occupy modes such that a single photon can be easily realized. If you go too far into the infrared (IR) however, thermal photons become an issue. For lower frequency systems, polarizing to the ground state involves active cooling or putting the system in a cryostat.

Some examples of other quantum objects that are harmonic are magnons (spin-waves), mechanical oscillators, optical and microwave cavities. The coupling of these physically different harmonic and two level systems together constitutes a *hybrid quantum system*, and includes fields such as optomechanics[49]. Exploring these hybrid systems is motivational for the work described in chapters 9 and 10. In general, hybrid systems allow for transferring and controlling quantum states through different modalities. One word of warning: sometimes an ensemble of N two level systems such as atoms or spins is said to have a $\sqrt{N}$ enhancement

of the coupling (g, see 2.8), which is also used in the DLCZ protocol[38]. This is true, but describes a collective excitation of the whole ensemble (*Dicke states*) that looks like a harmonic oscillator even though it is comprised of many two level systems. Additionally, a much more bizarre type of qubit and quantum computing uses topological physics and braided 'anyons' to perform gates. This is an active area of research but is not covered here.

Finally, a major goal of the community is to create a *microwave-to-optical converter* that transforms the microwave frequencies in systems like spins and superconducting circuits that fulfill the Divencenzo criteria for quantum computing into flying qubits/photons that fufill the second set of Divencenzo criteria for quantum communications. Opto-mechanics, electro-optics and hybrid systems using either atoms or spins have all been proposed as possible pathways towards this goal.

Chapter 4

Spin Defects for Quantum Science

"Forget everything you know"

This chapter begins the discussion of the systems which are investigated in this thesis. In general, no crystal is exactly perfect and is riddled with *defects*. These can range from purely crystallographic issues such as domain walls, stacking faults, and screw dislocations all the way to individual single missing atoms or substitutional impurities (the wrong type of atom is on a site) in the crystal structure. Defects in materials are a huge area of study that affects the mechanical, thermal, optical, and electrical properties of semiconductors and other materials. Single vacancy, impurity along with vacancy-impurity or vacancy-vacancy complexes are atomic in size and drive the majority of issues and opportunities in solid-state devices. We had discussed the effect of adding impurities that can donate and accept electrons in 1.1.2 which change electrical properties. If a defect is 'deeper' in the band gap (away from the bands) it can capture charges, but the energy to free the charge again is prohibitively large to be done thermally. It is worth knowing as well that the addition of even a small impurity concentration drastically shifts the Fermi level and affects conductivity. Controlling impurities can reduce conduction by reducing the carrier concentration. However, no system is perfect and *compensating* a crystal that contains residual donors and acceptors through adding many deep defects will suppress conductivity

by capturing carriers but then not releasing them (Fig. 1.4). In this way, defects can be added to create extremely high resistivity materials with the Fermi level 'pinned' at 'midgap' (the Fermi level gets pinned to the deep defect position deep in the bandgap). On the other hand, if I want a region to be conductive and to have carriers in the conduction band to have high mobility, then deep defects can be a problem. Unwanted capturing of carriers due to 'lifetime killing' defects can degrade device performance.

Furthermore, certain defects can be 'optically active' and are called *color centers*. A normal semiconductor or insulator will not absorb light below its band gap, while above the band gap the light is absorbed by exciting electron-hole pairs across the bandgap. Color center defects cause absorption and emission in the semiconductor that differ from what is expected from the bandgap alone, giving the crystal color. For example, a sapphire is just Al_2O_3 with trace iron and titanium, while a ruby is still Al_2O_3 but with trace chromium. Many of the original lasers were made of the optically-active Cr defects in ruby. For gemstones (such as diamond) and 'fake' gemstones (like SiC), impurities and defects can either cause wanted or unwanted coloration. Color center defects (at least the ones we care about) cause coloration by absorbing light, exciting charges in the atomic-size defect into a higher excited state *orbital*. The ground state and the excited state of the defect both lie in the bandgap of the material making certain defects look like trapped molecules or atoms in a solid-state host (Fig. 5.2).

Finally, defects that trap charge can have unpaired electrons or holes. These carriers have spin, and can effect the magnetic properties of materials. These electron spins were also the basis of the original MASER in the 1950's, which was made of Cr defects in ruby. More importantly though, this means that one can understand the defects in a material by looking at electron-spin resonance.

For this thesis, our interest is in defects that are optically active *and* host an electron spin. Using the optical signatures to study the magnetic properties of defects is called *ODMR* (Optically Detected Magnetic Resonance), and has been a widely used tool to understand

materials since 1959 [50, 51] (once again, in ruby). The sad reality is that the quantum technology community is just rebranding and rediscovering defects, measurement techniques and effects from the solid state community that was just trying to understand pesky defects in their materials. Other common ways to understand defects in materials are DLTS (deep level transient spectroscopy), optical absorption/transmission, PL (photoluminescence), measuring the bound exciton lines (excitons binding to defects have specific 'fingerprints' of emission near the bandgap), EDMR (electrically detected magnetic resonance), ODMR, MCD (magnetic circular dichroism- a form of ODMR), and many others.

Perhaps the most well known example of an 'optically active spin defect' is the NV^- center in diamond. That being said, another candidate system that has been developed in recent years is the neutral divacancy defect VV^0 in SiC, which is the subject of this thesis. With the current advanced state of spin defects in SiC, we will only describe the VV^0 system and make comparisons instead to other candidate systems along the way. There are plenty of other theses describing the NV^-center. In general, spin defects display long coherence and T_1 times and contain a natural interface to flying qubits for quantum networks. With some systems displaying nanoscale and room temperature operation they are good quantum sensors, but are harder to scale into quantum computers.

4.1 Other Spin Defect Systems

While this thesis focuses on the VV^0 center, there are other defects developed in SiC such as the NV^-, V_{Si}^-, and CAV vacancy complexes along with various transition metal impurities (TM) covered in chapter 7[52]. Investigating qubit candidates which have various advantages is an exciting pathway for developing quantum technologies in the solid state. The NV^- in SiC is promising (closer to telecom) and may act quite like the VV^0, but at this point is not well developed, and has some confusing optical and spin properties. V_{Si}^- has been focused on heavily, and has room temperature ODMR (but has reduced contrast compared

to cryogenic temperatures[53]) but suffers from low quantum efficiency (QE) and a far-from ideal spin-photon interface that only allows 6 photons to be emitted before a spin-flip [54] (compared to 100-1000's from VV^0[55]). This will be explained further in sections 5.2 and 8.7. TM's are recently developing and promising, but single defects with a well characterized spin-photon interface are lacking (for now). Stacking faults in the SiC crystal create local environments for defects that look different from the bare crystal. In particular, VV^0 exist near these stacking faults that have stable photophysics and room temperature operation [56].

'Good' defects can be found in the 6H polytype of SiC, but single defect isolation and control has mostly been limited to the 4H polytype which is the most well developed. The 3C polytype can be grown on silicon, and many dreams have been formed about it because of this. That being said, although single VV^0 have been isolated in 3C SiC[55], this layer was grown on 4H-SiC. 3C-SiC on silicon is actually a fairly horrible material for VV^0 with low creation efficiency, weird photophysics and huge strains from the lattice mismatch. Single defects have not been isolated in this material for these reasons. With the development of fabrication and undercut capabilities in 4H-SiC[3, 57], the uniqueness of 3C is reduced.

Outside of SiC, diamond based spins have evolved as well. the 'group IV' *SiV, GeV, SnV, PbV* are 'split-vacancy' systems that have high symmetry (D_{3d}) and are quite promising for quantum technologies. In particular, their insensitivity to electric field noise makes them easily integratable into nanostructures where surface noise is an issue. That being said, they suffer from short T_1 due to a nearby orbital that mixes with the ground sate, along with low quantum efficiency[58], though solving these issues is an active area of research.

Additionally, there's a large effort in using rare earth based (*Er, Yb, Ce*, etc) systems in oxides such as *YVO, YSO* for quantum technologies. These systems can have long coherence, but importantly the Erbium based impurities emit exactly at the telcom wavelength of ∼1550 nm and can be used for quantum memories for single photons. Nanophotonic integration may also provide a solution to the extremely low photon emission rate of the these defects

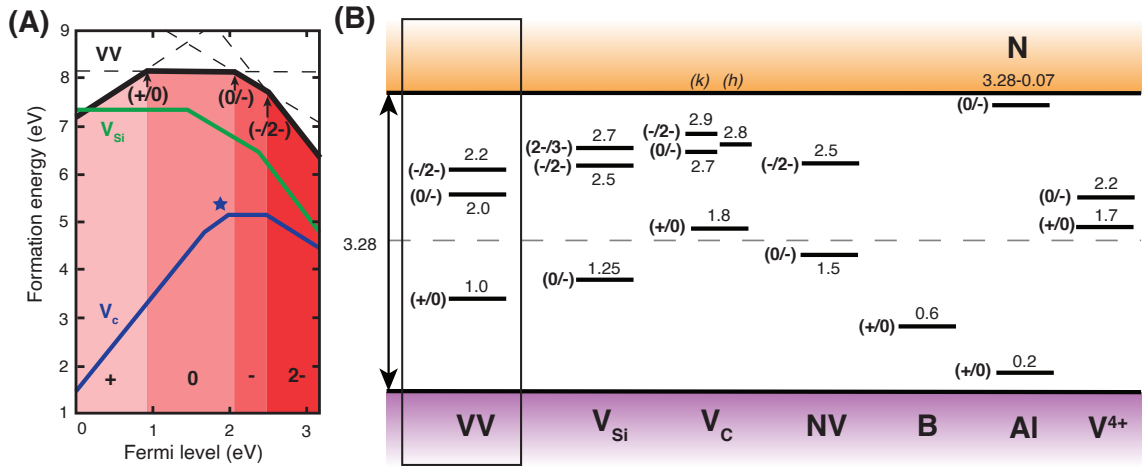

Figure 4.1: **Formation energies and charge transition levels in SiC. (A)** Formation energy diagram of VV, V_C and V_{Si} [61]. DFT values must be scaled to experiment from the bandgap underestimate. The regions for stability of the +1,0,-1,-2 charge states of VV are shaded in red. Dotted lines show the formation energies of the different charge states, while the solid black line only shows the lowest energy charge state. The charge transition levels are marked for VV where the lines intersect. The blue star corresponds to the charge neutrality point of V_C where the Fermi level is pinned if V_C is the dominant defect.**(B)** Charge transition levels of relevant deep and shallow defects in 4H-SiC [62, 63].

[59, 60]. Finally, impurities can bind excitons or provide Rydberg like levels that can but used for quantum information, but need to be investigated further.

4.2 Deep Defects in Semiconductors

When a defect is 'deep' its energy levels are far away from the bands of the host crystal. This means that thermal excitation of the trapped charges is not sufficient to ionize the defect. It's also the case that the bands of a crystal correspond to *delocalized* states of carriers. Shallow defects tend to have their wavefunction/spatial extent be relatively larger and more delocalized since they are much closer to the bands. Deep defect states tend to correspond to extremely *localized* states of charges, essentially confined to a single atomic site. These highly localized states are more robust to effects from the lattice such as the spin-orbit interaction, valley splittings and other more exotic solid-state physics effects. Highly confined defects are (mostly) isolated from the host crystal and are tightly confined. The common analogy is

that the crystal host is a 'semiconductor vacuum' that can host isolated, atomic-like qubit states. Importantly, these qubits are stationary, stable, and trapped in place without the need for any external gates, controls or lasers. This makes them particularly attractive for quantum technologies.

How can we know where a defect or impurity 'is' in the band gap? A convenient way to calculate or understand is by thinking about thermodynamic *charge transition levels*. These are calculations that tell us how much energy it takes to add another electron to the system. Specifically, one can use density functional theory (DFT) to calculate the energy of the system of a defect in a crystal. In particular, we can calculate the thermodynamic energy that it would take to 'form' a certain defect in the lattice *as a function of the Fermi level*. For a defect D in charge state q (D^q), we can calculate the energy difference between the pure crystal $E_{tot}[bulk]$ and the crystal with that defect $E_{tot}[D^q]$. We can also see that if a certain defect is negatively charged, for example, that as the Fermi level is increased the defect is easier to form (lower formation energy) because the crystal is becoming more and more n-type and is more electron rich. This means that the formation energy goes down as we increase the Fermi level. Generally [64]:

$$E_{formation}[D^q] = E_{tot}[D^q] - E_{tot}[bulk] + \mu_{\bar{D}} + q(\epsilon_{Fermi} + \epsilon_{VBM} + \Delta V) \tag{4.1}$$

Where ΔV matches the reference energy for the calculation to the semiconductor valence band maximum (VBM), and $\bar{D}$ is the energy of the constituent parts needed to create the defect. For example, a NV^- has $\mu_{\bar{D}} = -\mu_N + \mu_C$ for the nitrogen and the vacancy (lack of a carbon atom). We can see in 4.1 that the slope of the formation energy with changing Fermi level tells us the *charge state* of the defect. With the formation energy, *in equilibrium* we can know the defect concentration given a number of possible sites N_s:

$$C = N_s e^{-E_f/(k_B T)} \tag{4.2}$$

However, most defect formation occurs through non-equilibrium processes or equilibrium is never reached. That being said, the relative magnitudes of the formation energy are still informative. As we change the Fermi level and perform these calculations there are different lines corresponding to differences in the *charge state* of the defect in the *formation energy diagram*. The slope of each section (see Fig. 4.1) corresponds to the charge state of the defect with Eq. 4.1. The places where the lines intersect show where the most favorable charge state to form *changes*. During defect formation, which usually involves high temperature growth or annealing, the Boltzmann factor depending on the relative formation energies will give the ratio of final defect populations (Eq. 4.2). Sometimes, only the lowest energy line will be shown in the formation energy diagram. The points where the defect formation energy slope changes are called the *'charge transition levels'*. For example, the point where a positively charged defects becomes less energetically favorable compared to a neutral defect is called the '$(+/0)$' level. These levels correspond to the energies of the whole defect (sometime a defect complex) including all of the contributing orbitals of the crystal, impurity or vacancy and the charges around. As such, they take into account the whole energy of the defect system in its ground state. If we remember what a Fermi level is, we will notice that the $(+/0)$ level then corresponds to where the energy of the defect in its neutral state *is*. If our Fermi level is at this point, then the state becomes filled and gains a charge from $+ \rightarrow 0$. Similarly, a $(0/-)$ level in the formation energy diagram corresponds to the energy level of the negative charge state of the defect. Abstracting further, the Fermi level position of $(+/0)$ in these diagrams, for example, tells us *how much energy* an electron needs to gain to pop into the defect and turn $+ \rightarrow 0$. This becomes important in for photodynamics of charge in 6.3. An important point to make is that these levels and the Fermi level correspond to the behavior ('point of view') of *electrons only*, and treating holes needs to be done with some care. For a given defect, we don't know how many different possible charge states are possible in the band gap from first principles. DFT calculations will tell us then what charge states are possible and where they lie in the gap. Similarly, these levels can be measured from experiment using a

variety of electrical and optical techniques (photoconductivity, photo-epr, DLTS, BE lines, etc). In equilibrium, these energies and the knowing the Fermi level of your material will tell you *which charge state your defect is in*. That being said, this idea is usually taken too literally. As discussed in 1.1.2, for most systems the concept of equilibrium is not always applicable where photodynamics may dominate (see 6.3).

4.2.1 Defect Formation and Kinetics

Formation energies and charge transition levels help us understand the thermodynamics and energetics of formation and of the multi-particle defect states. However, the *kinetics* of how the defects actually form is equally important. Defect formation isn't driven by thermodynamics only. The exact details of all the different ways defects can form is beyond the scope of what will be covered here. In general, the defects in this thesis correspond to vacancy complexes and impurities. Damaging a crystal by physically displacing atoms through irradiating with relativistic electrons or high-energy ions creates interstitials, substitutions and vacancies. Interstitials are just atoms that sit 'off-site' in the lattice, between the normal crystal sites (Fig. 5.1D). After creating defects, the crystal can be healed by annealing at high temperatures. Atoms can pop back into place and importantly, vacancies can move around. Vacancies can find a missing atom, or a surface and annihilate, or can find a substitutional atom or another vacancy, forming a vacancy complex. These complexes are usually very energetically stable and do not move. There are usually significant energy barriers for defects in crystals to move around, but these barriers are much higher for substitutional impurities and complexes (usually isolated vacancies are the only things moving). The exact energetics of vacancy complex formation requires a treatment of the Coloumb repulsion, diffusion, crystal structure, energy barriers and can be quite complicated. Some vacancies are naturally occurring in as grown crystals. In SiC, tuning the Si and C gas ratio during growth can make the crystal have more or less Si or C vacancies. This is how high-resisitivity SiC is grown, as these vacancies pin the Fermi level midgap (sometimes referred to *high-purity-*

semi-insulating, or HPSI SiC). As a rule of thumb, ion implantation is quite destructive and leaves a trail of damage as the ion barrels through the crystal until it finally stops and leaves a spray of displacements. However, ion implantation doping and healing (with annealing) the crystal to get the ion impurities on site is a common technique for making classical transistors. Ions can be masked with lithography and thus damage and doping can be controlled spatially. Ions only usually penetrate the surface of your material $< 1\ \mu m$.

Relativistic electron irradiation on the other hand, has a very low probability to interact with the sample and uniformly damages the whole crystal (randomly!). When an electron does interact, it usually displaces only single atoms at a time. This makes electrons the preferred choice to form sparse defects and defect complexes without causing irreparable harm and the formation of unwanted nearby defect complexes. In general, the chance of formation for a particular defect complex is quite low (1-10%) while activating impurities at substitutional sites can approach 100%. Further details of the formation of VV^0 can be found in section 5.3.2.

The spin defects created in chapter 7 utilize implantation at elevated temperatures, which allows for healing of the crystal damage during incorporation, and helps impurity activation and total damage reduction. They also used very high energy ion implantation to create enough defects, but at a lower density and with less damage due to the greater spread in depth. This was achieved in part with assistance from *Sandia National Labs*.

Chapter 5

Spins in Silicon Carbide

This chapter begins the discussion of the divacancy in SiC, which is an optically active deep defect in a semiconductor host. First, I will cover why SiC is an excellent material for quantum technologies, followed by a description of the specifics of the divacancy system.

5.1 Silicon Carbide as an Ideal Host

Silicon carbide is a widely developed material for classical technologies. As early as 1958, William Shockley proposed that SiC would be the prominent semiconductor to follow silicon [65]. It exists as both a ceramic and in multiple crystal *polytypes* that were alluded to previously. These polytypes contain the same alternating Si and C atoms bonded together but have different geometries in 3D space. The important polytypes are 3C-SiC, 4H-SiC and 6H-SiC as they are all readily accessible and developed by industry. SiC was actually the material that birthed the concept of polytypism[66]. 3C-SiC has a cubic (C) structure much like diamond, while 4H and 6H-SiC are hexagonal (H). Looking at a cross section of the crystal, we can view the spatial stacking of the Si and C atoms in a plane. Importantly, we can see a repeating structure that is either 3, 4 or 6 atoms long which correspond to the numbers in the labelling of the polytype (see Fig. 5.1). These polytypes have different bandgaps and other properties, but in general are quite similar.

For silicon carbide, high quality (low defect) *epitaxy* can be achieved with controlled doping. Aluminum is a p-type dopant for SiC (acceptor) with an ionization/activation energy of $\sim 200\ meV$, while nitrogen is a n-type dopant with an ionization energy $\sim 50\ meV$ (h site) and $\sim 90\ meV$ (k site)[67]. These can be introduced as gas precursors during growth. In comparison, diamond is lacking in an available n-type dopant. Silicon carbide has a distinct directionality, as opposed to diamond. The crystal axis along this direction, called the *c-axis*, picks this axis/direction in the crystal as defined in Fig. 5.1. Specifically, in stacking the unit cells we can see that opposite faces of the crystal will be terminated with either Si or C atoms. These are called the Si-face and the C-face of a wafer, respectively, and have different physical properties. For growth, a 4° miscut (optimized by the industry) of the crystal allows for *step flow* growth the proceed along the c-axis, and is usually done on the Si-face. Additionally, due to the presence of Si, SiO_2 thermal oxides can be grown on SiC. With the sublimation of silicon at elevated temperatures, in oxygen free environments, extremely high quality epitaxial graphene can be formed on SiC from the remaining single layer of carbon atoms, providing exciting research and device opportunities ([68, 69] as some examples, see chapter 14).

Natural SiC was initially discovered in 1893 by *Henri Moissan* in a meteor crater. He originally thought what he found to be diamond, and only realized in 1904 it was in fact silicon carbide. Interestingly, by that point SiC had already been synthesized in the lab for over two years[70]. The mineral was named Moissanite. SiC is hard, clear, chemically inert, and thermally conductive (Henri thought it was diamond!). This stems from the similarly strong covalent Si-C bond as the C-C bond in diamond. In fact, SiC/Moissanite makes up a large fraction of 'fake', or alternatives to diamond (besides cubic zirconia). Its thermal and mechanical properties make it widely used in abrasives, high temperature applications, and much more. Because of its low thermal expansion, SiC is even used in mirrors for precision astronomy.

SiC (sometimes also called *carborundum*) has a moderate bandgap ($\sim 3\ eV$), high thermal

conductivity (2× silicon), and large breakdown voltage (10× silicon). Combined with the ability to dope the crystal easily with p- and n-type dopants, this has made SiC widely used in the high-temperature, high-power, high-voltage electronics industry. Surprisingly, SiC even formed the basis of the first LED (light emitting diode) in 1907[71], and early diode-based wireless telegraph systems in 1906[72]. Growth of crystalline SiC began with the *Lely* method[73], followed by *physical vapor transport (PVT)* which led to the first commercially available SiC wafers in 1990's (& the formation of *CREE*)[74], alongside *high temperature CVD (HTCVD)* substrates. Recent epitaxial growth is achieved through *'hot-wall' chemical vapor deposition (CVD)* on these substrates which yields very high quality SiC layers[75].

Today, SiC is used not only in the high power electronics industry, but is also used for epitaxial growth of nitrides (that are used in modern commercial LED light bulbs) and is used in everything from electric vehicles to the upcoming 5G wireless revolution. Today the SiC market is over $1 billion. SiC can be grown with very few defects at the *wafer scale* and is compatible with standard nanofabrication and CMOS (complementary-metal-oxide-semiconductor, describing a type of MOSFET design, see 1.1.2) technologies developed by the electronics industry. SiC can grow a *thermal oxide*, allowing for high-quality insulating layers for devices. The SiC MOSFET, for example, is a particularly good (see 1.1.2) high power device that outperforms silicon based electronics. Essentially, silicon carbide is a blend between the excellent properties of diamond with the development, electronics capabilities and cost-effectiveness of silicon. Importantly, the material is available in high quality 4"+ wafers for much cheaper than diamond and has mature fabrication techniques developed by industry to leverage.

Besides being an excellent semiconductor for electronics, SiC is an ideal material for quantum technologies. In particular, we will first go over why it is a good host for optically active solid-state spins. Then I will describe other desirable quantum properties of SiC. In general, the WKV criteria[64] outlines (much like the Divencenzo criteria) the properties an ideal material would have to host spin qubits. They are that a host should have:

- *A wide band-gap*, so that it can accommodate a deep center.
- *A small spin-orbit coupling*, in order to avoid unwanted spin flips in the defect bound states.
- *Availability of high-quality bulk or thin-film single crystal*, in order to avoid imperfections or paramagnetic impurities that could affect the deep center's spin state (see chapter 13).
- *Constituent elements with naturally occurring isotopes of zero nuclear spin*, so that spin bath effects may be eliminated from the host via isotopic engineering (see chapter 13).

In the original paper that proposed these criteria[64], SiC was identified as an exciting host for spins. Silicon carbide has a fairly large band gap, in the middle ground between diamond (5.5 eV) and silicon (1.1 eV). Additionally, because silicon and carbon atoms are light, spin-orbit coupling in the crystal is low. Because of the development from industry in high-quality growth, commercially available wafers that are pure enough for quantum applications are viable. Finally, both silicon and carbon have *stable* isotopes that contain zero nuclear spin. Not only that, but in naturally occurring isotopic species, the fraction of silicon (4.7%) and carbon (1.1%) that carry non-zero nuclear spins is quite low. Nuclear spins in the host lattice are a resource as quantum memories, but they are also a source of decoherence. Understanding this is the subject of chapter 13. In general, the ability to control the isotopic fraction of these nuclear spins through growth and materials is paramount.

Besides these criteria, SiC is an excellent material for *mechanical* devices. It has a high speed of sound and ultralow acoustic loss, which has made SiC find use in the MEMS (Micro Electro-Mechanical Systems) industry which makes gyroscopes, accelerometers, microphones, microswitches and oscillators. Additionally, SiC is weakly piezoelectric. Hybrid quantum systems with spins in SiC and MEMs devices forms the basis of the work described in chapter 10.

Similarly, the work described in chapter 9 leverages the fact the SiC is an excellent *photonic* material. SiC has intrinsically low optical losses, and interestingly has a high χ^2 nonlinearity that can be used for frequency conversion and quantum transduction. The fact that 3C-SiC can be grown on Si which can be easily undercut, and that opto-electronic and photonic nitride-based devices can be grown epitaxially on SiC provides a plethora of opportunities. The oxide growth available also allows for wafer-bonding and thinning, and use of the oxide-SiC index contrast for photonic devices. As covered in chapter 9, SiC can also be undercut using a dopant-selective, photo-electro-chemical (PEC) etch which does not involve the damage from focused ion beam (FIB) or complexity of anisotropic or angled etches.

Finally, SiC is biocompatible and can be functionalized easily which offers pathways for quantum sensing of biological systems. SiC can be made into nanoparticles as well, which is the subject of 12.2. Furthermore, SiC is a low loss tangent microwave material that could be used as a substrate for superconducting quantum systems and resonators. In general, the surfaces of SiC are heavily studied (for making good power electronics), making control and optimization of surfaces for quantum technologies feasible. Since surfaces are a common issue among all candidate quantum systems, leveraging this expertise is a valuable asset for SiC.

5.2 The Neutral Divacancy (VV^0) in SiC

The divacancy in SiC is a missing carbon atom next to a missing silicon atom in the lattice. It is a widely studied defect in SiC, corresponding to the *UD-2* series in photoluminescence spectra and to the *P6/P7* defects in EPR. Photo-EPR showed spin polarization as early as 2006 [79] with light $> 1.1\ eV$ (and in 2003 for V_{Si}^- in SiC [81]), preceding the pioneering work in [82] establishing the divacancy for quantum science by five years.

The vacancies in this defect result in *dangling bonds* that occupy the space where the

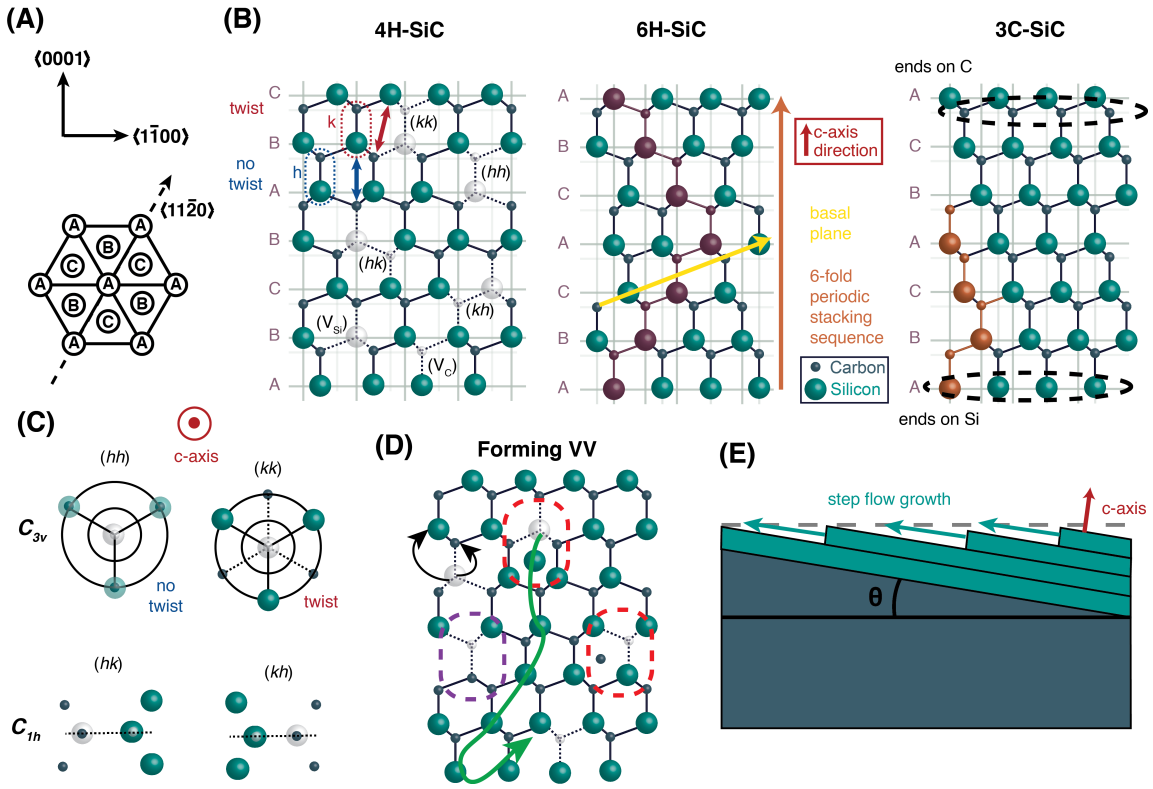

Figure 5.1: **Polytypes, defects and growth in SiC. (A)** Crystal axes (Miller indices) and hexagonal structure of SiC. A,B,C sublattices can be stacked in different orders to produce the different polytypes. **(B)** Crystal structure of 4H, 6H and 3C SiC. The c-axis orientation, basal planes and stacking sequences are shown. The C and Si faces are shown that arise due to the directionality of the silicon-carbon bonds. In the 4H-SiC lattice, the 4 possible VV^0 configurations are shown alongside the major defects V_c,V_{Si}. The hexagonal (h) and cubic (k) sites are shown, which can be seen by the stacking having or not having a 'twist' (red and blue). **(C)** Symmetries and local structure of the 4 possible VV^0. The C_{3v} symmetry is broken in the basal VV^0 cases due to an elongated distance to the upper and lower (out of plane) carbon and silicon atoms, resulting in only 1 mirror plane (dotted lines). **(D)** (red dotted line) Frenkel defect pairs that are produced by damaging the lattice. (purple dotted line) Carbon antisite defect which can be formed with a V_{Si} swapping with a nearby carbon site (black arrow). The other black arrow shows a $V_{Si} \rightarrow V_{Si}$ diffusion of the vacancy under annealing. The V_C stays stationary and the V_{Si} diffuses [76–79] to form a VV defect complex. **(E)** Step flow epitaxial growth of SiC showing the miscut angle. Lattice adapted from [80].

atoms were. There are 6 dangling bonds resulting from the two vacancies, contributing 6 electrons to the system. Since there are 6 electrons from the dangling bonds and no electrons are lost or gained from the lattice, the defect we create from these electrons will be a *net neutral* for the lattice and is thus called VV^0 (there are other charge states, which we will

discuss in chapter 11). It turns out (as will be described later) that 4 of these electrons pair up their spin and fill two orbitals, but that two electrons are left over. Each of these electrons carries their own electronic spin. For spin, we need to remember that while a single spin has states $m_s = \pm\frac{1}{2}$ (a *doublet*), the state of two spins can be either in a *singlet* or a *triplet*. Two spins have the four possible states: $\uparrow\uparrow, \uparrow\downarrow, \downarrow\uparrow, \downarrow\downarrow$. Combining the two electrons, there are two options for the total spin angular momentum. First, there are states with total S=1, these are:

- $|\uparrow\uparrow\rangle, m_s = +1$
- $|\downarrow\downarrow\rangle, m_s = -1$
- $\frac{|\uparrow\downarrow\rangle + |\downarrow\uparrow\rangle}{\sqrt{2}}, m_s = 0$

There are three possibilities, making this a *triplet state*. Then there are states that have total S=0, for which the only option is: $\frac{|\uparrow\downarrow\rangle - |\downarrow\uparrow\rangle}{\sqrt{2}}$. To fully understand the formation of singlets vs triplets, a more detailed treatment of addition of angular momentum in quantum is needed (or *Clebsch-Gordon* decomposition). Roughly, we can see how the '+' sign in the triplet $m_s = 0$ adds angular momentum to result in $S = 1$, while the '-' sign in the singlet results in a total $S = 0$. These are the symmetric and anti-symmetric superpositions of the spins.

Triplet spin systems are described by the 3×3 $S = 1$ spin matrices (S_x, S_y, S_z) which are the analogs to the 2×2 Pauli matrices in Eq. 1.3. Thankfully, we can map the subspace of two of the possible $m_s = 0, \pm 1$ states onto the Pauli matrices as long as we are only considering those two levels. These two levels become our qubit states. However, only transitions that change $\Delta m_s = \pm 1$ can be driven by magnetic fields, such that $|0\rangle \leftrightarrow |1\rangle$ or $|0\rangle \leftrightarrow |-1\rangle$ are our usual qubit states (with notable exceptions covered later in this thesis). This can be seen by looking at which matrix elements are available in the $B \cdot S$ matrices for $S = 1$.

If we have one orbital, then electrons will pair up in opposite directions to fulfill *Pauli's exclusion principle*. Essentially this is just the statement that for electrons to be in the same orbital state, they must have different spin quantum numbers. Furthermore, if there are two available orbitals of the same energy (*degenerate*), then the electrons would rather have their own orbitals instead of having to interact. This is called *Hund's rule* (if you remember your chemistry class). How many orbitals are available, how many electrons there are, and what the spin-pairing energy is in the system determines the total spin of the system (single electron doublets, paired up singlets, or unpaired triplets).

The divacancy defect can be found in the silicon carbide lattice in multiple inequivalent sites. For the 3C polytype there is only one possibility for the location of the divacancy. On the other hand, for 4H there are 4 possibilities and for 6H there are 6. This can be seen in Fig. 5.1. For vacancies in the lattice in the hexagonal crystal polytypes, they can either be on a *quasi-cubic (k)* or *hexagonal (h)* site that describes the local symmetry of individual atomic positions. Whether a site looks quasi-cubic or hexagonal can be understood by looking at the twisting angles of tetrahedrally coordinated sites with respect to its neighbors. A cubic crystal will have the bonds from adjacent sites twisted 180 degrees, while a hexagonal crystal will show direct vertical stacking.

Because 4H-SiC is the most available and technologically mature polytype of SiC, we focus on it for the remainer of this thesis. Using the $V_C V_{Si}$ convention for the divacancy, we can label the possible divacancies in the 4H-SiC crystal: $(hh), (hk), (kh), (kk)$. In particular, we can see that the hh and kk divacancy defects are oriented along the c-axis and that the kh and hk divacancies are oriented at an angle and are along what is called a *basal* plane of the crystal. Depending on the exact site in the crystal, VV^0 can have varying optical and spin properties. Specifically, the photoluminescence lines label these divacancy configurations as ordered by increasing energy $PL1 : (hh), PL2 : (kk), PL3 : (hk), PL4 : (kh)$ (Fig. 5.7).

Going back to the physical orbitals of the 6 dangling bonds with their 6 electrons: The orbital states that these electrons can take are described in various theoretic treatments

and can also be described by DFT. In general, the orbitals that confine the electrons follow nomenclature from the molecular/atomic community that describe both the spin and orbital multiplicity. What determines the spin and orbital characteristics of these defects in largely their *local symmetry*. In examining the symmetry of the defect complex, the c-axis divacancies display C_{3v} symmetry while the basal divacancies show C_{1h} symmetry. These labels correspond to the point groups (from group theory) that the structure of the bonds around the defect display. The C_{3v} label means that the symmetry of the defect has a threefold axis of rotational symmetry that also has 3 vertical reflection planes. On the other hand, C_{1h} has lower symmetry corresponding to a distortion along a perpendicular axis to the C_{3v} symmetry. Making these bonds unequal means that the only symmetry is a reflection across the horizontal plane. These points are illustrated in Fig 5.1C. We will start with the discussion of the c-axis divacancies with high symmetry and discuss important differences with the basal defects along the way.

The orbitals where the single electrons can live have certain shapes and symmetries (following group theory). The label 'a' refers to a symmetrical rotation about an axis, while 'e' refers to an orbital that is asymmetrical under transformation. The transformations also dictate that there is only one 'a' orbital, while an 'e' orbital will be doubly-degenerate and correspond to two orbitals (furthermore, 'b' is singly degenerate but anti-symmetric under rotation, and 't' is triply degenerate). These are called the *Mulliken* symbols. To further label these (molecular) orbitals we can use the subscripts g (symmetric under inversion), u (anti-symmetric under inversion), 1 (symmetric with a perpendicular mirror plane), 2 (anti-symmetric with a mirror plane).

For the C_{3v} point group, we can look at the *character table* and find the *irreducible representations* A_1, A_2 and the doubly-degenerate E that relate the Mullikan symbols for the possible orbitals (in terms of nomenclature). These correspond to orbitals and discrete symmetries (rotations, reflections) that make up the overall C_{3v} symmetry. For reference on group theory and symmetry, see [83]. We will refer to the multiplicity/degeneracy of the

orbitals as being either 'orbital singlets' or 'orbital doublets', which does not describe spin. In labelling the overall symmetry of the defect's wavefunction (not just the single particle orbitals) the system will follow one of A_1, A_2 or E, and will have a superscript that describes the total spin of the system. For example, ${}^3E$ is a *spin-triplet, orbital-doublet* and ${}^1A_1$ is a *spin-singlet, orbital-singlet*. Once again, occupation of the single particle orbitals which are described by the Mullikan symbols (single particle e, a), builds up an overall symmetry label for the multi-particle orbitals of the defect (capital letters with spin multiplicity superscripts).

For VV^0, the dangling bonds end up forming two a_1 and two e (doubly degenerate) single particle orbitals (adding up to the 6 contributed orbitals). Essentially they are combinations of the sp^3 hybridized atomic orbitals of the Si and C atoms that are tetrahedrally coordinated. The energies of these orbitals can be calculated through DFT with respect to the valence and conduction bands for electrons. For VV^0, there is first a low energy a_1 state which gets filled with two of the available electrons that pair up. This level is essentially in the valence band and is (probably) always filled. The next highest energy level is the other a_1 level which is similarly filled but lies above the valence band, leaving two electrons left. The last two electrons fill up the two available degenerate e states that mostly sit on the silicon vacancy site, close to the carbon atoms that are *more* electronegative (want electrons more) than the Si atoms surrounding the C vacancy. These electrons are not forced to pair up in one orbital and thus form a triplet state $S = 1$ occupying these two orbitals for the ground state (e^2). Finally, the last two e orbitals are near the C vacancy and are much higher in energy. In general, the degenerate e orbitals are labelled e_x and e_y as they have definite but orthogonal wavefunctions in the crystal (see Fig. 5.2).

In looking at the full state of the global wavefunction of all 6 particles including spin, this ground state is ${}^3A_2 = \left|e_x e_y - e_y e_x\right\rangle \otimes |S = 1\rangle$ which is an allowed irreducible representation of the C_{3v} point group with a spin triplet. This just means our ground state mostly follows the C_{3v} symmetry of the defect but is anti-symmetric with respect to the mirror planes ('2' as a subscript). The details of how all this works 'under the hood' can be found in [86]. The

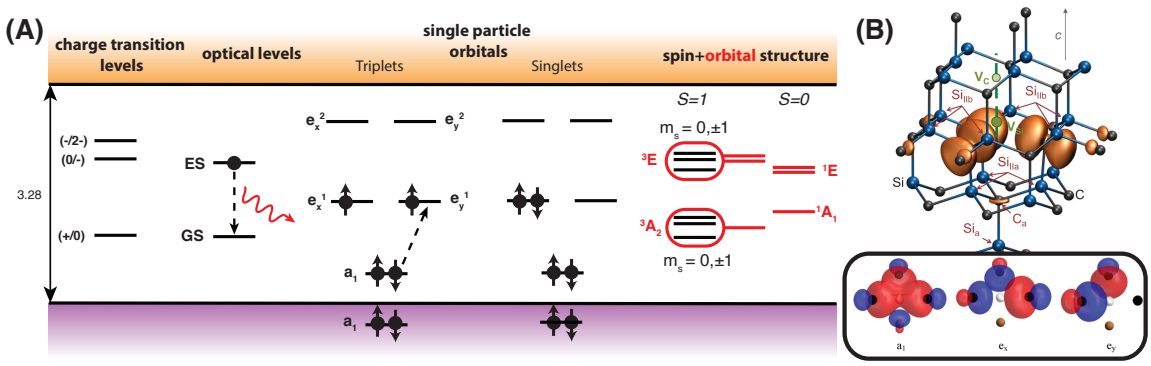

Figure 5.2: **Levels in the gap for the divacancy in SiC. (A)** The multiple pictures of states in the gap for VV^0. The dotted black lines show optical excitation. Both the triplet ground state and excited state singlets are shown. On the far right, the orbital degeneracy is displayed with the red lines and the spin with the black lines.**(B)** The ground state orbital 'spin isosurfaces' for the VV^0, adapted from [84].(bottom) representative wavefunctions for the single particle orbitals (here for the NV^- adapted from [85]).

actual shape of the wavefunction can be seen in Fig. 5.2. These fancy labels just represent rough shapes of these orbitals which are just blobs of the spatial wavefunction in the crystal. Importantly, the single particle picture in Fig. 5.2, does not represent the true energetics of the full multi-particle system, which can be computed directly and needs to include the relaxation of the structure, inter-particle interactions and *Jahn-Teller distortions*. Generally, a better metric for calculating the total energy of the multi-particle system is to look at the formation energy diagrams. In this context, the position of the divacancy's charge transition levels can be found in reference to the SiC bands through DFT. It is worth noting that as a rule of thumb, accuracy in DFT is usually limited to $\pm 0.1\ eV$. We can see in Fig. 5.2 that the divacancy in its neutral charge state sits nicely in the band. Interestingly, VV^0 was originally used as a deep compensating defect in SiC to grow high resistivity material by pinning the Fermi level at the (0/-) level ('older' HPSI material has lots of VV^0).

We then have a ground state spin triplet, which we can use as a qubit. However, the whole point of these systems for quantum technologies is in coupling to flying qubits/photons. In looking at Fig. 5.2, we can roughly visualize what (generalized) excitations of this system would be. In particular, we can imagine taking an electron from the second a_1 state and promoting it to one of the degenerate e_x, e_y states. When we do this, we would still have

Config.	Spin	State	Symmmetry	Note
e^2	S=1	$\left\|e_x e_y - e_y e_x\right\rangle \otimes \begin{cases} \|\uparrow\uparrow\rangle \\ \|\uparrow\downarrow\rangle + \|\downarrow\uparrow\rangle \\ \|\downarrow\downarrow\rangle \end{cases}$	${}^3A_2$	GS $m_s = 0, \pm 1$
e^2	S=0	$\left\|e_x e_x - e_y e_y\right\rangle \otimes \|\uparrow\downarrow - \downarrow\uparrow\rangle$	${}^1E_1$	Lower singlet
e^2	S=0	$\left\|e_x e_y + e_y e_x\right\rangle \otimes \|\uparrow\downarrow - \downarrow\uparrow\rangle$	${}^1E_2$	Lower singlet
e^2	S=0	$\left\|e_x e_x + e_y e_y\right\rangle \otimes \|\uparrow\downarrow - \downarrow\uparrow\rangle$	${}^1A_1$	Upper singlet
ea	S=1	$\|E_-\rangle \otimes \|\downarrow\downarrow\rangle - \|E_+\rangle \otimes \|\uparrow\uparrow\rangle$	A_1	ES, UB $m_s = \pm 1$
ea	S=1	$\|E_-\rangle \otimes \|\downarrow\downarrow\rangle + \|E_+\rangle \otimes \|\uparrow\uparrow\rangle$	A_2	ES, UB $m_s = \pm 1$
ea	S=1	$\|E_-\rangle \otimes \|\uparrow\uparrow\rangle - \|E_+\rangle \otimes \|\downarrow\downarrow\rangle$	E_1	ES, LB $m_s = \pm 1$
ea	S=1	$\|E_-\rangle \otimes \|\uparrow\uparrow\rangle + \|E_+\rangle \otimes \|\downarrow\downarrow\rangle$	E_2	ES, LB $m_s = \pm 1$
ea	S=1	$\left\|E_y\right\rangle \otimes \|\downarrow\uparrow + \uparrow\downarrow\rangle$	E_y	ES, LB $m_s = 0$
ea	S=1	$\|E_x\rangle \otimes \|\downarrow\uparrow + \uparrow\downarrow\rangle$	E_x	ES, UB $m_s = 0$
ea	S=0	$\|a_1 e_x + e_x a_1\rangle \otimes \|\downarrow\uparrow - \uparrow\downarrow\rangle$	${}^1E_x$	
ea	S=0	$\left\|a_1 e_y + e_y a_1\right\rangle \otimes \|\downarrow\uparrow - \uparrow\downarrow\rangle$	${}^1E_y$	
a^2	S=0	$\|a_1 a_1\rangle \otimes \|\downarrow\uparrow - \uparrow\downarrow\rangle$	${}^1A_1$	

Figure 5.3: **Orbital and spin character of the possible VV^0 states.** ES= excited states, GS = ground states, UB = upper branch, LB = lower branch. $E_\pm = |a_1 e_\pm - e_\pm a_1\rangle$ with $e_\pm = \mp(e_x \pm i e_y)$. $|E_x\rangle = (|E_-\rangle - |E_+\rangle)/2$ and $\left|E_y\right\rangle = (|E_-\rangle + |E_+\rangle)i/2$. Adapted from [86]. These states only exist in C_{3v} symmetry. The equivalent assignments for the ground and excited state triplets can be found in [7].

two unpaired electrons in separate orbitals, and the spin that is excited would have to have the opposite spin of the two spins that were in the e orbitals to start with. This state is still a triplet, but is higher in energy with one spin in an a state and one in an e state (ea). There are different symmetric and antisymmetric combinations of these orbitals that result in a multitude of excited states (see Fig. 5.3). In general, this is an ${}^3E$ excited state, which through spin-orbit and spin-spin effects (D in the ground and excited state, see section 5.3) is split into 6 discrete states that correspond to the orbital+spin state. These are $A_1, A_2, E_1, E_2, E_x, E_y$, which are distinct in energy and referred to as the *orbital fine structure*. Under small crystal strains that obey the defect's symmetry, these lines shift as a set (longitudinal strain), but under transverse strain these lines split further, breaking the C_{3v} symmetry of the system. These lines under strain move as two distinct groups called

the *upper branch* (A_1, A_2, E_x) and the *lower branch* (E_1, E_2, E_y) which are higher and lower in energy, respectively. In our commercial samples, this transverse splitting $(\delta_\perp)$ is around $2 - 50\ GHz$. A useful schematic is found in Fig. 5.4. A low but nonzero $\delta_\perp$ is desired to keep the lines separated and cyclicity high. The ground state wavefunction is relatively confined, resulting in long T_1's, but the excited state wavefunction is more extended whereby spin-orbit effects become important ("feels the lattice" more)- just enough to allow for the orbital splitting we need.

Furthermore, the addition of an electric field can shift the wavefunction around and change these energies slightly. This becomes very important for later sections. Just like atoms, the defect in its excited state naturally radiates light (dipole-emission) into free space giving it a natural optical lifetime and creating single photons. Since photons carry no spin, optical transitions to and from this excited state are allowed $({}^3A_2 \leftrightarrow {}^3E)$. These excited states are outlined in Fig. 5.3 in terms of which particular *spin projections* they couple to. The *magic* here is that there are orbital excited states that *directly correspond to different spin states*. Because these orbitals are split in energy, by looking at the energy of light that is absorbed or emitted by these defect orbitals we can *exactly tell which spin state we are in*. These states describe the *spin-photon interface* in that they correspond to entangled states of the orbitals with the spin of the defect (Fig. 5.4). In a sense, this structure gives us strong coupling between spin and light for free. In the fine structure, we desire a large spin-orbit term λ_z that splits that $m_s = 0$ lines from the $m_s = \pm 1$ lines such that they are resolved (which gives the 'strong coupling'). However, we also want a small spin mixing term Δ_2 that slightly hybridizes the spin sublevel's associated orbitals, which causes unwanted spin flips/branching in the excited state. Here we have such a system, with large splittings and a small spin mixing (smaller than the NV^- in diamond [55]). The various spin-orbit and mixing parameters for the VV^0 species can be found in Fig. 6.1.

It's worth driving this into the ground a little. Because there is a spin in the ground state, confined to the defect's potential and far away from the bands, there is an atom-sized,

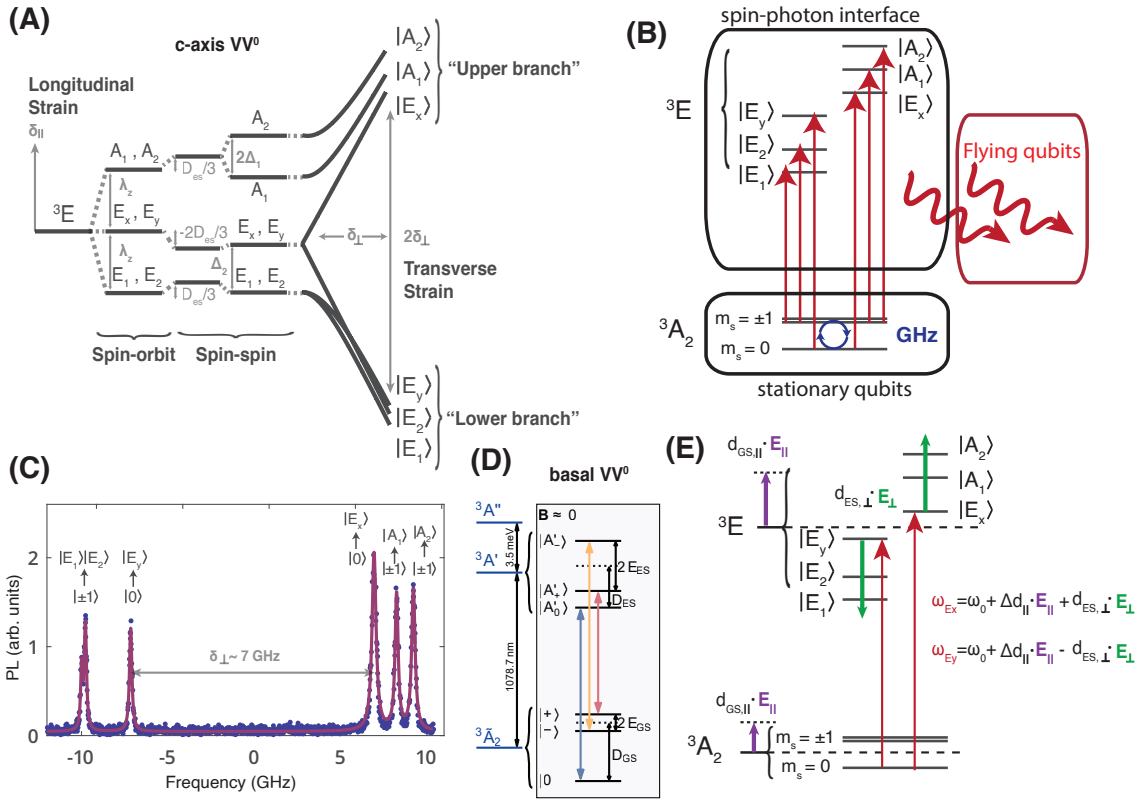

Figure 5.4: **The optical fine structure of VV^0.(A)** Optical fine structure of c-axis VV^0 showing the effects of strain, spin-orbit, and D (spin-spin) on the ^3E excited state. The upper branch and lower branch orbitals are defined.**(B)** The spin-photon interface showing which orbitals coupled to what levels of the ground state spin. Spin-selective absorption produces flying qubits (photons) correlated with the spin state. **(C)** Photoluminescence excitation (PLE) scans of an example defect with a non-zero transverse strain $\delta_\perp$ showing the resolved spin lines of the upper and lower branches of a VV^0 in 3C ($f_0 \approx 265\ THz$). Adapted from [55]. **(D)** The optical structure of a basal kh VV^0, corresponding to a highly transverse-strained defect as in (A). The ground state spin and excited state have new eigenstates and symmetry labels. The same spin photon interface as in (B) exists. Adapted from [7]. **(E)** Stark shifting the optical structure of a c-axis VV^0 differences in the energy shifts of the ground and excited state corresponds to transition frequency shifts under applied bias. Under electric fields along the defect's symmetry, the orbitals move together. Under transverse field, the upper and lower branches move closer and further in energy to each-other.

stable, trapped state of two electrons forming a spin in an orbital. This spin is barely coupled to its crystal host and displays ultralong T_1 such that we can barely measure them at our standard measurement temperatures of 4K. Molecule/atom-like optical excitations of the ground state orbital can be done that *change the orbital state but do not disturb the spin.* In particular, the excitation will only happen if the energy matches a certain transition that

depends on the spin-qubit's state. If such an excitation occurs, the defect will be promoted to its excited state, maintain its spin, and then emit a single photon. Because the spin is not destroyed, the transition is said to be *cycling*. In this sense, the transition can be probed again and again without destroying the spin when measuring in one of the spin eigenstates. Non-projective repetitive readout can also be performed on superposition states with some extra considerations. Of course, no system is perfect and a small amount of *mixing* is present. This mixing is described further in section 5.2.3. Generally, the amount of mixing will set the spin-photon entanglement fidelity as it sets the chance that your emitted photon still correlates to the state you started with. For VV^0, the E_x and E_y orbitals are highly cycling. Both the upper and lower branches of the orbital structure contain cycling and noncycling transitions. For the basal divacancies, we can think about the orbital fine structure as a perturbation on the C_{3v} structure of the c-axis VV^0 that looks like a large transverse strain. This results in the upper and lower branches being split by a large energy difference. In experiment, we can observe the lower branch whose structure is described in [7] that still contains cycling lines and performs similarly to the c-axis VV^0, but the upper branch is not observed and most likely rapidly relaxes to the lower excited state orbital (see Fig. 5.4).

This orbital structure is very nice (atom-like), but unfortunately the system still couples to *phonons* in the lattice. As the temperature is raised, the phonons can cause broadening and mixing between these orbitals that degrade the spin-photon interface [87]. In thinking about the excited state orbitals, the relaxed potential energy diagram of the system has a slightly different configuration of the atoms in the system compared to the ground state. In a generalized *configuration coordinate* energy diagram in Fig. 5.5A, we can see that although optical excitations are *vertical*, the energy minimum of the excited state is offset in position along a 'normal mode' of the lattice (a generalized diagram will have many dimensions). The excited and ground state will also couple to the localized phonon modes giving the harmonic spectrum shown in Fig. 5.5. This vertical nature of the optical excitation is called the *Franck-Condon* principle and is a statement that electronic transitions do not involve

instantaneous displacements of the atoms.

In terms of the possible vertical electronic absorptions and emissions, we can see that there is actually a spread in what can be absorbed and emitted based on this *vibronic* spectrum. After transitioning between the ground and excited state, the state will rapidly fall down the local potential releasing phonons ($\sim ps$). However, there does exist a transition from the bottom of the ^3E excited state to the bottom of the $^3A_2$ state that doesn't involve phonons at all. Spectrally, this line is called the *zero-phonon line* (ZPL). We can see that based on the overlap integral (*Fermi's Golden Rule*) between the vibronic states in the ground and excited states, this transition's probability will be more or less likely. Upon excitation, the fraction of emitted light that occurs in the ZPL is called the *Debye-Waller factor (DWF)*. The DWF is related to another spectroscopic paramter called the *Huang-Rhys* factor. The ZPL itself contains all the structure ($A_1, A_2, E_1, E_2, E_x, E_y$) described above. The emission spectrum will in general consist of this ZPL, along with a very broad *phonon sideband*. At low temperatures, the sideband may display structure and peaks related to the vibration frequencies ('replicas') at the defect. The shift in energy from the ZPL is sometime called the Franck-Condon shift. Overall, each of the vibronic levels in Fig. 5.5 also have orbital structure associated, but the structure is distorted with respect to our previous understanding such that for each vibronic state things are different. Not only that, but as we rapidly fall down the vibrational spectrum, the orbitals lines get 'blurred out' as we rapidly change the position of the atoms. Because the phonons are fast, the minimum of the excited state is reached before any emission can happen (the spin doesn't care about this vibronic relaxation and is conserved). Thus, *off-resonant* excitation (not on the ZPL) can still efficiently optically excite the defect, which rapidly relaxes to the bottom of ^3E, but does not have the spin-selective excitations described above. When the defect emits, the light in the ZPL will still depend on the spin-selective transitions from before. However, the light emitted in the phonon sideband is just a broad mess that describes the radiative decay to the 'blurred' out transitions in the ground state (not spin-selective from the spin-photon

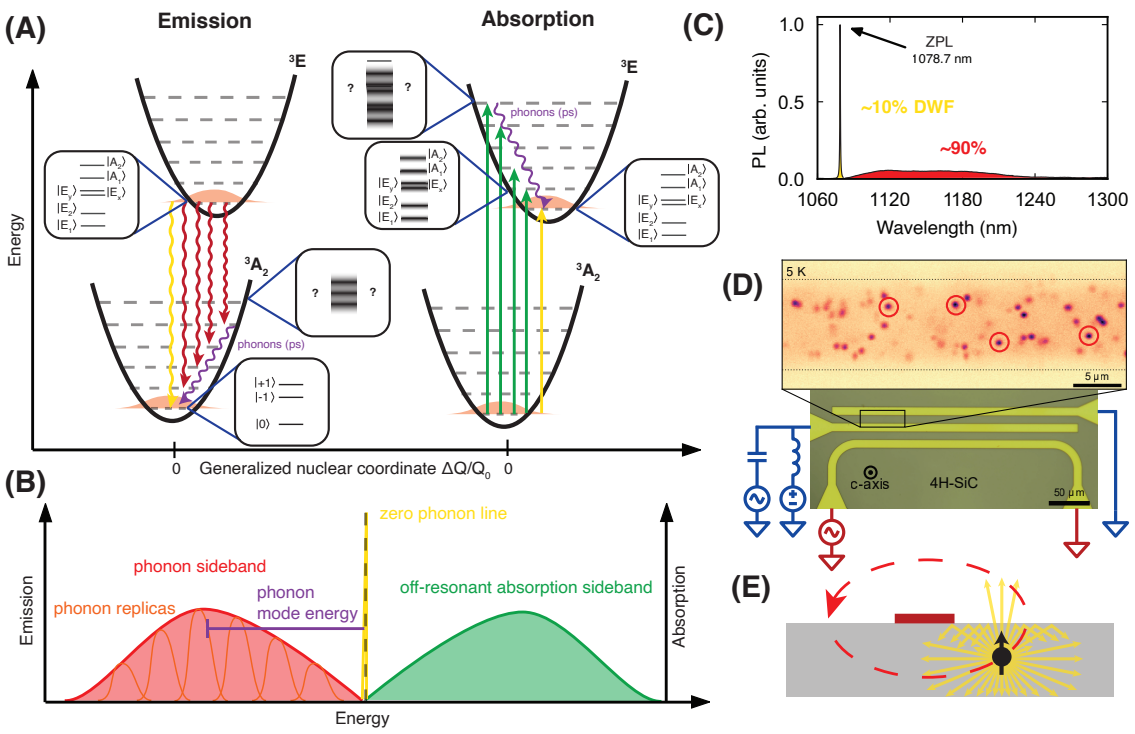

Figure 5.5: **Vibronic structure and single defect measurement**. **(A)** (left) Franck-condon principle of vertical transitions. The black lines represent the energy structure of the ground and excited states with displacements of the defect's structure along a particular vibrational mode. Emission from the bottom of the harmonic potential (with the ground state wavefunction in orange) of the excited state can occur due to varying overlap (Fermi's golden rule) with the ground state structure. In red, the phonon sideband of lower energy photons emitted. In yellow, the ZPL from the bottom of the ES to the bottom of the GS, involving no phonons. Phonons (purple) relax the structure very quickly on the ps timescale. In the inset boxes, the fine structure at various configurations showing the non spin selective and blurred out emission energies. (right) Absorption from the ground state, which includes the ZPL and higher energies (constituting the absorption side-band), with fast relaxation from phonons. Similarly, the fine structure is shown at various configurations, demonstrating that the well-known optical fine structure only exists at the ZPL and gets blurred out upon interactions with phonons and distortions.**(B)** Schematic of the 'mirrored' absorption and emission spectrum across the ZPL. Schematic phonon replicas (orange) are blurred together to form the phonon sideband. **(C)** Emission spectrum of a single kh VV^0 showing a Debye-Waller Factor (DWF) which is the fraction of the emission in the ZPL (yellow) of $\sim$ 10%. **(D)** Spatial photoluminescence scan pumping on the absorption side band and collecting the emission side band. The isolated dots corresponds to single defects. These spins are manipulated using fabricated striplines and gates (red, blue). Adapted from [7]. **(E)** Schematic cross section of a SiC showing the microwave drive line and field direction (red) for a c-axis SiC spin. The yellow lines correspond to the emitted light from the defect which is mostly totally-internally reflected off the SiC-vacuum interface.

interface). Looking at Fig. 5.5C, we can see that the absorption spectrum and the emission spectrum will be roughly mirrored across the ZPL. For quantum applications, we usually want a system with a large DWF meaning that a larger fraction of the light contains the narrow spin-photon interface we want to use. Lowering the temperature narrows the ZPL (phonons disturb the structure and blur the lines) and increases the fraction of the light it contains due to decreased thermal occupation of phonons and reduced line broadening (see appendix A). However, the ultimate limit of the DWF is the details of the configuration coordinate energy diagram, even at low temperature. Luckily, as the defect is excited from the ground state to excited state, and as we relax with phonons, the spin state retains its coherence[88].

5.2.1 Singlets and ODMR

What about the possibilities for spin singlet states using these same orbitals? We described how the ground state of the system is a triplet based on filling up the single particle orbitals, but other excited states can exist. In particular for VV^0, the two singlets that matter exist by pairing up the two spins in the 'same' e orbital (e^2) with different combinations of the single particle orbitals. These are ${}^1E$ ($\left|e_x e_x - e_y e_y\right\rangle$) and ${}^1A_1$ ($\left|e_x e_x + e_y e_y\right\rangle$) which are different superpositions of the two spins in the same orbital (where they pair up, forming a singlet). These singlet states are shown in Fig. 5.2. For VV^0, the ${}^1E$ state is below the ${}^1A_1$ state in energy where both states lie between the triplet ground and excited states (Fig. 5.6).

Jahn-Teller distortions refer to a symmetry breaking that lowers the total energy of the system. Both Jahn-Teller and spin-orbit mixing allow for a small overlap between the triplet excited ${}^3E$ state and the higher singlet ${}^1A_1$. This forms an *intersystem crossing (ISC)* where the spin-triplet manifold couples to the spin-singlet manifold, which is optically 'forbidden'. The other piece of magic in this system is that the transition rate from ${}^3E \rightarrow {}^1A_1$ is *different* depending on which spin state ($m_s = 0, \pm 1$) you are in. The orbitals in Fig. 5.3 that contain

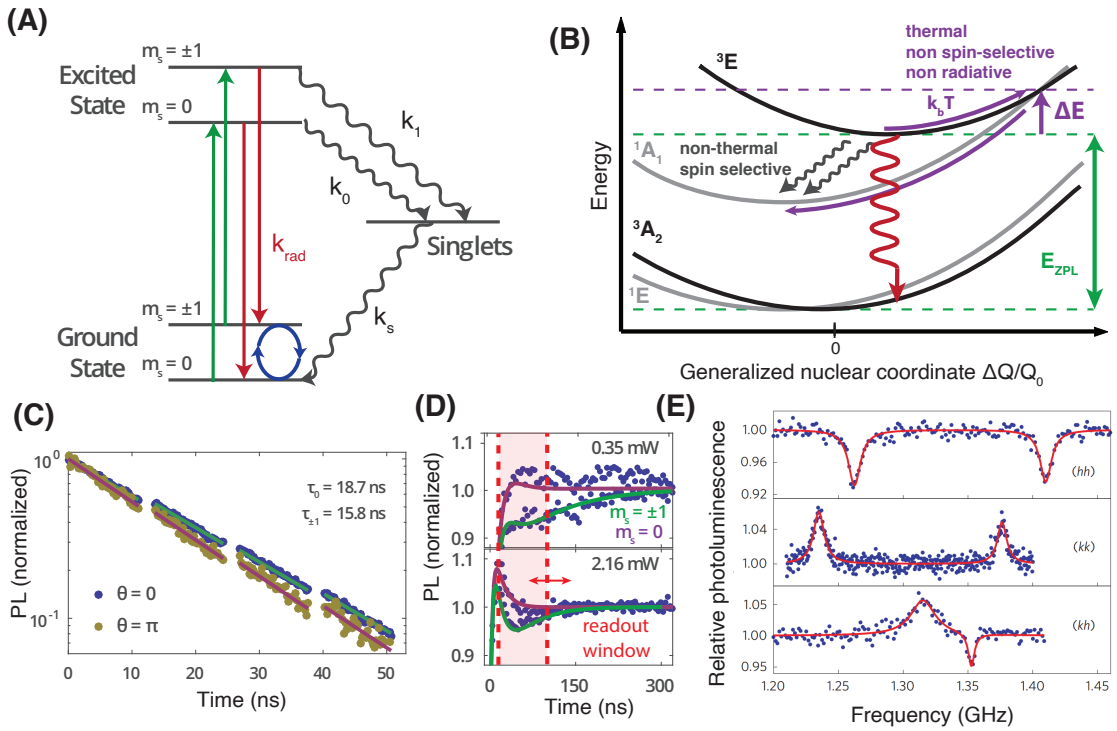

Figure 5.6: **Singlet dynamics and ODMR. (A)** Radiative absorption and emission (green and red) processes conserve spin (k_{rad}), while the intersystem crossing rates from $m_s = \pm 1$ (k_1) and from $m_s = 0$ (k_0) transition to the $S = 0$ manifold. From these singlets, the state crosses back over to $S = 1$ through a second ISC (k_s). In VV^0 this is proposed to happen predominantly to the $m_s = 0$ state. Because of this, continuous excitation polarizes in $m_s = 0$. Microwave mixing (blue) can drive between the spin states and cause a different balance of radiative and nonradiative rates, resulting in ODMR. **(B)** Schematic configurations coordinate diagram [89] for spin 1 systems like the NV^- in diamond or the VV^0. The ISC transitions are shown with grey arrows, while thermal excitations can cause a non-spin selective crossing into the $S = 0$ states. This is the mechanism for reduced contrast and QE at high temperatures. **(C)** Example excited state lifetime modification in a 3C-SiC VV^0 in either $m_s = 0$ (blue dots) or $m_s = \pm 1$ (gold dots), showing that in this defect $k_1 > k_0$. **(D)** Example time trace of fluorescence of a single defect with off-resonant excitation at different optical powers prepared in either $m_s = 0$ or $m_s = \pm 1$. Contrast (total photons difference under the curve) changes with differing readout windows. When the $m_s = 0$ and $m_s = \pm 1$ lines overlap the spin has polarized/been completely read out. The rates in (A) can be fit through the power dependent time-traces. **(E)** CW ODMR of different VV^0 species achieved through microwave mixing the spin states, changing the balance of radiative/nonradiative rates, causing increases or decreases in fluorescence. The signs and magnitudes correspond to differences in k_0,k_1,k_s. Figures adapted from [55, 90].

$m_s = \pm 1$ character, for example, can have a greater (or less) overlap with the higher singlet orbitals. Through *Fermi's golden rule* the wavefunction overlap determines the transition

rate.

Once the system has crossed over to the singlet manifold into $^1A_1$, the state can decay either radiatively or nonradiatively down to ^1E or potentially to the $^3A_2$ ground state directly. For VV^0, emission or direct measurement of the singlet energies has not been achieved and this understanding mostly stems from DFT calculations. However, measurements of the spin-dependent crossing rates and the *shelving* times (the time the state is stuck in the singlet) have been measured for the divacancy in the 3C polytype[55]. Once in the lower ^1E state, the system can go through another ISC to cross to the true ground state $^3A_2$. Similarly, the rate into the ground state $m_s = 0, \pm 1$ from ^1E can be different.

The thing to realize here is that *even if we cannot perform the spin-selective excitation in the ZPL*, the $m_s = 0, \pm 1$ will couple differently into or out of the ISC. When the defect decays through the ISC, instead of being purely radiative (into the emission spectrum in Fig. 5.5), there are different amounts of nonradiative components. This means that *how radiative* (how much light comes out of our defect) the defect is *depends on the spin state*. Therefore, by looking for differences in the number of photons coming out of our system, we can measure the associated spin state *without* the need for a high-fidelity spin-photon interface. Not only that, but by continuously pumping 'off-resonantly', depending on the ratio of the ISC rates, the spin can be efficiently polarized (initializing the qubit). In particular, the rates in both VV^0 and NV^- in diamond have the spin-flip transition of $m_s = \pm 1 \rightarrow m_s = 0$ through the ISC happen readily, meaning that if we start in $m_s = \pm 1$, after cycling through the excited state enough times we can be sure that no matter the starting state, our system is initialized into $m_s = 0$. Here, the initialization time and fidelity depends on the delicate balance of rates. Similarly, under continuous off-resonant excitation we can extract many photons correlated with the spin state before going through the ISC and flipping (Fig. 5.6), allowing for high signal (there is an interesting trade-off here between polarization fidelity and detection contrast). This is nature's gift to us. It just so happens that we found a system with the right sorts of levels, corresponding to the right sorts of spin-selective rates,

VV^0 type	orientation	ZPL	D (GHz)	E (MHz)	Contrast ($\pm$)	T_C
PL1 (hh)	c-axis	1.095 eV, ∼1132 nm	1.336	0	∼ 9% ($-$)	∼ 225 K
PL2 (kk)	c-axis	1.096 eV, ∼1131 nm	1.305	0	∼ 14% ($+$)	∼ 175 K
PL3 (hk)	basal	1.119 eV, ∼1108 nm	1.222	82.0	? ($-$)	∼ 75 K*
PL4 (kh)	basal	1.150 eV, ∼1078 nm	1.353	18.7	∼ 16% ($\pm$)	∼ 50 K
PL5 ($kh-ssf$)	basal: stacking fault	1.189 eV, ∼1043 nm	1.373	16.5	? ($-$)	∼ 500 K
PL6 ($kk-ssf$)	c-axis: stacking fault	1.150 eV, ∼1078 nm	1.365	0	? ($-$)	$300K^{\dagger}$

Figure 5.7: **Table of important VV^0 parameters.** From references [13, 56, 90, 91]. "?" are unknown parametesr. "*" there may be a revival of contrast at high temperatures. "†" the upper limit has not been measured. T_C is the temperature where the contrast drops by a factor of two. 'ssf' refers to divacancies near stacking fault inclusions [56].

such that we can polarize and readout our spin this way. The real kicker here is that this means that readout of a single defect's spin can be done using only off-resonant excitation and collecting the broad thermally blurred out phonon sideband fluorescence, even at room temperature! By applying a microwave pulse or tone resonant to a spin transition that changes the relative balance of $m_s = 0, \pm 1$, the amount of light emitted by the spin changes ('contrast'). This measurement is then *optically-detected magnetic resonance* (ODMR) of the quantum state of a *single spin*. For context, other methods for measuring spins such as ESR only work for ensembles, such that this is one of the few systems where one can play with single spins.

These facts are why the spin defect community exploded in terms of interest, and have broad applications for room-temperature quantum sensors and for easy demonstrations of quantum physics on the benchtop. Each particular defect that displays ODMR has different signs and magnitudes of this ODMR, shown in Fig. 5.7. As each of the VV^0 sit in different physical parts of the lattice, their spin and orbitals will be slightly different, the exact details of how this all works changes as well. In general, VV^0 have moderate ODMR contrast of 5-10% and high fidelity initialization (90+%) based on the rates of the ISC. Unfortunately, while the NV^- center in diamond works at room temperature, most of the VV^0 show reduced contrast (with notable exceptions[56]) at elevated temperature.

Variations in operation temperature can be understood (and is widely confused in general)

by looking again at the configuration coordinate diagrams, including the singlet states (Fig. 5.6). The spin selective rates to go to the top of the ISC are mixing/tunneling to cross to the other spin manifold. However, there is also a direct crossing available with enough distortion that lowers the overall energy. This crossing has a corresponding energy barrier for the spin to turn from a triplet to a singlet. Depending on the exact details of the system, this barrier can be higher or lower. If there is enough thermal energy, instead of radiating light, phonons can bump the state over to the singlet which is a *non-spin-selective, non-radiative process*. This means that at elevated temperature, the contrast decreases, and also the *Quantum Efficiency (QE)* decreases. QE just refers to the fraction of the time a trip to the excited state results in a photon (versus a non-radiative pathway to get back to the ground state). QE is an important metric that determines the quality of a single photon emitter. The QE (sometimes called a quantum yield) for the NV^- center in diamond is between 70-100% depending on the reference source and is effected by the ISC or any other nonradiative rates (for example, directly dropping to the ground state by emitting phonons). The contrast and the QE for the diamond (NV^-) survive up to around 600 K[89], which is a statement of the barrier height between the singlet and triplet manifolds. For VV^0, each defect has different behavior that is outlined in Fig. 5.7. In general, cryogenics are needed to reach the temperatures for full QE and contrast. Certain other systems in SiC, such as the isolated V_{Si}^- defect, have contrast that survive to room temperature[92], but this is greatly reduced due to the elevated temperature[53] much like many of the VV^0 species (but is *not* associated in a reduction of counts/QE). Interestingly, VV^0 near stacking faults in SiC have unique spin and orbital properties that allow for room temperature operation and above[56, 91]. The different species of VV^0 have different ZPL energies, DWF and details of the optical structure which is summarized in Fig. 5.7. In general, the QE for VV^0 will need to be measured carefully using a controlled altering of the photonic density of state and some fitting [93], alongside fitting the intersystem crossing rates (see [55]) and measuring the true cyclicity of the different types of VV^0.

We can then see that VV^0 in SiC fulfills the second set of WKV criteria[64] that describes an ideal optically-active spin in the solid-state:

1. *A bound state that is suitable for use as a qubit.* This state must be paramagnetic and long-lived, and an energy splitting must exist between at least two of the state's spin sublevels. If the qubit state is to be manipulated via electron spin resonance, the size of this energy splitting must fall within an appropriate range of the radio frequency spectrum. (For VV^0, this is 1-2 GHz)

2. *An optical pumping cycle that polarizes the qubit state.* This cycle will most likely consist of an optical transition from the ground state to an excited state, followed by a spin-selective decay path that includes one or more nonradiative transitions between states of differing spin multiplicity.

3. *Luminescence to or from the qubit state that varies by qubit sublevel in some differentiable way, whether by intensity, wavelength, or other property.* If fluorescence from an excited state is used to probe the qubit, the fluorescent transition should be spin-conserving. In addition, the strength of this fluorescent transition, which depends on the lifetime of the excited state, should be large enough to enable efficient, high fidelity measurement of individual defect qubit states. (For VV^0, the optical lifetime is $\sim 15\ ns$ and this is fulfilled)

4. *Optical transitions that do not introduce interference from the electronic states of the host.* All optical transitions used to prepare and measure the qubit state must be lower in energy than the energy required to transfer an electron into (out of) the center from (to) the electronic states of the host. (For VV^0, this extremely important and related to the work of this thesis in chapter 11)

5. *Bound states that are separated from each other by energies large enough to avoid thermal excitation between them.* If the energy difference between two bound states is too small, thermal excitations may couple states and destroy spin information

In these original WKV criteria, the idea was to find a system that displayed the same ISC physics as the NV^- center in diamond to see off-resonant, room temperature ODMR. That being said, for the applications of quantum communication which use low temperatures and utilize the spin-photon interface in the ZPL, these singlets are actually a *problem*. For VV^0, from both DFT and experiment it looks like even if the spin is in $m_s = 0$ (where we want things to be radiatively cycling), the defect has a chance of crossing to the ISC. This extra rate reduces the optical lifetime, and means that the QE is reduced. Luckily, since the ISC returns us to the $m_s = 0$ ground state, the overall transitions are still largely 'cycling' but have a significant non-radiative component. In experiment, the VV^0 in 3C-SiC have a QE of around 80%, though the defects in 4H are less well characterized. Comparing to theory, some results predict a 60 ns radiative lifetime [94], which implies a roughly 30% QE (using the experimental optical lifetime of around 15 ns), while more recent results compute lifetimes of around 20 ns for the c-axis VV^0 corresponding to roughly 80% QE [95]. Although the ISC is nice for the ease of spin initialization, in an ideal system for quantum communications, we would avoid it altogether as it can cause unwanted spin flips and nonradiative rates (maybe our spin goes through the ISC when we don't want it to). In fact, some systems in the field operate with only $S = \frac{1}{2}$ such that there is no intersystem crossing (such as the SiV^- in diamond).

5.2.2 Spin Flips, Resonant Initialization and Strain

Borrowing optical pumping techniques from atomic physics and relying on the small mixing in the excited state means that we can avoid relying on the ISC and use *resonant initialization*. Each of the lines in the orbital fine structure couple differently to the ISC, and have different amounts of mixing to each other. Just considering the mixing in the excited state, we can estimate the predicted cyclicity or number of photons that can be extracted from this transitions before the spin 'flips' into the wrong state (a branching ratio). This is shown in Fig. 5.8 as a function of a 'transverse strain'. As transverse strain is added (and the C_{3v}

symmetry is broken), the mixing between states changes and the cyclicity can drastically change. Strain here refers to a physical disturbance in the lattice, or could also be an electric field. Transverse strain can better be thought as a generalized energy shift that breaks the Hamiltonian's symmetry. The actual shifting dipole per unit strain have had preliminary measurements [13], but require further investigation. Luckily, the predicted quality of the spin-photon interface in VV^0 is quite high (better than the diamond NV^-[55]). However, these numbers do not take into account ISC induced mixing or QE reduction. The actual quality of the spin-photon interface is still an open question, though things look promising.

This mixing in the excited state means that some fraction of the time we pump an $m_s = 0$ transition, we end up in $m_s = \pm 1$. However, once we are in $m_s = \pm 1$, our laser is no longer resonant and the system gets trapped in a $m_s = \pm 1$ 'dark state' (does not emit light). Continuously pumping on $m_s = 0$ means eventually we will spin flip, and after enough time we are almost sure to be in $m_s = \pm 1$. This is called *optical pumping*. Conversely, pumping on $m_s = \pm 1$ with a second laser can pump us into $m_s = \pm 0$ and also benefits from the ISC. This is 'resonant initialization'. For spin qubit readout, we similarly cannot probe the readout cycling transition for too long, otherwise we will just be averaging nothing because the spin has already flipped and no photons are coming out (except noise). The readout time must be optimized along with the optical power to maximize the signal-to-noise. Interestingly, in this scenario: 'a slowly initializing qubit is a good readout qubit and vice-versa'. These considerations can be seen in Fig. 5.8.

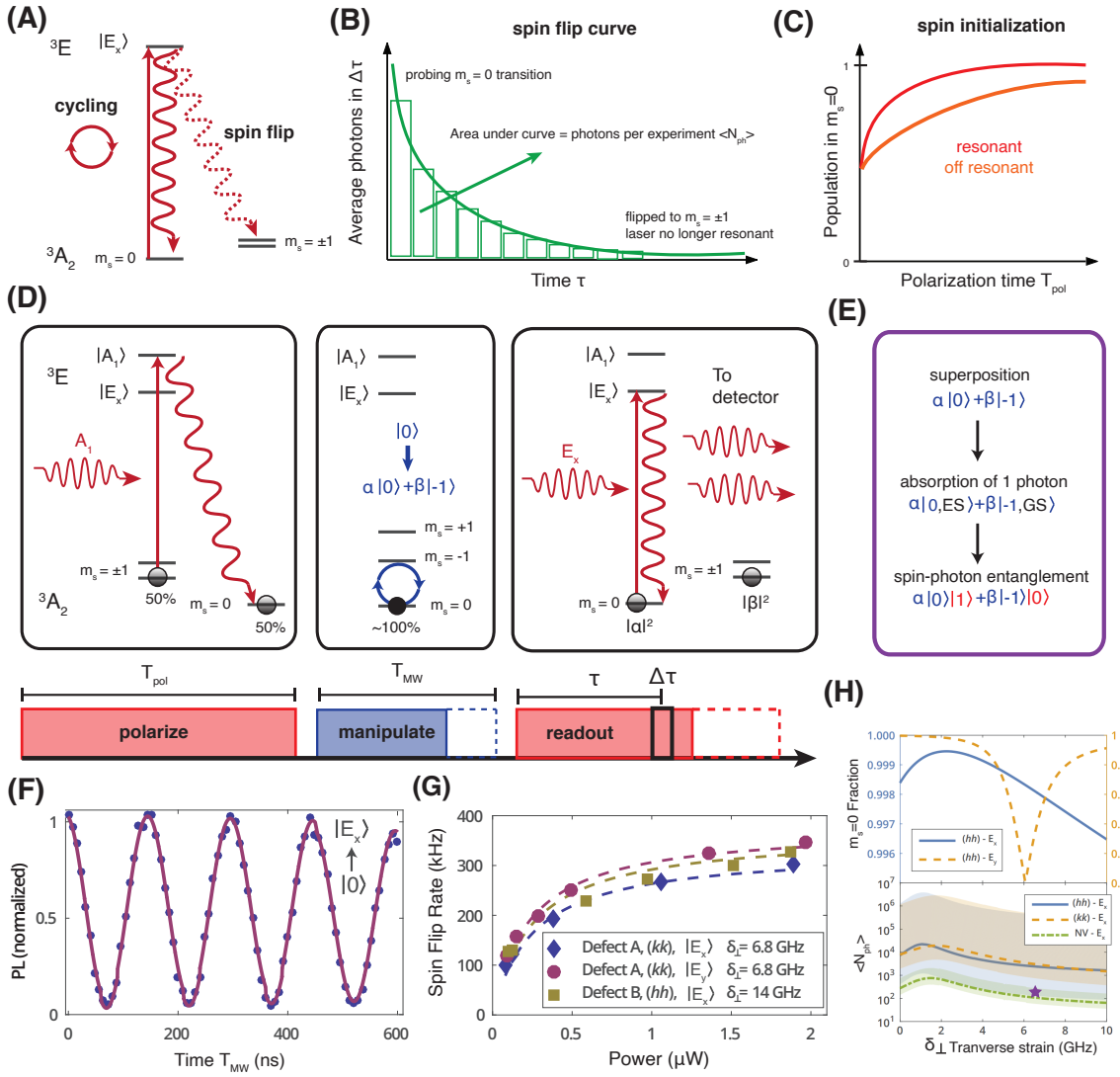

Figure 5.8: **VV^0 initialization, control and readout** **(A)** Cycling and spin flip transitions in VV^0. **(B)** Schematic spin flip curve, exponential decay. The integration window τ must be chosen to collect all the photons, but not be so long that only noise is added. **(C)** Schematic spin initialization curve. Initialization can be achieved with off-resonant light using the ISC, or using optical pumping with resonant light as shown in (D). **(D)** Schematic for resonant initialization, microwave control and resonant readout of a VV^0 spin. **(E)** Spin-photon entanglement using spin-selective optical excitation. **(F)** Example Rabi oscillations of a single spin using off-resonant initialization and resonant readout in 3C-SiC. **(G)** Exponential decay rate of (B) for single VV^0 as a function of optical power for multiple VV^0. With an optical lifetime of ~ 15 ns, this corresponds to roughly (1/(15 ns))/300 kHz $\sim$ 222 photons extracted per shot at saturation. **(H)** Average number of photons extracted before a spin flip event given the known excited state mixing as in Fig. 5.4 and comparisons to the NV^- in diamond. The mixing reduces the $m_s = 0$ character of the excited state, causing a branching and spin flips. The purple star is the measured value from (G). The model in these plots do not take into account the ISC. Adapted from [55].

5.2.3 Degradation of the Spin-Photon Interface

For VV^0, the excited state lifetime is roughly 13-18 ns depending on the defect and the spin state (Fig. 6.1). This sets the lifetime limited linewidth of the photons absorbed and emitted from the spin-photon interface at $\sim$ 10 MHz (see Eq. 2.11). Fortunately, the splitting between the orbitals in the fine structure is on the order of GHz such that overlap/unwanted driving of nearby lines can be avoided (this is not necessarily a given). The two lines that have the highest cyclicity are the E_x and E_y lines. With nonzero strain, they split significantly and are usually a few GHz to 100's of GHz apart in our materials. These orbitals are orthogonal and couple to (orthogonal) linearly polarized light. In the very high strain limit, mixing with the other orbitals gives the polarization a slight circular character. Phonon induced processes can directly cause transitions between the $E_x \leftrightarrow E_y$ which causes changes in the energy and polarization of the emitted light [87]. Other processes are available and are discussed in appendix A. In general, even moderate temperatures near 10 K are high enough to cause unwanted broadening in the optical lines through phonon-assisted processes[6]. Phonon-assisted broadening was recently theoretically treated for the V_{Si} in SiC [96]. Luckily, commercial closed-cycle 4 K cryostats with optical access are available and used for all the work in this thesis.

A common metric is not only to measure the linewidth of your optical line, but to perform *optical Rabi oscillations* between the ground and excited state, whose decay is indicative of the coherence of the *excited state orbitals*. The coherence and spectral/temporal shape of the emitted light from the spin are extremely important for performing the two-photon interference necessary for long-distance quantum communications covered in chapter 8. Laser drift, measurement inaccuracy and exact sample temperature are also important things to consider. Finally, *spectral diffusion* randomly shifts the defect's lines around (dephasing it) due to surrounding environmental noise and is covered in section 6.2. The two levels (the ground and excited state) are just like the qubits we covered in chapter 2 and have the same descriptions of coherence and line broadening as for spin ground states (T_1, T_2^*, T_2).

In general, the c-axis VV^0 are extremely similar to the NV^- in diamond in terms of the behavior of its excited state and singlets which allows for easy connections to techniques, terminology and existing literature in diamond. We just got lucky that there's an NV^- analog in SiC.

5.3 The Spin Ground State

We now have the basic understanding of the orbital structure of VV^0 and how it relates to spin. Going back to the $S = 1$ ground state, we can write the Hamiltonian of our spin:

$$H = S \cdot D \cdot S + \gamma_e B \cdot S + \sum_j S \cdot A_j \cdot I_j \tag{5.1}$$

γ_e is the electron gyromagnetic ratio which actually contains a full *g tensor* (multiplied by other factors) that describes the magnetic moment for arbitrary directions of the field. In general, spins in solids can display highly asymmetric g factors. For isolated electron spins this term is purely isotropic. Interestingly, the g factor of the electron is one of the most well-understood physical quantities ever measured and theoretically treated by humans (≈ 2). Luckily, the divacancy also has a nearly isotropic g factor ≈ 2. Importantly, this g factor is the same in *both the excited state and the ground state*. This means that the optical lines (more specifically, the energy differences between the ground and excited states) discussed in section 5.2 do not move with magnetic fields. In this Hamiltonian, D is the *zero field splitting tensor*, and A is the *hyperfine tensor* that describes the central spin coupling to many nuclear spins indexed by j with spin operators I. The hyperfine coupling tensor includes the dipole-dipole coupling of the spins along with the 'contact' term of the wavefunction overlap between the electron and nuclear spin (which becomes important for nuclear spins within the first few lattice sites). For reference, measurement of the hyperfine tensor is a great way to identify your defect, as it will need to obey certain symmetries and can be well matched to DFT predictions (as done for the VV^0[79]). The zero field splitting describes the energy differences

between $m_s = 0, \pm 1$ due to the orbital shape and symmetry that the spin lives in. Think of it as an electron repulsion interaction energy of the two electrons in the defect enforced by the lattice that depends on the spin state [97]. Because of the symmetry of the defect, the D tensor can be simplified. For control of the spin with phonons, variations from this simplification can give rise to terms that drive spin transitions (chapter 10). Assuming the quantization axis and applied field are along z, we use this simplification and write (using the *secular approximation*):

$$H = DS_z^2 + E_x(S_x^2 - S_y^2) + E_y(S_xS_y + S_yS_x) + \gamma_e B_z S_z + \sum_j (A_{||,j} I_{j,z} + A_{\perp,j} I_{j,x}) \cdot S_z \quad (5.2)$$

$A_{||} = A_{zz}$ and $A_\perp = \sqrt{A_{xz}^2 + A_{yz}^2}$ describe the hyperfine component along and perpendicular to the defect (z) axis. E_x and E_y relate to zero field splitting terms. In particular, they correspond to particular deviations from C_{3v} symmetry. For VV^0, the c-axis defects have $E_x = E_y \approx 0$ while the lower-symmetry basal defects have significant E terms[7]. A summary of the various spin Hamiltonian parameters for the different VV^0 can be found in Fig. 5.7. Ignoring the nuclear spins surrounding the defect, we can see the energy spectrum of the spin of VV^0 in Fig. 5.9. D is around one gigahertz, putting VV^0 in the microwave regime where exquisite microwave control and electronics are available commercially. The spin sublevels can be shifted and transitions between them can be easily driven by applied magnetic fields. There are a significant number of terms missing in this Hamiltonian, including the nuclear Zeeman term $\gamma_n B_z I_z$, the nuclear-nuclear dipole interaction terms $\sum_{i \neq j} I_{z,i} \cdot I_{z,j}$, the interaction of surrounding electron spins (S_k) in the material with our central spin $\sum_k S_{z,k} \cdot S_z$ (some strength prefactors missing here), and electron-electron interactions $\sum_{n \neq m} S_{z,n} \cdot S_{z,m}$ among those spins. Additional perturbations due to electric fields are small but couple like the E_x and E_y terms and can shift or drive transitions [98, 99]. Similarly, external strain couples into the full D tensor which add extra terms that can shift and drive transitions[9]. At some point we have to stop, though! One final note is that

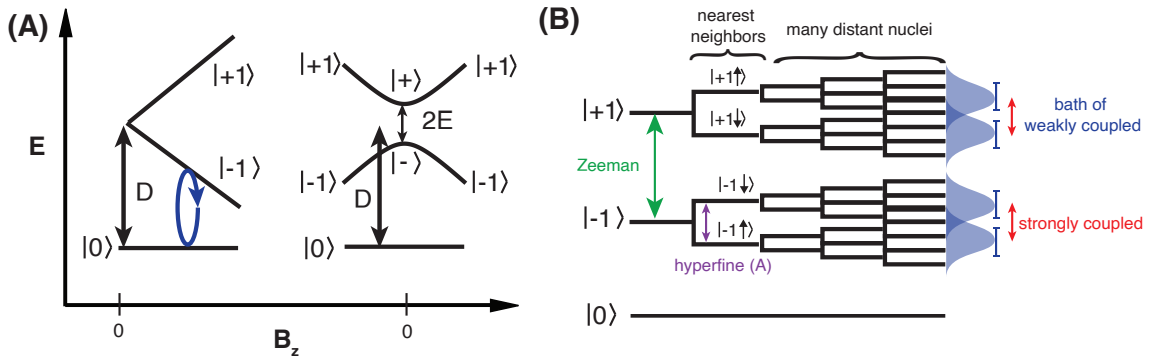

Figure 5.9: **The spin ground state. (A)** Energy of the spin sublevels as a function of magnetic field. The c-axis VV^0 (left) show a linear Zeeman splitting and a zero field splitting D, while the basal VV^0 (right) show a ZEFOZ and hyrbidization at $B = 0$ due to the E term in the Hamiltonian.**(B)** Schematic showing strongly and weakly coupled nuclear spins to a c-axis VV^0. The weakly coupled bath results in a broadening, but strongly coupled nuclear spins can split the lines by more than a linewidth.

the spin Hamiltonian changes dynamically as we go to the excited state orbitals; this can cause issues when spin control of electrons and nuclei is combined with interleaved optical excitation.

5.3.1 Spin T_1 and T_2 in the Solid-state

If we consider our electron spin qubit, uncontrolled hyperfine and electron-electron interactions, electric fields, magnetic fields and strains can cause our spin to decohere (reduction of T_2 and T_2^*). Furthermore, we need to think about what mechanisms will cause T_1 decay for this system. For T_1, direct radiative decay of our spin from the higher energy $m_s = \pm 1$ to the lower $m_s = 0$ is possible, but direct decay this way would take longer than the lifetime of the universe [100]. This is why spins are exciting long-lived qubits. Unfortunately, spins in the solid state have weak but non-negligible coupling to the host lattice. Luckily, due to the confined potential of the defect's spin combined with the high *Debye temperature* of SiC (and diamond), spin lifetimes can remain robust up to room temperature. A high Debye temperature means that the phonons are high energy and further away from the energy scales of the spin states. In general, for spin-lattice induced T_1 decay, there are *direct* processes where

the spin emits or absorbs a phonon at the resonance frequency and *Raman* processes where a lattice phonon scatters off the defect and gains or loses energy corresponding to the spin's energy (creating a higher or lower energy photon). Finally, there are *Orbach* processes that correspond to phonons that excite/mix the spin to a different orbital state with a particular energy. For ground states with nearby electronic orbitals only 10's to 100's of GHz away, this effect is dominant a dramatically reduces coherence (such as in the SiV^- in diamond). Fortunately, lattice-induced T_1 decay can be drastically reduced by going to lower temperatures. Each type of phonon-induced T_1 process has a particular temperature scaling which can be informative for identification. Direct and Orbach-induced decay may be frozen out using phononic band-gaps [101], though this has not been demonstrated. Additionally, a low spin-orbit interaction (which gives a low spin-strain coupling) also reduces these effects. For VV^0, T_1 at room temperature is 100's of μs, while at 4K it is already well over a second and is difficult to measure (and by this point, it's long enough). In particular, residual laser leakage (and therefore optical excitation) from the *acousto-optic modulator (AOM)* which turns the lasers on and off in our experiments is the dominant 'T_1' decay source if you are not careful. One of the major benefits of spin defects are these ultralong T_1 times. Because the defects are deep, interactions with charge carriers (the spin of traps is a different story) and ionization are basically negligible as well (without illumination) and this spin state can live for a very long time. Finally, in terms of hybrid systems coupling spins to phonons, it's worth noting that a good coupler to strain couples to phonons easily and will have low T_1. On the other hand, more extended states like excited state spins states or orbital levels can couple drastically to strain.

Coherences for solid-state spins determine the performance of any quantum device. Usually, electron spins are mainly limited by the surrounding *nuclear spin bath*. This is a whole field in itself, but is easily understood. Nuclear spins associated with atoms in the lattice are quite abundant and each corresponds to a tiny magnetic dipole moment. If this environment fluctuates in time, then the electron spin will see a uncontrolled time-dependent magnetic

field that causes decoherence. While the T_1 time of nuclear spins are quite long, a given pair of nuclear spins can perform a *flip-flop interaction*. If the two nuclear spins have the same energy splitting, one nuclear spin can give up its excitation to flip a nearby spin of opposite direction $|\uparrow_1\downarrow_2\rangle \leftrightarrow |\downarrow_1\uparrow_2\rangle$. Because the before and after states have the same energy, this interaction happens readily among all the resonant spin pairs in the lattice. This means that even if the temperature is zero, the nuclear environment is going crazy. If these two nuclear spins couple differently to the central electron spin, then these flip-flops cause magnetic noise at the defect (a fluctuating hyperfine coupling). An important tool to understand these effects is *Cluster-Correlation Expansion (CCE)* which treats the nuclear bath interactions by breaking the problem into clusters of pairs of spins (CCE2), three nuclear spins (CCE3), etc, instead of treating the entire system of the huge number of nuclear spins which would be incalculable. These calculations are used in chapter 13.

In general, the Larmor frequency of the nuclear spins are usually in the kHz range at moderate fields. The slow fluctuating nuclear bath in silicon carbide roughly sets the spin resonance linewidth to $\sim 1\ MHz$ and the $T_2^* \approx \mu s$ in natural isotopic abundance. For nuclear spins with strong hyperfine coupling, the spin resonance lines split and Ramsey will show a beating corresponding to the hyperfine value. For a Hahn-echo, the oscillating magnetic fields from a nuclear spin can have differing amounts of phase accumulation in the first and second half of the echo. This means that as the time is swept, oscillations will be seen corresponding to the Larmor frequency. With multiple species, multiple frequencies can be observed, and depending on the exact bath of nuclei and the magnetic field these modulation will have different depths. This is called electron spin-echo modulation (ESEEM). The overall result of the nuclear bath however, is an overall decay, with $T_2 \approx 1\ ms$. Interestingly, this coherence time is greater than that of NV^- center in diamond for a multitude of reasons [102], making the VV^0 quite attractive. For the basal defects in SiC, a significant E term in the spin Hamiltonian causes a mixing near zero field which creates a ZEFOZ transition, which results in long coherences [7].

For dynamical decoupling, the overall coherence can be extended up to T_1, and coherence dips can be found that correspond to matching the precession frequency of different nuclei in the lattice [103]. Essentially, the electron spin can flip at the right integer multiple of the Larmor period of the nuclei to exactly add up the phases. This forms the basis of the results in chapter 13. Obviously, removing the nuclear spins from the lattice can boost coherence. Unfortunately, even after isotopically purifying the material, other decoherence mechanisms can come into play.

To begin, thermal/strain drift changes the D parameter in the Hamiltonian which may be an issue. Furthermore, drift of the permanent magnet used to apply the external magnetic field can be a problem, alongside with unwanted electrical noise. That being said, the most important decoherence mechanism other than nuclei is *other electronic spins*. With their large magnetic moments and appreciable densities ($1e13 - 1e15$ cm^{-3} even in 'pure' SiC materials), their effect on coherence limits isotopically purified samples and is covered in chapter 13. For defects near surfaces, the dangling bonds containing electron spins are one of the main mechanisms for decoherence. Decoherence due to surfaces is a major problem for nearly all quantum technologies.

5.3.2 Creating VV^0

Through the course of my graduate work, constant work on creating VV^0 in a consistent and controllable way has been necessary. I will give a quick account of best practices to create single defects here. High-quality (low defect) materials can be obtained from collaborators or from high quality epitaxy from commercial companies (Norstel AB, now ST Microelectronics). The VV^0 are stable in intrinsic 'i' type material. These layers are grown on 4° off-axis 4H-SiC that is usually n-type (though epitaxy on HPSI is possible and used in [7] and other work). A small n-type buffer layer is grown first before the desired epitaxy is begun. In as-grown materials, the dominant defects will be residual shallow nitrogen ($1e13 - 1e15$ cm^{-3}) and deep carbon vacancies ($1e14 - 1e15$ cm^{-3}). Usually, in intrinsic materials the

vacancies pin the Fermi level midgap and the resistivity is high (see Fig. 4.1). There are no VV^0 in the material to begin with. Relativistic electron irradiation at 2 MeV in SiC has a rough penetration depth on the order of 1 mm, corresponding to a rough absorption coefficient of 10 cm^{-1}[104]. Relativistic calculations put the rate of 'primary-knock-on' events at $\sim 3\ cm^{-1}$ which corresponds to the rate of making *Frenkel pair* (vacancy+interstitial) defects which is confirmed by experiment[105]. Multiplying by an electron dose of units cm^{-2} gives the resulting density. Each primary scattering event has a chance of making secondary damage, which is low for electron irradiation[105]. By looking at the rate of deep defect creation which compensates carriers, a 'carrier-removal rate' of $\sim 0.5 - 1\ cm^{-1}$ has been measured with 2 MeV electrons for surface epilayers of SiC[105, 106]. Experimental conversions between dose and deep defects as measured by DLTS is around $0.1 - 0.9\ defects\ cm^{-1}$ for multiple possible species[106]. Other results show doses at $1e14\ cm^{-2}$ produce roughly $3e14\ cm^{-3}$ total defects of multiple types through DLTS[107]. As such, we can safely put the conversion efficiency between dose and vacancy creation to be $0.5 - 3\ defects\ cm^{-1}$. For relativistic electrons at 2 MeV, the transmitted energy to the lattice is very close to the displacement energy for single Si and C nuclei (creating V_{Si} and V_C) such that displacement cascades don't occur. As such, only sparse point defects are created[105]. Interestingly, carbon related defects can be created at about 100 keV electron energy whereas silicon-related defects occur above 200 keV (such that the kind of damage can be tuned with energy)[104]. When displaced, the atoms go into nearby interstitial sites (Fig. 13.6). Importantly, as dose is varied the concentration of deep defects and thus the Fermi level is changed which can drastically change defect formation kinetics and stability and complicate things.

Once V_{Si} and V_C are created, annealing mobilizes the vacancies. Some of the displacements reincorporate the displaced atoms, but some vacancies become mobile and diffuse through a complicated (and Fermi-level-dependent[108]) process potentially involving antisites or interstitials[109]. However, the current understanding is that V_c does not diffuse once formed (it is a stable defect during the high-temperature growth), and that V_{Si} diffu-

sion drives the formation process. At around 300-500 $^{\circ}C$ in SiC, some lattice healing will occur and at 600-700 $^{\circ}C$ these vacancies will become fully mobilized. Annealing past 750 $^{\circ}C$ is very efficient at forming VV^0, which happens when a V_{Si} finds a stationary V_C. Best practices put the annealing for VV^0 at 800-850 $^{\circ}C$[79]. Annealing should take place in an inert environment, such as Ar gas, but no differences were found in air-annealed materials. Importantly, *annealing in Ar/H_2 forming gas is detrimental to VV^0 formation and SiC stability!*. The current understanding is that hydrogen can easily diffuse into SiC and form defect complexes and affect charge dynamics. Hydrogen defects have been a long studied issue in SiC [110] that we had to rediscover the hard way (leading to what we called the 'Dark Ages', which had no single defects produced). Furthermore, at high temperatures hydrogen causes a premature degradation of the SiC surface at around 1200 $^{\circ}C$. The VV^0 complex itself is very stable up to over 1400-1600 $^{\circ}C$[79], but at those temperatures any other vacancies can find the VV^0 can form larger multi-vacancy clusters[111]. On the other hand, V_{Si} signal diminishes after about 600$^{\circ}C$[112]. High-temperature annealing forms the basis for dopant activation for devices and for creating larger substitutional defects in SiC such as Cr and V covered in chapter 7. These transition metals are incorporated with high efficiency at 1300-1600 $^{\circ}C$, but residual damage and strain can be further reduced along with increased incorporation upon annealing even up to 1800 $^{\circ}C$. Importantly, in these cases the SiC surface must be *carbon-capped* to avoid surface degradation/sublimation, combined with fast annealing ramp rates. High temperatures are also needed for CMOS processing and creating Ohmic contacts.

Commonly, no VV^0 single defects are 'seen' after annealing until a threshold dose is reached (whereby the Fermi level is pinned midgap), after which a linear density for a given dose is observed. A dose of $1e13 - 1e14\ cm^{-3}$ is consistent in creating resolvable single VV^0 (though this has changed over time with changing materials, charge, and dose calibration). The doses needed for single defect creation tend to be on the low side of the resolution of the irradiation facilities, while ensemble studies can have doses as high as $1e19\ cm^{-3}$ which take

weeks of beamtime (as used to create high density samples in chapter 14). Even if off-resonant excitation cannot resolve an ensemble of VV^0, using resonant lasers we can address a specific defect in the optical spot based on defect-to-defect variations in strain which shifts around the orbital fine structure (though this can be hard to disentangle). Overall, the annealing behavior is highly dependent on the starting material composition before irradiation.

For example, a dose of $3e13\ cm^{-2}$ corresponds to roughly $1e13\ cm^{-3}$ vacancies. We observe that at these doses we see about 10 defects in a $10 \times 10\ \mu m$ spatial scan, with a confocal depth of order $10\ \mu m$, corresponding to a defect density of $1e10\ cm^{-3}$. We can see then that the vacancy-to-VV^0 conversion is around 0.1%. In comparison, the ion-to-VV^0 conversion is around a few %[13], but each ion creates thousands of vacancies, making it even less efficient. Potentially, the residual V_C from growth can be as high as $1e15\ cm^{-3}$, such that V_C is supplied naturally and V_{Si} is rate-limiting. It is still unclear how far the a given vacancy must diffuse before forming VV^0, though initial results place it well below 1 μm. This has important implications in localizing defects into devices. An outstanding mystery in VV^0 formation is the fact that the *single* PL3 hk VV^0 have not been created or observed in experiment, while PL1 (kk), PL2 (hh) and PL4 (kh) all form in equal concentrations. This defect exists in ensemble experiments, but may have complicated or unfavorable formation processes. One possibility is that this defect's absorption dipole is small when pumped with $E \perp c - axis$, which is our normal experimental scenario [95].

Finally, much of the 'vodoo' around defect formation can be avoided by carefully thinking about charge state dynamics. With the wrong choice of laser color, a material can seem to be far from ideal, but may actually be a much cleaner material. The complications from these photo-dynamics are covered in section 6.3. In particular, because $VV^0 \rightarrow VV^-$ occurs readily as discussed in the following sections, then a slightly *p-type* material will have its quasi-equilibrium be very hole rich, such that continuous illumination results in consistent PL (a 'good' sample). A compensated sample will also have its quasi-equilibrium such that the divacancy is stable in its midgap charge neutral state. Much of the difficulty in dialing in

the VV^0 parameters were because of these effects. Furthermore, care should be taken when the charge state balance of your material is delicate. E-beam fabrication procedures should use an anti-charging metallic layer, for example. Luckily, many of these considerations can be alleviated using the proper excitation color (see chapter 11).

5.4 Measuring Single Defects

The experiments in this thesis are performed in a home-built confocal scanning microscope that operates in the infrared. The lasers and the emission from VV^0 are invisible to the human eye. Illumination and photon collection from the defect is focused through a NIR objective with NA=0.85. The NA is a number that describes the angle of focused light. In reality, light follows Gaussian optics (not just rays) and has a mode waist/size at the focus described by the paraxial equation. For a given focal length optic, a larger input beam will give a tighter and tighter spot. The corresponding light will have a steep angle and a high NA. Our high NA objective collects a large cone of light from the defect and focuses the incident lasers tightly. The full NA of the objective is only used when the full *back-aperture* of the objective is filled by light. For reference, the *objective field number (OFN)* refers to the image size in a *standard optical column* of a microscope (which we don't use!) which includes an eyepiece and some extra magnification. Similarly, the quoted magnification of an objective only has meaning with respect to this optical column. Depending on how the number is quoted, the OFN divided by the eyepiece magnification corresponds to the size of the image right after objective. Usually this is a factor of 10. Given a 1" eyepiece diameter for traditional microscopes, the OFN tends to be around 20-25 mm (corresponding to a 2-2.5 mm beam diameter). Alternately, the estimated focal length (EFL) and the so-called $f/$ relates to the image/beam diameter (D) after the objective with $f/ = EFL/D$. The incident laser and the collected photoluminescence are filtered from each other using a *dichroic beamsplitter*. The emitted light is then passed through several filters and focused

into a *single mode fiber*. This fiber optic cable confines light in a single spatial mode, and the mode has a particular mode waist (mode-field diameter) and therefore a corresponding NA. The photons from the defect must be mode matched to this fiber, corresponding to an overlap integral of the collected light to the acceptance of the fiber. Spherical, spatial and chromatic aberrations of the light as it goes through the optical path can drastically reduce this coupling efficiency. Maximizing this throughput is paramount for increased SNR and for single-shot readout and entanglement (chapter 8). For detectors with non-single mode input, the mode-matching requirements are greatly reduced and higher count rates are easier to obtain (such as for the NV^- in diamond).

This single-mode fiber runs to a *superconducting nanowire single photon detector (SNSPD)* which has a high quantum efficiency (in this context, it is the fraction of incident photons that result in a 'click' or *count*) and can detect single photons with low 'dark counts' (background noise). SNSPD's can detect IR photons, which can not be detected easily at high QE with traditional single photon detectors like Geiger-mode APDs (Avalanche Photodiodes). SNSPD's are excellent detectors with low timing jitter and are being adapted across almost all areas of quantum science. Essentially, the superconducting nanowires have a current run through them the nearly breaks the superconductivity. When a single photon hits the metal, it is absorbed and creates a hotspot in the wire. This hotspot breaks the superconducting behavior of the wire resulting in a huge resistance spike that is easily measured. The hotspot rapidly thermalizes and the system is ready for another photon. SNSPDs are luckily just commercial turn-key systems the size of a kitchen microwave (with a big helium compressor attached).

Unfortunately, due to the high index of refraction of materials like SiC, most of the emitted light from the defect (which follows a classical dipole emission pattern) is *totally internally reflected (TIR)* at the vacuum/SiC interface (Fig. 5.5E). This issue, combined with the entire collection, optics, fiber coupling and detection efficiency chain reduces the fraction of collected light to below 1%. Boosting this efficiency is the subject of major work

in the field. If we assume a 15 ns lifetime for VV^0, when the defect is *saturated* we expect ~ 60 Million counts per second ($\sim \frac{1}{15\ ns}$) if the QE is 100%. Saturation corresponds to the point where the defect is absorbing as fast as it can emit, limiting the rate at which photons come out under continuous illumination. With an estimated 4% for pure collection (from TIR, the NA, and losing half the photons since they were emitted away from the collection optic), a worst case QE of the defect 0.3, a detector QE of 0.8, and losing half of the photons through the collection optics (a guess), we expect roughly $288,000\ Cts/s$. In experiment, we normally measure $40 - 50\ kCts/s$, meaning that even with these assumptions we are losing around 6 times the photons we expect. Gaining these factors back with optical design and by using *solid immersion lenses (SIL)* is critical for future experiments. In our experiments, our best guess of the total collection efficiency is around or below 0.5%. In the NV^- center in diamond, with SILs [113] $> 1000\ kCts/s$ are measured for similar optical lifetimes (this count rate should hopefully be achievable for VV^0).

In the confocal microscope, scanning can be achieved either by moving the objective on a *periscope* that translates the input and output light as the optic is moved, or by a *4f pair*. Due to the wonders of optical design, with lenses with focal length f and the configuration: $objective - f - lens - 2f - lens - mirror$, angular displacements at the mirror will map directly the angular displacements at the back of the objective without translations (related to *telecentric* imaging systems). This system makes use of the fact that small angular displacements on a lens correspond to spatially scanning the beam around on the focal plane. With a *fast scanning mirror (FSM)*, quick raster scans over the sample can be achieved. We can perform these scans and see isolated bright dots that correspond to single VV^0 (see Fig. 5.5D). If I have a single color center it will be a *single photon emitter*. The single photon emitter nature of these bright spots is confirmed using a second order correlation $g^{(2)}$ (autocorrelation) measurement using a *Hanbury Brown-Twiss interferometer*. Essentially, the idea is to send light into a 50:50 beamsplitter that goes to two separate detectors. For a single photon, it can only go one of the two paths and give a click at one detector. For

a single photon source, there is no chance that both detectors get a click at the same time, because that would mean two photons were present at the same time. By comparing the arrival times of photons at the two detectors, a dip near $\Delta\tau = 0$ will appear. If this dip $g^{(2)}(0) < 0.5$ then single photon emission is confirmed. The exact shape of $g^{(2)}$ can further be used to understand the radiative and nonradiative rates in the system (such as in [3], for example).

Our SiC samples are measured inside a closed-cycle helium cryostat. This is a commercial system that recycles liquid helium by recompressing it after it has been used to cool the sample. With internal heaters this system can reach anywhere from 3 K to 350 K in vacuum. Optical access to the sample is provided by a window. Corrections for distortion through this glass in certain cases can be achieved by *coverslip* correction or a variable *correction collar* on the objective. SiC is mounted to a cold copper piece of the cryostat using rubber cement, or with conductive adhesives/epoxies for access to electrical back gates. (note copper pieces should be coated with gold to reduce oxidation, but some electroplating techniques use magnetic layers which cause issues in experiment). The sample holder is attached to a 3-axis set of piezo-actuators that move the sample inside the cryostat. Microwave driving of the spin states are provided either by coplanar waveguides on the PCB mount, or by on-chip fabricated striplines (usually 1-10 μm wide, ~ 200 nm thick) which are wirebonded to the PCB microwave ports. Wirebonds themselves are thin (~ 25 μm) enough that the field intensity close to the wire can be quite high and drive spins effectively. Proximity of the spins to these drive wires provides high Rabi rates for low powers and low added heating. Care must be taken to ensure that the microwave drive field is oriented correctly (perpendicular) to the defect axis. Microwaves are sourced with a signal generator and pulsed using an arbitrary waveform generator (AWG) which also pulses the lasers and the readout. The microwaves are amplified and sent into the crysostat, through the sample, then out to a 50 Ω load. Microwaves can also be shorted, creating a standing wave (be wary of nodes!) with $E = 0$ at the short and thus maximum B for driving. For microwaves, consideration

of the *skin depth* or attenuation through conductive materials and layers means the top-side striplines are preferred for conductive SiC devices. Finally, I will note that microwave pulses have a finite *bandwidth* based on length and shape from the Fourier-transform that determines the frequency selectivity and sensitivity of experiments.

Off-resonant initialization of the spin is achieved with a 905 or 975 nm laser. Choice of this laser color dramatically effects charge dynamics as discussed later in chapter 11. Resonant readout and initialization is performed using a tunable, narrow line laser whose wavelength is read out with a *wavemeter*. For a given experiment, spin initialization is done optically using either off-resonant or resonant light, followed by microwave manipulation of the spin. Readout is done by either off-resonant or resonant light (Fig. 5.8). The spin selective measurement contrast is usually $\sim 5\%$ for off resonant readout, but can approach $\sim 100\%$ for resonant. The polarization and read-out of the spin usually takes order μs, and a microwave π pulse is usually $\sim 100\ ns$.

Chapter 6

The Spin-Photon Interface

6.1 PLE and Stark Tuning

Resonant measurement of the excited state is called *photoluminescence excitation spectroscopy (PLE)*. This is the absorption spectrum of light that produces photoluminescence. We scan a narrow line laser over the excited state spectrum, and measure the resulting PL emitted in the phonon sideband (the laser excitation is filtered out). Given the spin polarization that happens naturally under continuous resonant excitation (pumping to a 'dark' state), we can perform 'CW PLE' using a *microwave mixing tone* that continuously mixes $m_s = 0$ and $m_s = \pm 1$ such that all lines in the orbital fine structure are visible and we don't get trapped in a dark state. Alternatively, we can polarize the spin into $m_s = 0$ or $m_s = \pm 1$ using optical and microwave tones and then sweep the readout resonant laser frequency for a set pulse time and confirm *which optical lines are associated with which spin.* The absorption spectrum in PLE is representative of where the resonances of the optical fine structure are, and reflects the spectrum of the emitted light as well. For measurement of the indistinguishable photons emitted in the ZPL, we can *cross-polarize* the excitation and the collection. Both will have a non-zero projection onto the optical dipole of the emitter, but in this way laser light can be filtered from the emission. In general, each of the lines

in the orbital excited state will have their own polarization dependence (some may even be circularly polarized).

The optical fine structure, as mentioned in section 5.2, can be tuned by either strain or electric fields (Fig. 5.4). Given that both the ground and excited state energies can shift, tuning corresponds to differences in the dipole between the ground and the excited states. In a sense, the Stark effect is just an electrostatic distortion of the wavefunction of the defect which causes energy shifts of the orbitals. In centers with inversion symmetry, this Stark dipole is, to first order, exactly zero such that the defects are electric field insensitive. With large electric fields, a second-order Stark effect will still take place, however. In centers with inversion, strain instead can be used to tune the levels[114].

For C_{3v} centers, such as the NV^- in diamond and VV^0, V_{Si}^- in SiC, this dipole is nonzero. This can be understood by remembering that the overall symmetry of the ground (A_2) and excited states (E) are different and respond differently to electric fields. On the other hand, for V_{Si}^- in SiC the ground and excited states have the same ($^4A_2$) symmetry making the first-order Stark shift small (though recent reports contradict this [115]). In practice, for electric fields along the C_{3v} axis, the entire orbital structure is shifted symmetrically. Different VV^0 throughout the sample will have different local strain that shifts the ZPL. Stark tuning can be used to make two emitters emit photons that are the same frequency and are *indistinguishable*. On the other hand, transverse electric fields can cause or correct for inherent asymmetry in the excited state. This can be used to tune up the defect to sit in an optimal position on Fig. 5.8.

For VV^0, we can write the Stark dipoles and the frequencies for the E_x and E_y lines of the c-axis divacancies:

$$\begin{aligned} f_{E_x} &= f_{E_x,0} + d_{\parallel}E_{\parallel} + d_{\perp}E_{\perp} \\ f_{E_y} &= f_{E_y,0} + d_{\parallel}E_{\parallel} - d_{\perp}E_{\perp} \end{aligned} \tag{6.1}$$

For the basal VV^0, the Stark parameters are slightly different (discussed in [7]) but have similar dipole moments. We summarize the known Stark parameters in Fig. 6.1. Following

VV^0 type	Range of PLE	D_{ES}, E_{ES}(GHz)	λ_z(GHz)	Δ_1(GHz)	Δ_2(GHz)	$d_\parallel, d_\perp(\frac{GHz}{MV/m})$	Lifetime (ns)	DWF
PL1 (hh)	265.1-265.3 THz	0.855, 0	3.54	0.577	0.031	11 (19*),∼2.5 (1.6*)	∼15	∼5%
PL2 (hh)	264.9-265.1 THz	0.852, 0	6.09	0.584	0.044	4.5,?	15.0	>5% ?
PL4 (hh)	277.8-278.1 THz	1.203, 0.237†	0	?	?	4.0(19*), 35(0.23*)††	11.6	∼10%

Figure 6.1: **Optical fine structure parameters and Stark shift parameters.** From references [6, 7, 55, 90, 99, 116]. PLE ranges are sample dependent. "*" are theoretical predictions from [7]. "†" are in the rotated basis from [7]."††" the correction for the titled basal axis has not been made in the experiment, which may account for some of the discrepancy. Optical lifetimes are reported in the $m_s = 0$ spin state. For comparison, the DWF of the V_{Si} in SiC is around $6 - 9\%$[53]

the discussion in 2.6, both the Stark effect and the radiative optical dipole emission are related to the *electric dipole of the orbitals*. However, the emission is due to the 'vacuum' driving a transition/emission (like a 'transverse' dipole). In contrast, the Stark effect is both a tuning knob and a source of orbital decoherence (like a 'longitudinal' dipole). A short lifetime is desired for a bright defect, but needs to be balanced with spectral broadening. The decoherence and broadening are analogous to the issues covered in chapter 2. For the two-photon interference covered in chapter 8, the emitted photons have to have the same phase and frequency to interfere such that orbital (and thus photon) coherence is extremely important.

6.2 Spectral Diffusion

Spectral diffusion of single-photon emission is a near-universal problem for quantum technologies. Trapped atoms near surfaces, and quantum dots or defects in the solid state, are all effected by the fluctuating (charge) environment in their surroundings. In the solid state, defects are both our qubits and our source for decoherence in the orbital and spin states. Specifically, external defects and impurities to our optically addressed VV^0 have their own associated *trapped charges*. These trapped charges at external defects to our spin are either

neutral or have charge that produces an electric field following:

$$\vec{E} = \frac{q}{4\pi\epsilon r^2}\hat{r} \tag{6.2}$$

As mentioned in section 5.3.2, no semiconductor is perfect and SiC in particular will have residual nitrogen donors and vacancies after growth (usually V_C). Under optical excitation, the charge state of these traps *changes* (see section 6.3). Spectral diffusion occurs not from electric fields, but changes in those fields. We start by assuming that each defect in the lattice can take one of two charge states with a difference in the charge states e. The difference in electric field between these two states is then:

$$|\Delta\vec{E}| = \frac{e}{4\pi\epsilon r^2}\hat{r} \tag{6.3}$$

The random switching of a state between two levels is called *telegraph noise*. In general, for symmetric (mean = 0) telegraph noise we will shift the frequency up by strength 'a' with probability p_{+a} and down '$-a$' with probability p_{-a}. The variance of such a two-state system is then:

$$\sigma_a^2 = \frac{(+a)^2}{p_{+a}} + \frac{(-a)^2}{p_{-a}} \tag{6.4}$$

In our case, we will make the assumption that 1) fluctuations are slow compared to the optical lifetime and that 2) the probability to find a charge in one state or another is 50/50 under continuous illumination. Things get more complicated if these are not fulfilled. For one noise source:

$$\sigma_a^2 = a^2 \tag{6.5}$$

The variance of a telegraph noise source is just the strength squared! If we add another telegraph noise source with a different strength b, then we can see that we have a 1/4 chance

to be in either $(+a+b), (+a-b), (-a+b)$,or $(-a-b)$ and thus the variance is:

$$\sigma^2_{a+b} = \frac{(+a+b)^2}{4} + \frac{(+a-b)^2}{4} + \frac{(-a+b)^2}{4} + \frac{(-a-b)^2}{4} \tag{6.6}$$

Working this out, a lot of things cancel, and we nicely get:

$$\sigma^2_{a+b} = a^2 + b^2 = \sigma^2_a + \sigma^2_a \tag{6.7}$$

Similarly, we can see that for three telegraphic noise sources we add a third source with strength c, this yields eight different configurations:

$$\sigma^2_{a+b+c} = \sum_{configs} (\pm a \pm b \pm c)^2/8 = \sigma^2_a + \sigma^2_a + \sigma^2_c \tag{6.8}$$

For telegraphic noise sources of this type, the variance of the frequency is then the *sum* of the variances from the individual sources (even though they can be drastically different strengths and timescales). This is a great result. Variances of uncorrelated noise add together (as expected).

Now we consider the spherical coordinates around our emitter along the z axis. We place a trapped charge/fluctuator at distance r with azimuthal angle θ and polar angle ϕ. Luckily, $d_\perp$ is calculated to be small compared to $d_\parallel$, such that we can approximate the shifts and use Eq. 6.3 (especially since we are squaring them):

$$\begin{aligned} \Delta f &= d_\parallel \Delta E_\parallel \\ \hat{r} &= \cos\theta \sin\phi \hat{x} + \sin\theta \sin\phi \hat{y} + \cos\phi \hat{z} \\ \Delta f &= \tfrac{e}{4\pi\epsilon r^2} \cos\phi d_\parallel \end{aligned} \tag{6.9}$$

For a single charge, telegraphic noise for the Stark shift then has the variance:

$$\langle f^2 \rangle - \langle f \rangle^2 = \sigma^2_f = (\frac{d_\parallel e}{4\pi\epsilon})^2 \frac{\cos\phi^2}{r^4} \tag{6.10}$$

It is unclear in VV^0, but experimental results ([116]) suggest instead that $d_\perp \approx d_\parallel = d$, which would give instead:

$$\sigma_f^2 = (\frac{de}{4\pi\epsilon})^2(\cos\phi + \sin\phi(\cos\theta + \sin\theta))^2/r^4 \tag{6.11}$$

The total variance from N charges is:

$$\sum_i^N \sigma_i^2 \tag{6.12}$$

We can then see that in the very simple scenario where all fluctuating charges have the same strength, the optical frequency will have a standard deviation:

$$\sigma_i = \sqrt{N}\sigma \tag{6.13}$$

In reality, the strengths vary due to the position with respect to the defect. However, even if the strengths vary, the sums of variances correspond to the width of a distribution that looks Gaussian with large N. In a sense, we are making a *Markov chain* through frequency space and the process can be related to a *Orenstein-Uhlenbeck* noise process, a *random walk problem* or *Brownian motion*. For example, we can simulate N telegraph noise sources M times and look at the resulting distribution. We can confirm that the treatment of the sum of variances produces the correct Gaussian distribution of values (Fig. 6.3).

For the defect surrounded by a uniform density of telegraphing charges ρ, the big issue is that there is a non-zero probability of the fluctuating charge being near $r = 0$. This means that the resulting distribution will have values at or near infinity. In a sense, we are sampling from a $1/r^2$ distribution from $(0, \infty)$. Such a distribution is *pathological* in that it has no well-defined mean or variance (try for yourself). This means the *central limit theorem* does not hold.

There are two ways to approach this problem. First, we can simulate N telegraphing

$(kk)\ VV^0$	mode		median	
$\rho\ (cm^{-3})$	$\sigma(MHz)$	$\Gamma(MHz)$	$\sigma(MHz)$	$\Gamma(MHz)$
1e13	4.25	10.0	5.5	13.0
1e14	20.0	47.1	28.5	67.1
1e15	95.0 3	223.7	119.8	282.1
1e16	420.0	989.1	554.6	1306.1
1e17	1850.0	4356.8	2500.8	5887.5

Figure 6.2: **Spectral diffusion Monte-Carlo results**. Simulations are for an anisotropic Stark dipole $d_{\parallel} >> d_{\perp}$ of a $(kk)\ VV^0$. Assuming $d_{\parallel} = 4.5\ GHz \cdot m/MV$

charges with uniform spatial density ρ and add up their squared strengths according to Eq. 6.10, giving the total variance of the resulting system. We then create M such distributions, and histogram the resulting distributions of $\sqrt{\sum_N \sigma^2}$ as shown in Fig. 6.3E. As we change the density, the shape of this distribution remains the same. We can see that the distribution (of variances) is non-Gaussian and has a long tail that extends out to infinity. Once again, if we tried to calculate the mean of this distribution (to get the average variance/spectral width), it becomes skewed towards infinity and blows up (non-physical). However, what we want to calculate is not 'what is the average linewidth for a given fluctuator density?' but *'what is the most likely linewidth for a given fluctuator density?'*. This corresponds to the *mode* of the distribution. In this problem, the mean is ill-defined but the *median and mode* are finite and calculable.

Using this Monte-Carlo simulation, we can find the median and modes of σ for different densities using the dipole moment of the $(kk)\ VV^0 = 4.5\ GHz \cdot m/MV$ and $d_{\parallel} >> d_{\perp}$. We also compute the FWHM ($\Gamma \approx 2.355\sigma$), with the results summarized in Fig. 6.2.

We can run the same simulation but with $d_{\parallel} = d_{\perp}$ according to Eq. 6.11, and obtain the heuristic that the mode and median are bigger by $\sim 1.7x$, but unless otherwise noted we assume $d_{\perp}$ is small. Since we don't know $d_{\perp}$ exactly but know $d_{\perp} \leq d_{\parallel}$, we can bound ourselves appropriately. We also can see that the mode and median are close to each-other. In VV^0, the lifetime limited line is $\Gamma \approx 10\ MHz$ such that to not be broadened by spectral diffusion, we need to have around $1e13\ cm^{-3}$ or lower fluctuating charge impurities. In materials, this

is an extremely low limit that pushes growth capabilities. To compare, only one diamond has really shown consistent lifetime-limited lines (for the NV) 'the magic russian diamond' from the Ural mountains[117]. which probably has exceptionally low impurity content. Remembering our discussion of damage, irradiation at too high of a dose (above 1e13-1e14 cm^{-3}) will likely cause extra charge fluctuators and degrade the spin-photon interface.

Now we can back out the scaling by fitting the mode and median as a function of density. It turns out both follow the power law $\sigma \propto \rho^{\frac{2}{3}}$ (Fig. 6.3). In experiment, the defects we see are (by definition) most likely to have a width at the mode of this distribution, for which we extract:

$$\Gamma(\rho) \approx \frac{1}{50}[\rho(cm^{-3})]^{\frac{2}{3}}\ Hz \tag{6.14}$$

We can also compute (numerically) just the pesky geometry factors without the physical parameters of the defect:

$$\begin{aligned} mode[\sqrt{\sum \tfrac{\cos\phi^2}{r^4}}](\rho) &\approx 2.6\rho^{\frac{1}{3}} \\ mode[\sqrt{\sum \tfrac{1}{r^4}}](\rho) &\approx 4.75\rho^{\frac{1}{3}} \end{aligned} \tag{6.15}$$

The second method for tackling this problem is to add up the variances by performing an integral over all space, but with a twist. Because the chance to find a charge in the volume element in spherical coordinates is $\rho r^2 dr d\phi d\theta$, we can integrate the variances over the probability distribution just like if we were computing the mean of variances $\langle\sigma^2\rangle$:

$$(\frac{d_\parallel e}{4\pi\epsilon})^2 \int_0^{2\pi}\int_0^{\pi}\int_r \frac{\cos\phi^2}{r^4}\sin\phi\rho r^2 dr d\phi d\theta \tag{6.16}$$

The angular components integrate easily:

$$(\frac{d_\parallel e}{4\pi\epsilon})^2 \rho\frac{4\pi}{3}\int_r \frac{1}{r^4} r^2 dr \tag{6.17}$$

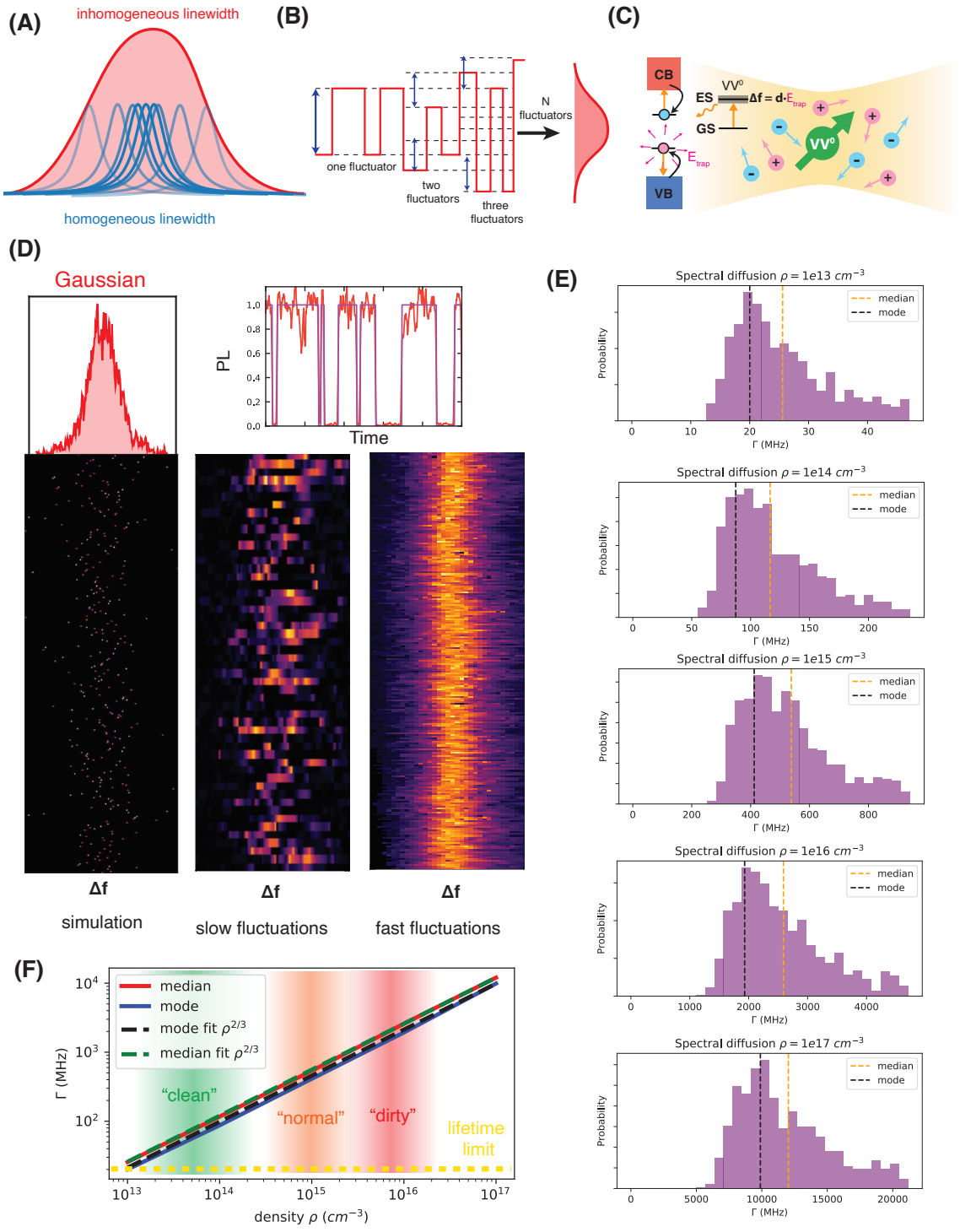

Figure 6.3: **Spectral diffusion in VV^0.(A)** Many homogeneous lines (blue) make up the inhomogeneous line (red) as the homogeneous line jitters around due to spectral diffusion. **(B)** Telegraphing noise adds up to produce Gaussian lineshapes. **(C)** From section 11.4, schematic of laser-induced scrambling of the charge environment of an emitter, causing fluctuating electric fields and Stark shifts.

Figure 6.3: **(D)**(left) Monte-Carlo simulation of an emitter with randomly populated nearby traps of uniform density and ($d_{\parallel} = d_{\perp}$). Spectral diffusion is shown from the individual realizations of the fluctuating bath by the many small homogeneous lines. The resulting average (red) is a Gaussian shape. (center) Schematic spectral diffusion with slow fluctuations showing discrete jumps. (right) Schematic spectral diffusion showing the same linewidth but with faster fluctuations. With slow fluctuations, discrete jumps in PL may be seen when sitting with a narrow line laser at $\Delta f = 0$ (top), while these dynamics may be hard to observe with fast spectral diffusion. **(E)** Monte-Carlo simulated distributions of defect linewidths (FWHM) for a $kk\ VV^0$ with isotropic Stark shift $d = 4.5\ GHz/(MV/m)$ at varying fluctuator densities ($d_{\parallel} >> d_{perp}$). The asymmetric, long-tailed distribution is present for all densities. The median and mode of the distributions are shown. **(F)** Mode and median FWHM linewidths as a function of defect density. The relation is well fit to a $\rho^{2/3}$ scaling. The lifetime-limited linewidth is shown in yellow, with various rough material cleanliness regions shown in green, orange and red.

Normally, we would then integrate r on $[0, \infty]$, but that's the source of the whole divergence issue. The easiest way to approach this is to think about the average distance between the defect and the first charge, which is:

$$\langle r \rangle \approx \rho^{-\frac{1}{3}} \tag{6.18}$$

More specifically, in spherical coordinates we can use the *Wigner-Seitz* radius $a = (\frac{3}{4\pi\rho})^{1/3}$ and the fact that the distribution of nearest neighbors peaks at:

$$r_{peak} = (\frac{2}{3})^{1/3} a = (\frac{1}{2\pi\rho})^{1/3} \tag{6.19}$$

On average, we won't have our first charge until this distance. Configurations that do have $r < \langle r \rangle$ *or* r_{peak} are part of the pathological tail. Therefore we integrate first using $\langle r \rangle$:

$$(\frac{d_{\parallel} e}{4\pi\epsilon})^2 \rho \frac{4\pi}{3} \int_{\langle r \rangle}^{\infty} \frac{1}{r^2} dr = (\frac{d_{\parallel} e}{4\pi\epsilon})^2 \rho \frac{4\pi}{3} (\frac{1}{\langle r \rangle}) = (\frac{d_{\parallel} e}{4\pi\epsilon})^2 \rho \frac{4\pi}{3} \rho^{\frac{1}{3}} = \sigma^2 \tag{6.20}$$

leading to:

$$\sigma = (\frac{d_{\|}e}{4\pi\epsilon})\sqrt{4\pi/3}\rho^{2/3} = (\frac{d_{\|}e}{4\pi\epsilon})(\sim 2.04)\rho^{2/3} \tag{6.21}$$

Using r_{peak} instead of $\langle r \rangle$ the numerical factor is ~ 2.78. Amazing! We reproduced the scaling with density and the numerical factor (~ 2.6) from the simulation in Eq. 6.15 *almost exactly*. Using Eq. 6.11 instead where $d_{\|} = d_{\perp}$, the angular integral gives 4π instead of $\frac{4\pi}{3}$, scaling the results of the linewidth by $\sqrt{3} \sim 1.73\times$, just as we found in the Monte-Carlo! Perhaps a more accurate description can be achieved with a better statistical toolbox or by borrowing from nearest-neighbor distance distributions from statistical mechanics, or by knowing $d_{\perp}$ accurately. That being said, now we know how to treat spectral diffusion for the orbital structure of our defect as a function of the fluctuating charge density surrounding it. Other scenarios may have surfaces of fluctuating charges such as in nanostructures which should be calculable more easily. If the fluctuations are fast, *motional narrowing* and a splitting of the peaks into two may occur, but are not treated here. Certain configurations have a 'strongly coupled' charge trap (also seen in experiment) where the lines split into two, offering interesting possibilities for readout and control with single charges. Once again this treatment is probably a overestimate, since most charge traps will not contribute to fluctuations and some correlations and charge conservation will reduce the magnitude of the noise.

Practically, as mentioned in section 5.3.2, residual nitrogen and deep V_c can have densities as high as $1e15\ cm^{-3}$ in commercial, epitaxially grown SiC. This means that the spectral diffusion should give around $\sim 200\ MHz$ lines. As discussed in sections 11.4 and in appendix A, this is exactly the magnitude of our observed PLE linewidths in these materials. Furthermore, in materials with high doping levels, even when the source gas is turned off, residual doping may occur as the growth chamber becomes slowly purifies. This means that nominally intrinsic layers may have a significant amount of doping if they are thin and grown immediately after doped layers, causing broad spectral lines (as in chapter 9). Commonly, for SiC characterization, carrier density is characterized with a C-V measurement, or by

measuring a calibrated loss when the sample is introduced into a high Q-factor microwave resonator. However, spectral diffusion occurs not through free carriers (which could be few due to many deep traps) but through fluctuations of defect charge states. Nitrogen impurity density can be measured by looking at the bound-exciton lines [118] (when below the detection limit of SIMS), while V_c densities can be determined with DLTS (the Z_1/Z_2 level[119]). How these common defects and impurities in SiC fluctuate under optical excitation is covered in the next section, which drives spectral diffusion. In specially-grown ultrapure samples, nitrogen, boron (another dopant that may be present) and V_c can all be in the $1e13\ cm^{-3}$ range [2]. For the NV^- center in diamond, ion-implanted defects cause large amounts of spectral broadening [120] due to the large number of created nearby vacancies, despite initial reports [121]. For the landmark experiments using the spin-photon interface, the NV^- displays linewidths that are $\sim 100 - 200\ MHz$[117, 122, 123]. 'Electronic grade' diamond $< 5\ ppb$ of nitrogen impurities still corresponds to a defect density of $\sim 1e15\ cm^{-3}$[124], which given the similar Stark dipole[125], would explain this level of broadening. With an atomic density of $\sim 5e22 atoms/cm^3$, sub *ppb* levels of all impurities would be necessary to observe lifetime limited lines (Fortunately, not all hope is lost, as discussed in section 11.4).

6.3 Photodynamics of Defects

The last section dealt with how fluctuating charges can degrade the spin-photon interface. We also mentioned how trapped charges (paramagnetic impurities) can contribute to magnetic noise for the spin. The ionization and recapture of carriers by these defects is dominated by the non-equilibrium *photodynamics* from the laser excitation at low temperature. Furthermore, VV^0 itself can undergo ionization and recharging depending on the photodynamics. This is the subject of chapter 11, but we will introduce key concepts here.

Going back to the discussion of charge transition levels for electrons and defects, the distance between the VB and a (0/-) level of $E_{(0/-)}$ for example, means that with laser

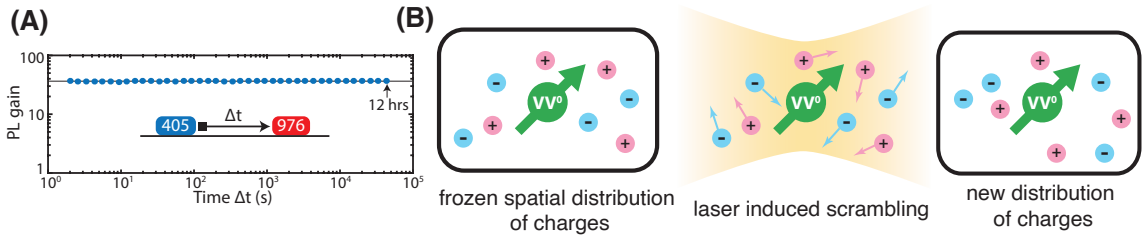

Figure 6.4: **Photodynamics of defects and surroundings. (A)** Charge state lifetimes of VV^0. At UV pulse of light creates and out of equilibrium excess of VV^0. At T=4 K, this population cane be read out with the photoluminescence from a 976 nm laser pulse, where the population is frozen for more than 12 hours. Adapted from [11]. **(B)** Schematic of laser driven charge dynamics in the bath. When the light is off, charges are frozen in different configurations.

excitation $\hbar\omega > E_{(0/-)}$ we can bring an electron from the VB and charge the level from the $0 \rightarrow -$ charge state. There are multiple considerations to make here. One is the density of states in the VB, which determines the rate of this process. The density of states in the VB and CB can have structure, and may have an energy difference from the band edge to the rate maximum (see Fig. 11.7). The VB and CB just say where the bands start, not where there are lots of states. Second, the charge transitions levels are ground state relaxed levels such that Franck-Condon shifts for optical excitations are not taken into account. Finally, orbital excited states (such as the one for VV^0) are not included in the charge transition level picture, but may effect photodynamics (especially with two-photon processes). However, the exact transitions to and from bound charges states of defects can be treated theoretically [94]. For holes, the same levels are involved, with the relation that the energy needed to add a hole (or equivalently, to remove an electron) and go from $- \rightarrow 0$, for example is $E_{(-/0)} = E_{gap} - E_{(0/-)}$. Because of this fact, if the optical excitation energy is greater than both the energy to add and remove an electron for this example $E_{(-/0)} < \hbar\omega > E_{(0/-)}$ then *illumination will continuously cycle* $- \leftrightarrow 0$. This is a horrible situation to be in for spectral diffusion. In general, if a charge transition level is exactly midgap (worst case) this sets the relevant choice of illumination energy to avoid this effect $\hbar\omega < E_g/2$. In this sense, the goal is to have charge dynamics that do not continuously cycle.

Under illumination, the defect and the surrounding traps in the lattice undergo a balance of ionization and recapture that drives the photophysics and charge stability of defects. Depending on the other traps around, your defect may be more or less photostable; but this is a statement about the photophysics, *not the Fermi level!*. Recapture of carriers can happen quite fast, and diffusion or drift depending on the laser spot or bias can change the balance of rates of *carrier generation and recombination*. This is how the discussion here is related to the semiconductor physics discussed in 1.1.2. For devices (as in section 11.4) at the low temperatures near 4 K in this thesis, the aluminum acceptor and the nitrogen donors are *frozen out*[67, 126] and are out of equilibrium with the bands. The shallow donors and acceptors, along with the much deeper defects (such as V_c), all trap charges and do not give them up thermally. Under optical excitation, however, these trapped charges can be photoionized. Free carriers are created and can drift, diffuse and become trapped at the same defect or at different defects. A sort of *quasi-equilibrium* is reached, such that the effective carrier temperature can be quite 'high'.

In chapter 11, we will look at the DFT computed levels in SiC and investigate relevant photodynamics at play in VV^0, as shown in Fig. 11.7. The charge transition levels in 4H-SiC with the relevant impurities and defects are shown in Fig. 4.1. Besides blinking of the emitter, charge dynamics of the other defects in the solid state are the major driving force that degrades the spin-photon interface.

Carriers can recombine with deep defects following a *Schockley-Read-Hall (SRH)* process or an *Auger* process. In general, each deep defect has a *capture cross section* for both electrons and holes where conducting charges become recaptured by the defect. SRH recombination is the dominant process in most semiconductor devices. This is especially true in indirect band-gap semiconductors like SiC. In this model:

- An electron in the conduction band can be trapped in a trap state.
- An electron can be emitted into the conduction band from a trap level.

- A hole in the valence band can be captured by a trap. This is analogous to a filled trap releasing an electron into the valence band.
- A captured hole can be released into the valence band. Analogous to the capture of an electron from the valence band.

Given the photo-assisted emission of carriers from traps to the CB and VB, and the re-capture rates based on the capture cross sections, different steady-state balances of charges can be obtained and SRH-type recombination occurs. In section 11.4 we describe how a semiconductor depletion effect simplifies this picture and allows for careful studies of photodynamics. Because the different charge states of defects absorb and emit light differently, the process of charge conversion with light that causes differences in the optical behavior is called "photochromism."

6.3.1 Photodynamics of the NV^- in diamond: an example

Photodynamics of the NV^- in diamond and its surroundings are the cause of many issues for quantum technologies with these systems. For the NV^- itself, continuous illumination with 532 nm light can both two-photon ionize ($NV^- \rightarrow NV^0$) the defect and reset it ($NV^0 \rightarrow NV^-$)[127]. The steady state balance of these rates means that the NV^- emits fewer photons under 532 nm light than expected. This lowers the QE and ODMR contrast in experiments to around 70% [128]; the NV^- is only in the right charge state 70% of the time. Under resonant illumination, this may be even lower. Choosing different excitation colors can change the balance of rates [129]. For the protocols in chapter 8, photodynamics of nearby charge traps to the NV^- cause spectral diffusion (Fig. 6.4). Combined with unwanted ionization, steps that involve resonant excitation may produce less photons than expected. Although resonant excitation only needs low power, it is still enough to cause ionization of the surroundings. The 532 nm laser used for polarization/charge repumping can cause even more drastic spectral diffusion. This reduces both the possibility of single-

shot readout and for entanglement generation as discussed in chapter 8. In particular, every experiment needs to check both that the optical line is on resonance, and that the charge of the defect is in the correct state[130], drastically reducing the success rate.

Chapter 7

New Defect Discovery

This chapter and figures are adapted from the publications [4, 5]

Before delving into the work focusing on VV^0, I want to briefly mention work in discovering new defects in SiC that may offer different advantageous properties. Given that the first NV^- center in diamond paper was in 1985, it took the field a while to discover its full potential. Similarly, many defects in SiC (even the VV^0) have been well studied since the 1980's, even with ODMR[131]! By revisiting known defects with a 'quantum' lens, and by thinking deeply about what properties we want, we can develop exciting new qubit candidates. Nature nicely gave us the NV^- and the VV^0, but there's no telling if something better might be just around the corner. The explosion of work in the group *IV's* in diamond illustrates this point nicely. In particular, I'll briefly mention two transition metal defects in SiC that I helped develop. We also investigated Erbium centers in SiC with mixed success, and investigations are ongoing and encouraged by recent reports in the literature[132].

7.1 Chromium in SiC

Transition metal ions provide a rich set of optically active defect spins in wide bandgap semiconductors. Chromium (Cr^{4+}) in silicon-carbide (SiC) produces a spin-1 ground state

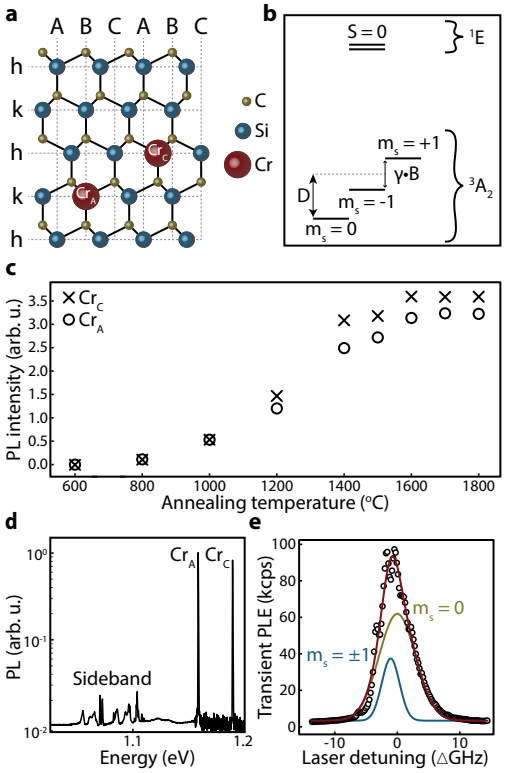

Figure 7.1: **Structure, creation and spectroscopy of chromium defects in 4H-SiC.** **a** An illustration of substitutional Cr^{4+} ions in silicon sites of a 4H-SiC lattice. **b** The electronic level structure of Cr^{4+} in SiC. The $m_s = 0$ and $m_s = \pm 1$ sublevels are split by the crystal field (D), and under a magnetic field, the $m_s = \pm 1$ sublevels are Zeeman split. **c** Cr^{4+} activation as a function of annealing temperature is measured by integrating the zero-phonon lines (ZPLs) intensity of the photoluminescence under off-resonant (730 nm) excitation at T=30 K. **d** A photoluminescence spectrum of the sample used for spin and optical control at T=30 K. Cr_A and Cr_C , two different sites of Cr^{4+} in 4H-SiC, ZPL's and their sidebands can be observed. **e** Cr_A photoluminescence excitation (PLE) at T=30 K is measured by sweeping the resonant laser and recording the transient sideband signal in counts per second (cps). The PLE is fit to two Gaussian peaks with a known D=1063 MHz splitting. The full width at half maxima are 6.87(27) GHz for $m_s = 0$ and 3.34(39) GHz for $m_s = \pm 1$. The one sigma errors of the data are smaller than the point size and are not displayed.

with a narrow, spectrally isolated, spin-selective, near-telecom optical interface. However, previous studies [133] were hindered by material quality resulting in limited coherent control. In [5], we were able to implant Cr into commercial 4H-SiC and show optimal defect activation after annealing above 1600 $°C$. We measure an ensemble optical hole linewidth of 31 MHz, an order of magnitude improvement compared to as-grown samples. An in-depth exploration

of optical and spin dynamics reveals efficient spin polarization, coherent control, and readout with high fidelity (79%). We report T_1 times greater than 1 s at cryogenic temperatures (15 K) with a $T_2^* = 317$ ns and a $T_2 = 81$ μs, where spin dephasing times are currently limited by spin-spin interactions within the defect ensemble. Our results demonstrate the potential of Cr^{4+} in SiC as an extrinsic, optically active spin qubit.

7.2 Vanadium in SiC

Solid state quantum emitters with spin registers are promising platforms for quantum communication, yet few emit in the narrow telecom band necessary for low-loss fiber networks. Here [4], we create and isolate near-surface single vanadium dopants in silicon carbide (SiC) with stable and narrow emission in the O-band (1278-1388 nm), with brightness allowing cavity-free detection in a wafer-scale CMOS-compatible material. In vanadium ensembles, we characterize the complex d^1 orbital physics in all five available sites in 4H-SiC and 6H-SiC. The optical transitions are sensitive to mass shifts from local silicon and carbon isotopes, enabling optically resolved nuclear spin registers. Optically detected magnetic resonance in the ground and excited orbital states reveals a variety of hyperfine interactions with the vanadium nuclear spin and clock transitions for quantum memories. Finally, we demonstrate coherent quantum control of the spin state. These results provide a path for telecom emitters in the solid-state for quantum applications.

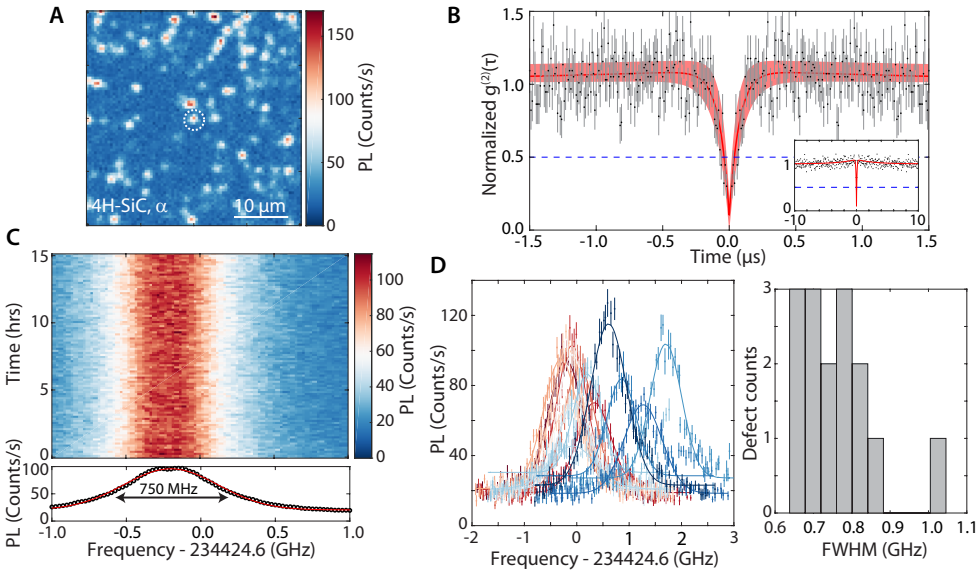

Figure 7.2: **Single V^{4+} α site emitters implanted in 4H-SiC.** All experiments are at 3.3 K. **(A)** Spatial (near-surface) PL mapping of single and few V defects by resonant excitation at 1278.8 nm. (B) and (C) are obtained at the circled bright spot with spatial feedback to prevent drifting. **(B)** $g^{(2)}$ autocorrelation measurement obtained with a single detector with 20 ns deadtime and 10 ns resolution. The autocorrelation signal is normalized using its value at long delay time and the dark count contribution is calculated and subtracted ($\sim$ 3% of total). The red line is the fit ($g^{(2)}(0) = 0.1(1)$) and the red shadowed area the 95 % confidence interval. In the inset, the autocorrelation intensity is shown for longer times. **(C)** Resonant spectrum taken over 100 acquisitions for a total duration of 15 hours, with averaged intensity shown in bottom. The spectrum shows two maxima from the slightly resolved electron spin states. **(D)** Resonant spectrum taken for a variety of likely single emitters (not confirmed with $g^{(2)}$). Their fitted linewidths (right) remain consistent at about 750 MHz full width half maximum (FWHM). All the single defect experiments are conducted at around 700 G to narrow the linewidth (high field limit). A weak 365 nm continuous illumination helps stabilize the PL from charge conversion (possibly from two-photon ionization). (C) and (D) are calibrated using a wavemeter with below 50 MHz accuracy. All error bars are one standard deviation from experimental acquisition.

Chapter 8

Long Distance Entanglement and Quantum Networks

The real advantage spin defects have is in the spin-photon interface, which can be applied to long distance *quantum communications*. Here, we will go through the motivations and implementations of such a system.

8.1 Cryptography and QKD

Quantum key distribution (QKD) is one of the most well-developed quantum technologies with an understandable near-term goal. Forget 'quantum': It turns out that any classical communications channel can be made *provably, perfectly secure* by utilizing a *'one time pad'*. If I want to send a message to you, I just have to make sure that you and I have a copy of a (random) 'cipher' or *key* that is just a string of ones and zeros. If I take my message, represent it in binary and *CNOT* it with the key, I get a resulting encrypted string. I can send this message to you (broadcasting openly), and even if someone intercepts the message, as long as they don't have the key, they can't decode it (*cryptanalysis* is impossible). You, on the other hand, simply use the same key and CNOT it with the received string: $U_{CNOT}^2 = \mathbb{I}$. This recovers the original message. Applying a CNOT with a random key is enough to completely

scramble, but doing a CNOT again with the key completely unscrambles the message. The only caveat is that I can only use the cipher/key *once* before someone could start to figure out what's going on.

Provably secure quantum communications then boils down to distributing the *key* between parties. Instead of sending a messenger or a classical communication where the key could be stolen or copied, we use quantum mechanics to distribute the key. If anyone tried to steal the key: 1) the key is destroyed and 2) we can measure that someone is interfering. Even if someone interferes, we can perform *privacy amplification* [134] to minimize the knowledge an attacker might gain of our key.

These facts led to landmark QKD schemes including *BB84* [135] which just uses single photons and *E91* [136] which uses entangled particles. As such, spins that send single photons or that can distribute entanglement are valuable for applications in QKD. Using QKD, we can have a perfectly secure quantum communications channel. Given the scope of encrypted data transfer and implications for security, such a technology would have massive societal impacts.

8.2 Distributed Entanglement and Computing

Quantum communication is useful for more than distributing quantum keys. In particular, one can think about creating a *quantum internet* [137, 138] which links up quantum computers over a distance. In this scenario, entanglement and two-qubit gates would need to be mediated at distance to let quantum computers talk to each other. This could lead to *distributed quantum computing* which may be the key to scaling quantum computers. Distributing entanglement at macroscopic distances and across many nodes can drive interesting physics and advances in quantum communications and QKD. It is not enough to send entangled particles to different nodes: we need to be able to *hold onto* the entanglement at each site in order to do anything besides QKD. This is where is concept of *quantum memories*

comes into play that can store the entanglement. Once again, we don't really know what all the applications of quantum communications might be, but distributing entanglement at scale (as a resource) will be key.

8.3 Quantum Repeaters

While photons are great flying qubits to mediate long distance entanglement, there are always losses. Photons in free space diffract and scatter over long distances, while guided photons in fibers attenuate due to absorption in the fiber.

For example, 'telecommuncations' wavelengths near 1550 nm are optimized to have low loss in optical fiber, but still have an attenuation of $\sim 0.2\ dB/km$ (exponential with distance). Interestingly, the dB was defined originally to quantify loss in telegraph wires. From Chicago to New York, this means that we would have $\sim\ 250\ dB$ of loss, meaning that 1 out of every 10^{25} photons would make it. This is insane. The way we can still communicate on a global scale is because of the existence of many classical *repeaters* which continually boost the signal along the way. Another strategy is to use satellite or free space based communications to send quantum states, which may have lower loss[139].

The problem with quantum is the existence of the 'no cloning theorem'[140], which is also the thing that prevents an eavesdropper from copying my quantum key. The act of looking at a quantum state disturbs it- such that I can't measure, copy and send it along without inherently changing things. This means I can't boost my signal to deal with losses. The solution is to make a device called a *quantum repeater*. Instead of trying to distribute entanglement over the whole distance, we can break the problem into small segments. Instead of dealing with exponential loss for a total inter-node distance L which has a photon-transmission success probability of $e^{-\alpha L}$, we divide the distance into N many small segments with higher transmission success $e^{-\alpha L/N}$. We then rely on the fact that we can hold onto each 'success' while we wait for the other segments to complete their links.

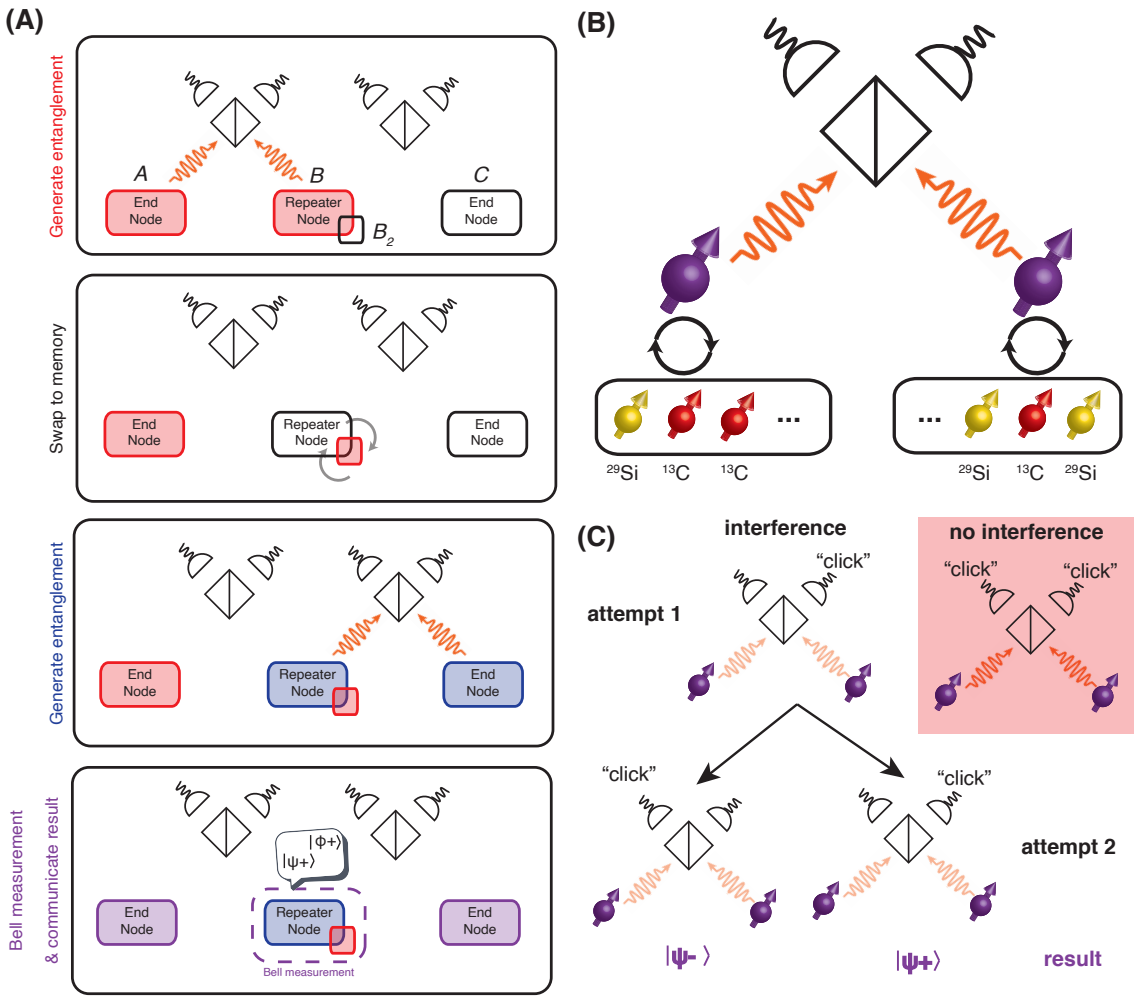

Figure 8.1: **Quantum repeaters with defects.(A)** Schematic quantum repeater scheme. Entanglement is generated by photon interference at a beamsplitter and heralding at the detectors. The repeater node has a local quantum memory/ancilla qubit (small box). Entanglement is generated between two distant qubits. The repeater node then swaps its entangled state to a memory, then attempts to generate entanglement with the other node. After success, at the repeater node a Bell measurement is performed on the memory and the entangled qubit. The result projects the state into one of two entangled states at the distant nodes. **(B)** Schematic repeater nodes with optically active spins (purple) linked to many local nuclear spins memories. **(C)** The Barret-Kok scheme where two entanglement attempts are performed where only one click is desired. The 'which-way' path information of where the photon came from is destroyed by the beamsplitter. A second attempt must also result in a single click, where the relative location of the click projects to one of the two Bell states.

For example, one possible scheme for quantum repeaters (there are a few, depending on if you are using entangled photon sources from SPDC or not) is shown in Fig. 8.1. To

illustrate, we assume a simple 3 node example, called 'Alice', 'Bob' and 'Charlie'. Bob, in particular needs a quantum memory 'B2'. We then proceed as follows:

- Assume we have a method of distributing entanglement (we will cover one such scheme in the next section). Generate entanglement between A and B (assume entanglement creates the bell state $\left|\Phi^{+}\right\rangle = \frac{|00\rangle+|11\rangle}{\sqrt{2}}$). Forgetting about the normalizations:

$$|0_A 0_B\rangle + |1_A 1_B\rangle \tag{8.1}$$

  Adding in B2 and C which we haven't done anything with yet:

$$|0_A 0_B ?_{B2} ?_C\rangle + |1_A 1_B ?_{B2} ?_C\rangle \tag{8.2}$$

- Swap the entangled state at Bob's node into his memory B2:

$$|0_A ?_B 0_{B2} ?_C\rangle + |1_A ?_B 1_{B2} ?_C\rangle = (|0_A 0_{B2}\rangle + |1_A 1_{B2}\rangle) \otimes |?_B ?_C\rangle \tag{8.3}$$

- Generate entanglement between B and C:

$$\begin{aligned} &(|0_A 0_{B2}\rangle + |1_A 1_{B2}\rangle) \otimes (|0_B 0_C\rangle + |1_B 1_C\rangle) \\ &= |0_A 0_B 0_{B2} 0_C\rangle + |0_A 1_B 0_{B2} 1_C\rangle + |1_A 0_B 1_{B2} 0_C\rangle + |1_A 1_B 1_{B2} 1_C\rangle \end{aligned} \tag{8.4}$$

- Perform a $C_{B2}NOT_B$ on B and B2 (just a local two-qubit gate at Bob's node):

$$|0_A 0_B 0_{B2} 0_C\rangle + |0_A 1_B 0_{B2} 1_C\rangle + |1_A 1_B 1_{B2} 0_C\rangle + |1_A 0_B 1_{B2} 1_C\rangle \tag{8.5}$$

- Rotate B2 by $\pi/2$, this is equivalent to performing a Hadamard gate:

$$\begin{aligned} &|0_A 0_B 0_C\rangle \otimes (|0_{B2}\rangle + |1_{B2}\rangle) \\ &+ |0_A 1_B 1_C\rangle \otimes (|0_{B2}\rangle + |1_{B2}\rangle) \\ &+ |1_A 1_B 0_C\rangle \otimes (|0_{B2}\rangle - |1_{B2}\rangle) \\ &+ |1_A 0_B 1_C\rangle \otimes (|0_{B2}\rangle - |1_{B2}\rangle) \end{aligned} \tag{8.6}$$

- Measure Bob's qubit B (a CNOT, Hadamard then measurement constitutes a *Bell State measurement*. The opposite: a Hadamard then a CNOT creates an entanglement instead). Depending on the result we then know the state of A and C:

$$\begin{aligned} |0_B\rangle \to (|0_A 0_C\rangle + |1_A 1_C\rangle) \otimes |0_{B2}\rangle = \left|\Phi^+_{A,C}\right\rangle \\ |1_B\rangle \to (|0_A 1_C\rangle + |1_A 0_C\rangle) \otimes |0_{B2}\rangle = \left|\Psi^+_{A,C}\right\rangle \end{aligned} \tag{8.7}$$

The result is that we create two of the possible Bell states (entangled states) of A and C. Since we know the result of the measurement of B, we know what entangled state we are in, and are able to perform single qubit rotations of the states based on this result to deterministically go to any other arbitrary entangled state (for example by applying a Hadamard to qubits A and C). The upshot here is that we have generated entanglement at a distance by generating two shorter-distance links combined with entanglement swapping. Because the quantum memory can store the information and the exponential loss of transmission is broken up into smaller segments, the scaling is *polynomial* in distance instead of exponential. Roughly, the time to distribute entanglement (T_e) without repeaters is $\propto e^{\alpha L} = (e^{\alpha L/N})^N$, while the time to success with repeaters is $\propto N e^{\alpha L/N}$. We use the fact that most entanglement is *probabilistic* at a distance, such that a memory is required to 'hold onto' the entanglement as it waits for the other nodes to generate their entanglement. Otherwise, we would need all nodes to succeed at once, which brings us back to the original scaling issue.

Using such quantum repeater schemes, we can drastically boost entanglement generation

at a distance. For reference, most quantum communications schemes aim for approximately 1-100 km repeater spacings (at 10 km we already lose half the photons in the telecom). Furthermore if each node has multiple memories, we can expand the connectivity of each node to make a network.

One of the first 'feasible' quantum repeater protocols is the DLCZ protocol ([38], named after the authors) based on atomic ensembles which show a $\sqrt{N}$ enhancement of the coupling to light and where entangled photons can be stored (memories) and retrieved. This proposal is still researched today with exciting developments[39]. That being said, the wavelength ranges, doing the entanglement swapping, memory times, scaling, and the interferometric stability of the links (further discussed in the following sections) are all issues that need to be resolved. In the next section, we will describe the scheme for generating entanglement between nodes that could be implemented using the VV^0 in SiC. There are many advantages to this system, including nanophotonic integration, scalability, and telecom-compatible emission with exceptional quantum memories which are discussed in chapter 13.

Once entanglement is generated at a distance, its fidelity can be boosted using *entanglement purification*[44] and the entanglement can be used to 'teleport' quantum information[141] from point A to the qubit at C. This can be done at great distance, and consists of just 'Alice' having a memory qubit she wants to teleport (A2) and measuring this qubit in the Bell basis with her entangled state shared with 'Charlie' (qubit A). Based on the result, Charlie can perform a deterministic single-qubit gate to recover the state Alice wanted to send in A2. Note here that the particles did not physically move, but their states did (at some level of fundamental particles, this is the same thing). This effect of Alice's measurement on Charlie's qubit is *instantaneous*, but Charlie can only recover the information after he received the classical result (by sending over a message). Thus, we *cannot send quantum information faster than the speed of light*, as much as we may want it. The teleportation schemes have been developed for solid-state defect spins [113], and have even been used to teleport a photon's states over 140 km of free space [142].

8.4 Hong-Ou Mandel Interference

The DCLZ protocol and the protocol for entangling optically active spins at a distance both rely on *Hong-Ou-Mandel* interference (HOM). HOM is a way to get photons from two sources to interact by impinging them on a *beamsplitter*. With a 50:50 beamsplitter, two photons that are perfectly *identical* and arrive at the same time will always pair up as they exit the beamsplitter. We can see this explained in Fig. 8.2. One way of representing this mathematically is that this corresponds to the transformation of the photons from the input ports A, B to the output ports C,D:

$$\begin{pmatrix} \hat{a}^\dagger \\ \hat{b}^\dagger \end{pmatrix} = \frac{1}{\sqrt{2}} \begin{pmatrix} 1 & 1 \\ 1 & -1 \end{pmatrix} \begin{pmatrix} \hat{c}^\dagger \\ \hat{d}^\dagger \end{pmatrix} \tag{8.8}$$

Where $\hat{a}, \hat{a}^\dagger$ are the *annihilation and creation operators*, respectively, that subtract or add a photon from a mode. Two photons at the inputs $|1_A 1_B\rangle$ result in either two photons out port C, *or* two photons out port D:

$$\begin{aligned} |1_A 1_B\rangle &= \hat{a}^\dagger \hat{b}^\dagger |0_A 0_B\rangle \\ \implies & (\hat{c}^\dagger + \hat{d}^\dagger)(\hat{c}^\dagger - \hat{d}^\dagger) |0_C 0_D\rangle \\ = & (\hat{c}^{\dagger 2} - \hat{d}^{\dagger 2}) |0_C 0_D\rangle = \frac{|2_C 0_D\rangle - |0_C 2_D\rangle}{\sqrt{2}} \end{aligned} \tag{8.9}$$

Here the kets are for *Fock states* of occupation (number of photons) of a mode (not a qubit with just 0 and 1). The indistinguishability of the two photons allows for the proper interference for the states to add up this way. This type of interaction is the basic entangling mechanism in linear optics quantum computing. Usually, we then place single photon detectors at ports C and D. These detectors (usually) can only measure single photons, where two photons at a time still looks like a click. A click at C, then projects our state into $|2_C 0_D\rangle$, for example. Commonly, by looking at the coincidence counts much like a $g^{(2)}$ of the two detectors, by sweeping the frequency or timing of the two photons we can see a 'HOM dip' corresponding to no correlations at the detectors: $g^{(2)} = 1$ when no interference

occurs, to this 'bunching' behavior corresponding to $g^{(2)} = 0$ (Fig. 8.2B). The width (the coherence time of the photons, t_c) and depth of this dip determines the projection fidelity into one of the states in Eq. 8.9. One way of stating this effect is that the beamsplitter *erases the 'which way' information* of the photons. We can't tell which of the two resulting photons in either C or D came from A or B (they are totally indistinguishable). Broadening in the photon coherence (such as from spectral diffusion) makes the HOM dip narrower (a shorter t_c) and lowers visibility. In general, we can write the $g^{(2)}(\Delta t)$ function for timed photons from identical emitters with lifetime τ, dephasing rate γ (lifetime limited and other contributions), inhomogeneous linewidth Γ, and frequency detuning δf that arrive at the same time (on average)[143–145]:

$$g_i^{(2)}(\Delta t) = e^{-|\Delta t|/\tau} - e^{-\gamma|\Delta t| - (2\pi\Gamma\Delta t)^2}\cos(2\pi\delta f \Delta t) \tag{8.10}$$

A detuning adds oscillations, and we can see that while a continuous stream of untimed events gives a uniform distribution as shown in Fig. 8.2B, the function for timed wavepackets shows the exponential envelope from the emitter's lifetime. In a perfectly distinguishable case (for example by making the polarizations perpendicular), then $g_d^{(2)}(\Delta t) = e^{-|\Delta t|/\tau}$. We see that in the case of indistinguishable photons, we get a dip to zero coincidences at zero time delay, but that as spectral diffusion and inhomogeneous broadening is added, the width of this dip is smaller and smaller. The depth of the dip is usually called the *visibility, V*, which here *always goes to 1 at* $\Delta t = 0$. This does not take into account dark counts, scattered photons or timing jitter, however. In experiment, we need to pick a 'window' of Δt that we collect events over. Too narrow, and although the dip is low and interference happens, we miss out on events. Too high, and we get extra coincident clicks on the two detectors $g^{(2)} \neq 0$. However, for distinguishable photons this is also what we get. Therefore our ability to distinguish between the two cases relates to the average *fidelity* of the interference and is

the *average visibility* $\langle V \rangle$ over the window. With the visibility[122]:

$$V(\Delta t) = \frac{g_d^{(2)}(\Delta t) - g_i^{(2)}(\Delta t)}{g_d^{(2)}(\Delta t)} \tag{8.11}$$

We weight the average by the frequency of total events, which is just $g_d^{(2)}(\Delta t)$ (the probability density function).

$$\langle V \rangle = \frac{\int \frac{g_d^{(2)}(\Delta t) - g_i^{(2)}(\Delta t)}{g_d^{(2)}(\Delta t)} \cdot g_d^{(2)}(\Delta t)\ d(\Delta t)}{\int g_d^{(2)}(\Delta t)\ d(\Delta t)} \tag{8.12}$$

With window width t_w centered at $\Delta t = 0$.

$$\langle V \rangle(t_w) = \frac{\int_{-\frac{t_w}{2}}^{\frac{t_w}{2}} g_d^{(2)}(\Delta t) - g_i^{(2)}(\Delta t)\ d(\Delta t)}{\int_{-\frac{t_w}{2}}^{\frac{t_w}{2}} g_d^{(2)}(\Delta t)\ d(\Delta t)} \tag{8.13}$$

This ends up being a function of Erf's and exponentials that looks like Fig. 8.2C, where we see that the average visibility changing as we change the integration window. As spectral diffusion and inhomogeneous broadening gets worse and worse, the acceptable window is shorter and shorter. We also see that the fraction of events (success probability) that are contained in this window grows as the window is increased.

$$\eta_w = 1 - e^{-t_w/(2\tau)} \tag{8.14}$$

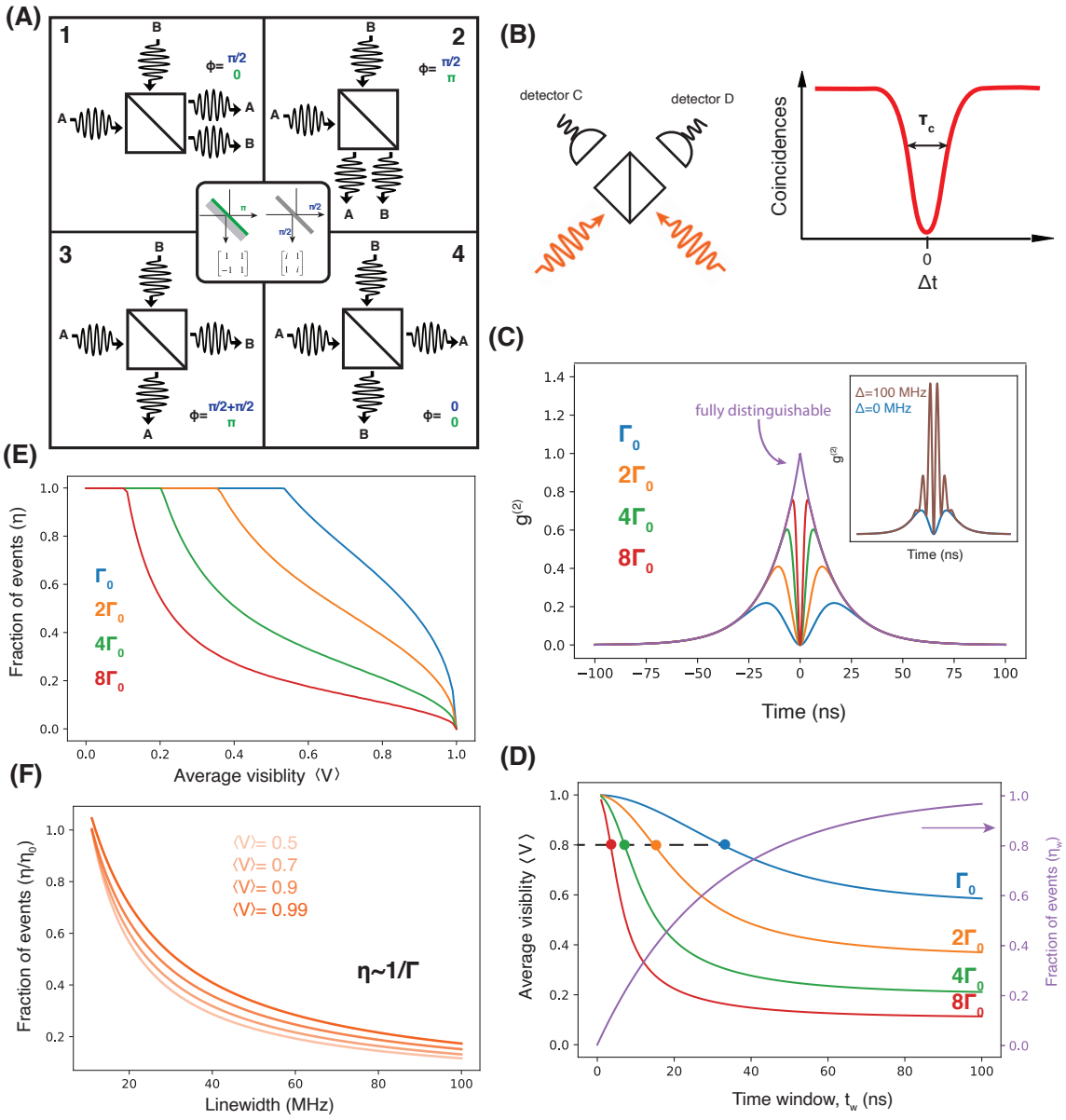

Figure 8.2: **Hong-Ou-Mandel interference (A)** The four possible outcomes for two photons coming into the beamsplitter. (inset) The two possible conventions/understandings of the relative phases from reflections on a beamsplitter, see [146, 147] are color coded. Adding the four possibilities we see a relative π phase cancelling the amplitudes in cases (3) and (4). **(B)** Schematic of the detection of HOM interference. Looking at the coincidences at the two detectors, a HOM dip appears when the photons are indistinguishable and arrive at the same time. The dip with a continuous stream of photons with coherence time t_c is shown. **(C)** HOM interference coincidences, g^2 as a function of the spectral width for a VV^0 (15 ns lifetime). Γ_0 is the homogeneous linewidth. (inset) g^2 with and without detuning Δ.

Figure 8.2: **(D)** Average visibility $\langle V \rangle$ over an integration time window t_w for various values of the spectral width. As the spectral diffusion and line width is broadened, the acceptable range of time delays is reduced (dots) for a given desired $\langle V \rangle$. The horizontal black dotted line is 80% visibility. The purple line is the fraction of photon arrival events contained in the window. **(E)** The relative success rate (fraction of events η) for a desired $\langle V \rangle$ for different values of the inhomogeneous linewidth. **(F)** Fraction of events that are collected at a given average visibility normalized to the fraction of events with a perfect emitter Γ_0, as a function of linewidth.

Even for a perfect emitter with $\Gamma = 0$, this means there exists a tradeoff between the desired average visibility (fidelity) and the fraction of events that are detected as shown in Fig. 8.2D and Fig. 8.2E. This effect is illustrated in entanglement experiments with the NV^- center [122]. As mentioned before, this means that *for a given fidelity/visibility, the fraction of successful events we collect decrease with spectral diffusion.* This is shown in Fig. 8.2F, and shows that the success rate scales roughly inversely with the total linewidth (Γ_T): $\eta_{TPQI} \approx \eta_0/\Gamma_T$, with η_0 being the success probability of a lifetime-limited line according to Fig. 8.2E.

The upshot is that *the success probability for a given two-photon quantum interference (TPQI) visibility/fidelity will scale roughly inversely with the emitter's linewidth broadening (Γ/Γ_0).* Recent HOM interference with the V_{Si} in SiC have been achieved [148], while the early interference experiments with NV^- in diamond were in 2012[149], which allowed for the entanglement covered in the next section one year later[122].

8.5 The Barrett-Kok Entanglement Scheme

The *Barrett-Kok entanglement scheme*[150] is one of the many possible ways to generate entanglement at a distance. Here, we will phrase how the procedure would proceed in a solid state defect such as VV^0 in SiC or the NV^- in diamond[122]. The basic idea is to create spin-spin entanglement by utilizing the HOM effect of emitted photons from our defect, which are entangled with the spin state. A certain set of clicks on detectors will *'Herald'* or

project us into a particular entangled state. The procedure is as follows:

- Initialize both spin A and spin B into $m_s = 0$ using either off-resonant or resonant initialization
- Rotate both A and B by $\pi/2$ into $\frac{|\uparrow\rangle+|\downarrow\rangle}{\sqrt{2}}$, where $|\uparrow\rangle$ is either $m_s = \pm 1$ and $|\downarrow\rangle$ is $m_s = 0$
- Perform a resonant excitation on one of the cycling transitions E_x, E_y that corresponds to a fast *optical π pulse*. This pulse transfers the ground to excited state in time δt (usually < 10 ns), whereby the excited state releases a photon into the ZPL with a fraction determined by the DWF, a timing uncertainty determined by the optical lifetime and a frequency uncertainty set by the natural linewidth and any spectral broadening. Importantly, the *phase* of the emitted photon is determined by the phase of the excitation light.
- Because the spin was initialized into $\frac{|\uparrow\rangle+|\downarrow\rangle}{\sqrt{2}}$, and the laser is only resonant with E_x when $m_s = 0$, a trip to the excited state is entangled with the spin being $m_s = 0$ for both spin A and B:
$$|\Psi\rangle = \frac{|\downarrow, ES\rangle + |\uparrow, GS\rangle}{\sqrt{2}} \tag{8.15}$$
- With the spontaneous emission from the excited state, this results in the entanglement of the state for each spin with the presence or absence of a single photon (at a particular frequency ω and spatial mode):
$$|\Psi\rangle = \frac{|\downarrow, 1\rangle + |\uparrow, 0\rangle}{\sqrt{2}} \tag{8.16}$$
- This photon is collected from spin A and spin B (usually with low probability), and propagates over distances d_A, d_B to a central station. Upon propagation, the electron spin state is stationary, but the quantum state of the photon acquires a phase according

to the frequency and time of propagation, $\phi = kd - \omega t$ (if it exists):

$$|\Psi\rangle = \frac{|\uparrow, 0\rangle + |\downarrow, 1\rangle\, e^{-i\phi}}{\sqrt{2}} \tag{8.17}$$

The electron spins here are assumed to have the same qubit frequency such that no relative phase is built up over the propagation [151]. Schemes may exist where this requirement is not necessary, which would take into account the frequency-difference phase accumulation and correct for it.

- The photons (or no photons) from A and B are spatially overlapped onto a 50:50 beamsplitter with input ports 'A' and 'B' and output ports 'C' and 'D'. The input state is then:

$$\frac{1}{2}(|\uparrow_A, 0_A\rangle + |\downarrow_A, 1_A\rangle\, e^{-i\phi_A}) \otimes (|\uparrow_B, 0_B\rangle + |\downarrow_B, 1_B\rangle\, e^{-i\phi_B}) \tag{8.18}$$

Following Eq. 8.9 for the individual terms results in:

$$\begin{aligned}
|\uparrow_A\uparrow_B\, 0_A 0_B\rangle &\implies |\uparrow_A\uparrow_B\, 0_C 0_D\rangle \\
|\uparrow_A\downarrow_B\, 0_A 1_B\rangle\, e^{-i\phi_B} &\implies |\uparrow_A\downarrow_B\rangle \otimes (\tfrac{|0_C 1_D\rangle - |1_C 0_D\rangle}{\sqrt{2}}) e^{-i\phi_B} \\
|\downarrow_A\uparrow_B\, 1_A 0_B\rangle\, e^{-i\phi_A} &\implies (|\downarrow_A\uparrow_B\rangle) \otimes (\tfrac{-|0_C 1_D\rangle + |1_C 0_D\rangle}{\sqrt{2}}) e^{-i\phi_A} \\
|\downarrow_A\downarrow_B\, 1_A 1_B\rangle\, e^{-i(\phi_A+\phi_B)} &\implies (|\downarrow_A\downarrow_B\rangle) \otimes (\tfrac{|2_C 0_D\rangle - |0_C 2_D\rangle}{\sqrt{2}}) e^{-i(\phi_A+\phi_B)}
\end{aligned} \tag{8.19}$$

We can gather the terms which are the result of getting only one click on either 'C' or 'D', which happens *half the time*:

$$\begin{aligned}
(|\uparrow_A\downarrow_B\rangle\, e^{-i\phi_B} - |\downarrow_A\uparrow_B\rangle\, e^{-i\phi_A}) \otimes |0_C 1_D\rangle \\
(-|\uparrow_A\downarrow_B\rangle\, e^{-i\phi_B} + |\downarrow_A\uparrow_B\rangle\, e^{-i\phi_A}) \otimes |1_C 0_D\rangle
\end{aligned} \tag{8.20}$$

A single click thus puts us into a state that looks like the entangled state $\frac{|\uparrow\downarrow\rangle - |\downarrow\uparrow\rangle}{\sqrt{2}}$ but has some pesky phases. These phases are highly sensitive to frequency and path length

fluctuations of the entanglement channel. Given that this is uncontrolled and may be unknown, the resulting fidelity can be low. Furthermore, there is a 1/4 probability of getting a click that corresponds to 2 photons at a given detector. Looking at Eq. 8.19, this result is not an entangled state. A photon number resolving detector (which exists) would be able to reject these events. Alternatively, a superposition with smaller amplitude in the photon-producing state reduces the chance of this event (Fidelity at the cost of success rate). Finally, there are 'dark' counts or other events which may give a single click but do not correspond to an entanglement event.

- To fix all of these issues, we start by flipping spins A and B using a microwave π pulse.
- The optical π pulse is repeated again for both spins, producing a second photon (or no photon) at the beamsplitter with a time delay τ.
- Just like Eq. 8.19, after skipping some math, we get:

$$\begin{gathered}
\left|\uparrow_A\uparrow_B 0_{C_E}0_{D_E}\right\rangle \implies \left|\downarrow_A\downarrow_B 0_{C_E}0_{D_E}\right\rangle \otimes (\left|2_{C_L}0_{D_L}\right\rangle - \left|0_{C_L}2_{D_L}\right\rangle)e^{-i(\phi_{A_L}+\phi_{B_L})} \\
\\
\frac{1}{\sqrt{2}}\left|\uparrow_A\downarrow_B\right\rangle \otimes (\left|0_{C_E}1_{D_E}\right\rangle - \left|1_{C_E}0_{D_E}\right\rangle)e^{-i\phi_{B_E}} \implies \\
\frac{1}{\sqrt{2}}\left|\downarrow_A\uparrow_B\right\rangle \otimes (\left|0_{C_E}1_{D_E}\right\rangle - \left|1_{C_E}0_{D_E}\right\rangle)e^{-i\phi_{B_E}} \otimes (-\left|0_{C_L}1_{D_L}\right\rangle + \left|1_{C_L}0_{D_L}\right\rangle)e^{-i\phi_{A_L}} \\
\\
\frac{1}{\sqrt{2}}(\left|\downarrow_A\uparrow_B\right\rangle) \otimes (-\left|0_{C_E}1_{D_E}\right\rangle + \left|1_{C_E}0_{D_E}\right\rangle)e^{-i\phi_{A_E}} \implies \\
\frac{1}{\sqrt{2}}(\left|\uparrow_A\downarrow_B\right\rangle) \otimes (-\left|0_{C_E}1_{D_E}\right\rangle + \left|1_{C_E}0_{D_E}\right\rangle)e^{-i\phi_{A_E}} \otimes (\left|0_{C_L}1_{D_L}\right\rangle - \left|1_{C_L}0_{D_L}\right\rangle)e^{-i\phi_{B_L}} \\
\\
\frac{1}{\sqrt{2}}(\left|\downarrow_A\downarrow_B\right\rangle) \otimes (\left|2_{C_E}0_{D_E}\right\rangle - \left|0_{C_E}2_{D_E}\right\rangle)e^{-i(\phi_{A_E}+\phi_{B_E})} \implies \\
\frac{1}{\sqrt{2}}(\left|\uparrow_A\uparrow_B\right\rangle) \otimes (\left|2_{C_E}0_{D_E} - \left|0_{C_E}2_{D_E}\right\rangle\right\rangle)e^{-i(\phi_{A_E}+\phi_{B_E})} \otimes \left|0_{C_L}0_{D_L}\right\rangle
\end{gathered} \tag{8.21}$$

Where the first and second photons arriving to 'C' and 'D' (from the two rounds) are referred to 'C_E','C_L' and 'D_E','D_L', respectively (early and late photons) and the

phase accumulation of the photons is defined similarly. This is a mess.

- We eliminate all cases except where we got a single photon in both the early and the late bin (in either C or D). This eliminates half of the possibilities. Regrouping in terms of the results on the detectors:

$$\begin{aligned}
&\left|1_{C_E}1_{C_L}0_{D_E}0_{D_L}\right\rangle \otimes (-\left|\downarrow_A\uparrow_B\right\rangle e^{-i(\phi_{B_E}+\phi_{A_L})} - \left|\uparrow_A\downarrow_B\right\rangle e^{-i(\phi_{A_E}+\phi_{B_L})})\\
&\left|1_{C_E}0_{C_L}0_{D_E}1_{D_L}\right\rangle \otimes (\left|\downarrow_A\uparrow_B\right\rangle e^{-i(\phi_{B_E}+\phi_{A_L})} - \left|\uparrow_A\downarrow_B\right\rangle e^{-i(\phi_{A_E}+\phi_{B_L})})\\
&\left|0_{C_E}1_{C_L}1_{D_E}0_{D_L}\right\rangle \otimes (-\left|\downarrow_A\uparrow_B\right\rangle e^{-i(\phi_{B_E}+\phi_{A_L})} + \left|\uparrow_A\downarrow_B\right\rangle e^{-i(\phi_{A_E}+\phi_{B_L})})\\
&\left|0_{C_E}0_{C_L}1_{D_E}1_{D_L}\right\rangle \otimes (-\left|\downarrow_A\uparrow_B\right\rangle e^{-i(\phi_{B_E}+\phi_{A_L})} - \left|\uparrow_A\downarrow_B\right\rangle e^{-i(\phi_{A_E}+\phi_{B_L})})
\end{aligned} \tag{8.22}$$

- Taking out a global phase of $e^{-i(\phi_{A_E}+\phi_{B_E})}$ and defining the differences of phases over the two attempts $\Delta\phi$, we can see that based on the results we project into the states:

$$\begin{aligned}
C,C &\implies \left|\downarrow_A\uparrow_B\right\rangle e^{-i\Delta\phi_A} + \left|\uparrow_A\downarrow_B\right\rangle e^{-i\Delta\phi_B}\\
C,D &\implies \left|\downarrow_A\uparrow_B\right\rangle e^{-i\Delta\phi_A} - \left|\uparrow_A\downarrow_B\right\rangle e^{-i\Delta\phi_B}\\
D,C &\implies \left|\downarrow_A\uparrow_B\right\rangle e^{-i\Delta\phi_A} - \left|\uparrow_A\downarrow_B\right\rangle e^{-i\Delta\phi_B}\\
D,D &\implies \left|\downarrow_A\uparrow_B\right\rangle e^{-i\Delta\phi_A} + \left|\uparrow_A\downarrow_B\right\rangle e^{-i\Delta\phi_B}
\end{aligned} \tag{8.23}$$

Therefore, based on the click results, we can be sure that we are in an entangled state. We've eliminated the chances that we actually had two photons or spurious dark counts. In the limit where the two attempts can be performed faster than the interferometric stability of the two channels and possibly the spin T_2^* (with $\tau \sim 100$'s ns, this is fulfilled), then both $\Delta\phi$ are small, and the results group nicely into whether two attempts results in clicks at the same detector $|+\rangle$ or opposite $|-\rangle$:

$$\begin{aligned}
|+\rangle &\implies \left|\downarrow_A\uparrow_B\right\rangle + \left|\uparrow_A\downarrow_B\right\rangle = \left|\Psi^+\right\rangle\\
|-\rangle &\implies \left|\downarrow_A\uparrow_B\right\rangle - \left|\uparrow_A\downarrow_B\right\rangle = \left|\Psi^-\right\rangle
\end{aligned} \tag{8.24}$$

Which are two of the possible Bell states.

The result here is that one click on both excitation attempts heralds (announces) the successful creation of the entangled state. We only were able to use half of the possibilities in Eq. 8.21, which combined with the probability η of a HOM-like event gives a total success probability $\frac{1}{2}\eta^2$. η depends on the losses in the system (fiber), photon collection efficiency, the QE, DWF, emitter linewidth and therefore the integration bin for the HOM interference, among other considerations. This entire scheme is therefore attempted many, many, times until a successful set of clicks (most of the time we see nothing), at which point we stop and know exactly what entangled state we are now in.

Importantly, the average visibility (fidelity) from the choice of the integration window for the HOM-like interference affects the total success rate, and the *fidelity of the resulting entangled state* as mentioned in the previous section, such that[113, 122]:

$$F_{\Psi^{\pm}} = \frac{1}{2} + \frac{1}{2}\langle V \rangle \tag{8.25}$$

This scheme has been used for landmark experiments on loophole-free Bell tests[151], entanglement distillation[44] and quantum teleportation[113] at a distance[152]. Specifically, spins in the solid-state allow for long coherences of the spin as the photon travels over long distances. Once the photons make their clicks, the states that are entangled are still alive. Local quantum memories consisting of *weakly coupled* nuclear spins serve as ideal memories in these applications and are discussed in chapter 13.

8.6 Other Schemes

Other entanglement schemes are possible as well. These include 'one way entanglement'[153], the use of 'graph states'[154] that are robust to error, or schemes using SPDC sources and photonic quantum memories[155]. In particular, multiple possibilities exist for the SiC defects [156]. Recently, spin quantum memory assisted quantum communication was achieved [157]. Furthermore, entanglement distillation or deterministic entanglement delivery[130]

can boost rates and alleviate fidelity or timing requirements. With strong coupling to photonic modes, spin-selective cavity coupling allows for the reflection, transmission or absorption of photons to be entangled with the spin state[158, 159]. Furthermore, absorption-based schemes[160] or dynamically stabilizing the quantum communications channel (used in [130]) may allow for drastic speed ups of the entanglement rate. Importantly there are two major types of heralded entanglement schemes:

- Heralding through *two photon quantum interference* scales as the success probability per channel squared. Largely insensitive to phase/distance fluctuations in the channel (as seen in section 8.5), at the cost of slow entanglement.

  Entangled state: $\Psi^{\pm}_{TPI} = \frac{1}{\sqrt{2}}(|01\rangle \pm |10\rangle)$

- Heralding through *single photon quantum interference* scales linearly as the success probability per channel. The entangled state is very sensitive to phase/distance fluctuations in the channel ($\Delta\phi$), with the benefit of fast rates[39, 130].

  Entangled state: $\Psi^{\pm}_{SPI} = \frac{1}{\sqrt{2}}(|01\rangle \pm e^{i\Delta\phi}|10\rangle)$

Despite the exact scheme, the hardware requirements for our quantum system is basically the same. Some of the original schemes are for atomic systems, which sometimes use the polarization of photons, which are similarly heralded through interference on a beamsplitter [39, 41, 161, 162].

8.7 Requirements

The requirements for quantum entanglement channels driven by solid-state quantum emitters all wrap up in the factor η, but also in the ability to control and tune up emitters, developing quantum memories, along with the ability to perform *single-shot readout*. As a baseline, the *entanglement rate* depends on the rate that the process can be attempted. This is the combined time for qubit initialization, an optical π, a microwave π, and another optical

π. Practically, the initialization step is $\sim 1 - 10\ \mu s$ and is the limiting factor, putting the attempt rate at $0.1 - 1\ MHz$. Recent proposals suggest that reinitialization may not be necessary [163]. However, in initial experiments with NV^- centers, the success probability per attempt is less than 10^{-7} at 3 meters [122] and 10^{-9} at 1.3 km [151](due to fiber losses), putting the entanglement rate at $\sim 0.1 - 1\ mHz$. Demonstrations that use phase stabilization and only one entanglement attempt have had rates as high as 39 Hz [130] for the NV^- center in diamond. For trapped ion-based entanglement, short distance rates of 182 Hz have been demonstrated [40].

Both the success probability and the attempt rate are important parameters for creating entanglement at useful speeds. Practically, entanglement generation needs to wait for classical confirmation on failure or success from the measurement node, which scales with the entanglement distance, placing a rough limit of 1 km before the entanglement rate is limited by photon propagation speeds instead of the attempt rate. In realistic scenarios at long distances, this means that relatively slow entanglement attempt rates can be a non-limiting factor.

Practically, the laser sources at the nodes in a network need to retain a definite phase relation (and frequency) so that the corresponding emitted photons display high visibility interference at the beamsplitter. This technical challenge has been solved for proof-of-principle experiments with atoms and defects [39, 151].

8.7.1 Telecommunications, Fiber Optic Networks and QFC

In any quantum communications channel, issues of losses during transmission are paramount. This was mentioned in section 8.3. This is a big advantage for the VV^0 ($\sim$0.8 dB/km) versus the NV^- in diamond ($\sim$8 db/km) in transmitting through current optical fiber, which may drastically increase quantum links using solid state-spins. It may be the case that one day, fiber that is optimized for a different wavelength is developed (such as ZBLAN) but it looks like wavelengths around 1500-2500 μm are low frequency enough to avoid losses, but high

enough to avoid thermal occupation of modes to room temperature.

A strategy to avoid high fiber loss in the visible is to use *quantum frequency conversion (QFC)* that converts single photons from the visible to the low loss telecom bands. This is achieved using *difference frequency generation (DFG)* or down conversion by mixing the single photons in a nonlinear crystal with a strong pump tone such that the difference in photon energies corresponds to a telecom photon. This conversion process has been demonstrated for the NV^- center, but suffers from added noise photons at the frequency of interest[164]. Because the NV^-'s ZPL (637 nm) is less than half the telecom wavelength of 1550 nm, the pump laser required is lower in wavelength (higher in energy) than 1550 nm. Practically, pumping the non-linear crystal with a strong tone to do the high fidelity conversion produces Raman, and other scattered noise photons at *lower energies than the pump* which includes the telecom wavelength of 1550 nm[165]. Because the process is trying to preserve single photons, barely any noise is allowable. On the other hand, for defects with wavelengths above half the wavelength of 1550 nm such as VV^0, the corresponding pump laser is above 1550 nm in wavelength and mostly produces noise photons $>$ 1550 nm, which do not contribute unwanted photons for the conversion. QFC for the DLCZ protocol was recently demonstrated [39].

8.7.2 Photon Collection Efficiency

Because of total internal reflection, as mentioned in section 5.4, most of the photons do not make it to our collection objective. This issue is usually alleviated using *solid immersion lenses (SILS)*, in which a hemisphere of the host material can be ion milled into the surface around a defect. The light emitted from the defect will then be always normal to the surface and not be internally reflected. This has been used to boost the collection efficiency by about a factor of 5-10$\times$ from a few percent to around 10% in diamond[129]. Cavity-based schemes such as nanophotonics, waveguides, tapered and lensed fibers, fiber cavities or metalenses can also help guide the light out of the material more effectively and is a huge

area of research[166–169]. These techniques can boost the collection efficiency to around 100% (though everything comes at a cost[170]). Collecting every photon determines η, but also importantly determines if single-shot readout is possible, as will be discussed in section 8.7.6.

8.7.3 Tuning

Every spin defect in a given sample has different axial and transverse strain. This means that the quality of the spin-photon interface and its spectral location are different for every defect. As mentioned in section 6.1, Stark tuning can both correct the inherent asymmetry and tune two remote defects to be in resonance with each other. Other systems have been investigating strain tuning in nanostructures as a way to tune emissions into resonance[114]. In general, it's important to retain a tuning knob for the orbital fine structure that does not degrade the spin or spin-photon interface. This sort of knob is developed for VV^0 in section 11.4 where the drastic tuning maintains the defect's symmetry and does not add unwanted mixing in the excited state. Dynamic tuning of the excited state on the timescale of the emission lifetime can be used to temporally and spectrally shape emitted photons[171, 172], while slower tuning can correct for spectral wandering, or in tuning to photonic devices, for example. Tuning may even be achieved during the QFC processes with tunable pump lasers.

8.7.4 Photonics and Purcell Enhancement

For defects, the low DWF (and therefore rate of indistinguishable photons) results in a low η. *Purcell* enhancement, which modifies the photonic density of states an emitter can couple to, results in a reduction in the emitter lifetime and a focusing of the emission into a particular spectral band. This can be used to increase the effective DWF by tuning the defect into a cavity resonance with high *quality factors* and low *mode volume*[3]. The focusing of the emission into a particular cavity mode also results in more spatially coherent emission, which can be more easily collected. Furthermore, for defects with poor cyclicity,

an increase of the radiative rates versus the nonradiative ones results in increased QE and an improved spin-photon interface. This has been used to unlock single-shot readout for rare earth ions in oxides, for example[59, 60], and may allow quantum communications in these systems [173]. Strong coupling of the emitter to a nanophotonic cavity, meanwhile, allows for deterministic schemes for photon mediated entanglement. In general, the ability to create high-quality photonic devices *without destroying* the quality of the spin-photon interface is a huge advantage that can boost entanglement rates by orders of magnitude. Proof-of-principle photonic enhancement of VV^0 is provided in chapter 9. One small note is that there is a limit to photonic enhancement: if the Purcell factor gets too high, the lifetime gets short and the homogeneous linewidth gets larger. If the lines are too close spectrally, they may start to overlap, reducing selectivity.

8.7.5 Spectral Diffusion and Charge Instability

For solid-state defects, blinking (charge instability under optical excitation) and spectral diffusion (section 6.2) are major problems. Any time a defect is in the incorrect charge state, it does not emit photons as desired and its spin state is unusable. Spectral diffusion not only drastically reduces η, but similarly reduces the fidelity of single-shot readout. For demonstrations of single-shot readout[174] and long-distance entanglement[130] with NV^- centers in diamond, a *charge-resonance check* is performed for initialization and single-shot readout of the spin. With this check, events are only counted that correspond to the existence of a defect *in the correct charge state, at the right frequency.* In general, an overarching problem in the field is integrating quantum emitters into nanostructures, like photonic devices, while keeping spectral diffusion in check. Electric field insensitive group IV defects in diamond have a distinct advantage in this regard. The NV^- center in diamond usually shows spectral widths many times the lifetime limit.

8.7.6 Single-Shot Readout

Single-shot readout is absolutely necessary to confirm entanglement, and to perform quantum tasks such as teleportation, and in implementing quantum repeaters. An entangled state describes correlations between sets of measurements of qubits, *not changes in average results on measurements*. Entanglement can be mapped onto measurement bases through *quantum state tomography (QST)*, but this requires two qubit gates between the entangled pair. At long distances, we only have probabilistic entanglement generation and no two-qubit gates. Therefore, quantum correlations and classically conditioned gates ("if I measure $|0\rangle$, do X. If I measure $|1\rangle$, do Y") require high-fidelity *projective* measurement that can distinguish between $|0\rangle$ and $|1\rangle$ in *every experimental instance*.

"You only get one shot, do not miss your chance to (know)
This opportunity comes once in a (spin) lifetime"

Single-shot readout in a sense gives maximum signal-to-noise for a quantum measurement as all the information is extracted. Furthermore, projective readout allows for *initialization by measurement* which has been demonstrated in both electron and nuclear spins in the solid state [174, 175]. Achieving single-shot readout was *the* experiment that opened the floodgates of long-distance communications with spin defects. Unfortunately single-shot readout for VV^0 has not been achieved to date, but the outlook looks promising.

To demonstrate single-shot readout for defects, we utilize the spin-selective orbital states that are highly cycling from $m_s = 0$ and (usually) measure the photons in the phonon sideband. As such, we can continuously excite this transition and extract photons entangled with the spin state until a *spin-flip occurs*. A 'spin-flip curve' consists of measuring the average number of photons in a time bin under continuous excitation. This will decay exponentially depending on the optical power (rate of trips to the excited state) and the branching ratio (see Fig. 5.8). As we measure longer and longer, we can extract more photons on average, but we can be less sure that we are *still in* $m_s = 0$ (this is an issue for

some schemes, but not if we're just verifying entanglement). Our goal is to measure enough photons to make a call on whether we were in $m_s = 0$ (getting some photons) or $m_s = \pm 1$ (no photons). As such, we need a high collection efficiency along the lines of what was discussed in section 8.7.2 combined with high cyclicity to measure (hopefully) *a few photons*. Photon counting follows *Poisson* statistics, so the fidelity of determining the quantum state is determined by the overlap integral between a Poissonian peaked near zero (with possible contributions of dark counts, laser scatter, etc.) and one peaked near the average photons extracted. In practice, high-fidelity readout can be achieved with around 5 photons in the 'bright' state. The NV^- center in diamond, when properly tuned up, emits $\sim 100 - 1000$ photons, which combined with a 10% collection efficiency and other losses results in a few photons per shot. The VV^0 is expected to have less mixing in the excited state purely from the excited state Hamiltonian, which could result in over 10^4 photons emitted[55]. In experiment, using the NV^- and VV^0 center's lifetime and the spin flip rate at saturation ([55, 174]) we can estimate that both defects emits roughly 200 photons before a spin flip.

$$\langle N_{ph} \rangle \approx \frac{\frac{1}{\tau}}{R_{sf}^{sat}} \tag{8.26}$$

Where τ is the emitter lifetime and R_{sf}^{sat} is the spin flip rate in Hz at saturation. This is probably an underestimate due to photonionization issues at high power. However, with a 2-3% collection efficiency in diamond this corresponds to the measured few photons per shot[174]. In practice, for VV^0 we still are in need of more photons and could be limited by a variety of effects like charge, QE or collection efficiency. In particular, our detectors are single-mode fiber which makes mode matching a big issue.

The dirty secret is that this discrimination relies on assuming that if no photons are extracted, *we were in* $m_s = \pm 1$. The problem is that there are a few other things that can produce no photons, like the defect being off resonance with the laser (spectral diffusion) or being in the wrong charge state (blinking). In practice, a charge-resonance check occurs

after the readout, which confirms that the defect was on resonance and in the right charge state, *and only these attempts are counted*. The check is achieved by pumping on both an optical line with $m_s = 0$ character and also an optical line with $m_s = \pm 1$ character. If both are on resonance, the state cannot be trapped in any of $m_s = 0, \pm 1$ and continuously produces photons. Integration can occur without concern for the spin flip rate, and a highly deterministic determination with many photons can be made on if the defect was 'behaving'. In initial demonstrations, only 2-5% of tries passed this check! (for the NV^- in diamond). In a naive experiment, this means that the defect is 20-50× 'dimmer' than expected (and skews the photon statistics). This reduces the rate of entanglement heralding drastically, and means that classically controlled gates can only be attempted a fraction of the time. Therefore, reduction of spectral diffusion and blinking is of huge importance for not only two-photon indistinguishability and QE, but also for the prospects of achieving single-shot readout. The major work of this thesis in section 11.4 attempts to alleviate these issues.

While the NV^- in diamond has shown single-shot readout, achieving it in other systems is a challenge. In particular, the other well developed qubit in SiC V_{Si}^- only emits 6 photons on average before a spin flip, making single-shot readout difficult[54]. There are alternate strategies towards single-shot readout. One possibility is swapping the state to a nuclear memory and then performing repeated QND measurement on the nuclear spin with the electron[175, 176]. This boosts the number of extracted photons and has been used to boost SNR in quantum sensing. The other possibility is *spin-to-charge* conversion[177]. If the spin state of a defect can be mapped onto the defect either ionizing or not ionizing, the freed electron or hole can be measured electrically. The other option is that after the conversion, a high fidelity readout of the defect's charge state can be achieved (usually at low optical power to avoid further charge dynamics) and photons can be collected continuously without worry of 'flipping the spin'. In this way, quantum sensing has similarly been improved[178] and single-shot readout may be possible. Spin-selective ionization can be achieved multiple ways, either by using the spin-selective intersystem crossing to control photodynamics, or by

using spin selective excitation. The photodynamics and understanding in chapter 11 drives the possibility of spin-to-charge conversion for VV^0.

8.7.7 Quantum Memories

When photons are propagating in quantum networks, or after entanglement has been heralded, we can utilize the spin's long coherence or even use dynamical decoupling to extend to T_1 which could be as long as seconds to hours at low temperature. However, besides the need to read out our states and entangle them efficiently, we need quantum memories to hold onto our coherence at each node and perform entanglement swapping. In general, the metric η_{link} establishes this consideration as the ratio of the memory lifetime over the time to create entanglement[39, 130]. $\eta_{link} > 1$ has been demonstrated in the NV^- center in diamond[130], and in ion traps [41]. This metric is very small ($\eta_{link} < 10^{-4}$) in quantum dot systems due to their short coherence, limiting applicability[42, 43]. Our communication qubit (the spin) needs to be continuously reset to attempt entanglement and thus can't retain quantum information as links need to be established. We need something else to be our memory qubit. In this case, weakly coupled nuclear spins (not strongly coupled) with hyperfine coupling much less than spin T_2^* are promising candidates[179, 180]. Furthermore, we can use these memories to store many low-fidelity copies of the entanglement and use *entanglement distillation* to create one high fidelity entangled state[44].

Nuclear spins surround the central electron spin which can be optically addressed and provide many possible qubits to use. These spins can be controlled with direct RF driving[181, 182] or by using dynamical-decoupling-based control which can create conditional and unconditional rotations of the nuclear spins, constituting single and two-qubit gates with a single electron spin[183]. While gates are slow, the coherence times can exceed seconds at least (the Hahn-echo T_2). This corresponds to a quantum network that could span the diameter of the earth 25 times! In particular, for solid-state spins, nuclei with very low hyperfine in the few to 10's of kHz range (corresponding to nm away from the defect) the nuclear memory

is very resilient multiple entangling attempts[179].

In a quantum repeater, many failed attempts must occur at each pair of nodes before entanglement is generated, all while retaining the quantum state stored in each node's quantum memory. For defect spins, each attempt constitutes an electron spin repolarization/initialization, followed by microwave manipulations of the electron and then the resonant excitation pulse. For nuclear spins, a higher coupling to the electron means that it is more sensitive to errors and fluctuations on the electron. During initialization, the electron spin spends a *stochastic* amount of time in the intersystem crossing and in the optical excited states, and takes a set amount of time to go from $m_s = \pm 1 \rightarrow m_s = 0$. In the ISC and in the excited state, or even between the possible ground states $m_s = 0, \pm 1$, the hyperfine coupling is also different. Therefore there is a change in coupling/qubit frequency for an unknown amount of time. This causes dephasing of our nuclear spin quantum memory. Furthermore, control errors on the electron cause unwanted changes in the coupling strength that drive decoherence [180]. With very weak hyperfine, the memories can withstand the 1000's of entanglement attempts needed due to the low success probability at each node[179]. Optimizing and controlling these quantum memories in SiC is the focus of the work in chapter 13.

8.7.8 Summary

We summarize the salient feature defect spin systems need in creating quantum communication channels:

- the defect needs a near lifetime limited linewidth.
- defect needs to have controllable or small slow spectral wandering.
- the defect's optical structure must be tunable, without degrading the spin-photon interface.
- a high DWF, or enhanced without degrading other properties.

- the defect should not blink or undergo unwanted charge dynamics.
- the defect needs to have spin-selective optical transitions.
- the defect needs to have a cycling transition.
- the defect needs to have a long T_1 at the desired temperature.
- the defect needs to operate in one of the *telecommunications bands*. Alternatively, the defect needs to be able to be frequency converted to these bands *without* adding significant noise.
- the defect needs to have many nuclear spin registers that can be controlled with high fidelity. These memories cannot be significantly affected by entanglement attempts.
- single-shot readout of the spin must be possible.

Chapter 9

Spins in Photonic Devices

This chapter and figures are adapted from the publication [3]

Silicon carbide has recently been developed as a platform for optically addressable spin defects. In particular, the neutral divacancy in the 4H polytype displays an optically addressable spin-1 ground state and near-infrared optical emission. Here, we present the Purcell enhancement of a single neutral divacancy coupled to a photonic crystal cavity. We utilize a combination of nanolithographic techniques and a dopant-selective photoelectrochemical etch to produce suspended cavities with quality factors exceeding 5,000. Subsequent coupling to a single divacancy leads to a Purcell factor of ~ 50, which manifests as increased photoluminescence into the zero-phonon line and a shortened excited-state lifetime. Additionally, we measure coherent control of the divacancy ground state spin inside the cavity nanostructure and demonstrate extended coherence through dynamical decoupling. This spin-cavity system represents an advance towards scalable long-distance entanglement protocols using silicon carbide that require the interference of indistinguishable photons from spatially separated single qubits.

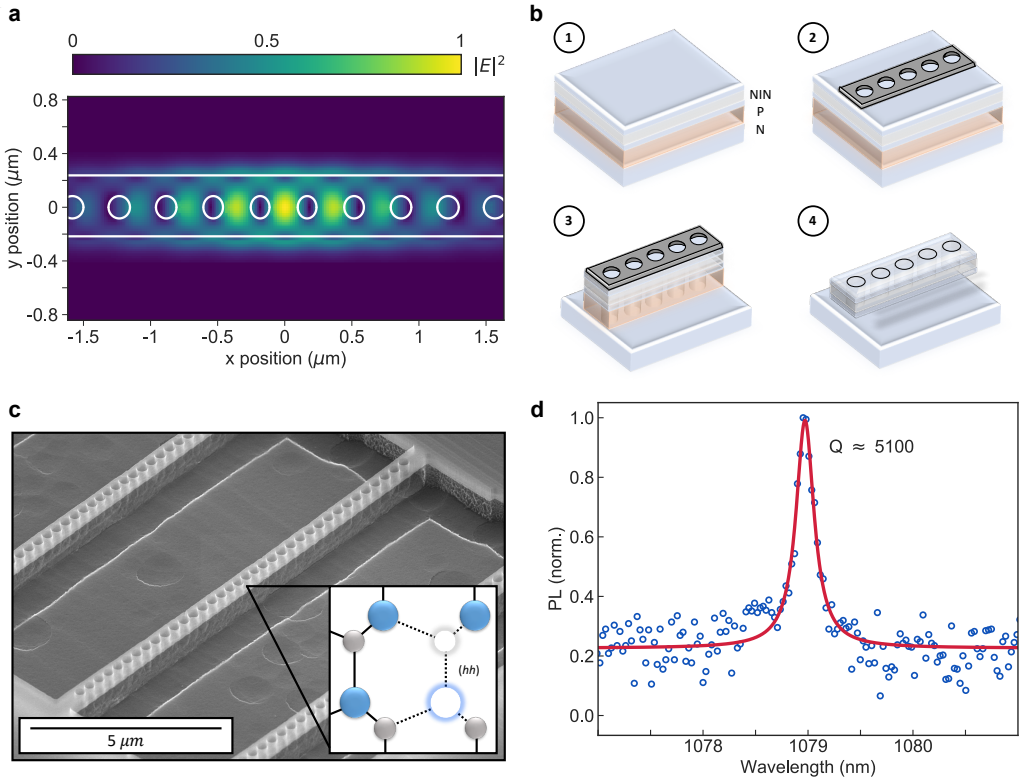

Figure 9.1: **Nanobeam photonic cavities in 4H silicon carbide.(a)** Simulation of nanobeam cavity mode performed with Lumerical FDTD, with a simulated quality factor of $Q \sim 3 \times 10^5$. **(b)** Outline of fabrication procedure. (1) A NINPN doped SiC chip is used as the starting material. (2) electron beam lithography defines a 25 nm thick nickel mask. (3) An SF6 based inductively coupled plasma (ICP) etch transfers the mask pattern to the SiC substrate. (4) A photoelectrochemical etch (PEC) selectively etches p-type SiC and creates an undercut structure. **(c)** Scanning electron microscope image of fabricated photonic crystal nanobeam cavities. Inset is a lattice representation of the (hh) VV^0. **(d)** Photoluminescence spectrum of a nanobeam cavity taken at room temperature, showing a quality factor of $\sim 5,100$ extracted from the full-width half-max of a Lorentzian fit.

9.1 Context

With the nanophotonic integration, a subsequent increase in the Debye-Waller factor from ∼5% to ∼70-75% is observed. The use of a doped nanostructure allows for the potential for electric field and charge control, *in-situ* Stark tuning, and improved collection efficiencies for optimized geometries, all of which would provide further improvements to the VV^0 optical properties. As a whole, this system advances the robustness of spin-to-photon transduction for the VV^0 in a technologically mature material. Looking beyond to many-qubit architec-

tures, photonic nanocavities will be a necessary component to maintain scalability across long-distance entanglement networks.

The spin coherences are short and the optical linewidths are broad in this initial demonstration, but a combination of surface treatment and depletion as in section 11.4 may drastically narrow these lines. Importantly, this work is the first single-defect photonics measurement and fabrication with VV^0 in 4H-SiC. The ability to use PEC etching is a valuable tool for SiC that leverages the ability to obtain doped epilayers of high quality. The ability to undercut structures is *the* determining feature for an easy-to fabricate photonic material. Other recent schemes such as SiCOI[57] may be promising, but direct comparisons have not been made to date. This technique creates a 'SOI' like wafer from bonding and thinning SiC utilizing the native oxide. Other techniques, such as a 'smart-cut' processes for creating membranes, results in *weak or no divacancy signal* because the procedure completely destroys the crystal (we have tried, avoid at all costs). Similarly, although 3C can be grown on silicon which can be easily undercut, there are unresolved materials issues (see section 4.1).

This experiment also displayed large strain in the nanostructures, likely due to rapid changes in the dopant concentration which is known to cause strain. The highly doped layers near the spin could be reduced from this experiment to produce narrower lines and lower strain. Larger photonic devices that have surfaces further away but a more moderate Purcell effect may balance the need for narrow lines while still retaining benefits from photonic enhancement. Finally, as SiC is an excellent photonic material, the potential for SiC nanophotonics is great. Other groups have demonstrated Q factors in excess of 630,000 with small mode volumes [184].

Chapter 10

Spins in Phononic Devices

This chapter and figures are adapted from the publication [9]

As mentioned in section 5.1, SiC is an excellent mechanical material with opportunities for linking spin and mechanics. That being said, the T_1 is quite long and the spin-strain coupling is weak. However, interesting physics and quantum control can be developed using *sound*, instead of magnetic fields.

Hybrid spin–mechanical systems provide a platform for integrating quantum registers and transducers. Efficient creation and control of such systems require a comprehensive understanding of the individual spin and mechanical components as well as their mutual interactions. Point defects in silicon carbide (SiC) offer long-lived, optically addressable spin registers in a wafer-scale material with low acoustic losses, making them natural candidates for integration with high-quality-factor mechanical resonators. Here, we show Gaussian focusing of a surface acoustic wave in SiC, characterized using a stroboscopic X-ray diffraction imaging technique, which delivers direct, strain amplitude information at nanoscale spatial resolution. Using *ab initio* calculations, we provide a more complete picture of spin–strain coupling for various defects in SiC with C_{3v} symmetry. This reveals the importance of shear strain for future device engineering and enhanced spin–mechanical coupling. We demonstrate all-optical detection of acoustic paramagnetic resonance without microwave magnetic

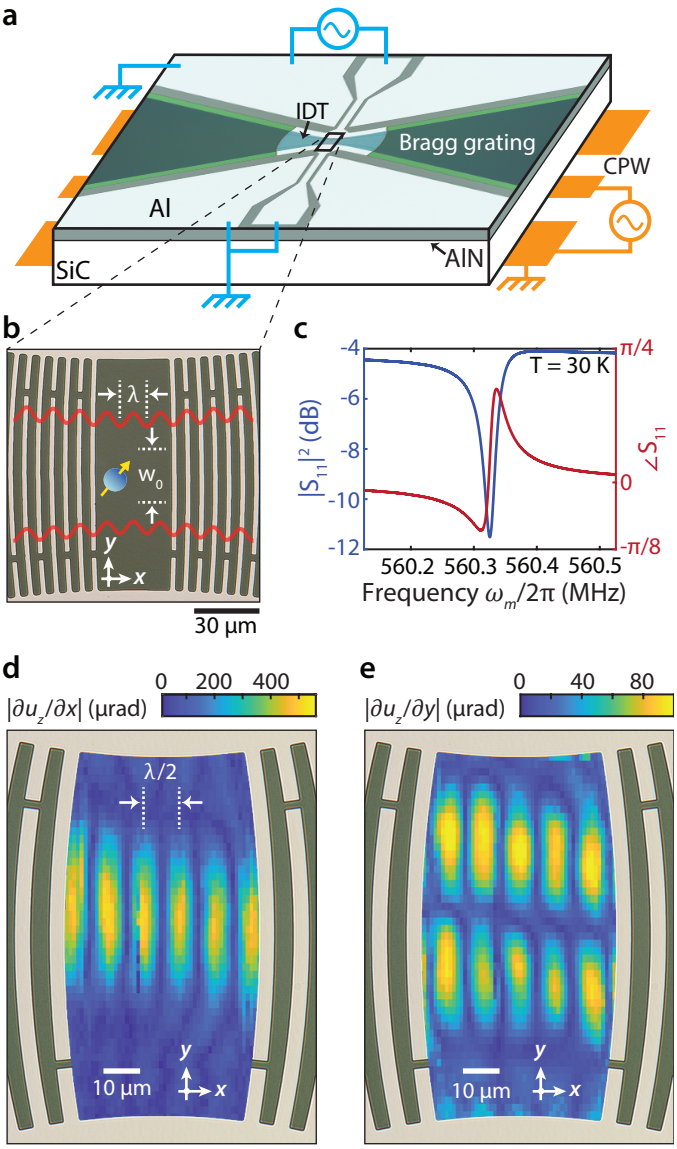

Figure 10.1: **Strain focusing with a Gaussian SAW resonator.a**, A schematic of the SAW device geometry fabricated on sputtered AlN on a 4H-SiC substrate. Microwaves drive spin transitions mechanically through the SAW resonator (cyan) and magnetically from the backside coplanar waveguide (orange). **b**, An optical micrograph of the Gaussian SAW resonator's acoustic focus ($\lambda = 12\mu m$, $w_0 = 2\lambda$) with red lines illustrating the wave's out-of-plane displacement (u_z). **c**, Magnitude (blue) and phase (red) measurements of the one-port reflection of the Gaussian SAW resonator used in spin experiments. **d,e**, The mechanical mode from a similar Gaussian SAW ($\lambda = 19\mu m$, $w_0 = 1.25\lambda$), directly measured with s-SXDM using the 4H-SiC [0004] Bragg peak. This quantifies the SAW peak-to-peak longitudinal (d) and transverse (e) lattice slopes at the acoustic beam waist. The image is skewed vertically due to sample drift during measurements.

fields, relevant for sensing applications. Finally, we show mechanically driven Autler–Townes splittings and magnetically forbidden Rabi oscillations. These results offer a basis for full strain control of three-level spin systems.

10.1 Context

Since a complete model of spin–strain coupling with C_{3v} symmetry requires six independent coupling parameters, strain cannot necessarily be treated as an equivalent electric field vector. Even so, the zero-field splitting tensor is also affected by electric fields with three independent coupling parameters and can be used for both $\Delta m_s = \pm 1$ and $\Delta m_s = \pm 2$ spin transitions. To further enhance defect–phonon interaction strengths for hybrid quantum systems, defect excited-state electronic orbitals [185, 186] and spins[187] could be utilized as opposed to ground-state spins[188], and strain effects on defect hyperfine couplings have not been well explored. In addition, new defects[152] with greater spin–spin or spin–orbit coupling, with minimal cost to their spin coherence, may greatly improve spin–phonon coupling strengths and be advantageous for quantum control of phonons with optically addressable spins. Our combined theoretical understanding and demonstrations of spin–strain coupling with SiC divacancies provides a basis for quantum sensing with MEMS[189] as well as engineering strong interactions with single phonons for quantum transduction[49], spin squeezing[190] and phonon cooling[191] applications. The coupling of strain to the VV^0 excited state is not known, but DFT calculations on the V_{Si} in SiC may guide future work [96].

Chapter 11

Spins in Electrical Devices

We finally begin the bulk of the experimental work for this thesis. We start by describing the first experiments on understanding charge states in ensembles of VV^0, then transition into how charge control allows for new forms of sensitive electrometry. Then, we describe how we can integrate single VV^0 into classical electronic devices (such as those described in section 1.1.2). This integration give interesting new control knobs, but importantly drastically improves the quality of the spin-photon interface in VV^0. This electrical control is extended to AC modulation of the optical structure which produces microwave-induced sidebands which will be described briefly. The integration of quantum states into electrical devices also opens opportunities for new quantum devices which will be motivated.

11.1 Optical Charge Switching

This section and figures are adapted from the publication [11]

Defects in silicon carbide (SiC) have emerged as a favorable platform for optically active spin-based quantum technologies. Spin qubits exist in specific charge states of these defects, where the ability to control these states can provide enhanced spin-dependent readout and long-term charge stability. We investigate this charge state control for two major spin qubits

in 4H-SiC, the divacancy and silicon vacancy, obtaining bidirectional optical charge conversion between the bright and dark states of these defects. We measure increased photoluminescence from divacancy ensembles by up to three orders of magnitude using near-ultraviolet excitation, depending on the substrate, and without degrading the electron spin coherence time. This charge conversion remains stable for hours at cryogenic temperatures, allowing spatial and persistent patterning of the charge state populations. We develop a comprehensive model of the defects and optical processes involved, offering a strong basis to improve material design and to develop quantum applications in SiC.

Overall, taking into account multiple impurities was necessary to obtain a complete picture of charge effects in the SiC samples; such considerations are crucial for tuning wafer growth techniques, samples with implanted layers, surface impurities or for devices with complex electric potentials. Finally, we confirmed that these optical charge conversions drastically improve the PL intensity and do not measurably impact the spin properties (ODMR, coherence). Combined with recent studies[55, 112] characterizing the spin and optical properties of VV or V_{Si} in 4H and 3C-SiC, this work on charge conversion/stabilization helps to complete the suite of techniques and technologies realized in NV^- centers in diamond for use in SiC, while allowing for novel applications such as optically controlling the charge of spins in electronic devices realized in SiC. This study will also be relevant to spin-to-charge conversion in SiC, though further work is necessary.

11.1.1 Context

This first work on the charge dynamics of defects in SiC showed that without the proper illumination color, ensembles of VV^0 completely convert to VV^-, which is optically 'dark' and does not contain the desirable spin properties. The charge state population can be read out by looking at the photoluminescence intensity from a short pulse (to avoid charge conversion and photodynamics from the laser). Importantly, by turning off the lasers and waiting, we found that the optically driven charge state populations were stable for over

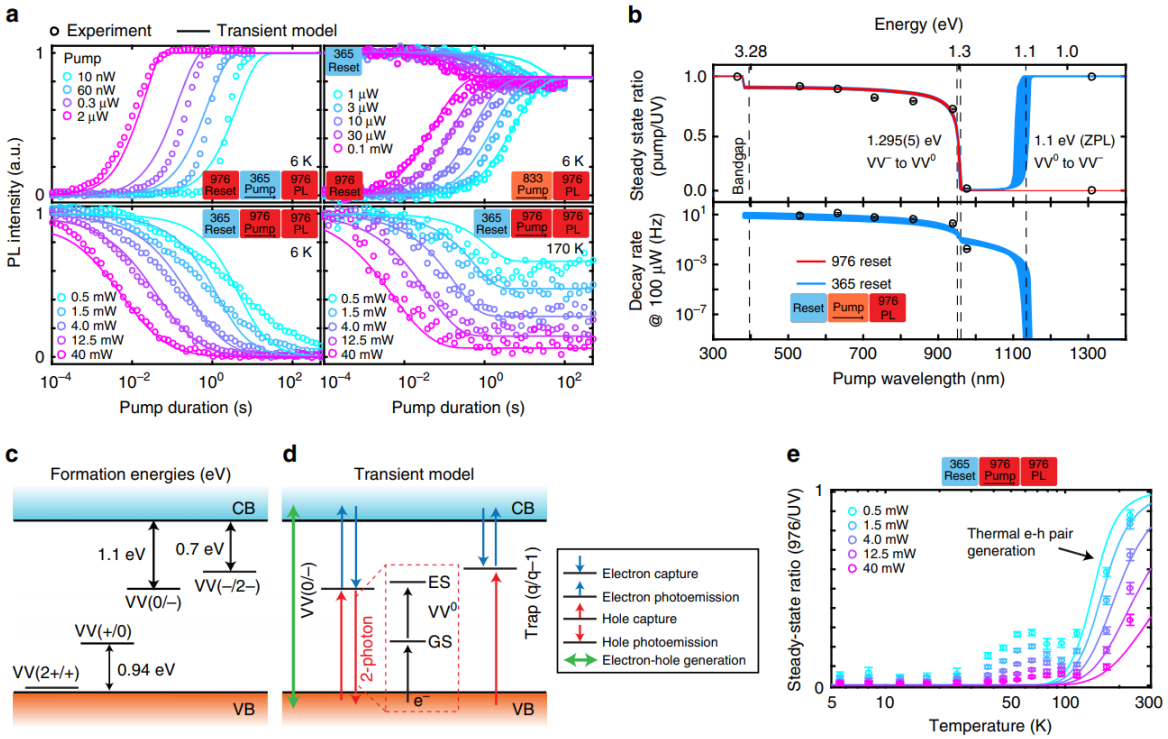

Figure 11.1: **Photo-dynamics and modeling in neutral divacancies in 4H-SiC.** The charge dynamics are probed using two and three color experiments, following a reset-pump-measure scheme. **a**, Typical decay curves obtained under various reset/pump wavelength and temperatures. The fit (line) is obtained from the model given in **d**. **b**, Top figure: ratio between pump and 365 nm steady-state PL intensities. Bottom figure: decay rates (normalized to 100 μW at every pump wavelength) obtained by fitting the decays in a with a stretched exponential function (error bars are 95% confidence intervals from the fit). In blue, the sequence starts after 365 nm pumping, while in red, after 976 nm. The lines are given by the model in **d**, with the area corresponding to 95% confidence intervals. For 1310 nm, no significant decay was observed over 100 s, hence the steady-state values are given without error bars. **c**, Formation energies of the divacancy in 4H SiC, taken from [61]. **d**, Model used for simulating all transients in **a, b, e,** including the VV^0 and VV levels of the divacancy, as well as an unknown trap with two charge states. Processes included in the model are given in the legend. Hole photo-emission converting VV^0 to VV^- involves a two-photon process, exciting VV^0 from its ground state to its excited state, followed by excitation and capture of an electron from the valence band. **e**, Temperature dependence of the steady state after 976 nm pumping (365 nm reset). Error bars are 95% confidence intervals from the decays' stretched exponential fit. Lines are given by the model in **d**, corresponding to thermal generation of electron-hole (e-h) pairs. The origin of the intermediate region between 30 and 100 K is unknown. Above 210 K, PL5 and PL6 signals become dominant, making the measurement unreliable as they are UV insensitive.

12 hours. This is expected given the low temperatures (4 K) and emphasizes that thermal dynamics are *not* at play. Interestingly, this work started largely as an accident of trying to

perform sensing on photoexcited carriers in a material on SiC which required UV excitation. Luckily, upon further investigation from other groups [62] and extensions to single defects [6](section 11.4), the major hypotheses in this work have been correct:

- 975 nm excitation photobleaches VV^0 into a 'dark' charge state of VV.
- VV^- is the dark charge state of VV^0. (which has a predicted but unobserved ZPL [192]).
- $VV^0 \rightarrow VV^-$ occurs through a two-photon process.
- Recovery of VV^0 can be achieved with $<\sim 930\ nm$ excitation, including UV (which re-establishes a quasi-equilibrium).
- Charge traps and other defects in the material play a dominant role in charge dynamics.

At the time (2017), there was an important discrepancy: ensembles of VV^0 photobleached drastically under 975 nm excitation, while single defect work had been using 975 nm excitation without issue. Furthermore, older samples of SiC had seemed to have less issues with photobleaching in ensembles. This turns out to be due to the last bullet point above, in that defect and charge trap densities in a particular sample play a large role in determining the exact balance of charges at play. Additionally, along the lines of the discussions in section 1.1.2, *electric fields* can alter this balance, which we will see in the following sections.

11.2 Charge Based Electrometry

This section and figures are adapted from the publication [4]

Sensing electric fields with high sensitivity, high spatial resolution, and at radio frequencies can be challenging to realize. Recently, point defects in silicon carbide have shown their ability to measure local electric fields by optical conversion of their charge state[193]. Here,

we report the combination of heterodyne detection with charge-based electric field sensing, solving many of the previous limitations of this technique. Owing to the nonlinear response of the charge conversion to electric fields, the application of a separate "pump" electric field results in a detection sensitivity as low as 1.1 (V/cm)/Hz, with a near-diffraction limited spatial resolution and tunable control of the sensor dynamic range. In addition, we show both incoherent and coherent heterodyne detection, allowing measurements of either unknown random fields or synchronized fields with higher sensitivities. Finally, we demonstrate in-plane vector measurements of the electric field by combining orthogonal pump electric fields. Overall, this work establishes charge-based measurements as highly relevant for solid-state defect sensing.

11.2.1 Context

The balance of charge states for VV under laser light that both ionizes and recharges the VV^0 is quite delicate. In initial demonstrations in SiC[193] this steady-state balance was shown to change with applied AC electric fields, where the magnitude of this effect is shown to be *quadratic* with electric field. In this work, we make use of this scaling and the fact that the electric field is a vector quantity. Therefore, a vector 'pump' electric field can be used to boost sensitivity along a particular direction ($E_{pump} \cdot E_{sensed} >> E^2_{sensed}$), for small sensed fields. In particular, the resulting sensitivities are competitive with use of the spin for electric field sensing. We estimate from the experimental acquisition time, signal, and noise intensity that our best sensitivity here is 1.1 $(V/cm)/\sqrt{Hz}$ for $E_{pump} = 750\ V/cm$ and a near diffraction-limited laser spot size (corresponding to an ensemble size of approximately 10^3–10^4 defects). This sensitivity can be compared with the spin-based measurement, where a sensitivity of 200 $(V/cm)/\sqrt{Hz}$ for a single defect was reached[194] or 0.1 $(V/cm)/\sqrt{Hz}$ for a very large ensemble ($\sim 10^{11}\ defects,\ > 50\ \mu m$ resolution)[195]. Since sensitivity is proportional to the square root of the number of defects (shot-noise limit), our charge-based technique is slightly more sensitive per defect than for single spins and more than two orders

of magnitude better for the ensemble. Surprisingly, because SiC is slightly piezoelectric, this effect can be used to sense AC strain fields as well[193].

The electric field dependence on the steady state balance of the VV^0 population under illumination can be understood in the context of the results in section 11.4. Roughly, because of space charge regions that can form under electric fields and charge redistribution, for DC fields under a certain strength no electric field is applied to the defect. The (photo-excited) charges redistribute to cancel out the applied field. This is sometimes called 'screening' the electric field. This is simply a statement that the effective dielectric constant is frequency dependent. The characteristic time to form a space-charge region that screens the electric field is the *Maxwell relaxation time* $\tau_M = \frac{1}{f_M} = \epsilon_0 \epsilon_r \rho / 2$ [196]. ρ is the resistivity, such that with a large photoexcited population of carriers, the region becomes conductive and τ_M can be *short*. This is also sometimes called *Debye relaxation*, relating to the Debye-Hückel model of the electric field screening. The quadratic dependence is a little harder to understand and is still an open question, but likely relates to the balance of rates, capture cross section radii and the size of the space charge region or the optical spot size. The devices in this work utilize basic electrodes on the surface of insulating SiC, where electric fields can modulate the charge states of defects under illumination.

11.3 Other Electrical Manipulations

Besides modulating the charge state balance of defects, electrical fields in SiC devices can Stark tune the optical fine structure, which has been achieved with similar devices on bulk insulating SiC [116]. Additionally, as discussed in section 5.3, electric fields can be used to drive spin manipulations with $\Delta m_s = 2$ transitions [98]. However, these demonstrations did not leverage the mature doping capability that SiC offers to make electrical devices. The next section describes this next step.

11.4 Electrical and Optical Control of Single Spins in Scalable Semiconductor Devices

This section and figures are adapted from the publication[6]

Spin defects in silicon carbide have the advantage of exceptional electron spin coherence combined with a near-infrared spin-photon interface, all in a material amenable to modern semiconductor fabrication. Leveraging these advantages, we integrate highly coherent single neutral divacancy spins in commercially available p-i-n structures and fabricate diodes to modulate the local electrical environment of the defects. These devices enable deterministic charge state control and broad Stark shift tuning exceeding 850 GHz. Surprisingly, we show that charge depletion results in a narrowing of the optical linewidths by over 50 fold, approaching the lifetime limit. These results demonstrate a method for mitigating the ubiquitous problem of spectral diffusion in solid-state emitters by engineering the electrical environment while utilizing classical semiconductor devices to control scalable spin-based quantum systems.

11.4.1 Introduction

Solid-state defects have enabled many proof-of-principle quantum technologies in quantum sensing [197], computation[198] and communications[152]. These defects exhibit atom-like transitions that have been used to generate spin-photon entanglement and high-fidelity single-shot readout[174], enabling demonstrations of long-distance quantum teleportation, entanglement distillation and loophole-free tests of Bell's inequalities[152].

However, fluctuating electric fields and uncontrolled charge dynamics have limited many of these technologies [122, 174, 197, 199, 200]. For example, lack of charge stability and of photon indistinguishability are major problems that reduce entanglement rates and fidelities in quantum communication experiments[122, 174, 199]. In particular, indistinguishable and

spectrally narrow photon emission is required in order to achieve high-contrast Hong-Ou-Mandel interference [143]. This indistinguishability has been achieved with some quantum emitters through dc Stark tuning the optical lines into mutual resonance[116, 201]. Meanwhile, a variety of strategies [113, 121–123, 197] have been proposed to reduce spectral diffusion[202] and blinking[203], but consistently achieving narrow and photostable spectral lines remains an outstanding challenge[120]. In addition, studies of charge dynamics[11, 204] have enabled quantum sensing improvements[197, 205], and spin-to-charge conversion[177] allowing electrical readout of single spin defects[206]. However, these experiments have largely been realized in materials such as diamond where scalable nanofabrication and doping techniques are difficult to achieve.

In contrast, the neutral divacancy (VV^0) defect in silicon carbide (SiC) presents itself as a candidate spin qubit in a technologically mature host, allowing for flexible fabrication, doping control, and availability on the wafer scale. These defects display many attractive properties including all-optical spin initialization and readout[82], long coherence times[90], nuclear spin control[181], as well as a near-infrared high-fidelity spin-photon interface[55]. However, VV^0 have suffered from relatively broad optical lines[55], charge instability[11] and relatively small Stark shifts[116]. Furthermore, the promise of integration into classical semiconducting devices remains largely unexplored. Here, we utilize the mature semiconductor technology that SiC provides to create a p-i-n structure that allows tuning of the electric field and charge environment of the defect. First, we isolate and perform high fidelity control on highly coherent single spins in the device. We then show that these devices enable wide dc Stark tuning while maintaining defect symmetry. Interestingly, we also demonstrate that charge depletion in the device mitigates spectral diffusion thus greatly narrowing the linewidths in the optical fine structure. Finally, we use this device as a testbed to study the photoionization dynamics of single VV^0, resulting in a method for deterministic optical control of the defect charge state. The effects presented here suggest that doped SiC structures are flexible and scalable quantum platforms hosting long-lived single spin qubits with an electrically-tunable

high-quality optical interface. The demonstrated reduction in electric field noise can lead to increased spin coherence[207], electrical tuning of 'dark' spins in quantum sensing[208], whereas charge control could extend the memory time of nuclear spins[209]. Additionally, this platform opens unique avenues for spin-to-charge conversion, electrically-driven single photon emission[210], electrical control[98] and readout[206, 211, 212] of single spins in SiC CMOS compatible and optoelectronic semiconductor devices.

11.4.2 Isolated Single Defects in a Semiconductor Device

We first isolate and control single VV^0 in a 4H-SiC p-i-n diode created through commercial growth of doped SiC epilayers. After growth, we electron irradiate and anneal our samples to create single, isolated VV^0 defects. We fabricate microwave striplines and Ohmic contact pads allowing for spin manipulation and electrical gating (Fig. 11.2A) (appendix A). In contrast to other defects in SiC such as the isolated silicon vacancy[92], the divacancy is stable above 1600 $^{\circ}C$ [79] making it compatible with device processing and high temperature annealing to form *Ohmic contacts*. Spatial photoluminescence (PL) scans of the device show isolated emitters corresponding to single VV^0 (Fig. 11.2B), as confirmed by second-order correlation ($g^{(2)}$) measurements (Fig. 11.2B, inset)(appendix A). The location in depth of the observed defects is consistent with isolation to the i-type layer. This is to be expected because formation energy calculations[192] indicate that the neutral charge state is energetically favorable when the Fermi level is between ∼1.1 eV to 2 eV and this condition must be satisfied somewhere in the i-layer [213](appendix A). This depth localization provides an alternative to delta-doping[214], which is not possible with intrinsic defects, facilitating positioning and control in fabricated devices (Fig. SA.1). Additionally, owing to the diode's highly rectifying behavior at low temperature, large reverse biases are possible with low current (Fig. 11.2C)(appendix A). Sweeping the frequency of a narrow-line laser, we obtain photoluminescence excitation (PLE) spectra of the optical fine structure of these single defects (Fig. 11.2D). Using the observed transitions for resonant readout and prepa-

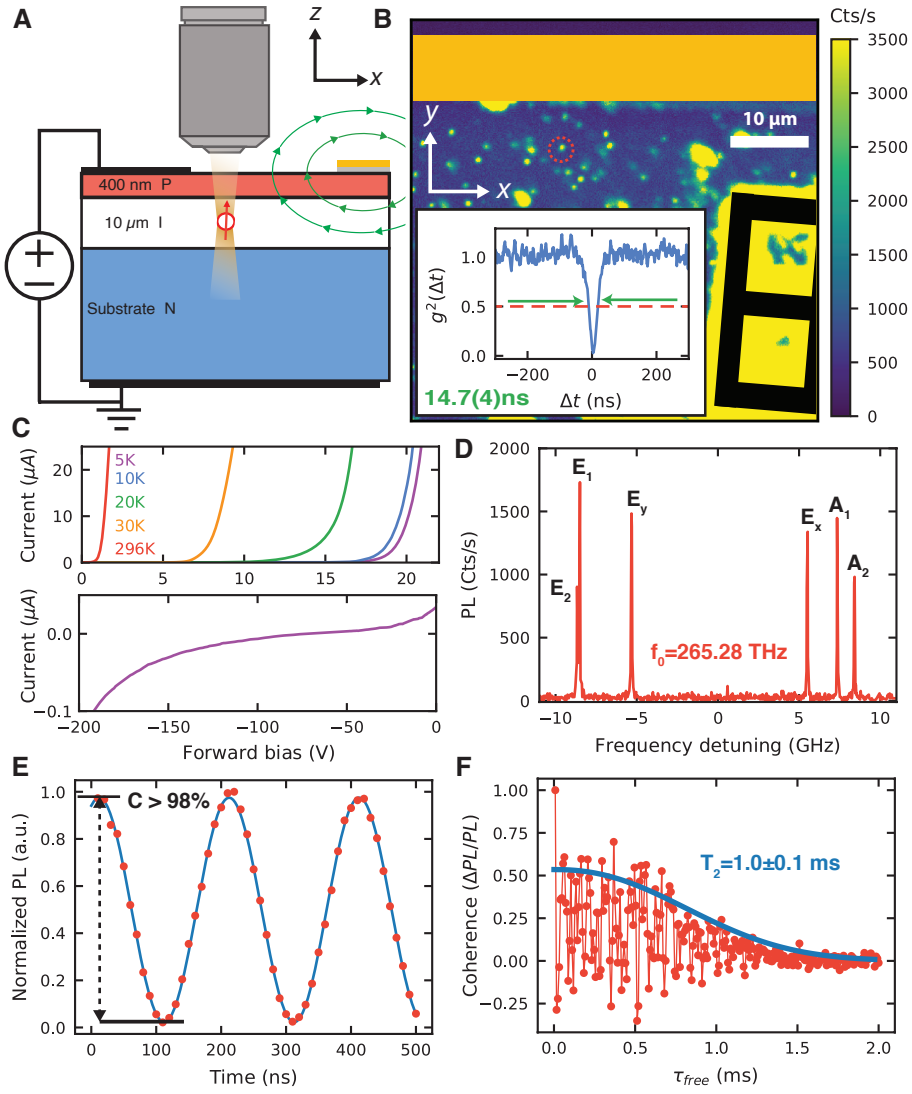

Figure 11.2: **Isolation of single VV^0 in a commercially grown semiconductor device.** **(A)** Schematic of the device geometry. **(B)** Spatial photoluminescence (PL) scan of an example device, showing isolated emitters (example circled in red) confirmed by autocorrelation (inset) showing $g^2(0) < 0.5$ (red line). Extracted emitter lifetime is 14.7 ± 0.4 ns (green arrows). Gate and microwave stripline features are drawn and color coded as in (A). **(C)** Top: I-V curves of the device at various temperatures; bottom: low temperature reverse bias behavior. **(D)** Photoluminescence excitation (PLE) spectrum of a single (kk) divacancy at 270 V of reverse bias.**(E)** Optically detected Rabi oscillations of a single (kk) VV^0 with >98% contrast (fit in blue) using resonant initialization and readout. **(F)** Hahn-echo decay of a single (kk) VV^0 in the diode. Rabi, Hahn and g^2 data are taken at 270 V of reverse bias and at approximately 240 Gauss at T=5 K.

ration, we perform high-contrast Rabi oscillations of isolated VV^0 in the p-i-n structure (Fig. 11.2E)(appendix A). The contrast exceeds 98%, improving on previous demonstra-

tions through the use of resonant spin polarization[55]. Additionally, a single spin Hahn-echo decay time of $1.0 \pm 0.1\ ms$ is measured for spins in the device (Fig. 11.2F), consistent with previous ensemble measurements[90]. The long Hahn-echo times and high-fidelity control demonstrate that integration into semiconductor structures does not degrade the spin properties of VV^0. This isolation and control of highly coherent spin qubits achieved in these functioning semiconductor devices unlocks the potential for integration with a wide range of classical electronic technologies.

11.4.3 Large Stark Shifts in a p-i-n Diode

Because the (hh) and (kk) divacancies(appendix A) in SiC are nominally symmetric along the c-axis (growth axis), the geometry of the diode allows for large electric fields which mostly conserve the symmetry of the defect. Therefore, wide tuning of the VV^0 optical structure is possible, while reducing unwanted mixing from transverse or symmetry-breaking components of the excited state Hamiltonian[55, 86, 201]. Because the i-type region can be relatively thin (10 μm here), the applied voltage is dropped over a much smaller region than if a bulk sample were used[116], leading to significantly larger Stark shifts for a given applied voltage. In principle, this region can be reduced to a thickness that exceeds limitations from optical access with metal planar gates (limited by the optical spot size of $\sim\ 1\mu m$). Furthermore, it is possible to use doped layers as *in situ* transparent native contacts to Stark tune and control localized defects in suspended photonic or phononic structures[9] enabling complex hybrid electrical, photonic and phononic devices. In our p-i-n junction device, we apply up to 420 V in reverse bias. Our results show Stark tuning of several hundreds of GHz on different defects of the same type and on inequivalent lattice sites where the Stark shift is between 0.4-3.5 GHz/V after a threshold is passed (Fig. 11.3A). For example, we observe a (hh) divacancy shifted by more than 850 GHz (2.5 meV) at a reverse bias of 420 V and a (kh) divacancy shifted by more than 760 GHz at a reverse bias of 210 V (Fig. 11.3B). These shifts are among the largest reported for any single spin defect to date and were only limited by the voltage

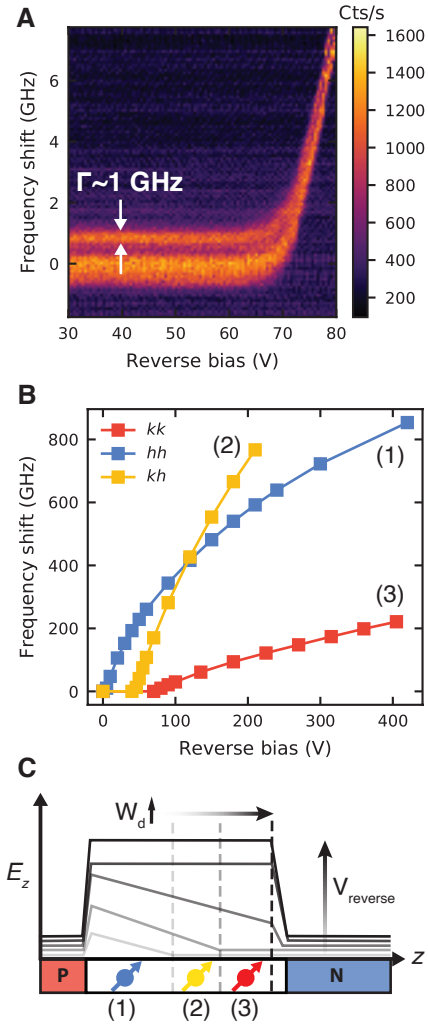

Figure 11.3: **Stark shifts in p-i-n diode. (A)** Low field Stark tuning of a single (kk) defect at T=5 K, showing a turn-on behavior for the Stark shifts and narrowing with voltage. This threshold is the same as in 11.5A. These scans contain the lower branch (E_1, E_2, E_y) where the linewidth of E_y is approximately 1 GHz and E_1 and E_2 are unresolved. The PLE lines show no shifting down to zero bias. **(B)** High field Stark shifts of multiple example defects (located at various depths and positions in the junction), showing >100 GHz shifts. **(C)** Schematic electric field distribution and depletion region width (W_d) in the diode for increasing reverse bias. Location in the junction can determine the local field experienced by the defects in (B). The error bars in (B) are smaller than the point size. All data was obtained at T=5 K.

output of our source. We expect that owing to the high dielectric breakdown field of SiC, even higher shifts of a few THz are possible (appendix A). The high-field limit of these shifts correspond to estimated dipole moments ($d_{\|}$) of 11 GHz m/MV and 4.5 GHz m/MV for (hh) and (kk) divacancies respectively, consistent with previous reports[7, 116]. For the (kh) basal

divacancy observed, the estimated transverse dipole moment is around $d_{\perp}$= 35 GHz m/MV. Furthermore, because the Stark shift represents a measure of the local electric field, we conclude that negligible field is applied to the VV^0 before a certain threshold voltage where the depletion region reaches the defect[215]. This results from non-uniform electric fields in the diode caused by residual n-type dopants in the intrinsic region (Fig. 11.3C, (appendix A)). Overall, our system could be used as a widely frequency-tunable, spectrally narrow source of single photons. In particular, our system enables one of the highest Stark shift to linewidth ratios ($> 40,000$) obtained in any solid-state single photon source (Table A.2). These characteristics make this system ideally suited for tuning remote defects into mutual resonance and for frequency multiplexing of entanglement channels[216]. Interestingly, the tunability range is so wide that it could even enable the tuning of a (hh) divacancy into resonance with a (kk) divacancy, allowing for interference and entanglement between different species of defects. This wide tunability stems from the rectification behavior of the diode which allows large electric fields without driving appreciable currents, which can degrade spin and optical properties. Furthermore, the observed sensitivity of the optical structure of single VV^0 defects could serve as a nanoscale electric field sensor enabling field mapping in these working devices with sensitivities of approximately 100 $(V/m)/\sqrt{Hz}$ or better, which is competitive with state of the art spin and charge based electrometry techniques [194, 217, 218](appendix A).

11.4.4 Reducing Spectral Diffusion Using Charge Depletion

Uncontrolled fluctuating electrical environments are a common problem in spin systems where they can cause dephasing[207], as well as in quantum emitters where they result in spectral diffusion of the optical structure and lead to large inhomogeneous broadening. For example, adding and removing just a single electron charge 100 nm away causes shifts on the order of 100 MHz for the optical fine structure of VV^0 (Fig. A.3). Previous work[55] has shown that by doing an exhaustive search through many defects in a specially grown

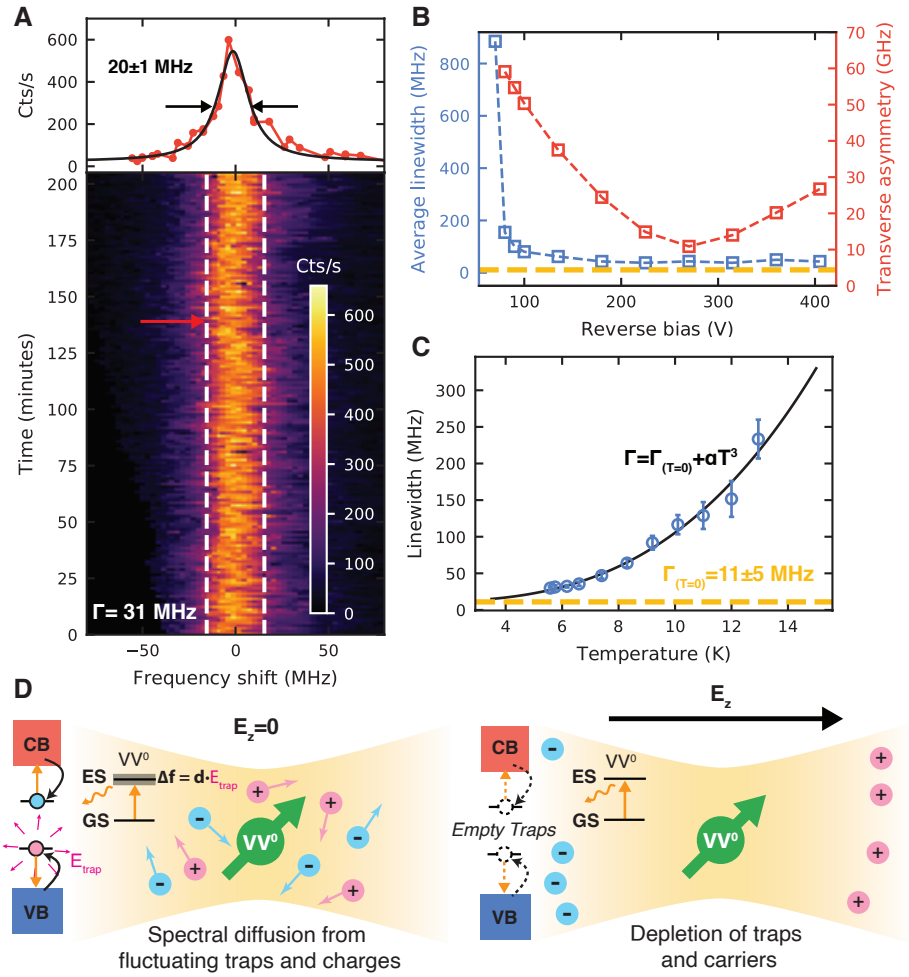

Figure 11.4: **Optical linewidth narrowing by tuning the electrical environment of a solid state emitter.** **(A)** Multiple PLE sweeps taken over 3.5 hours of the E_x line, showing small residual spectral diffusion (fitted inhomogeneous linewidth of 31 ± 0.4 MHz). The red arrow corresponds to the single scan shown with a fitted linewidth of ≈ 20 MHz. **(B)** Comparison of the average linewidth (blue) and defect transverse asymmetry (red) with respect to applied reverse bias. The yellow line is the lifetime limit. **(C)** Temperature dependence of the linewidth. A free power law fit gives an exponent of 3.2 ± 0.3. Constraining the fit to a T^3 relation, we extract a zero temperature linewidth of 11 ± 5 MHz (yellow line). Errors on the plot represent a 95% confidence interval. **(D)** Model for the effect of charge depletion on spectral diffusion in the illuminated volume (yellow). To the left of each diagram is a schematic band diagram with the relevant transitions. Errors for the fits values in (A) and (C) represent one standard deviation. All data is from a single (kk) VV^0. In (B), the laser power is slightly higher than in (A), causing some broadening. For (A) and (C) the E_x line is shown at 270 V of reverse bias. Data in (A) and (B) were obtained at T=5 K.

material, one can find defects with lines as narrow as 80 MHz (typically 100-200 MHz or larger), however, this is still much larger than the Fourier lifetime-limit of ∼11 MHz[55]. In

bulk intrinsic commercial material, the narrowest linewidths are significantly broadened to around or above 130-200 MHz[55] (Fig. A.4). Overall, spectral diffusion has been a notoriously difficult outstanding challenge for nearly all quantum emitters in the solid-state. Here, we introduce a technique for mitigating spectral diffusion. We demonstrate that by applying electric fields in our device we deplete the charge environment of our defect and obtain single scan linewidths of 20 ± 1 MHz (Fig. 11.4A) without the need for an exhaustive search. This reduction in PLE linewidth has a different voltage dependence than the transverse asymmetry in the defect, thus eliminating reduced mixing as a possible mechanism for narrowing (Fig. 11.4B). The temperature dependence of the linewidth is roughly consistent with a T^3 scaling at these low temperatures[219](fitted exponent 3.2 ± 0.3 and a zero-temperature linewidth of 11 ± 5 MHz, appendix A). Although the dominant temperature scaling may change at lower temperature, this trend hints at a possible explanation for the remaining broadening and is consistent with a temperature limited linewidth. Furthermore, the observed line is extremely stable, with a fitted inhomogeneous broadening of 31 ± 0.4 MHz averaged for over 3 hours (Fig 11.4A). This stability over time, narrowness, tunability, and photostability demonstrate the effectiveness of engineering the charge environment with doped semiconductor structures for creating ideal and indistinguishable quantum emitters. At zero bias the linewidth in our samples is much higher than in bulk material (around 1 GHz, Fig. 11.3A). We attribute this to a greater presence of traps and free carriers (under illumination). Thus, in these samples, the observed narrowing corresponds to an improvement in the linewidth by a factor of more than 50. We speculate that a combination of this charge depletion technique with lower sample temperatures, a lower impurity material, and further annealing could enable measurement of consistent transform-limited linewidths[10, 121]. This use of charge depletion for creating spectrally narrow optical interfaces (Fig. 11.4D) could be widely applicable to other experiments in SiC, or to other solid-state emitters such as quantum dots[220, 221]. Indeed, by applying the same techniques developed here to intrinsic SiC materials, lines as narrow as $\sim$ 21 MHz are observed[7]. Crucially, these results demonstrate that depleting

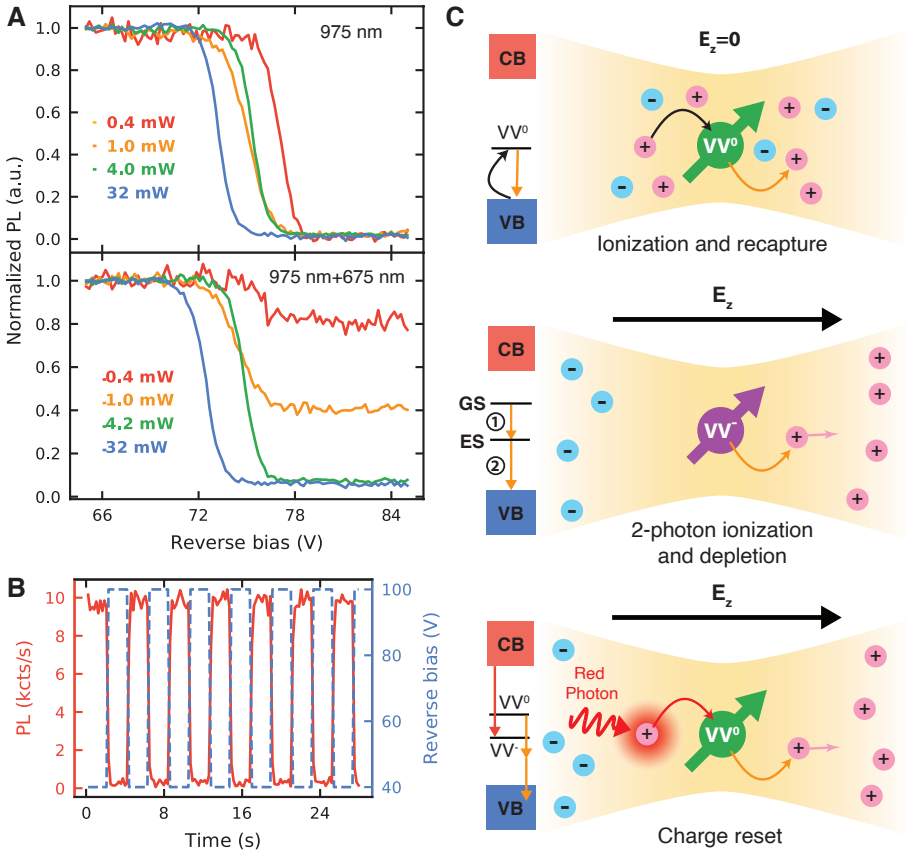

Figure 11.5: **Electrical and optical charge control of a single VV^0.** **(A)** Voltage and power dependence of the photoluminescence of a single (kk) VV^0 with 975 nm excitation (top), and with additional 188 μW of 675 nm illumination (bottom), showing a sharp threshold under reverse bias. With high 975 nm power, the two-photon ionization process dominates and the PL signal is low. **(B)** By controlling the voltage in time (blue) the emission from the single (kk) defect is switched on and off (red). **(C)** Model of rapid ionization and recapture at zero electric field (top). Two photon ionization and formation of a depletion region under reverse bias (middle). Charge reset under applied electric field using red light (bottom). All data was obtained at T=5 K.

local charge environments can transform a very noisy electric environment into a clean one, turning materials containing unwanted impurities into ideal hosts for quantum emitters.

11.4.5 Charge Gating and Photodynamics of Single Defects

Our observation of large Stark shifts and linewidth narrowing relies on understanding and controlling charge dynamics under electric fields. To achieve this, we study the stability of the observed single defects under electrical bias. This allows a careful investigation of the

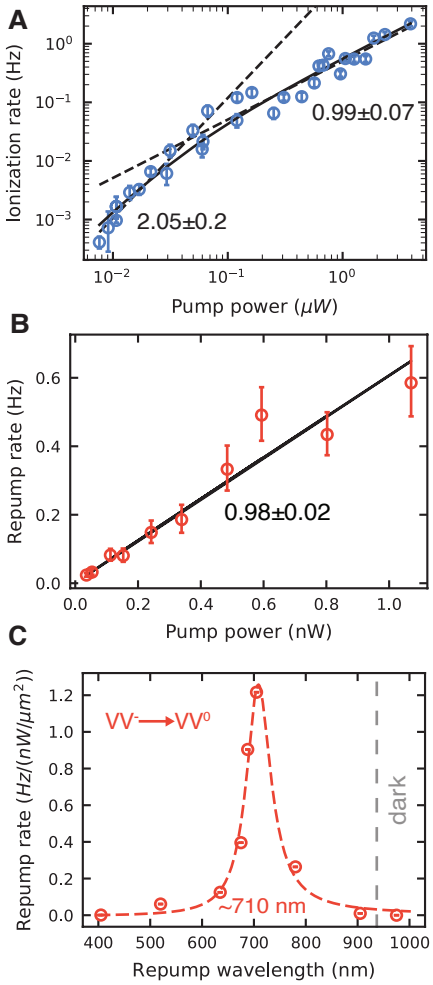

Figure 11.6: **Ionization and charge reset rates for VV^0.** **(A)** Dependence of the ionization rate on resonant laser power. Low and high power regime fits (black dotted lines) and their power laws ($m = 2.05 \pm 0.2$ and $m = 0.99 \pm 0.07$, respectively). The solid black line shows a full model fit. **(B)** Repump power dependence of the 688 nm laser, showing a linear exponent of $m = 0.98 \pm 0.2$. Fluctuations in the polarization or power of the laser limits the true error. (A) and (B) were taken at 90 V of reverse bias. **(C)** Repumping rate as a function of illumination wavelength at 270 V of reverse bias with a Lorentzian fit centered around 710 nm. With wavelengths longer than 905 nm (and at these powers) no PL is observed and the defect is 'dark'. All error bars represent 95% confidence intervals from the fit of the raw data from a single (kk) VV^0. All data was obtained at T=5 K.

charge dynamics of single VV^0 under illumination, from which we develop an efficient charge reset protocol. In our experiments, we observe that with 975 nm off-resonant light, the photoluminescence (PL) drops dramatically once the reverse bias is increased past a threshold voltage (Fig. 11.5A). This threshold varies between defects, which is expected given dif-

ferences in the local electric field experienced stemming from variations in position, depth, and local charge trap density. We attribute the PL reduction to photoionization to an optically 'dark' charge state[11]. We use this effect to create an electrically gated single photon source[222–224], where emission is modulated in time with a gate voltage (Fig. 11.5B)[116]. The threshold voltage has a slight hysteresis (Fig. A.5) and laser power dependence (Fig. 11.5A) suggesting that trapped charges may play a role[201, 225]. We note that the electric field dependence of the photoionization could also be used to extend sensitive electrometry techniques[193] to the single defect regime, while controlled ionization of the spin can extend the coherence of nuclear registers[209]. The threshold for Stark shifts (Fig. 11.3A) corresponds approximately to the same voltage where significant photobleaching occurs when using off-resonant excitation. This links the sharp photoionization threshold in Fig. 11.5A to the presence of moderate electric fields and the onset of carrier depletion. A possible explanation for this voltage-dependent PL is that at zero electric field, illumination constantly photoionizes the VV^0 and other nearby traps. However, the divacancy rapidly captures available free carriers returning it to the neutral charge state. Under applied field, carrier drift depletes the illuminated region of charges. Thus, when a VV^0 photoionization event occurs in this depleted environment, no charges are available for fast recapture, resulting in a long-lived dark state (Fig. 11.5C). Past works have shown that PL is enhanced in ensembles by repumping the charge with higher energy laser colors[11, 62, 226]. We extend this work to the single defect regime by applying various illumination energies and studying single defect photodynamics at 90 V of reverse bias (past the threshold voltage of approximately 75 V of reverse bias for this defect). We observe under resonant illumination the PL quickly drops to zero and does not recover, indicating that 1131 nm (1.09 eV) light (resonant with the ZPL of a (kk) VV^0) ionizes the defect, but does not reset the charge state. However, after applying higher energy light (688 nm, for example) the charge is returned to a bright state even with < 1 nW of applied power. This 'repump' of the defect charge state is vital for restoring PL for ionized or charge unstable VV^0 in SiC (Fig. 11.5A) and is essential to observe the effects

discussed in the previous sections (Fig. 11.5C). When both NIR resonant (1131 nm) and red (688 nm, 1.8 eV) light is applied to the defect, hopping between the bright (VV^0) and dark (VV^+ or VV^-) charge states results in a blinking behavior. From this blinking (Fig. A.6), we can extract photoionization and repumping rates of the defect[127]. We first examine the ionization rate of a single VV^0 (Fig. 11.6A) and observe that the power dependence is quadratic below defect saturation (exponent $m = 2.05 \pm 0.2$) and linear at higher powers ($m = 0.99 \pm 0.07$). We note that our observed data provide evidence for a two-photon process to VV^- (appendix A) suggested in previous ensemble studies[11, 62], and are less consistent with a recently proposed three-photon model converting to VV^+ [192, 226]. Thus, we conclude that the dark state caused by NIR resonant excitation is VV^-. Further study of the spin dependence of this ionization may lead to the demonstration of spin-to-charge conversion in VV^0. Similarly, we study the charge reset kinetics by varying the power of the repumping laser. We find a near-linear power law with $m = 0.98 \pm 0.05$ (Fig. 11.6B). This linear dependence of the repumping rate can be described by two potential models. One possibility is that the dark charge state is directly one-photon ionized by repump laser. The other possible explanation is that nearby traps are photoionized by this color and the freed charges are captured by the divacancy to convert back to the bright state. By varying the color of this reset laser, we find repumping to be most efficient around 710 nm (1.75 eV), suggesting a particular trap state energy or a possible defect absorption resonance[94, 206] (Fig. 11.6C). Overall, we observe negligible ionization from the optimal red repump laser and no observable reset rate from the resonant laser. This results in fully deterministic optical control of the defect charge state (discussion in appendix A), allowing for high-fidelity charge state initialization for quantum sensing and communications protocols.

11.4.6 Conclusions and Outlook

The electrical tuning of the environment demonstrated here constitutes a general method that could be applicable to various quantum emitters in semiconductors where spectral

diffusion or charge stability is an issue[227], or where electric field fluctuations limit spin coherence[207](appendix A). Furthermore, using our p-i-n diode as a testbed to study charge dynamics, we develop a technique to perform deterministic optical control of the charge state of single divacancies under electric fields[228]. The techniques presented will be vital to achieving single-shot readout and entanglement in VV^0 by enabling charge control and enhancing photon indistinguishability, suggesting doped semiconductor structures as ideal quantum platforms for defects. This work also enables high-sensitivity measurement of nanoscale electric fields and charge distributions in working devices[217] and facilitates spin-to-charge conversion[177] for enhanced quantum sensing and electrical readout protocols[206]. Finally, the introduction of VV^0 into classical SiC semiconductor devices such as diodes, MOSFETs and APDs may enable the next generation of quantum devices.

11.4.7 Charge Dynamics

Here, we will summarize briefly the charge dynamics at play in SiC and the corresponding energies. These are displayed mostly in Fig. 11.7.

- ($1.1\ eV < E < 1.3\ eV$). VV^0 can be excited on its phonon sideband. In the exited state, $VV^0 \rightarrow VV^-$ occurs constituting a two-photon ionization process. The rate of this second step may have a resonance in the band as in Fig. 11.7B. The common excitation in this range is 975 nm.

- ($1.3\ eV < E <\sim 1.6\ eV$). VV^0 is excited, though more weakly on the tail of the sideband. Two-photon ionization still occurs, $VV^0 \rightarrow VV^-$. However, $VV^- \rightarrow VV^0$ proceeds as a one photon process and recharges the defect. The common excitation in this range is 905 nm which produces ODMR and PL while maintaining some charge stability over time.

- ($E \sim 1.75\ eV$). Too far to the visible to excite VV^0 directly. However, a possible resonance in the band (Fig. 11.7B) makes $VV^- \rightarrow VV^0$ very effective. Too low

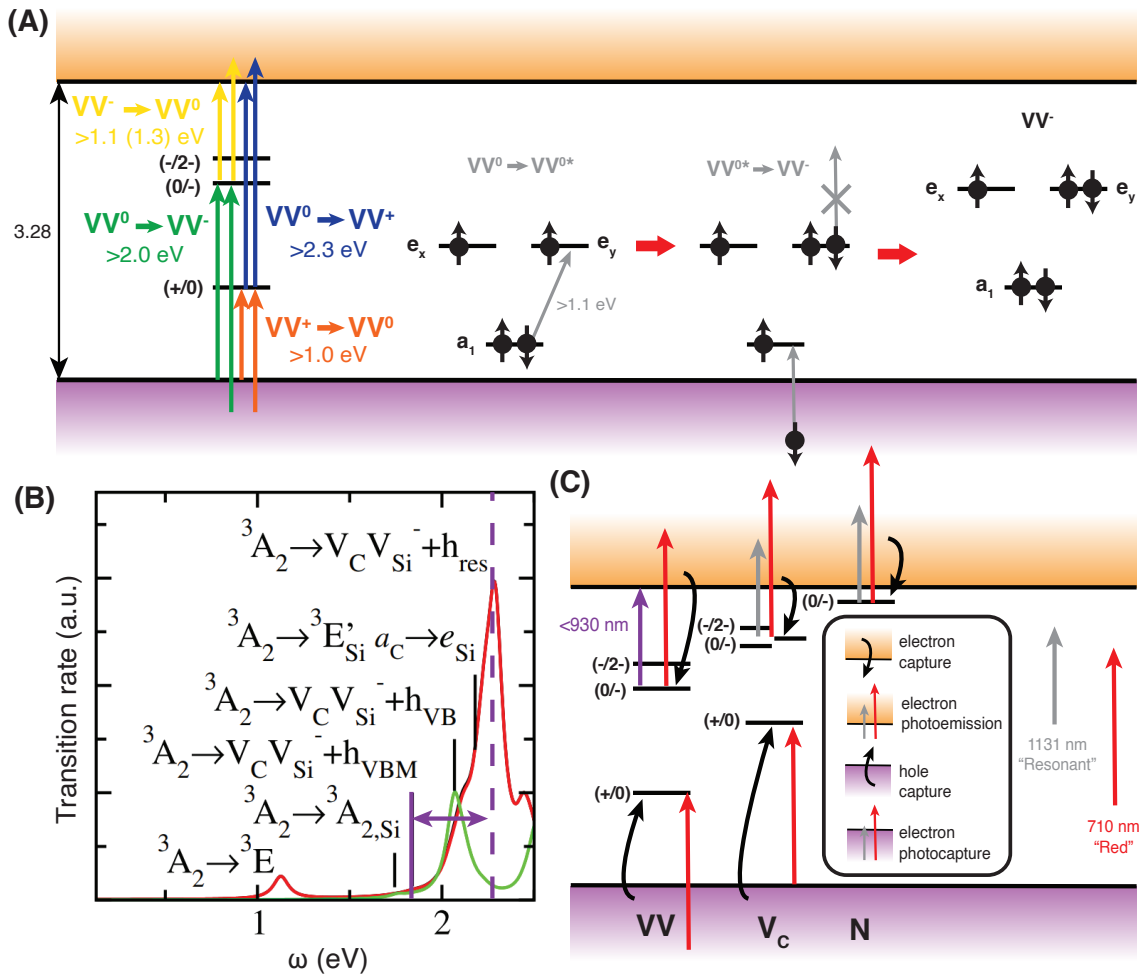

Figure 11.7: **Charge photodynamics in SiC. (A)** (left) The relevant photoemission and photocapture transitions for VV are shown and color coded. The values are obtained through DFT and the experimental $VV^- \rightarrow VV^0$ energy is given in parentheses. (right) The two-photon ionization process for VV^0 in the single particle orbital picture. **(B)** Example ionization transition rates from the VV^0 ground state (adapted from [94]), showing an offset between the transition onset and the energy for maximal rate (purple). Similar calculations can be used to validate the "red" optimal point for $VV^- \rightarrow VV^0$ in Fig. 11.6. **(C)** Photo-assisted and capture processes available for VV and the major impurities in SiC given the laser colors at play. Under depletion, there are no free carriers to be captured and photoexcited carriers get swept away. At zero bias all these processes happen creating a complex quasi-equilibrium.

energy for $VV^0 \rightarrow VV^-$ by a one photon process. The ideal charge reset color (710 nm, for example).

- ($E \sim 1.1\ eV$). Resonant light (for the c-axis VV^0). Two-photon ionization occurs,

though due to the lower needed power, it is slower than with off resonant.

- ($E < 1.1\ eV$). At low temperatures, no light is absorbed by VV^0. However, once in the excited state, $VV^0 \rightarrow VV^-$ may proceed at these wavelengths, though not much below 1 eV.

- ($E > 2\ eV$). $VV^0 \rightarrow VV^-$ occurs readily through a one-photon process. $VV^- \rightarrow VV^0$ as well.

However, at all of these wavelengths, the very shallow nitrogen dopants can be excited, and at high enough powers most of the deep ones as well. This causes spectral diffusion of the optical interface. Without depletion, a balance of ionization and recapture of VV^0 and the surrounding defects may make obscure the VV^0 dynamics given above.

In the original WKV criteria, a consideration for the charge state stability of the defect is made (# 4, section 5.2). This criteria is probably insufficient. Here, we describe new criteria that optimize charge stability and spectral diffusion:

- the defect's ZPL energy should be *lower* than the energy needed to change the charge state of the defect (at least at the one photon level).

- the defect's correct charge state should be recoverable without detrimental dynamics.

- for a given ZPL, the dominant traps should *not* be photoexcited.

- the defect's ZPL energy should be ideally *less than half the bandgap.*

11.5 Context

The p-i-n diode is one of the most basic electronic devices. However, by simply integrating our spin qubit into this device, we drastically improve the quality of single-photon emission from our defect spin. The idea of using devices to 'clean up' the environment of an emitter using classical semiconductor depletion is a new one, and has broad implications for other

qubit candidates with spin-photon interfaces like quantum dots, where similar ideas have been evolving[229]. We also gain the ability to drastically tune our spin photon interface while maintaining its narrowness, *and conserving the symmetry* of the defect's orbital fine structure which therefore maintains its quality. As such, we maintain a high degree of tunability without unwanted sensitivity or degradation. Defects integrated in devices such as these may therefore provide ideal nodes in quantum communications channels. The extension of this work into improving the notorious problem of spectral diffusion in nanophotonics would drastically improve the outlook for quantum networking devices with SiC. Importantly, the devices in this section still 'work' at 4 K, even though the p- and n-type dopants are nominally frozen out. Low temperature p- and n-doping can behave well if the semiconductor is *degenerately doped*, where the doping level is so high that the charges can hop site to site and the dopants form an 'impurity band' where charges can flow without thermal activation. This has been achieved in SiC (but not in this work) and is an interesting avenue for devices in the future. However, even without this degenerate doping, the electrical potentials are still spread over the p and n-type layers, and the depletion can proceed even at these low temperatures (with the help of photoionization/laser light causing a high 'electron temperature'). An understanding of how the depletion region moves the intrinsic region (which is slightly n-type) is crucial to understand both the photostability, Stark shifting and narrowing. Roughly, the electric field at a defect can start by not shifting at all with increased voltage, transitioning into a $E \propto \sqrt{V}$ regime where the intrinsic region is not fully depleted, then finally reaching a linear regime where $E \propto V$. This is the schematic shown in Fig. 11.3C.

11.6 Extensions of Stark Control

This section is adapted from the publication[7]

Interfacing solid-state defect electron spins to other quantum systems is an ongoing chal-

lenge. The ground-state spin's weak coupling to its environment not only bestows excellent coherence properties but also limits desired drive fields. The excited-state orbitals of these electrons, however, can exhibit stronger coupling to phononic and electric fields. Here, we demonstrate electrically driven coherent quantum interference in the optical transition of single, basally oriented divacancies in commercially available 4H silicon carbide. By applying microwave frequency electric fields, we coherently drive the divacancy's excited-state orbitals and induce Landau-Zener-Stückelberg interference fringes in the resonant optical absorption spectrum. In addition, we find remarkably coherent optical and spin subsystems enabled by the basal divacancy's symmetry. These properties establish divacancies as strong candidates for quantum communication and hybrid system applications, where simultaneous control over optical and spin degrees of freedom is paramount.

11.6.1 Context

In the previous section, we utilized DC Stark tuning of the optical fine structure. If instead we apply AC electric fields, we can perform a time-dependent modulation of the absorption and emission of single VV^0. This could allow for fast spectral reshaping of the absorption and emission of photon wave packets for increased coupling (The wave packet of absorption is actually opposite of emission!) between emitters[171, 172]. Similar schemes have been recently proposed in the V_{Si} in SiC [115]. Furthermore, if the modulation is periodic in time, interesting new physics arises as mentioned above. In this work, significant differences between the c-axis (C_{3v}) and basal (C_{1h}) divacancies are explored, including increased coherence from a ZEFOZ transition in these basal VV^0, as discussed in section 2.

11.7 Electrical Device Opportunities

In general, the possibilities of using SiC electronic devices remain largely unexplored for quantum science. Here, I will mention a few exciting pathways enabled by the SiC host and

the work in this section.

- Electrically driven single photon emission. Bright single photon emission from defects in SiC devices has been shown[210, 230–232], but linking this with electron spins remains a challenge.

- Electrically detected magnetic resonance of VV. This has been nominally demonstrated with ensembles [233], but has not been linked with optical activity or single defects. Relies on changes in conductivity depending on trap spin states.

- Electrical readout of defect spins. Similar to [206], but utilizing mature SiC devices. Relies on spin-to-charge conversion.

- Electrical spin polarization of defect spins. Possibly through a *spin blockade* effect, a spin polarized current, or though electrical excitation to the ISC.

- Fermi level optimization of VV^0 formation. Recent results in the NV^- center [234, 235] show that changing the Fermi level during defect formation can drastically enhance spin properties by reducing nearby impurities, and can also greatly increase formation efficiencies [236].

- Electrically controlling spin coherence. As described in chapter 13, paramagnetic impurities may limit spin coherence, while large enough electric noise can similarly limit certain defects. Depleting these sources using techniques in this chapter may be possible.

- More complicated devices such as SETs, MOSFETs, APDs and others may provide additional functionalities. These are completely unexplored.

- Photonic devices/nanostructures. Integrated *in situ* tuning and linewidth narrowing in nanostructures would provide ideal platforms for quantum communications

Chapter 12

Strain Inhomogeneities

This chapter and figures are adapted from the publications[10, 12]

The previous chapter describes in part our ability to reduce electrical noise for our quantum system. On the other hand, the next chapter (13) talks about using isotopic purification to reduce the fluctuating magnetic bath in the qubit's environment. Another type of noise/inhomogeneity, however, is *strain*. As mentioned in sections 5.3 and 5.2, strain not only makes defects have drastically different optical frequencies, but symmetry breaking strain can reduce the QE and ODMR contrast for defects. Furthermore, for ensemble based sensing, strain can cause shifts in the zero field splitting, causing a broadening which reduces sensitivity. Understanding dynamic strain allowed for the advances in chapter 10, while crystal damage and surfaces have been known to be issues for spin defects. Specifically, the temperature dependence of certain reconfiguring processes of the host lattice drive defect formation and healing of the crystal after defect formation.

With this context in mind, we investigate the 'healing' of commercial SiC and diamond nanoparticles. These systems are exciting for applications in quantum sensing where small sensor size is paramount. Furthermore, the general understanding of material dynamics under annealing guides materials and processes for both diamond and SiC. Specifically these results utilize a X-ray imaging technique which can pick out *one single nanoparticle* and

image its 3D strain and morphology!

12.1 BCDI with Diamond Nanoparticles

We observed changes in morphology and internal strain state of commercial diamond nanocrystals during high-temperature annealing. Three nanodiamonds were measured with Bragg coherent X-ray diffraction imaging (BCDI), yielding three-dimensional strain-sensitive images as a function of time/temperature. Up to temperatures of $800°C$, crystals with Gaussian strain distributions with a full-width-at-half-maximum of less than 8×10^4 were largely unchanged, and annealing-induced strain relaxation was observed in a nanodiamond with maximum lattice distortions above this threshold. X-ray measurements found changes in nanodiamond morphology at temperatures above $600°C$ that are consistent with graphitization of the surface, a result verified with ensemble Raman measurements.

Nanoscale quantum sensing with defects has developed into a promising field with a wide range of applications both in physical and biological systems. This work paves the way for developing efficient methods by which we optimize the structure of commercial nanodiamonds such that their internal strain is reduced to suitable levels for NV^-sensing applications.

12.2 Imaging Strain Relaxation in SiC

We extend the previous results from diamond to SiC. As mentioned before, the crystalline strain properties of nanoparticles have broad implications in a number of emerging fields, including quantum and biological sensing in which heterogeneous internal strain fields are detrimental to performance. Here, we used synchrotron-based Bragg coherent X-ray diffraction imaging (BCDI) to measure three-dimensional lattice strain fields within individual 3C-SiC nanoparticles, a candidate host material for quantum sensing, as a function of temperature during and after annealing up to $900°C$. We observed pronounced homogenization of the initial strain field at temperatures above $500°C$, and we find that the surface layers

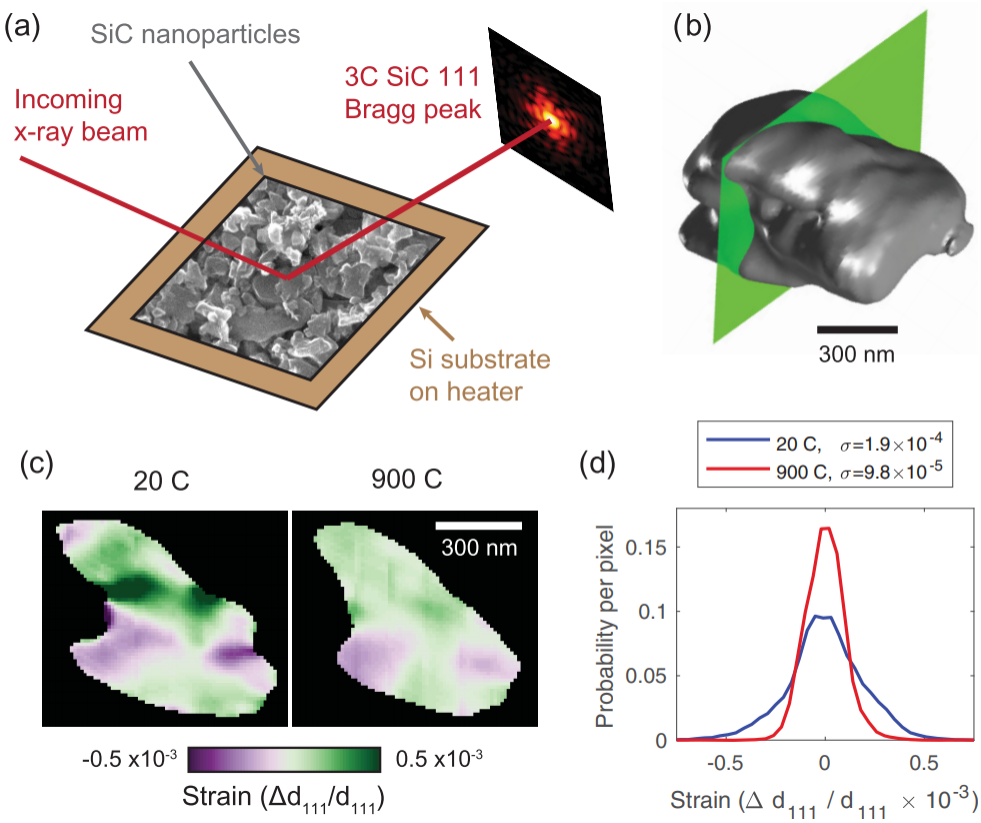

Figure 12.1: **Strain relaxation in SiC nanoparticles.** A schematic of the experiment is shown (a) in which a coherent Bragg peak from a single 3C SiC nanoparticle in an ensemble deposited on a Si substrate is measured. The heater below the substrate enables temperature-dependent measurements in an atmosphere of flowing Ar gas. Using BCDI, the Bragg peak measurements are inverted to real-space 3D images that reveal the shape of the particle [gray isosurface in (b)]. Additionally, BCDI gives the internal strain within the particle. The strain fields of this particle along the green cut plane in (b) are shown in (c) at two different temperatures along with histograms (d) of the pixel-wise strain values of the images that show evidence of strain homogenization at high temperature.

and central volumes of the nanoparticles reduce strain at similar rates, suggesting a uniform healing mechanism. Thus, we attribute the observed strain homogenization to activation of mobile point defects that annihilate and improve the overall quality of the crystal lattice. This work also establishes the feasibility of performing BCDI at high temperatures (up to $900°C$) to map structural hystereses relevant to the processing of quantum nanomaterials. In particular, recent demonstrations of chemically synthesized nanoscale SiC with high contrast, room temperature ODMR are particularly exciting [237].

Chapter 13

Entanglement and Control of Single Quantum Memories in Isotopically Engineered Silicon Carbide

This chapter is an early draft of a submitted manuscript[1]

Nuclear spins in the solid state are both a cause of decoherence and a valuable resource for spin qubits. In this work, we demonstrate control of isolated 29Si nuclear spins in silicon carbide (SiC) to create an entangled state between an optically active divacancy spin and a strongly coupled nuclear register. We then show how isotopic engineering of SiC unlocks control of single weakly coupled nuclear spins and present an *ab initio* method to predict the optimal isotopic fraction which maximizes the number of usable nuclear memories. We bolster these results by reporting high-fidelity electron spin control (F=99.984(1)%), alongside extended coherence times ($T_2 = 2.3\ ms$, $T_2^{DD} > 14.5\ ms$), and a >40 fold increase in dephasing time (T_2^*) from isotopic purification. Overall, this work underlines the importance of controlling the nuclear environment in solid-state systems and provides milestone demonstrations that link single photon emitters with nuclear memories in an industrially scalable material.

13.1 Introduction

Nuclear spins are one of the most robust quantum systems, displaying relaxation times that can exceed hours or days[238–240]. This makes them exciting candidates for quantum technologies requiring long memory times. In particular, nuclear spins are attractive quantum registers for optically active spin defects in the solid-state[182]. For example, nuclear registers can be used for repetitive quantum non-demolition (QND) optical readout[175], to enhance the signal-to-noise in quantum sensing[241], to implement quantum error correction schemes[183], or as vital components of quantum repeater[179] and quantum communications[44] nodes. Additionally, electron-nuclear hybrid systems provide a platform for studying measurement back-action[242] and the emergence of classicality in quantum mechanics[243].

Recently, commercial SiC has been shown to provide a technologically mature semiconductor host for multiple defect spin qubits[4, 5, 82, 90, 92]. In particular, this material allows the integration of isolated color centers into classical electronic devices which can be used to engineer and tune the spin-photon interface[6]. Combining such a tunable near-infrared emitter[3, 55] with a long-lived quantum memory is a promising basis for quantum network nodes fabricated at wafer scale by the semiconductor industry. To realize these quantum memories, SiC provides both carbon and silicon isotopes with non-zero nuclear spin. These isotopes have been shown to couple to various electronic spin defects[54, 181]; however, the isolation and control of single nuclear spins[103] in SiC has remained an outstanding challenge.

In this work, we report coherent control and entanglement of nuclear spin quantum registers strongly coupled to a single neutral divacancy spin (VV^0) in naturally abundant SiC. We then extend this control to weakly coupled nuclear spins, where isotopic purification enables the isolation of robust quantum memories. Using isotopic engineering, we also report both record coherence times and record single qubit gate fidelities[244] for spins in SiC. Throughout this work, we present both experiment and *ab initio* theory that explores the inherent

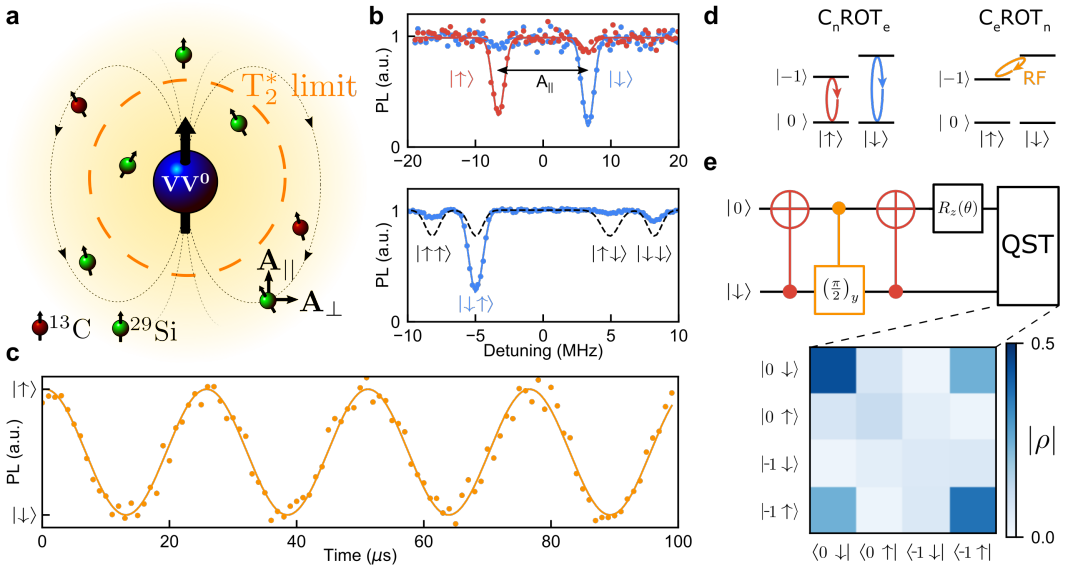

Figure 13.1: **Initializing, controlling and entangling strongly coupled nuclear spins.a**, Schematic of a single divacancy with surrounding nuclear spins. **b**, Optically detected magnetic resonance of a single (kk) VV^0 after initialization of both the electron and either 1 (top) or 2 (bottom) strongly coupled nuclear spins. Top: initialization in either the $|\uparrow\rangle$ (red) or $|\downarrow\rangle$ (blue) nuclear spin states. Detuning is from 1.139 GHz. Bottom: dashed line (black) represents the expected results from an uninitialized state, blue line is the experimental initialized state. Detuning is from 2.153 GHz. **c**, Nuclear Rabi oscillations (between $|1\downarrow\rangle$ and $|-1\uparrow\rangle$) obtained by driving an RF tone implementing a C_eROT_n. **d**, level structure schematic of a divacancy spin coupled to a single nuclear register. The $|+1\rangle$ electron spin state is not shown. (left) C_nROT_e manipulation drives colored as in **b**. (right) C_eROT_n RF drive corresponding to the oscillations in **c**. **e**, (top) Quantum circuit used to generate a bipartite entangled state between an electron and nuclear spins. Gates are driven using the manipulations shown in **d**. (bottom) Resulting density matrix ($|\rho|$). The third initialized qubit is omitted. All data are taken at T= 5 K.

tradeoffs between spin coherence and nuclear memory availability which are involved when isotopically engineering materials. These results develop a full suite of nuclear spin controls in SiC and provide a guide for future materials design of spin-based quantum technologies.

13.2 Strongly Coupled Nuclear Registers

In natural SiC, 1.1% of the carbon atoms and 4.7% of silicon atoms possess an I=1/2 nuclear spin. Thus, about a third of all single c-axis oriented (hh and kk, appendix B) divacancies will have a ^{29}Si register on one of the nearest-neighbor lattice sites (denoted

Si_I, Si_{IIa} or Si_{IIb})[79]. When the hyperfine coupling exceeds the linewidth (order $1/T_2^*$) of the electronic state (Fig. 13.1a), oscillations due to these nuclear spins are observable in Ramsey experiments. We refer to such nuclear spins as strongly coupled. This strong coupling splits the $m_s = \pm 1$ electronic ground state levels, which results in pairs of resolved transitions that enables direct selective control of this two-qubit state using external radio frequency (RF) magnetic fields.

Here, we demonstrate such a strongly coupled system by isolating a single c-axis (kk) VV^0 with a nearby ^{29}Si at the Si_{IIa} site (parallel hyperfine $A_{\parallel} = 2\pi \cdot 13.2\ MHz$) in natural 4H-SiC. In this case, because the electron spin linewidth (∼1 MHz) is much lower than the hyperfine splitting $A_{\parallel}$, we observe two individually addressable transitions corresponding to the two nuclear spin states (Fig. 13.1b). To polarize this nuclear register, we make use of two iterations of algorithmic cooling in which we optically polarize the electron spin and then swap this polarized state to the nuclear spin[198]. Using this method, we can achieve a high initialization fidelity (∼93%) as measured by the peak asymmetry in the optically detected magnetic resonance spectrum shown in Fig. 13.1b (appendix B).

After nuclear initialization, we prepare the electron spin in the $m_s = -1$ state and use a 13.2 MHz RF magnetic field to drive nuclear Rabi oscillations (Fig. 13.1c), which we read out by projecting onto the electron spin. Since these oscillations are only driven in the $m_s = \pm 1$ states, this allows us to demonstrate a $C_{\pm 1}NOT_n$ gate[181] which can be performed in 12.7 μs. Throughout these measurements, we also make use of fast (limited only by the hyperfine splitting of the lines) C_nNOT_e gates by applying a microwave pulses at one of the two frequencies shown in Fig. 13.1b (see Fig. 13.1d).

Having demonstrated control over a single nuclear spin, we then increase the number of registers by finding a (kk) divacancy which is strongly coupled to two ^{29}Si spins (with 6% probability for naturally abundant SiC). For this defect, we show that using both algorithmic cooling and dynamical nuclear polarization[84, 181] (DNP), we can polarize the full three-qubit system (Fig. 13.1b). We then demonstrate individual control of these registers and

calibrate gates operating on either register (appendix B).

In this three-qubit spin system, we apply the quantum circuit in Fig. 13.1e on the electron and one of the two coupled nuclear spins to create an electron-nuclear entangled state, and measure its full density matrix using quantum state tomography[181] (QST). We evaluate this density matrix using the positive partial transpose test, confirming unambiguously the entanglement in this system with an estimated entangled state fidelity of $\sim 81\%$ (appendix B).

These results demonstrate that single, strongly coupled nuclear spins can be used as quantum registers in SiC with relatively fast gate times. This type of register is useful for QND measurement of the nuclear spin and more generally for any applications that require fast operations[245] on ancilla qubits[246, 247]. However, the number of available nearby nuclear sites which can be controlled in this way is limited. Additionally, the high coupling strength makes these nuclear registers more sensitive to stochastic noise from the electron spin and limit applications where repeated electron initialization and control is necessary[179, 180], such as in long-distance quantum communications[151] or entanglement distillation[44].

13.3 Weakly Coupled Nuclear Memories

To complement these strongly coupled registers, we therefore investigate nuclear spins which are weakly coupled to divacancy electron spins. In order to access these memories and go beyond the $1/T_2^*$ limit, we use a XY8-based dynamical decoupling sequence to perform nanoscale NMR[103, 248–250] of the nuclear environment of a (kk) divacancy (Fig. 13.2a). This sequence (Fig. 13.2b) not only protects the electron spin from decoherence, but also allows for selective control of nuclear spins even when their hyperfine coupling is lower than the electron spin linewidth. In this measurement, each nuclear spin produces a series of dips in the coherence function at a pulse spacings[103] $\tau_k \approx \frac{(2k+1)\pi}{2\omega_L + A_1}$ at integer order k and

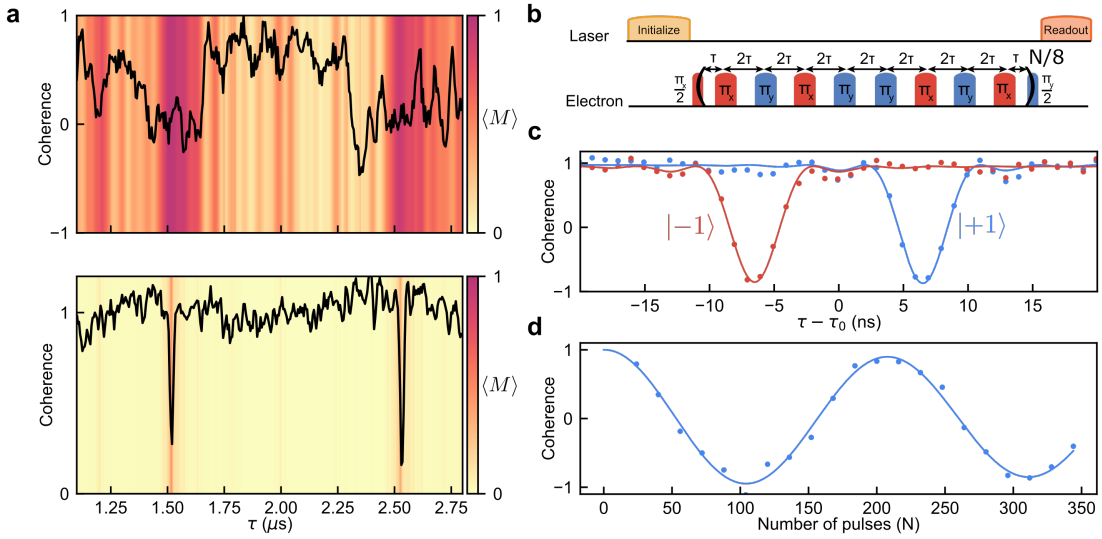

Figure 13.2: **Spectroscopy and control of weakly coupled nuclear spins. a**, CPMG based NMR spectroscopy of the nuclear environment of an example kk divacancy in a natural (top) and isotopically purified (bottom) sample. The data is shown as a black solid line. The background gradient represents the calculated average coherence function obtained over many nuclear configurations $\langle M \rangle$, which represents the expected density of coherence dips. **b**, Schematic of the XY8 pulse sequence. **c**, Coherence dips (8th order ($k = 8$), $\tau_0 = 6.125\ \mu s$) using either the $|-1\rangle$ (red) or $|+1\rangle$ (blue) electron spin state, providing a measure of $A_\partial \approx 2\pi \cdot 650\ Hz$. **d**, A $C_e ROT_{x,n}(\pm\theta)$ oscillation demonstrated on the 6th order ($k = 6$) of the isolated nuclear spin and achieved by varying the number of XY8 subsequence repetitions. After seven XY8 repetitions (total pulse number $N = 56$), a conditional $\pm\pi/2$ rotation is achieved with a fidelity of F=97(1)%. All data are taken at T= 5 K and B = 538 G.

Larmor frequency ω_L, corresponding to its specific nuclear precession frequency. With this spectroscopy, we observe that natural SiC has a crowded nuclear resonance spectrum due to the relatively abundant ^{29}Si, making it difficult to isolate single spins with low hyperfine coupling[180] (defined here to be $< 2\pi \cdot 60\ kHz$). This spectrum, along with *ab initio* cluster-correlation-expansion[102] (CCE) simulations of various possible nuclear spin configurations (Fig. 13.2a), demonstrates that natural SiC is not well suited for isolating single weakly coupled nuclear spins with low hyperfine values.

To address this issue, we use isotopically purified gases to grow 4H-SiC with 99.85% ^{28}Si and 99.98% ^{12}C (appendix B). In this sample, we once again measure nuclear environment of a few (kk) divacancies and find one with a single isolated dip in the coherence function (Fig. 13.2a). We find that the dip positions very closely match the different orders (k) of

the Larmor frequency of a ^{29}Si (differing only through the hyperfine value[103]). We further confirm the gyromagnetic ratio for this nuclear spin species by repeating the experiment at a different magnetic field (appendix B).

Having confirmed that the dips correspond to a ^{29}Si nuclear spin, we perform spectroscopy in both the $[m_s = 0, m_s = +1]$ and the $[m_s = 0, m_s = -1]$ basis (Fig. 13.2c), and measure a small $A_{\parallel} \approx 2\pi \cdot 650\ Hz$[103], which would not be resolvable in a Ramsey experiment. Low $A_{\parallel}$ nuclear spins are especially useful as robust quantum memories because the dephasing of the nuclear spin caused by stochastic noise from the electron is particularly sensitive to the parallel component of the hyperfine tensor, $A_{\parallel}$[179].

Fixing the pulse spacing (2τ) to a specific coherence dip ($k = 6$), we then vary the number of pulses (N) to coherently control this weakly coupled single nuclear spin[103, 183]. The corresponding $C_eROT_{x,n}(\pm\theta)$ oscillations observed (Fig. 13.2d) allows us to measure the perpendicular hyperfine component $A_{\perp} \approx 2\pi cdot11.45\ kHz$ (where $\theta \approx \frac{A_{\perp} \cdot N}{\omega_L}$) and confirms the successful application of a maximally entangling two-qubit gate[183](appendix B). If no other nuclear spins were present, one could choose any resonance order (k) to perform the two-qubit gate. In practice however, as k increases, the resonance of the isolated nuclear spin separates from the rest of the bath which drastically increases the two-qubit gate fidelity. Here, even in the isotopically purified sample where the nuclear spectrum is sparse, the electron-nuclear gate fidelity increases greatly at higher orders (k) as the resonance separates from the bath (up to 97(1)% at $k = 6$, appendix B). These results demonstrate the importance of reducing the nuclear spin bath for high fidelity control of isolated quantum memories with weak hyperfine interactions.

With these results in mind, we now turn our attention to estimating the optimal isotopic fraction required to maximize the number of isolated and controllable nuclear memories. Here, we need to strike a balance between too much purification which removes most usable nuclear spins and too little which results in a crowded and unresolvable spectrum. Limiting the gate time to a regime where nuclear-nuclear interactions are negligible (appendix B),

we developed a method to predict the average number of resolvable nuclear memories as a function of isotopic concentration. This is achieved by considering both the intrinsic gate fidelity from the electron-nuclear interaction and the average effect of unwanted rotations from all other nuclear species (appendix B). Our analysis demonstrates several important aspects of nuclear availability in SiC.

First, there exists an optimal nuclear spin concentration (Fig. 13.3a) that maximizes the average number of available nuclear memories which can be controlled within a maximum gate time and at a given minimum gate fidelity. Here, we find that naturally abundant SiC has a prohibitively high concentration of ^{29}Si, which prevents the isolation of nuclear memories with low hyperfine coupling ($< 2\pi \cdot 60\ kHz$). This reinforces the importance of isotopic engineering for nuclear memories in SiC and explains the spectrum observed in Fig. 13.2a. Second, the hyperfine values of the resulting controllable memories vary with isotopic concentration (Fig. 13.3b). At high concentration, nuclei with moderate hyperfine ($> 2\pi \cdot 60\ kHz$) contribute to most of the available memories, while low hyperfine nuclear spins are unresolvable. On the other hand, a lower isotopic concentration results in a less crowded spectrum and allows for the isolation of nuclei with lower hyperfine. The choice of nuclear concentration thus not only determines the total number of available quantum memories, but also the distribution of hyperfine values for these controllable nuclei.

Furthermore, we note that there is a tradeoff between the maximum allowable gate time and the number of available nuclear memories. While longer gate times allow for the resolution of more distant nuclei, this increase is shown to be only sublinear (appendix B). Additionally, when both nuclear species are utilized, the SiC binary lattice may provide roughly double the number of resolvable nuclear registers compared to a monoatomic crystal.

While the range of desired hyperfine values may differ depending on the particular application, a careful selection of the isotopic fraction is critical to maximizing the number of nuclear spins available in this range. This careful selection also determines the resulting average gate speeds and fidelities, allowing further optimization for the application at

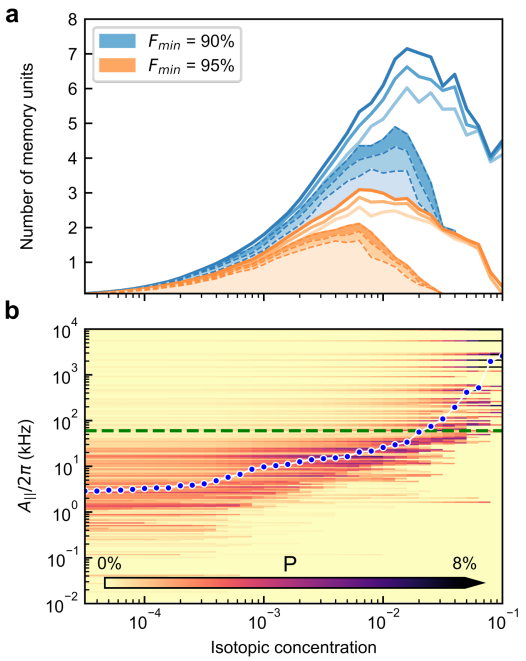

Figure 13.3: **Isotopic optimization of nuclear memories. a**, Calculated average number of memory units as a function of isotopic concentration where $[^{13}C] = [^{29}Si]$. A memory unit is defined as a nuclear spin that can be isolated and controlled above a given gate fidelity (F_{min}) within the maximum gate time. Solid lines correspond to all memory units whereas the dotted lines with shaded areas correspond to only memories with $A_{||} < 2\pi \cdot 60\ kHz$. Three different maximum allowable gate times are represented (lightest to darkest: 1 ms, 1.5 ms and 2 ms). **b**, Distribution of the hyperfine values for usable memory units as a function of isotopic concentration. Darker color corresponds to a higher probability (P) that memory units, if present and usable, will have the corresponding hyperfine value (maximum gate time = 1.5 ms, $F_{min} = 0.9$). Blue circles show the median of the distribution at the given concentration. The green dotted line corresponds to $A_{||} = 2\pi \cdot 60\ kHz$. The values are computed at the magnetic field of 500 G.

hand. These results therefore constitute not only a proof-of-principle demonstration of single weakly coupled nuclear spin control in SiC, but also provide guidance for future isotopic growth of materials for a variety of spin-based quantum technologies.

13.4 High-fidelity Qubit Control and Extended Coherences

Broadly, these experiments are all predicated on the divacancy electronic spin being a controllable and long-lived qubit. In this section, we discuss in detail the main factors that limit the coherence of divacancies in SiC and quantify our ability to perform single-qubit manipulation.

We begin by measuring both T_2^*(Ramsey spin dephasing time) and T_2 (Hahn-echo coherence time) of both c-axis (kk) and basally (kh) oriented defects in isotopically purified material. We measure the c-axis defects at B=48.8 G and the basal defects at B=0 G (to benefit from the magnetic insensitivity arising from a clock-like transition[7, 251]).

We report (Fig. 13.4a and 13.4b) T_2^* times of 48.4(7) μs and 375(12) μs for the c-axis (kk) and basal (kh) defects, compared to 1.1 μs[90] and 70-160 μs[7] in naturally abundant material. These numbers correspond to record dephasing times for spins qubits in SiC[54]. Additionally, despite only moderate isotopic purity, these results are very competitive with NV centers in diamond with much lower nuclear spin concentration[197, 252, 253]. This favorable scaling most likely arises from the SiC binary lattice and longer bond length, which results in reduced nuclear flip-flops[102]. These improvements in T_2^* are vital for DC quantum sensing schemes and for achieving strong coupling in hybrid systems[9, 254].

The significant increase in dephasing times arising from the isotopic purification for the c-axis defects shows that magnetic field noise from the nuclear environment is by far the main limiting factor to T_2^* for these defects. We provide further evidence of this by investigating the dephasing in isotopically purified SiC with *ab initio* cluster-correlation-expansion (CCE) simulations. Taking into account the remaining nuclear spin bath, these calculations predict average T_2^* values which are consistent with our experimental observations (Fig. 13.4a).

On the other hand, while basal divacancies benefit from first-order insensitivity to magnetic field noise at B=0 G, this magnetic noise protection comes at the cost of increased

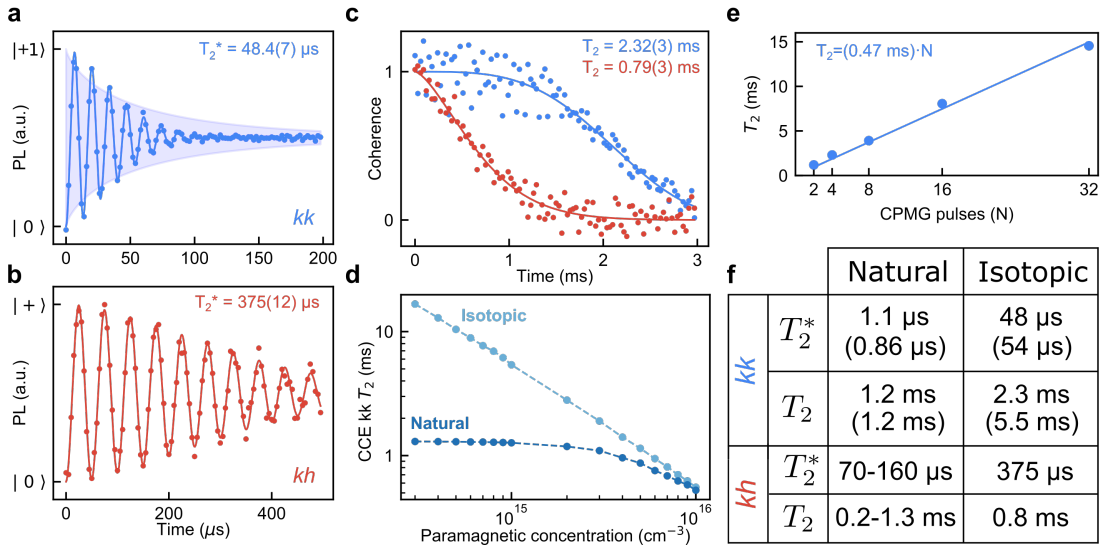

Figure 13.4: **Divacancy dephasing and decoherence times in isotopically purified material.** **a**, Dephasing of a c-axis (kk) defect in the isotopic sample at B=48.8 G. The shaded region represents the predicted average results from CCE (B = 50 G and paramagnetic density of 1×10^{15} cm^{-3}). **b**, Dephasing of a basal (kh) defect at B = 0 G. **c**, Coherence function under a Hahn echo sequence for kk (blue) and kh (red) single defects. **d**, CCE calculations (including the effects of paramagnetic traps) for a kk defect showing that the expected Hahn echo T_2 varies greatly based on paramagnetic spin density for both natural (dark blue) and isotopic (light blue) material (at B = 500 G). **e**, Coherence time for a (kk) defect in the isotopic sample under a varying number of CPMG pulses (N) shows that T_2 increases roughly linearly with pulse number (B = 48.8 G). **f**, Table summarizing representative numbers for T_2^* and T_2 (Hahn echo) in kk and kh defects in both natural and isotopic samples. Natural SiC coherences are taken from literature[7, 90, 251]. Numbers in parentheses are the theoretical numbers obtained by CCE (at B = 50 G) with both the nuclear spin bath and a paramagnetic spin bath of 1×10^{15} cm^{-3}. All data are taken at T= 5 K.

sensitivity to electrical fields[255]. Since charge fluctuations can cause significant electric field noise[6], this may explain why the increase in T_2^* obtained from isotopic purification (Fig. 13.4b) is less pronounced than that of the c-axis divacancies. Furthermore, this magnetic protection also makes nuclear control difficult in the basal (kh) divacancies. This underlines the tradeoffs involved when choosing a defect species to work with.

Next, we perform Hahn-echo experiments to measure T_2 in isotopically purified SiC (Fig. 13.4c). Although we find a factor of ∼2 improvement in the coherence time for (kk) defects in this material (2.32(3) ms versus 1.1 ms[90]), we remark that this is a more modest

improvement than that of T_2^*. Nevertheless, this T_2 is comparable to the longest observed Hahn-echo coherence time in isotopically purified diamond samples with much greater isotopic purity[234, 256]. Interestingly, but the measured T_2 deviates from the predictions from nuclear spin induced decoherence obtained with CCE calculations, which yield an average coherence time of ∼37 ms. To understand these results, we carried out second order CCE simulations to study the effect of non-interacting electron spin pairs on the coherence time[257]. At the estimated paramagnetic density (impurities and radiation induced defects in the $3 \times 10^{14} - 3 \times 10^{15} cm^{-3}$ range, appendix B) we find good agreement with the experiment (Fig. 13.4d), thus confirming both the accuracy of our theoretical model and the important role of paramagnetic defects in limiting coherence. Our results are consistent with magnetic noise from a weak, but quickly fluctuating paramagnetic spin bath combined with noise from a strong, but slowly fluctuating, nuclear spin bath[26]. As a consequence, T_2^* is limited by nuclear spins, while T_2 is limited by paramagnetic impurities for the c-axis defects. On the other hand, differences in the basal divacancy's coherence compared to other reports[7, 251] likely stems not only from the isotopic purification, but also from sample-to-sample variations in electric field noise, which could be mitigated using charge depletion techniques[6].

The demonstrated coherence can be further extended by additional refocusing pulses. We provide a proof-of-principle demonstration by varying the number of pulses (N) in a dynamical decoupling sequence. At $N = 32$, the coherence is increased to 14.5 ms (for a kk defect, Fig. 13.4e). With more pulses, the coherence should continue to increase linearly until the T_1 limit is reached, which we measure to be on the order of one second under these experimental conditions (appendix B).

Finally, we characterize our single qubit gate fidelities through randomized benchmarking experiments and obtain an average gate fidelity of 99.984(1)% (Fig. 13.5). These bare fidelities are amongst the highest for single spins in the solid state[244, 258, 259] and exceed the threshold for error correction codes[260–262]. Furthermore, high fidelity control of the

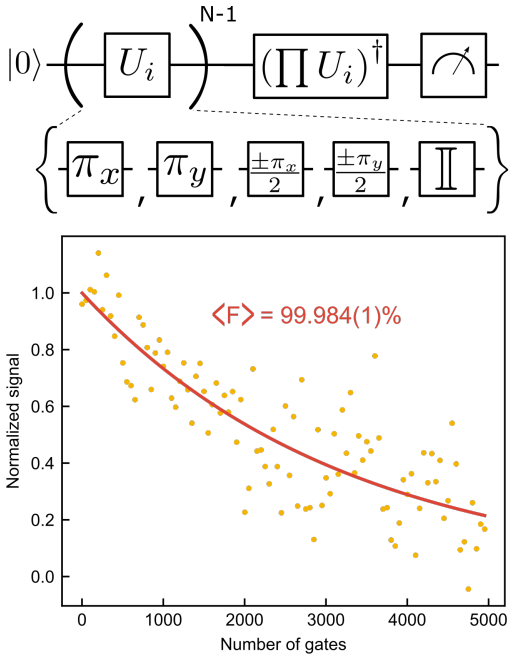

Figure 13.5: **Average single qubit gate fidelity as measured by randomized benchmarking.** Results obtained by applying N Clifford gates (as represented by the quantum circuit) on a kh defect in the isotopically purified material at T= 5 K, B= 0 G. From this decay we extract an average gate fidelity of 99.984(1)%

electron spin is crucial to prevent reduced coherence in nuclear spin memories[180]. The long coherence ($T_2^{DD} > 14.5\ ms$) and high fidelity control (99.984(1)%), combined with a $> 99\%$ resonant initialization and readout fidelity (appendix B) demonstrated in this work establishes the divacancy in SiC as a promising system for future solid-state quantum devices.

13.5 Conclusion

Defect spins in SiC are exciting candidates for wafer-scale quantum technologies requiring stationary qubits and a photonic quantum communication channel. In this work, we provide milestone demonstrations of nuclear memory control of both strongly and weakly coupled nuclear memories in a technologically mature semiconductor material. This work also examines, both experimentally and theoretically, the tradeoffs that are inherent to isotopic purification and offers a pathway towards optimizing nuclear spin concentration to maxi-

mize the number of usable nuclear memories.

Our results underline the importance of isotopic engineering in designing materials for solid-state quantum applications. Such engineering can provide a two-fold benefit for quantum memories: it enables control of more nuclear spins by unlocking access to memories with low hyperfine coupling, while also drastically increasing the coherence of these nuclear spins[263]. Moreover, isotopic engineering enables the selection of a hyperfine distribution that can optimally trade off the effect of the "frozen core"[264] against the electron spin induced noise inherent in realistic quantum communications protocols[180]. Further optimization may also be achieved by considering differing nuclear control methods[182, 265]. Additionally, the demonstrated proof-of-principle nanoscale NMR detection of a single nuclear spin (at a distance of $\sim$1.2 nm) in SiC provides a route for a functionalizable, biocompatible platform for quantum sensing with polarization and readout in the biological near-infrared window[266]. Overall, these results cement defects in SiC as attractive systems for the development of quantum communication nodes and underline the importance of isotopic control in material design for future quantum technologies.

13.6 Context

We possessed the isotopically purified sample for a long time before putting it to good scientific use. This was because the charge dynamics in the sample were drastically different than what we were used to, such that only after learning about charge control (chiefly, using 905 nm excitation) were single defects found and measured. In this work, our newfound ability to control weakly coupled nuclear spins is critical for the development of quantum network nodes with SiC. Nuclear spins are exception quantum memories due to the low coupling of nuclei to their environment, including a $\sim 1000\times$ smaller gyromagnetic ratio compared to the electron. These quantum memories are ideal for the highly probabilistic entangling protocols that defects use[179, 180], and in their coherence. In particular, as the memories

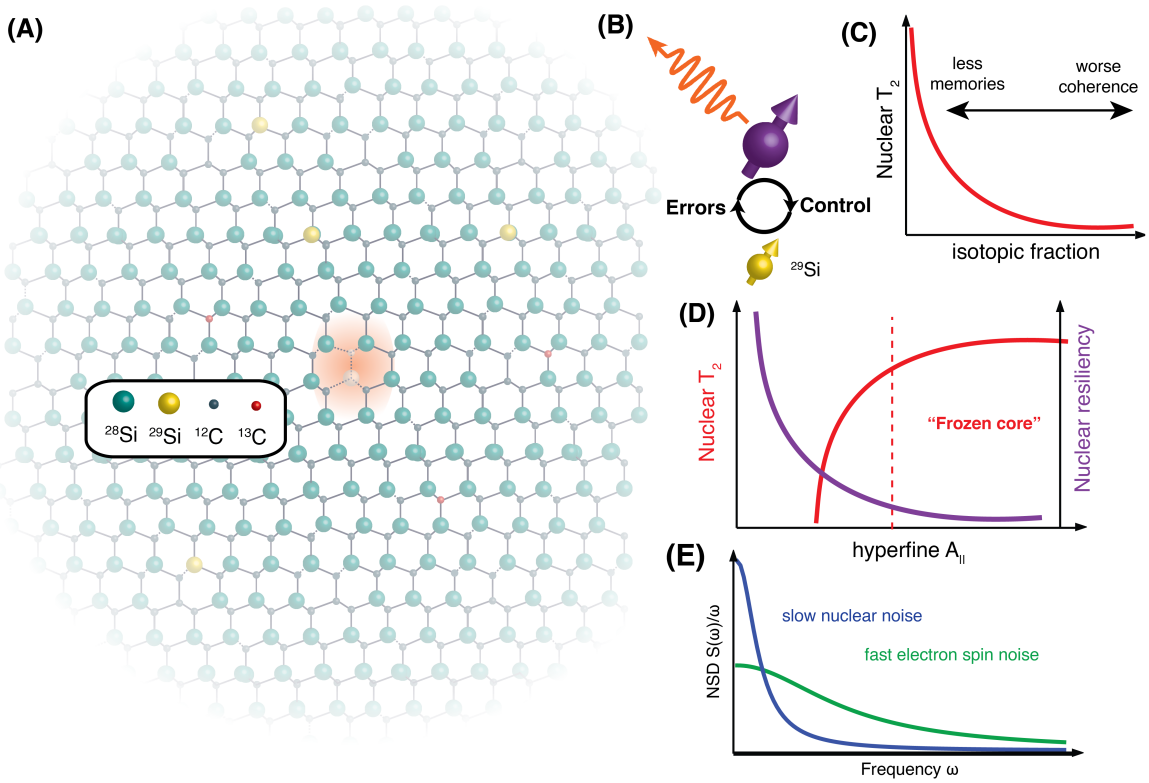

Figure 13.6: **Nuclear memories for optically active spins**. **(A)** Schematic lattice showing a central VV^0 and sparse nuclei in the surrounding lattice. **(B)** A quantum node with a nuclear memory. The same hyperfine coupling for control also causes errors on the electron spin to decohere the nuclear memory [180]. **(C)** Schematic tradeoff of isotopic purification, too much and there are no nuclear spin memories. Too many and they become low coherence (along with the electron) [263]. **(D)** Schematic tradeoff of the choice of the hyperfine value ($A_{\|}$) of the memory. Nuclear spins more strongly coupled have higher coherence [264], but are decohered easily (low 'nuclear resiliency') by manipulations of the electron [179, 180]. **(E)** Schematic noise spectral density (NSD) of the environment of a solid state spin. Nuclear spin noise is mostly slow but relatively large, while electronic spin noise can be faster and limit T_2.

become more weakly coupled they become exponentially more resilient to noise from the electron (see appendix B) in that they can endure many entangling attempts as needed for repeater and entanglement distillation protocols. Furthermore, full error correction with 5 nuclear registers may be possible [198]. We are able to control these nuclei using dynamical decoupling sequences, preserving the electron coherence and beating the T_2^* limit for sensing to couple to a nuclear spin at > 1 nm. The resulting spectral resolution of this sequence (and

others that used dynamical decoupling) follows the Fourier-transform of the pulse train and is a $Sinc^2$ that narrows with longer sequences. This proof-of-principle is the first detection of a single nuclear spin other than in diamond. We also answer the question: *"If you could have any nuclear spin concentration, what would you pick?"*. We explore the discuss how a balance that needs to be struck between too many nuclear spins which cause decoherence and low gate fidelity, and too few which limits the number of quantum memories (illustrated in Fig. 13.6). Additionally, as the nuclei become more weakly coupled, they have reduced coherence and do not benefit from the so called 'frozen core' (see Fig. 13.6D). With this theory, we develop a new framework that which guides and help and optimizes future quantum materials growth and design. The realization of the first entanglement, control, and spectroscopy of single nuclei in the SiC host, with the reported record-breaking coherences and gate fidelities establishes VV^0 as a leading qubit candidate.

Chapter 14

Boulevard of Broken Dreams

"nature never lets you win"

14.1 Overview

No good science is done that is not built on a pile of failed ideas, wasted efforts and lofty, but broken scientific goals. In hindsight, my early days as a graduate student were filled with learning and growth, but also with ambitious (or sometimes just ill-thought out) projects that essentially all *didn't work*. The reality is that this is part of the graduate education process, and some of the best learning comes through failure. Here, I'll briefly describe some of these early efforts.

14.2 Masers & Lasers & Graphene, oh my!

A large fraction of my graduate experience was concentrating on creating a room-temperature solid-state *maser* out of a very large ensemble of NV^- centers in diamond. This diamond was placed in a high-Q microwave resonator and pumped with a large 18 W 532 nm laser. Applying a large magnetic field Zeeman shifts $m_s = -1$ below the optically polarized $m_s = 0$ state creating a *population inversion*. This spin population inversion through optical pumping in

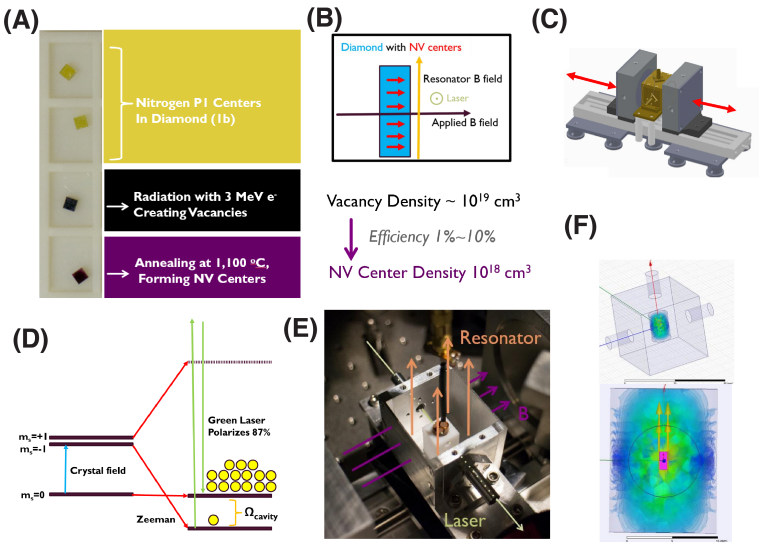

Figure 14.1: ***NV*$^-$ Maser schematic.** **(A)** Ensemble NV^- creation 'purple haze' from 1b high nitrogen content diamonds and high-dose irradiation.**(B)** Experimental geometry.**(C)** Uniform magnetic field tuning with magnet cart stages.**(D)** Population inversion by optical pumping.**(E)** Photograph of experimental setup, dielectric microwave resonator is held in a low loss teflon holder in a 3D metal box cavity.**(F)** Microwave mode confinement in the dielectric with diamond (pink) shown.

a microwave cavity produces spontaneous and *stimulated* emission (Fig. 14.1). If the *gain* is higher than the *loss*, then the maser serves as an ultralow source and amplifier of microwave signals, with potential applications in radio astronomy or quantum sensing. This result was achieved in 2012[267] with molecules and in 2018 with the diamond NV^-[268](while I was working on it), and has been proposed for defects in SiC as well[269]. A brief schematic of some of the early work is shown in Fig. 14.1.

Related schemes of ensembles of defect spins coupled to microwave cavities have been proposed for quantum-limited refrigerators or quantum memories for superconducting qubits. The major issues for this experiment was getting high NV^- density with good quality in a large diamond, along with making a *very* high quality factor microwave resonator. Non-uniform optical absorption, heating and laser-induced charge conversion were also problems. An extension of microwave cavity-NV^- ensemble coupling was to move to spheres of YIG (Yittrium-Iron-Garnet) that have an effective extremely high spin density with narrow spin-resonance. YIG-cavity strong coupling was measured in the maser experimental setup and

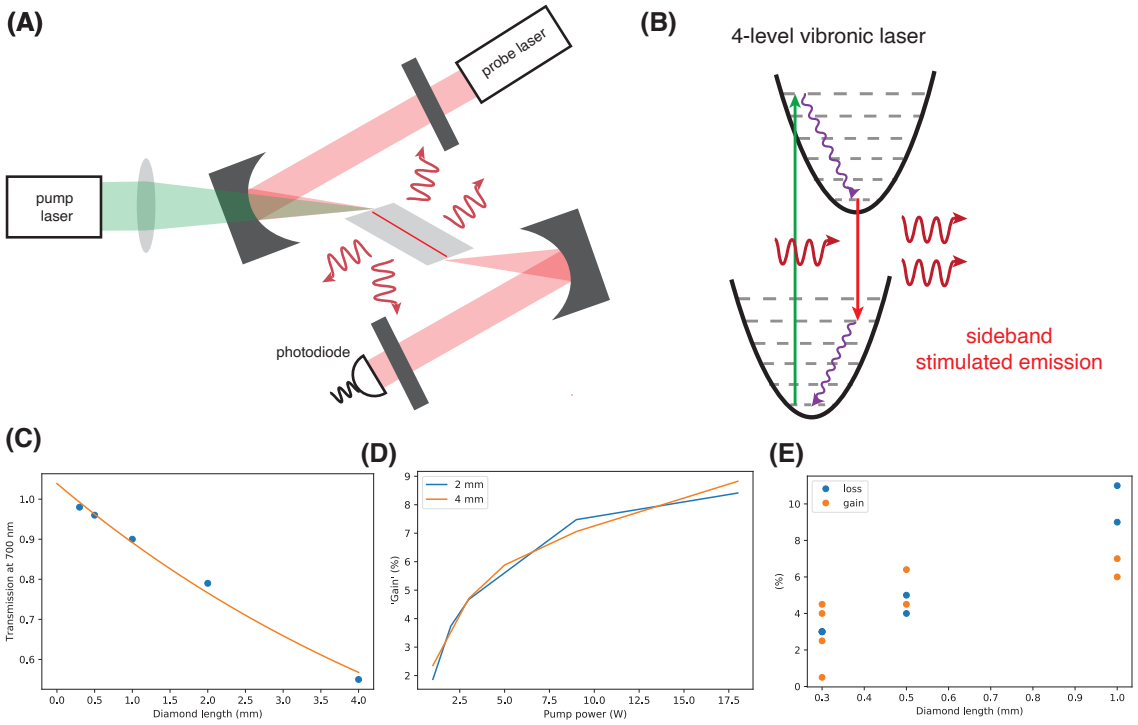

Figure 14.2: ***NV*$^-$ Laser schematic and preliminary results**. **(A)** Experimental geometry using a folded "Z" optical cavity to correct for aberrations. The central diamond (grey) is Brewster cut such that the polarized laser cavity mode has no reflections. A 18 W 532 nm pump laser excites through a custom dichroic curved mirror. partially transmissive end mirrors complete the laser cavity. A red probe laser can be transmitted through the pumped diamond to measure gain and loss. **(B)** The laser is an effective 4-level system with the vibrational states, where stimulated emission can occur on the phonon sideband. **(C)** Measurement of the absorption and scattering loss through a 1b diamond (un-irradiated) corresponding to and absorption coefficient of $\sigma \approx 0.16\ mm^{-1}$ (orange fit). This loss was significantly higher than what would have allowed laser action. **(C)** Measurement of the laser power dependent 'gain' of the high-NV density diamonds at two different thicknesses (in the path of the pump/probe). A few % gain is measured, but adding length to the crystal does not help gain, while it does contribute to loss. The gain saturates and probably arises from nonuniform absorption in the crystal. The 'gain' is mostly likely a loss reduction from a charge conversion effect ('photochromism'). **(E)** 'gains' and losses from multiple different samples of different lengths. Nearly universally, the gains and the losses were comparable and likely related due to the above consideration. No sample with confirmed stimulated emission gain greater than loss was ever found.

morphed into related work [270].

A related idea is to use a similarly high density diamond sample as a *laser* gain medium in a macroscopic optical cavity. The vibronic structure of the NV^- looks just like dye molecules used in lasers and constitutes an effective 4-level laser system. Due to the ISC, the gain would

be *spin-selective*. Because lasers are highly nonlinear (there exists a discrete *lasing threshold*) and stimulated emission into one spatial mode can boost collection efficiency, such a system has been proposed as a record-breaking solid-state magnetometer [271]. This goal has not been achieved to date, and a few groups are pursuing it. I spent a large amount of time focusing on this as well, where preliminary measurements of optical gain and loss in the NV^- PSB are shown in Fig. 14.2. Once again, NV^- density, quality and size are issues. In particular, optical loss through the 1b diamonds in the region of interest were prohibitive. Measurements were performed on various *Brewster cut* diamonds in a custom-built optical cavity, and 'gain' was measured by looking for stimulated emission from a weak probe laser on the PSB. Unfortunately, it seems that charge conversion from the powerful pump laser causes modulations in the loss coefficient and look like 'gain'. The issues of unwanted losses, and weak stimulated emission, charge conversion and defect ionization, are hurdles for the goal for NV^- lasing that may be solvable with better materials. Recent work illustrates these issues and efforts in the field [272–274].

Before the work in chapter 10 using SAW devices, we attempted to use HBAR (High-overtone Bulk Acoustic Resonators) devices to drive spins (In collaboration with the *Bhave group, Purdue*). Due to the larger mode volume, and some other issues, this experiment was dropped in favor of the focused SAW devices. Furthermore, we originally were creating superconducting SAW devices out of various materials (GaAs, LiNbO3, Quartz, SiC, etc) and cooled these resonators in a dilution refrigerator and measured ultra-high Q's. The goal was to look towards superconducting qubit-SAW strong coupling. This was achieved in 2018 by a different, but related scientific team [275].

A parallel idea was to explore spin-phonon strong coupling, or cQAD (cavity quantum acousto-dynamics) with spins. Spins in diamond and SiC have very small coupling strengths to strain which makes this very difficult. Because of this, we made initial investigations into defects with larger coupling strengths (along with other more broad defect discovery efforts). Even then, most likely only ensemble enhanced coupling seems possible. Along

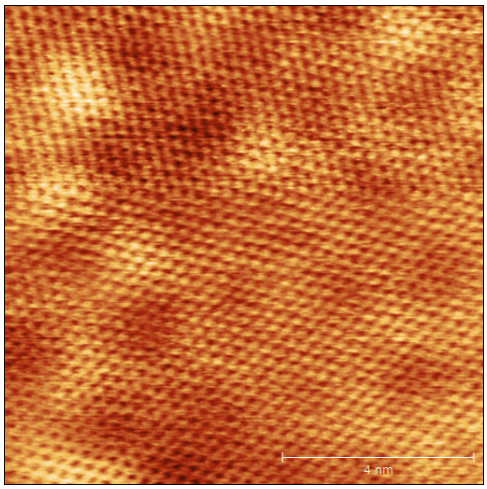

Figure 14.3: **STM of graphene on 4H-SiC.** The Moiré pattern and individual atoms are observable on this epitaxial graphene layer.

these lines, one can think about engineering the *phononic density of states* to reduce spin-lattice relaxation for certain defects, which is something we briefly pursued where we created phononic crystal cavities in SiC. This extension of T_1 would constitute a *Anechoic chamber for spins*. Finding a defect that has reasonable T_1's that are limited by the direct occupation of phonons (not Raman) is difficult, however.

Other efforts included being involved in SiC nanoparticle biosensing projects, exploring defect-mediated ferromagnetism in SiC[276], and in building a preliminary room-temperature V_{Si}^{-} in SiC setup for possible mechanical coupling or lasing. Finally, I was involved in multiple projects involving *graphene*. FRET (Förster Resonance Energy Transfer) can be achieved using graphene on near-surface NV^{-} centers for electrical readout (which we tried) along with using the NV^{-} center to sense defects and condensed matter physics in graphene. This also involved STM imaging of graphene on diamond in which we made samples and made initial measurements (*Jeff Guest, Argonne*). Luckily, SiC can grow high-quality epitaxial graphene which can be used for electrical gating of charge, along with detection of and coupling to spins in SiC (including spectroscopy of the states using STS). Towards these goals, we grew graphene on 4H-SiC and took STM images, revealing the expected Moiré pattern shown in Fig. 14.3 (*Sibener Group, UChicago*). Our collaborators were even able to

create defects in graphene by sputtering ions at the material. Unfortunately these projects still need much more investigation.

Chapter 15

Conclusions

In this thesis, we've gone through the context and background for quantum technologies. Specifically, the outlook for VV^0 in SiC for quantum communications networks is described. The work of this thesis broadly develops new engineering and physics for optically active defects in the solid state.

In particular, the ability to drastically tune the spin-photon interface and eliminate the issues of spectral diffusion and blinking for a quantum emitter in the near-telecom band, combined with long coherences and the understanding and development of nuclear quantum memories, solidifies VV^0 as an exciting candidate for quantum technologies. Leveraging these wafer scalable systems, and using classical electronic devices, new opportunities for spin qubits are unlocked.

15.1 Roadmap for Quantum Technologies with Spins

However, there are still outstanding challenges to be met. Here, I will provide a roadmap for the VV^0 system:

- Achieve single-shot readout. This is the most important outstanding challenge. This is largely a matter of getting enough correlated photons *measured* before the information

is destroyed. There are a few avenues to pursue:

  - Boosting collection efficiency by setup design, SILs or photonic integration. Waveguides and tapered/lensed fibers are also very promising. Developing custom high NA NIR objectives could improve on the largely lacking options in the IR. Adaptive optics could help mode match the collected light into single mode fiber. Multimode or sideband-optimized SNSPDs could also drastically increase the number of photons collected. This has resulted in a factor of 2 for the NV^- center[151]. This also boosts η for entanglement efficiency.
  - Spin-to-charge conversion. This allows for single-shot despite low collection efficiency, but η will still be low. A good strategy for defects with low cyclicity. This can be achieved by utilizing spin-dependent ionization with the ISC or some other mechanism. There is also the possibility for single-shot electrical/APD readout in SiC devices.
  - Swapping to a nuclear memory and performing repetitive QND on the nuclear spin[176]. This is a slow process, and does not boost η. The depolarization of the nuclear spins in SiC with repeated electronic readout and initialization has not been explored.
  - Understanding post selection/charge dynamics/spectral diffusion/phonon-induced mixing/QE that cause less photons to be emitted per experiment. Pick a defect in SiC that has favorable properties.

- Demonstrate two-photon interference with one defect (with a delay line), or with two spatially separated defects.
- Show proof-of-principle entanglement between two distant VV^0
- Investigate nuclear memory robustness to the entangling protocol. This is known for the NV^-, but may be drastically different for VV^0. Develop protocols with these

memories [44, 130], including error correction.

- Develop QFC with VV^0 to the true telecom and extend the links.
- Move to a three-node system, utilizing quantum memories, and show proof-of-principle entanglement swapping.
- Choose a photonically enhancing structure to boost the DWF, but that *does not drastically broaden the PLE lines*. Lifetime reduction is less important, and moderate DWF increases go a long way. This is an important problem that needs to be tackled early. Degradation from device integration is a near-universal problem, mostly due to problems at surfaces.
- Integrate electrical tuning and nanophotonics with properly chosen isotopic concentration (chapter 13) to create optimized devices for the quantum nodes.
- Investigate spectral multiplexing and non-linear networks.
- Develop on-chip detectors, converters, electro-optical components.
- Scale and package into 'black-box' closed cycle cryostat systems.

Broadly, this roadmap sets a course for the field in leveraging the advances from this thesis for a real-world quantum technologies. This will require a combination of materials, engineering and new physics. That being said, it's quite likely that things will not proceed as expected, new avenues will be discovered, or other candidate systems may take the lead. However, the broad results of this thesis should be applicable to many quantum solid-state systems and applications.

Appendix A

Electrical and Optical Control of Spins in Scalable Semiconductor Devices: Details

"*do it right, don't do it wrong*"

A.1 Materials and Methods

A.1.1 Defect Formation

Single defects can be isolated in commercially available and laboratory-grown wafers of SiC. In particular, custom grown wafers containing intrinsic, non-intentionally doped epilayers have sufficiently low enough defect density to isolate sparse single defects through confocal microscopy. After growth, we use 2 MeV electron irradiation at a dose of $3e13\ cm^{-2}$ to introduce vacancies in the lattice, that upon annealing (850 $^{\circ}C$, 30 minutes, Ar ambient), form VV^0 and other defect complexes and traps. These defects form in the neutral charge state if the Fermi level is near mid-gap. In these samples, PL1 (hh), PL2 (kk) and PL4 (kh) divacancies are observed, consistent with previous reports as confirmed by photolumines-

cence (PL) spectra, ODMR signatures and photoluminescence excitation (PLE) resonances. Interestingly, as in other work, we do not observe single (hk) divacancies. In this work, we use the ($V_C V_{Si}$) convention for the divacancy where k and h refer to the quasi-cubic and hexagonal sites, respectively.

A.1.2 Device Fabrication

In this work, we use a commercially grown (by Norstel AB, now ST Microelectronics) wafer of 4H-SiC. The wafer has a n-type substrate ($[N] = 1e18 - 1e19 cm^{-3}$, $12 - 30\ m\Omega \cdot cm$) with $10 \mu m$ i-type ($[N] < 1e15\ cm^{-3}$, $[Vc] \sim 1e15\ cm^{-3}$) and 400 nm p-type ($[Al] = 7e18\ cm^{-3}$) epilayers grown on top, creating a vertical p-i-n junction. After forming isolated VV^0 in these wafers, Ohmic contact is made uniformly on the back n-type surface using $\sim 300\ nm$ of NiCr (80/20). This n-type contact is made Ohmic using a 5 minute RTA anneal in Ar ambient at 950 $^\circ C$. Subsequently, lithographically patterned Ohmic contact is made to the top p-type layer (30 nm Ti, 100 nm Al, 30 nm Au). The top contact is made Ohmic with an anneal in a quartz tube furnace in Ar at 850 $^\circ C$ for 10 minutes. These patterned structures allow for optical access of the defects under bias. Ohmic contact is confirmed through linearity of the I-V response between two pads on the same layer for both the top and bottom contact. After top and bottom contact formation, nearby microwave striplines are fabricated (10 nm Ti, 150 nm Au), allowing microwave coherent control of the spins.

Additionally, the slight 4 degree off-axis cut of our sample (used for high-quality epitaxy) means we also apply a slight transverse field to our defect with Stark tuning. In some defects, this accentuates the inherent strain asymmetry, but in other defects it works against the local transverse strain and improves the symmetry of the defect. This is a convenient way to both tune the optical lines and restore symmetry with a single gate demonstrated in Fig. 11.4B.

A.1.3 Device Characterization

Although the exact interpretation of the I-V characteristics of the device is beyond the scope of this work, the behavior in Fig. 11.2C is consistent with the temperature dependence of the built-in voltage and possible non-Ohmic behavior of the top p-contact as the relatively deep ($\sim 0.2\ eV$) aluminum acceptors become frozen out at low temperature. Voltages of up to -420 V without exceeding a leakage current of 1 μA ($\sim 100\ A/m^2$) are possible. Reduction of the leakage current is important to reduce charge dynamics and heating, while allowing for large electric fields.

A.1.4 Confocal Microscope

Our measurements are performed in a home-built confocal microscope using a 100x near infrared (NIR) objective with a numerical aperture (NA) of 0.85. The sample is at 5 K (unless otherwise specified) inside a Montana Cryostation s100 closed-cycle cryostat. The emission is collected through a 1060XP fiber and detected on a Quantum Opus Superconducting Nanowire Single Photon Detector (SNSPD). All quoted powers are measured at the sample, accounting for losses in the setup.

A.1.5 Instrument Error and Linewidth

Photoluminescence excitation (PLE) scans of the optical fine structure convolve the resolution of our wavemeter and the laser stability (Gaussian) on the true linewidth (Lorentzian). This results in a Voigt profile. We estimate an upper bound on this total instrumentation error of 8 MHz from scans on a control cavity. Thus, using the Voigt equation our true linewidth (from 20 MHz in Fig. 11.4A) may be as narrow as 16 MHz.

A.1.6 Pulse Sequences and Hahn-echo

For Fig. 11.2B (inset), 11.2D, 11.2E, 11.2F only resonant lasers are used to reduce ionization. In the inset of Fig. 11.2B lasers tuned to the A_1 and E_x line are used simultaneously to produce constant PL. With the low powers used, the exponential $g^{(2)}$ fit corresponds to the optical lifetime, from which we can extract an expected lifetime limited linewidth of approximately 11 MHz. In Fig. 11.2E, 11.2F, 11.2 A laser pulse on the A_1 optical line polarizes the spin state to $m_s = 0$ with high fidelity. Subsequent pulsed microwave control drives the spin. For readout, counts are collected during a pulse on the cycling E_x transition. In the Rabi data in Fig. 11.2E, the contrast is not dark count subtracted. In principle the contrast could exceed 99% with this correction. For Fig. 11.2F, the measurement is differential by projecting the coherence to either $m_s = 0$ or $m_s = \pm 1$ and taking the difference. The Hahn-echo is fit with an envelope $e^{-(\tau_{free}/T_2)^2}$.

A.1.7 Photoluminescence Excitation (PLE) Scans

For PLE, a tunable resonant laser (Toptica DLC PRO) is scanned over to optical fine structure. For all scans presented here, a constant microwave drive is applied to prevent initialization into a dark spin state. This drive is fast enough to not interfere with the slow ionization dynamics. PLE scans are performed at zero magnetic field unless otherwise noted. For the illumination color dependence in Fig. 11.6, these experiments are run with a rapidly interleaved pulse sequence where the resonant and repumping laser are never on at the same time to avoid multi-photon interplay between the two lasers.

A.1.8 Interleaved Charge Control Sequences

All measurements unless otherwise noted are at zero magnetic field. This regime allows us to use a single microwave tone to mix both $m_s = +1$ and $m_s = -1$ with the $m_s = 0$ state. This prevents a "dark" spin state where population could get trapped and thus enables

continuous PLE experiments without the need for an off-resonant reset. For Fig. 11.6, the power dependence of the ionization and repump was taken with a total sequence duration of 1.25 ms, red pulse time 100 μs, resonant on for 1.1 ms. The repump and resonant are not on at the same time. The 688 nm diode laser is directly modulated. For Fig. 11.6C an optical chopper was used synced to pulse the repump when the resonant was off. The total sequence duration was 2 ms, repump pulse time of 1 ms (50:50 duty cycle chopper) and the resonant laser was on for 800 μs.

A.2 Supplementary Details

A.2.1 Depth Control Using Doping

For defects complexes that lack a dopant (intrinsic defects), localization cannot be achieved by the traditional method of local implantation[277] or delta-doping through growth[214]. In SiC for example, this limits precise depth localization for both VV and V_{Si} defects and can be problematic for applications such as near surface sensing or photonic crystal integration. Using doped structures to tune the local Fermi level, we can control the defects stable charge state[203] and thus provides an alternative method for depth localization. In general, the VV is only stable in its neutral charge state (in equilibrium) when the Fermi level lies within the charge stability region of VV^0. This charge stability region can be understood through DFT calculations, which place this region $E_V + 1.1\ eV < E_f < E_c - 1.1\ eV$[11, 62]. With the total bandgap being $\sim 3.2\ eV$, this roughly localizes the VV^0 to only form and be stable in the middle 1/3 of the i region (Fig. A.1) in a p-i-n diode. Specifically, i-type layers can be grown near surface and be very thin $< 100\ nm$ for sensing, and localized i-type layers in the center of photonic cavities could increase coupling efficiencies while also offering *in situ* charge control and linewidth tuning techniques.

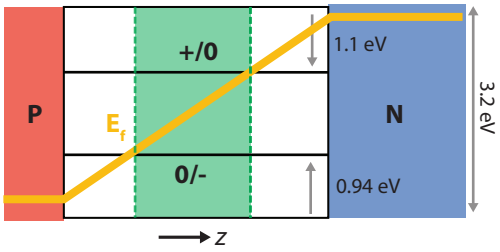

Figure A.1: **Charge stability region of VV^0 in a p-i-n diode.**

A.2.2 Limits of Stark Tuning

We estimate that the limit for Stark tuning will be the shift that occurs right before dielectric breakdown. From[278], the breakdown field at 300 K is around 300-500 MV/m (at cryogenic temperatures we expect this to be higher, but the 300 K value is used here). Therefore, we conservatively estimate a maximum possible Stark shift using the (hh) divacancy dipole of around 11 GHz/(MV/m) to be above 3 THz, and expect to exceed this in an optimally engineered cryogenic sample. This corresponds to 30 V in a 100 nm layer (easily achieved with growth) or 300 V on a 1 μm intrinsic layer.

A.2.3 Threshold Voltages and Stark Shift Dipoles

In general, the displayed Stark tuning in Fig. 11.3B represent just one example defect of each species in the diode. Within each defect configuration (hh), (kk), (kh) the threshold voltage where shifts start to occur changes. However, within each species the high field Stark shift slope remains roughly consistent. At high voltages, the 10 μm i-layer can become completely depleted and drop the voltage uniformly over the layer thickness (Fig. 11.3C). For example, we find four (hh) divacancies that have different reverse bias thresholds (5, 15, 40, 70 V), but have similar shift per volt at high fields (1.15, 1.10, 1.20, 1.10 GHz/V). Since we expect that at high voltage the field will be uniform in the i-region, we can estimate the field as a function of V to be E=V/10 μm. With this field estimate we obtain similar values for the (hh) electric dipole moment (11.5, 11.0, 12.0, 11.0 GHz/(MV/m)). Similarly, for

(kk) divacancies, we measured two defects that had reverse bias thresholds of 80 V and 100 V, with dipoles of 4.8 and 4.1 GHz/(MV/m) respectively. By averaging these Stark dipole moments, we therefore estimate the Stark electric dipole for (hh) to be 11 GHz/(MV/m) and for (kk) to be 4.5 GHz/(MV/m). We only report one (kh) defect Stark shift (equivalent to a dipole of 35 GHz/(MV/m)), but similar data can be found in [7]. In our estimate we do not take into account the exact angle of the (kh) VV^0 with respect to the c-axis. The small dipole of the (kk) divacancy makes it more resilient to electrical noise and spectral diffusion. As described in the main text, we attribute the differences in threshold voltages to the effect of a finite charge depletion region (at low voltage) slowly reaching different depths in the sample as we increase the applied voltage (Fig. 11.3C). In a sense, the depletion voltage needed represents the exact depth of the defect and could be presumably be used to precisely locate the defect in depth.

A.2.4 Electric Field in the Diode

In general, as described in the previous section, the electric field is non-uniform in the diode. As mentioned in 11.4, this results from a small residual n-type ("unintentional" doping) of the nominally "intrinsic" i-type layer. The fact that the i-type layer is not perfectly i-type means that the field can be dropped over small areas near the p-i or the i-n interfaces (depending on the residual dopant), instead of being uniformly dropped over the full i-type region. In particular, for our unintentionally n-doped (n^-) layer, a "trapezoidal" depletion in the p-i-n diode occurs starting near the $p - n^-$ interface (Fig. 11.3C)[279]. The exact shape of this trapezoidal field and charge distribution as a function of voltage can be calculated from semiconductor transport equations. When this trapezoidal depletion reaches through the entire intrinsic layer, it is commonly referred to as "punch-through", above which the field can be uniformly dropped over the intrinsic region. The width of the depletion and punch through voltage can be estimated with equation $W_d = \sqrt{\frac{2\varepsilon\varepsilon_o|V|}{eN_d}}$ [116, 278]. Using $N_d = [N] \sim 1e15\ cm^{-3}$, we can estimate a "punch-through" voltage of around 100 V (for a 10

μm i-layer). This is roughly consistent with the largest threshold voltages for Stark shifts and depletion observed. The electric field distribution also reflects the regions that are depleted. This is also sometimes referred to as a "space charge" region. The carrier concentration in diodes is known to follow an exponential relation in voltage/electric field[279].

A.2.5 Comparison of Stark Shifts and Linewidths with Other Quantum Emitters

Here, we define Δ as the ratio of the maximum frequency tuning to the observed linewidth. This metric balances the needs for emitters of tunability and narrowness. In the past, large tunability has been achieved at the cost of inhomogeneous broadening, and conversely, some narrow lines have been demonstrated at the cost of tunability. This makes sense since the shift ($S \sim d \cdot E$) and linewidth ($\Gamma \sim \Gamma_0 + d \cdot \delta E$) are both related to the dipole moment (d) and thus present an inherent tradeoff (note that Γ_0 is proportional to the"transition dipole moment" but is different from the Stark shift dipole d). Therefore, to account for this tradeoff, Δ is an interesting metric. Moreover, this metric also has practical relevance since it represents the number of resolvable spectral channels that could be used in a spectral-multiplexed quantum network. A summary of the demonstrated linewidths and tuning ranges for different solid-state single photon emitters is shown in Table A.2. Recent work has demonstrated that strain tuning can be a valuable substitute for the Stark effect in systems with weak dipole moments (d). This tuning capability was used to achieve large Δ (Table A.2) and to demonstrate dynamically stabilized single photon emission [114]. We would also like to mention recent work in non-solid state systems (single molecules) [280], quoting this metric (Δ) and achieving $\Delta \sim 40,000$.

System	*Linewidth (x lifetime limit)*	*Stark Shift*	*Ratio (Δ)*	*References*
Results presented (VV^0)	**20-30 MHz (2-3x)**	**850 GHz**	**28,000-40,000**	This work
Estimated limit (VV^0)	10 MHz (1x)	3 THz	300,000*	This work
NV center	13–150 MHz (1-10x)	200 GHz	1,300-15,000	(*9*, *12*, *75*)
SiV center (diamond)	125 MHz (x1.5)	450 GHz (strain)	3,600	(*76*, *77*)
Vsi (SiC)	60 MHz (x2)	N/A	N/A	(*78*, *79*)
InGaAs/GaAs QDs	1 μeV (1.5-2x)	25 meV	25,000*	(*49*, *80*, *81*)
InP QDs	270 μeV (540x)	5 meV	18	(*82*)
h-BN	0.3-300 μeV (1-1000x)	20 meV	66-66,000*	(*83*, *84*)
MoS_2	100 μeV (?)	21 meV	210	(*85*, *86*)

Figure A.2: **Comparisons of Δ, the tuning-to-linewidth ratio.** Comparison of the tuning range to linewidth ratio for solid-state single photon emitters (Δ). Numbers with "*" have not been realized experimentally and are a simple combination of the best linewidths with the largest tuning reported. Numbers without "*" have been experimentally realized. The references in this table are not adapted to this thesis and the corresponding references can be compared in [6]

A.2.6 Estimate of the Sensitivity of the Optical Fine Structure to Electric Fields.

Using the following Lorentzian model for our count rate as a function of excitation frequency c(f):

$$c(f) = \frac{A}{\pi\gamma\left[1+\left(\frac{f-f_0}{\gamma}\right)^2\right]} \tag{A.1}$$

where f_0 is the resonant frequency, γ is the half-width at half-maximum (i.e. half of the linewidth), $A = c_{max} \cdot \gamma\pi$, where c_{cmax} is the maximum counts per second on resonance. First we must compute:

$$\frac{dc}{df} = \frac{-2A}{\gamma^2\pi}\frac{(\frac{x-x0}{\gamma})}{(1+(\frac{x-x0}{\gamma})^2))^2} \tag{A.2}$$

Then we note that our signal for an electric field of magnitude E is:

$$E\frac{dc}{dE}\cdot t = E\frac{dc}{df}\frac{df}{dE}\cdot t \tag{A.3}$$

And if we assume a shot noise limited signal we see that our noise is $\sqrt{c\cdot t}$. Therefore, we are trying to maximize:

$$\max_{f_{pai}} \frac{E\frac{dc}{df}\frac{df}{dE}\cdot t}{\sqrt{c\cdot t}} \tag{A.4}$$

We find that the extrema of that expression are at $f = f_0 \pm \frac{\gamma}{\sqrt{2}}$ and at that point, the signal-to-noise per second is:

$$\frac{S}{N\cdot t} = \mp\frac{df}{dE}\frac{4E}{(3\gamma)^{3/2}}\sqrt{\frac{At}{\pi}}\cdot\frac{1}{t} = \mp\frac{1}{\eta}\cdot E\frac{1}{\sqrt{t}} \tag{A.5}$$

Where *eta* is the sensitivity which we defined as electric field necessary for the signal-to-noise (per $\sqrt{Hz}$) to be 1. Therefore:

$$\eta = \frac{3\gamma}{4\cdot\frac{df}{dE}}\sqrt{\frac{3\gamma\pi}{A}} = \frac{3\gamma}{4\cdot\frac{df}{dE}}\sqrt{\frac{3}{c_{\max}}} \tag{A.6}$$

Using $\gamma = 40\ MHz$, and an isotropic (this approximation will suffice for this estimation) $\frac{df}{dE} = 10\text{GHz}\cdot\left(\frac{\text{MV}}{\text{m}}\right)^{-1}$ we get a single spin sensitivity of about $116\frac{\text{V}}{\text{m}}/\sqrt{\text{Hz}}$ (a conservative estimate). State-of-the art in spin based electrometry has sensitivities of $20,000\frac{\text{V}}{\text{m}}/\sqrt{\text{Hz}}$ [194] for single spins and $10\frac{\text{V}}{\text{m}}/\sqrt{\text{Hz}}$ for extremely large ensembles [195].

A.2.7 Stark Shifts from Single Charges

One way to understand the spectral diffusion in this work is to assume some nearby traps are capturing or releasing charges. So it is relevant to calculate the effect of a single point

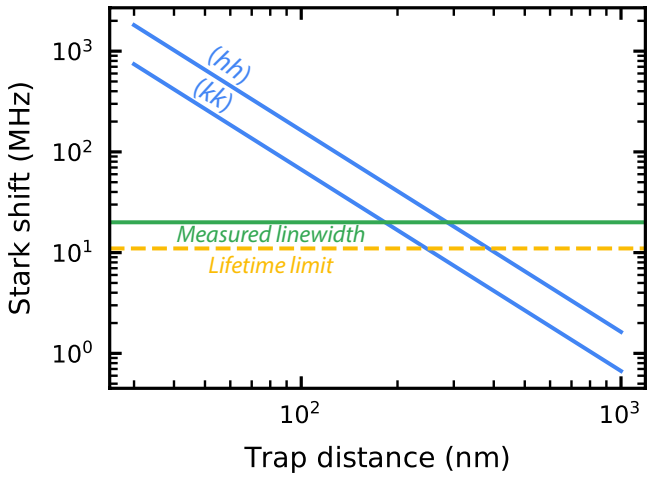

Figure A.3: **Stark shifts from single trapped charges.** Stark shift caused by a single trap at a given distance. The green line is the minimum measured linewidth and the yellow dashed line is the expected lifetime limit.

charge "appearing" in a trap near the defect. For this we simply use the Coulomb law:

$$\vec{E} = \frac{1}{4\pi\epsilon}\frac{e}{r^2} \tag{A.7}$$

Then if we assume a dipole strength of about $4-11$ GHz$\cdot$(MV/m)$^{-1}$ we get the rough relation shown in Fig. A.3. This suggests a very high sensitivity to free carriers and fluctuating trapped charges and helps us understand why charge depletion is useful.

We expect that the linewidth $\Gamma \propto \sqrt{N}$ from N uniform-strength fluctuators. With our measured reduction of the linewidth by a factor of 50, this corresponds to over three orders of magnitude reduction in fluctuating electrical charge traps. (A more accurate description is found in section 6.2, where $\Gamma \propto \rho^{2/3}$ and this is a $300\times$ reduction in fluctuating trap density) Note that the only relevant traps in these estimates are the fluctuating traps. For shallow traps like Nitrogen, most dopants will be fluctuating between charge states under illumination with almost any color.

A.2.8 Optical Linewidths in Other Commercial SiC Material, Generalizability

The narrowest linewidths achieved in commercial i-type material from the same company that provided the p-i-n diode material is around 120 MHz at best. For example, in the data in [7] the undepleted linewidth of a (kh) VV^0 is over 200 MHz for all observed defects for material from the same company (Fig. A.4A). A relatively good (hh) divacancy with linewidth of 135 MHz is shown in Fig. A.4B. For specially grown material, one defect was found with a 80 MHz linewidth, but most defects from that sample were above 120 MHz in linewidth[55]. These linewidths are sample dependent and depend on the impurity density that causes spectral diffusion.

We note that in Ref. [7], a similar narrowing effect with comparable magnitude is demonstrated as an extension of this work. Furthermore, all observed defects here displayed qualitatively similar linewidth reduction. In general, the techniques shown in this work offer a possibility to mitigate noise from residual impurities in a wide range of solid-state materials (not limited to SiC) with charge depletion.

A.2.9 Temperature Dependence of the Linewidth

The temperature dependence of the linewidth gives a physical understanding of the dephasing mechanism. At higher temperatures than those studied here (> 15 K) [55] the linewidth for single VV^0 follows a T^5 power law. This power law is consistent with a Raman two-phonon dephasing that exists for the NV^- center[281]. However, these previous studies were limited by broad lines that did not allow a study of the temperature dependence below 15 K (limited by impurities). At these low temperatures, the power law deviates from T^5 and is fitted to be closer to a T^3 power law for single (kk) VV^0. Power laws of the PLE linewidth in single emitters have been described ranging from linear to T^7, but a T^3 power law has been found to arise from two possibilities:

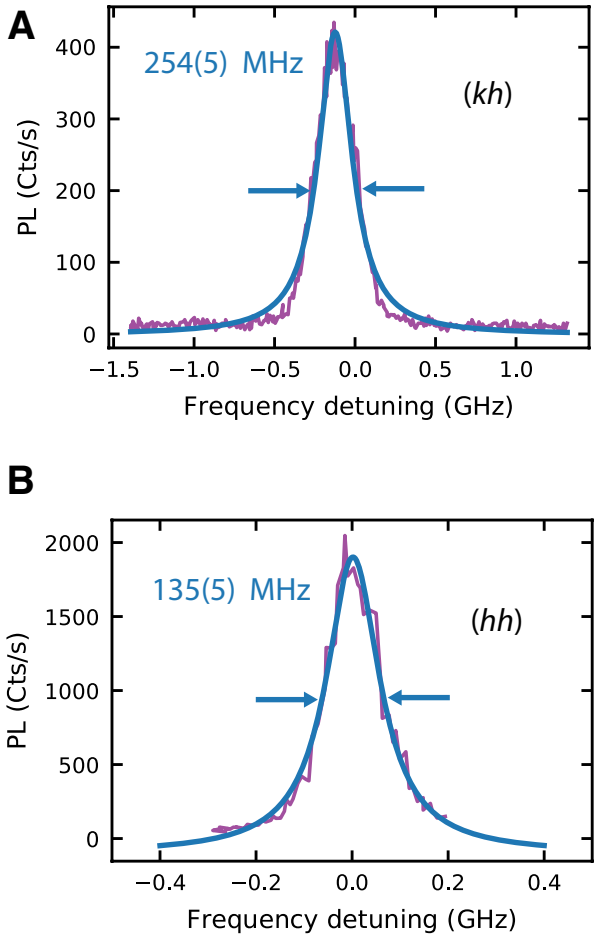

Figure A.4: **PLE spectra of defects in bulk intrinsic material.** **(A)** Example PLE scan of a single (kh) and a **(B)** single (hh) VV^0 in intrinsic commercial material (not the p-i-n diode measured here).

1. A two-phonon process in the limit where the strain is small compared to the spin-orbit interaction in the excited state [282], where at high strain it transitions to a T^5 power law.

2. A one-phonon process in a piezoelectric material [219].

Following [282], we believe case 1 is less likely due to the negligible effect of transverse asymmetry (strain) on the linewidth observed (Fig. 11.4B). Case 2 is plausible since SiC is a slightly piezoelectric material, in contrast to diamond. However, further investigation will be required to completely understand the origin of the observed power law. Furthermore,

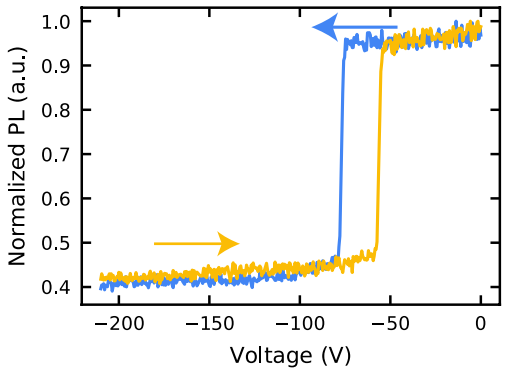

Figure A.5: **PL charge transition hysteresis.**

different temperature dependences and behaviors can be expected for the PL4 (hk) divacancy, due to the differences in orbital structure.

A.2.10 Threshold Hysteresis

The observed charge switching behavior under variable voltage has a hysteresis behavior, potentially related to trapping charges[201, 283]. An example curve is shown Fig. SA.5. Such trapping of charge under cyclic voltage waveforms forms the basis of performing EDMR[284] measurements in SiC.

A.2.11 Single Defect Charge Dynamics (Blinking)

In the main text, we mention a blinking behavior with continuous repump and ionization tones. An example of such behavior is shown in Fig. A.6. The binning of this "telegraph" behavior results in periods of high and low PL (near zero). In Fig. 11.6, we use the average time spent in the high state as a measure of the ionization rate and the average time spent in the low state as a measure of the repump rate. In this section, we demonstrate more formally why using these average times as a proxy for the rate is a valid approach.

First we assume that when we are in VV^0 state, there is a constant probability of ionizing (see the Markov chain in Fig. A.7). Therefore, the process is memoryless and the only memoryless continuous function is the exponential function. Thus, the probability of a

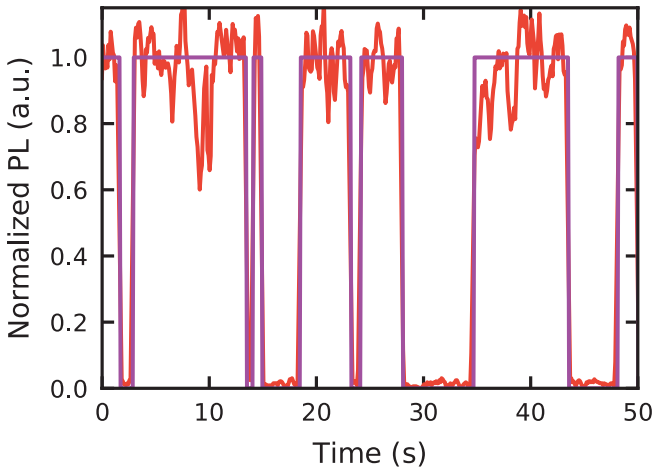

Figure A.6: **Blinking dynamics.** Example of blinking dynamics of PL (red) under continuous 688 nm and resonant excitation, with binning for analysis (purple).

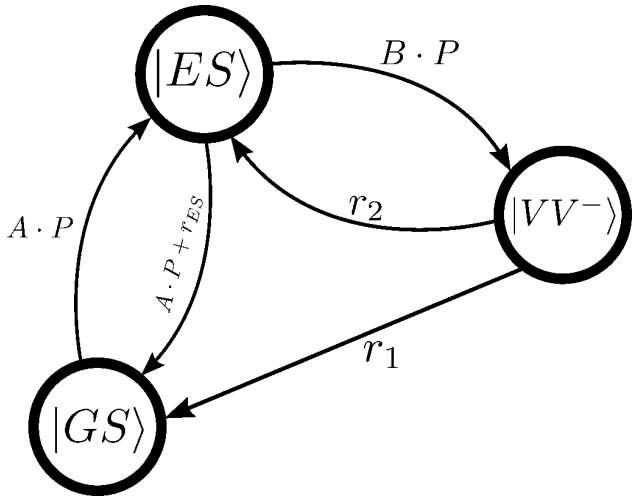

Figure A.7: **Markov chain of charge dynamics.** Markov chain diagram representing the transition rates involved in the ionization and repump processes.

"high event" having a duration t is:

$$P(t) = \frac{1}{\tau} e^{-t/\tau} \tag{A.8}$$

where $\frac{1}{\tau}$ is the ionization rate. In our analysis we take the duration of several "high events" and consider them as sampling $[X_0, \ldots, X_N]$ of a random variable X sampled from

the probability distribution above. Since we know that:

$$E[X] = \int_{x=0}^{\infty} x \cdot \frac{1}{\tau} e^{-\frac{x}{\tau}} dx = \tau \int_{\alpha=0}^{\infty} \alpha e^{-\alpha} d\alpha = \tau \tag{A.9}$$

We estimate the ionization rate τ^{-1} using the maximum likelihood estimator which corresponds to the sample mean $\hat{\tau} = E[X] \approx \bar{x}$. Additionally, we can calculate the error bar we should use for the sample mean by estimating the confidence interval. This is done first by transforming our random variable to $\tilde{X} = \frac{2 \cdot X}{\tau}$ (where τ is the actual distribution mean (as opposed to the estimator) and therefore $\tilde{X}$ now has a mean of 2). Then, by noting that the distribution of the sum of N exponential random variables $\tilde{X}_0 \ldots \tilde{X}_N$ (with mean 2) is equal to the Gamma distribution:

$$\sum_i \tilde{X}_i = \Gamma_{N,2}(\tilde{x}) = \frac{1}{\Gamma(N) 2^N} \tilde{x}^{N-1} e^{-\tilde{x}/2} \tag{A.10}$$

This is simply the pdf of the chi-square distribution with $2N$ degrees of freedom $\chi^2_{2N}(\tilde{x})$. Therefore,

$$\frac{2}{\tau} \sum_i X_i = \sum_i \tilde{X}_i = \chi^2_{2N}(\tilde{x}) \tag{A.11}$$

If we define the quantile function Q as the inverse of the χ^2_{2N} CDF (i.e. $Q_{2N}\left(CDF_{2N}(\tilde{x})\right) = \tilde{x}$) we see that $Q_{2N}(p) = \tilde{x} : p = P(\tilde{X} \leq \tilde{x})$ (For a continuous and strictly monotonic CDF). Therefore, for a confidence interval of $(1-\alpha)\%$ we want:

$$Q_{2N}(1-\alpha/2) < \frac{2}{\tau} \sum_i X_i < Q_{2N}(\alpha/2) \tag{A.12}$$

Therefore, we have:

$$\frac{2 \sum_i X_i}{Q_{2N}(1-\alpha/2)} < \tau < \frac{2 \sum_i X_i}{Q_{2N}(\alpha/2)} \tag{A.13}$$

which reduces to

$$\frac{2N\hat{\tau}}{Q_{2N}(1-\alpha/2)} < \tau < \frac{2N\hat{\tau}}{Q_{2N}(\alpha/2)} \tag{A.14}$$

Where $\hat{\tau} = \bar{x}$ is our sample mean. In our analysis we use the Python scipy.stats.chi2.ppf function to compute $Q_{2N}(p)$. For our error bars we used a 2-sigma equivalent interval of 95.6% ($\alpha = 4.4\%$). Reference for this analysis is described in [285].

A.2.12 Theory of Two-Photon Ionization

Two explanations have been suggested for the ionization of the divacancy in SiC. One proposes a two-photon ionization into the negative charge state VV^- [11, 62], the other suggest a four step process into VV^+ [192, 226] involving a total of three photons in the process. Our results (Fig. 11.6A) show a quadratic behavior (consistent with two-photon) below saturation and a linear relation after saturation is reached. The only way two reconcile these results with the proposed VV^+ scenario is to assume the second photon excitation (ΔE_2^a in Fig. 3 of[192] is much more efficient at $\sim 265\ THz$ then the initial excitation (ΔE_1^a in the same figure). We find this unlikely since the first excitation is specifically made to be resonant and the second excitation would most likely be off-resonant. Therefore, for the purpose of this section we will assume a simple two-photon ionization process consisting in:

- One excitation from the ground-state ($|GS\rangle$) to the excited state ($|ES\rangle$)
- One excitation from the excited-state ($|ES\rangle$) to the ionized state ($\left|VV^-\right\rangle$)

Two-photon ionization events are usually assumed to be quadratic in power. However, this is only a valid assumption in the limit of a very short (or even virtual) intermediate state lifetimes. For an intermediate state lifetime similar to excitation times or above (saturation), the behavior becomes linear. To see the analytical form of the power dependence, let's use the following states (shown in Fig. A.7)

$$\vec{\phi} = \begin{bmatrix} \phi_0 \\ \phi_1 \\ \phi_2 \end{bmatrix} = \begin{bmatrix} GS \\ ES \\ VV^- \end{bmatrix} \tag{A.15}$$

And setup the following rate equations:

$$\frac{\partial\vec{\phi}}{\partial t} = \begin{bmatrix} -AP & AP+\Gamma_{\mathrm{ES}} & r_1 \\ AP & -AP-BP-\Gamma_{\mathrm{ES}} & r_2 \\ 0 & BP & -r_1-r_2 \end{bmatrix} \cdot \vec{\phi} \tag{A.16}$$

We can get the steady state solution by getting the eigenvector corresponding to an eigenvalue of 0. In this case the non-normalized solution is:

$$\begin{aligned} \phi_0 &= \tfrac{(r_1+r_2)(AP+\Gamma_{\mathrm{ES}})}{ABP^2} + \tfrac{r_1}{AP} \\ \phi_1 &= \tfrac{r_1+r_2}{BP} \\ \phi_2 &= 1 \end{aligned} \tag{A.17}$$

From these we can calculate various quantities of interest.

Ionization Rate

For the ionization rate we are looking for the probability of transition to VV^- given that we are in VV^0. First we compute:

$$\mathrm{Prob}\left(\mathrm{ES}|VV^0\right) = \frac{\mathrm{Prob(ES)}}{\mathrm{Prob(ES)}+\mathrm{Prob}(GS)} = \frac{\phi_1}{\phi_0+\phi_1} = \frac{AP}{2AP+BP\frac{r_1}{r_1+r_2}+\Gamma_{\mathrm{ES}}} \tag{A.18}$$

Then the ionization rate is given by:

$$\mathrm{Prob}\left(\mathrm{ES}|VV^0\right)\cdot BP = \frac{ABP^2}{2AP+BP\frac{r_1}{r_1+r_2}+\Gamma_{\mathrm{ES}}} \tag{A.19}$$

This is used in the fit of Fig. 11.6A.

PL From Off-Resonant with a Red Repump

Here we assume the main source of repump is from the red (not the off-resonant NIR laser). If we hold the red power constant, the effective repump rates can still be empirically describe

by r_1 and r_2. Here we are interested in:

$$\text{Prob}(ES) = \frac{AP}{\frac{BP(AP+r_1)}{r_1+r_2} + 2AP + \Gamma_{\text{ES}}} \tag{A.20}$$

In the high power regime,

$$\text{Prob}(ES) \approx \frac{r_1 + r_2}{BP} \tag{A.21}$$

Since $\text{PL} = \Gamma_{\text{ES}} \cdot \text{Prob(ES)}$ this demonstrates why at high power the PL disappears for both singles and ensembles.

PL From Off-Resonant with an Off-Resonant Repump

In the case of 905 nm illumination for example, the repump power is proportional to the pump power therefore if we substitute r_i for $P \cdot r_{i,P}$ we find:

$$\text{Prob}(ES) = \frac{AP}{\frac{BP(A+r_{1,P})}{r_{1,P}+r_{2,P}} + 2AP + \Gamma_{\text{ES}}} \tag{A.22}$$

Therefore, at high power we have a finite constant equilibrium population:

$$\text{Prob}(ES) \approx \frac{A}{\frac{B(A+r_{1,P})}{r_{1,P}+r_{2,P}} + 2A} \tag{A.23}$$

A.2.13 Possible Resonances for the Charge Reset

The observed charge repumping and reset can have multiple origins (as described in the main text). Here we suggest two possibilities for this resonance. Charge Trap Photoionization The energy of 710 nm is approximately 1.75 eV, corresponding to a charge trap having a photoionization resonance [286] at this energy. Upon ionization, this trap can provide a carrier for the VV to capture. Looking for possible candidates for this resonance by matching with formation energies calculations [62] we identify V_c, which is the most common compensating defect in our SiC samples. Therefore, we find V_c to be the most plausible trap

candidate. V_c transitions from $0 \rightarrow +$ can occur at energies above $E_g - 1.8\ eV \sim 1.5\ eV$ and its transition from $+ \rightarrow 0$ can occur above $\sim 1.8\ eV$. Therefore, once that photon energy is reached, V_c can freely cycle between $0 \leftrightarrow +$ resulting a source of free carriers (both electrons and holes) which can recombine with the divacancy.

Direct Ionization

The other possibility is a direct ionization of VV^-. Direct ionization to the conduction band (CB) is predicted to occur at a pump energy $E_p > 1.3\ eV$ from experiment and theory [11, 62]. However, VV is known to have a second set of $e_x,\ e_y$ single particle orbitals that lay in or near the CB. These orbitals could result in a resonance in the band (near 1.75 eV) that very efficiently converts VV^- to VV^0. Such a resonance for ionization has been proposed for both the NV^- center in diamond [206] and for the VV[226]. Initial DFT results point to several possible resonances in the charge dynamics from the singlet and triplet states[94] that could be related to this or changes in the DOS in the CB.

A.2.14 Spectral Diffusion and Ionization Under Various Illumination Wavelengths

In optimizing the repump, we show that the reset rate is most efficient around 710 nm (Fig. 11.6C). Here, we show that this wavelength is also ideal in that there this little added spectral diffusion or ionization added (Fig. A.8). Sweeping over the PLE resonance many times (Fig. A.9) and integrating the total intensity over many sweep gives the time-averaged intensity of the line. This time averaged PL is high when there is no added ionization and low when significant photoionization is present. The inhomogeneous linewidth quoted represents the time-averaged PLE width over many scans and many minutes. This metric captures added spectral hopping from the choice of repump wavelength.

We observe that around 710 nm negligible ionization and broadening is added to the PLE lines, while higher energy illumination such as 520 nm (2.38 eV) is found to greatly increase

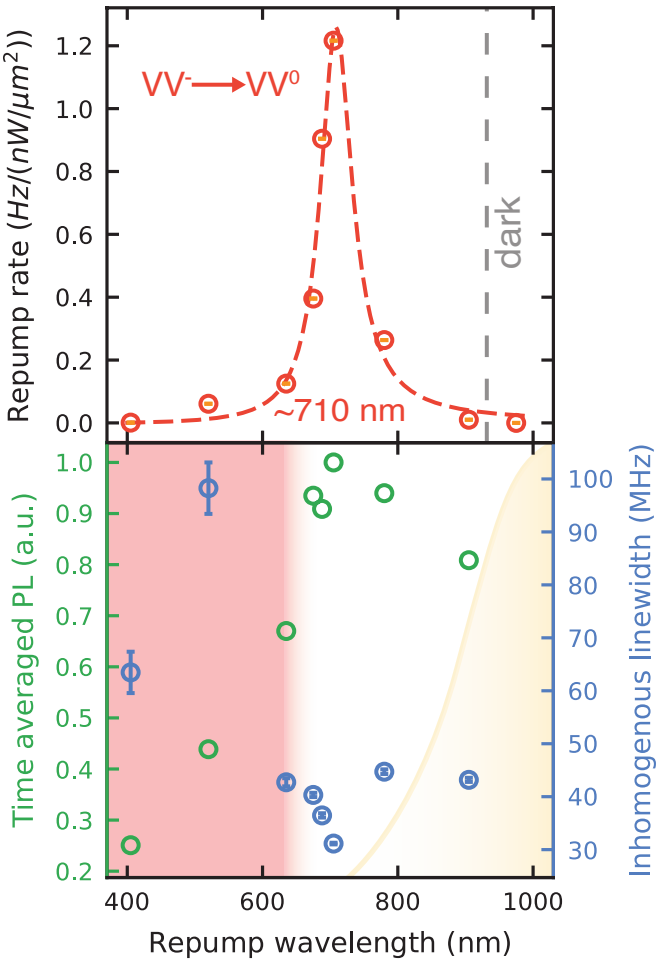

Figure A.8: **Optimizing the charge reset laser color.** (top) shows the data from 11.6C. (bottom) shows the total PLE integrated intensity (green) over many sweeps (such as in 11.4D), this metric includes blinking and any other photo-instability which manifests as reduced signal. PLE inhomogeneous linewidth (blue) over many scans with no compensation for jumps or drifts as a function of wavelength. Each wavelength has the same power at sample ($\approx$ 180 nW). The shaded areas are guides to the eye representing the onset of two-photon ionization (yellow) due to the absorption sideband of VV^0 and the energy by which VV^0 is directly one-photon ionized (red). All error bars represent 95% confidence intervals from the fit of the raw data and are from a single (kk) VV^0.

the added ionization and spectral diffusion, consistent with a direct ionization process predicted through defect formation energies[192]. In ensembles, off-resonant light around 905 nm (1.37 eV) was found to be near optimal in producing PL, as that wavelength both excites the defect and repumps the charge state [11, 62, 226]. Here, we confirm those dynamics in a single defect, where 905 nm adds a small amount of repumping, while a 975 nm (1.27 eV)

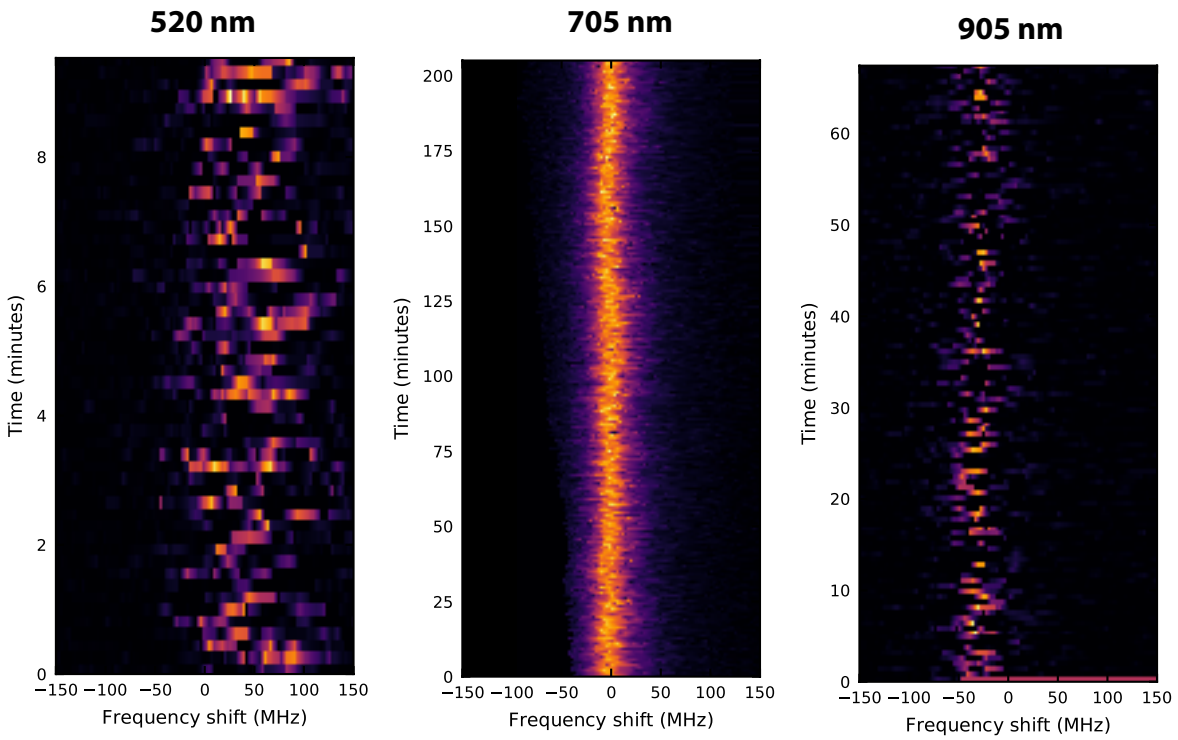

Figure A.9: **Color dependence of blinking and spectral diffusion.** PLE sweeps over many scans at different wavelengths. These scans were used to generate the data in A.8. Plots share same x-axis but different total times. Increased spectral diffusion is apparent with the 520 nm and additional blinking is observed with the 905 nm. These scans are at the same optical power. The 705 nm plot corresponds to Fig. 11.4A.

laser bleaches the defect without recovery with these powers (Fig. A.8). However, 905 nm excitation also increases the ionization rate and is much less efficient than red laser colors around 700 nm in resetting the charge (Fig. A.9). In addition, due to the higher powers necessary to stabilize the charge, 905 nm similarly adds to spectral diffusion of the PLE lines resulting in a broadening [202]. In general, because the absorption of resonant light is very efficient, it is preferable to use off-resonant light whose greater power causes much higher two-photon ionization rates. However, some off-resonant illumination energies (such as 905 nm) can additionally repump the divacancy into the correct charge state, while resonant light does not reset the charge charge of VV^0. Therefore, to reduce all unwanted ionization and to have independent and efficient control of the charge state, the ideal scenario is to use resonant light and a designated charge reset laser to stabilize the defect (red, ∼710 nm).

λ (nm)	σ_a (cm^{-2})	σ_i (cm^{-2})	σ_r (cm^{-2})
1131	$8 \pm 2 \times 10^{-12}$	$5.0 \pm 0.2 \times 10^{-19}$	0
975	$9.4 \pm 0.3 \times 10^{-12}$	$1.2 \pm 0.2 \times 10^{-17}$	0
905	$4.0 \pm 0.4 \times 10^{-17}$	$8.5 \pm 0.4 \times 10^{-18}$	$2.90 \pm 0.03 \times 10^{-20}$
705	0	-	$3.5 \pm 0.04 \times 10^{-18}$

Figure A.10: **Ionization and reset cross sections.** Cross sections for absorption (σ_a), ionizing (σ_i) and repumping (σ_r) with various illumination wavelengths. For reference, the saturation power at sample is 14 mW for 905 nm and 9 mW for 975 nm.

A.2.15 Charge Ionization and Repumping Cross Sections

With the power dependences of Fig. 11.5A, and Fig. 11.6A, along with the equations in section A.2.12, we can extract the relevant ionization and repumping cross sections as shown in Table S2A.10. This uses the relation:

$$\text{Rate } = \frac{P\sigma}{A\hbar\omega} \tag{A.24}$$

Where P is the optical power over area A (the spot size), and $\hbar\omega$ is the energy of a single photon of a given wavelength. We also use the fact that the saturation of the emitter occurs: $PL(P) = \frac{A}{1+P/P_{\text{sat}}}$, where $\frac{1}{\tau} = \frac{P_{\text{sat}}\sigma_a}{A\hbar\omega}$ and is the emitter lifetime of $\sim 15\ ns$.

A.2.16 Deterministic Charge Control

In the main text, deterministic charge control is claimed to be possible. Here, we will discuss that claim. In general, the charge control is deterministic if there is an independent control of both $VV^0 \rightarrow VV^-$ and $VV^- \rightarrow VV^0$, such that upon applying that control, the desired charge state can be set with high fidelity. The selectivity of these rates determines the maximum fidelity possible of the desired charge state, and the rates themselves determine the time the control needs to be on for a given fidelity. First, at these temperatures the

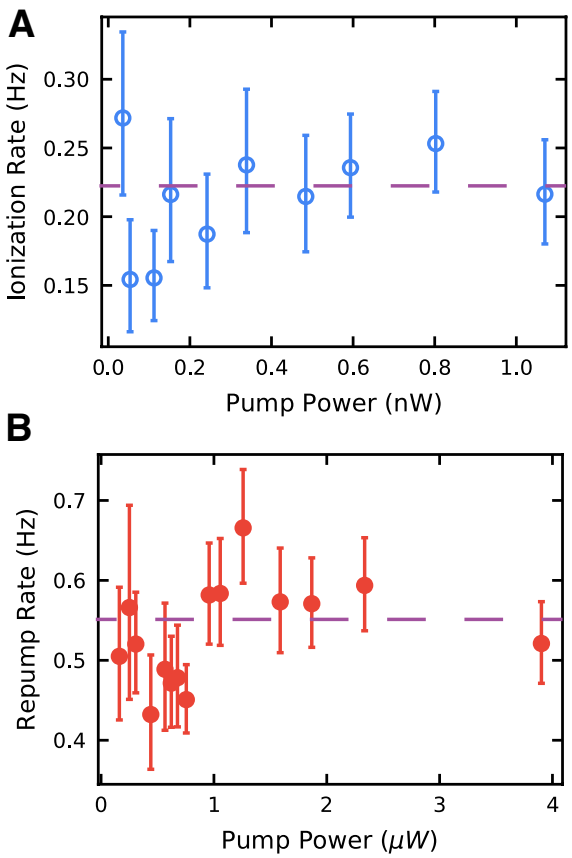

Figure A.11: **Deterministic charge control. (A)** Ionization rate with changing repump power. **(B)** Reset rate with changing resonant power. The independence of the charge reset rate on ionization power and the charge ionization rate on reset power demonstrated independent and therefore deterministic control.

charge states are extremely stable [11], so no thermal process can interfere with the control. Second, we demonstrate that upon changing the repump power, the ionization rate does not change (Fig. A.11A) and that upon changing the resonant power, the repump rate does not change (Fig. A.11B).

Thus, the red repump and the resonant two-photon ionizing laser are independent controls of the defect charge state. By pumping with red for an extended period of time, very high fidelity charge state initialization into VV^0 is possible. However, from Fig. S7 we note that the red repump may add a small amount of ionization. A conservative estimate from the errors on Fig. A.11 puts the ratio of the added change to about 1/10 to 1/20 of the

total ionization and reset rate, giving a lower limit of 90-95% deterministic charge state preparation fidelity. This fidelity is also for 688 nm repump wavelength, not the much more efficient reset around 710 nm. This already competes with the best charge state manipulation of the NV^- in diamond, and we expect the true fidelity to be higher [177]. In principle, the well-resolved periods of low and high PL demonstrated means that single-shot charge readout is attainable, allowing for measurement and correction towards a particular charge state. We note that this deterministic charge state control is optimal under electric fields, where ionization events cause the charge to drift and be lost, instead of being able to be recaptured by the defect. For example, at zero electric field most single defects are stable under resonant excitation, as they live in a bath of photoionized charges (undepleted).

A.2.17 Distinction Between Different Types of Inhomogeneous Broadening

In the main text we show how one can use electric fields to reduce spectral diffusion of the optical lines which contributes to the overall "inhomogeneous linewidth". However, the term "inhomogeneous linewidth" is used in various contexts to refer to several different effects which can broaden the line from the fundamental "homogeneous linewidth". As such, we would like to make a distinction here between a few different types of "inhomogeneous broadening" and discuss the relevance of these effects and how they relate to our system. First, for a single defect, spectral diffusion over time can cause inhomogeneous broadening of the optical line. We'll call this "temporal inhomogeneous broadening". This "temporal broadening" as compared with the homogeneous linewidth is indeed of critical importance and is one of the main issues addressed in this work. As we have shown in Fig. 11.4, the "temporal inhomogeneous broadening" seems to be mainly due to electric field noise and can be mitigated to a great extent by charge depletion. In Fig. 11.4A, we observe this temporal inhomogeneous linewidth to be around 31 MHz over 3 hours. As mentioned in Fig. 11.4C and in section A.1 section, we believe this could be further improved by slightly lower

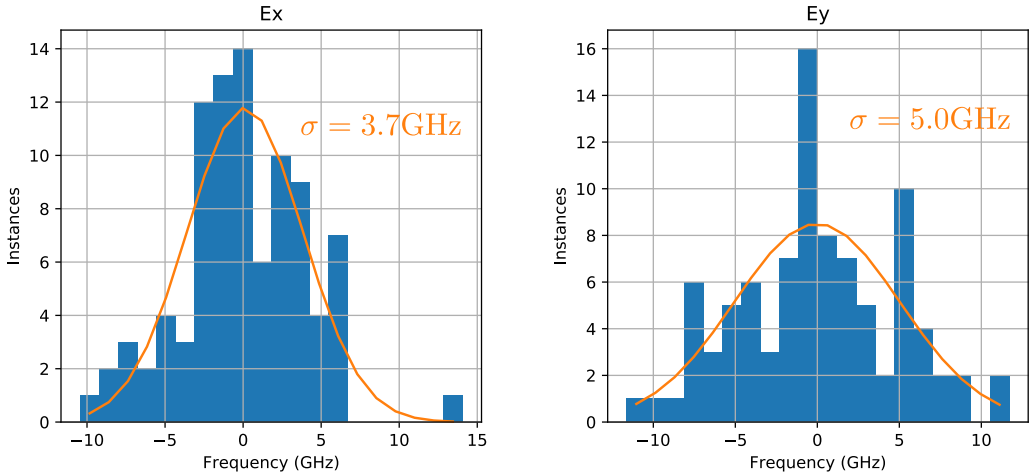

Figure A.12: **Histograms of PLE center frequencies.** Spatial inhomogeneous (defects at different spatial locations) optical frequency distribution for (kk) defects in a semi-insulating sample for both the E_x (left) and E_y (right) transitions.

sample temperature and less instrumentation errors on the wavelength readout. Second, for a set of defects spatially distributed in a sample, we can observe some shifts in the exact position of the optical lines most likely due to local strain variations. We'll call this "spatial inhomogeneous broadening". This is an important criterion, since it sets a lower bond for the Stark shift necessary to enable two random defects to be tuned into resonance with one another. Here, we have provided an estimate based on statistics taken on a semi-insulating sample (see Fig. A.12). This data suggests that the "spatial inhomogeneous broadening" is roughly around 5 GHz, well below the demonstrated tuning range.

Third, one could also wonder about the variation between significantly different samples (different wafers having different strain, epilayer composition, growth conditions, for example We'll call this "sample-to-sample variation". A precise measure of "sample-to-sample variation" is tricky since we only have a distinct number of wafers and we generally try to have these wafers as similar as possible. However, our experience with several types of wafers (both commercially and custom grown, and with different epilayers) suggest variations to be on the order of ∼100-200 GHz. Of course, the more extreme the changes to the host material is, the higher these variations are expected to be. However, in a practical implementation

of a quantum node the samples at play would most likely be chosen to be nominally identical, thus greatly reducing this number. In short, our demonstrated tuning range of ∼850 GHz easily covers both the "temporal" and "spatial" inhomogeneous linewidth (by orders of magnitude) and would undoubtedly cover the "sample-to-sample" variations present in nominally similar chips.

A.2.18 Effect of Charge Depletion on Spin Coherence

In this work, we demonstrate the effect of charge depletion on the optical linewidth. However, one could also wonder what effects depletion might have on the spin coherences. Although this is beyond the scope for this paper (and we did not directly observe any obvious effects), we do believe this is an exciting research avenue. There are two possible ways in which charge depletion could contribute to longer coherences. First, the direct reduction in E-field noise could help to mitigate dephasing due to the E-field coupling terms in the spin Hamiltonian. Second, by changing the charge state of nearby traps, the depletion region could modify the total spin of these traps, potentially changing the effective induced B-field noise.

A.2.19 Charge Feedback Protocol and Rates

Charge dynamics are a major problem that many solid-state systems need to contend with. In the NV^-center in diamond for example, this issue has been addressed using feedback protocols [174]. In particular, these protocols require readout and control of the charge state of the defect. This manuscript demonstrates two aspects of our system which will make it amenable to these types of feedback protocols. First, the divacancy simply goes dark once ionized (without a red repump) and does not return to the neutral state even when a resonant readout laser is applied. This facilitates reading out the charge state, as a weak resonant tone (such that two-photon ionization is negligible) can confirm the presence or absence of the divacancy in the correct charge state, without causing unwanted charge flipping. Second, we show that we can use red light to deterministically repump into the

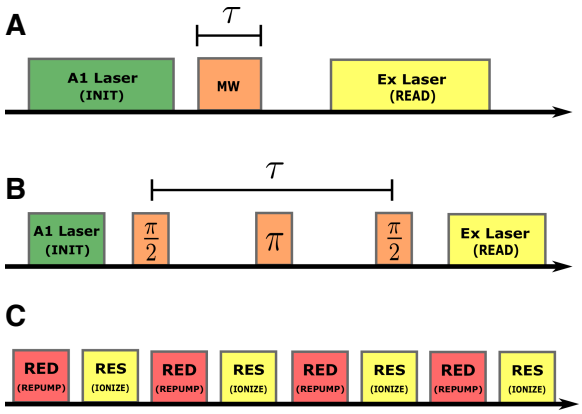

Figure A.13: **Pulse sequences.** Pulse sequences for **(A)** Rabi oscillations, **(B)** Hahn echo, and **(C)** charge hopping experiments. These correspond to the descriptions in A.1.

neutral charge state, giving us an ideal control for the feedback loop. Since this repump could be fast (by increasing the red power to a few mW) it would have minimal effect on the duty cycle. In general, the charge conversion rates demonstrated here are slow. However, this was mostly done for ease of experiment and to avoid timescales associated with the intersystem crossing. Despite this, there is no obvious limit for the ionization and reset rates, where we expect timescales of μs are readily accessible by increasing the powers from nW to mW [116].

A.2.20 Supplementary Plots

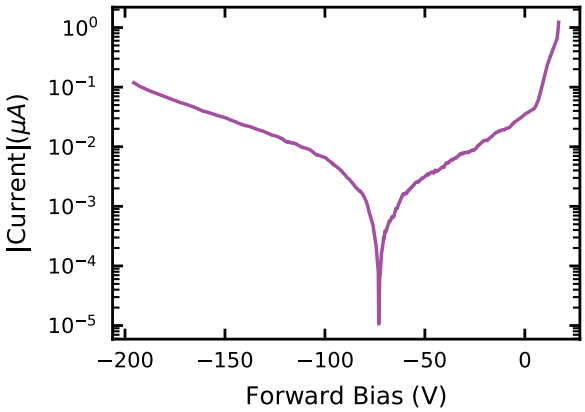

Figure A.14: **Semi-log plot of the absolute value of current from the IV curve for the device at 5K.**

Appendix B

Entanglement and Control of Single Quantum Memories in Isotopically Engineered Silicon Carbide: Details

This appendix contains preliminary supplemental details for [1].

B.1 Methods

B.1.1 Single Defect Observation and Control

Single defects are observed in a home-built confocal microscope operating at T= 5 K with a Montana Cryostation s100 closed-cycle cryostat. We utilize a high NA (0.85) NIR objective and single-mode fiber coupled (1060XP) IR-optimized SNSPD (Quantum Opus) and observe single defects with 40-50 kcts at saturation. 905 nm excitation is used along with a weak 705 nm tone for charge stabilization[6]. Microwave striplines are fabricated alongside an electrical control planar capacitor (10 nm Ti, 150 nm Au) using electron beam lithography. In 4H-SiC, single PL1 (hh), PL2 (kk) and PL4 (kh) defects are observed and are labelled following the V_cV_{Si} convention and where h represents the hexagonal lattice site and k the quasi-cubic

lattice site. The c-axis refers to the crystallographic axis in SiC which corresponds to the stacking direction of the hexagonal layers of SiC ([0001]). Basal defects are oriented along one of the basal planes. Resonant readout and initialization[6, 55] (realized using a tunable Toptica DLC PRO laser) can result in Rabi contrast exceeding 99% in optically detected magnetic resonance (ODMR) (Fig. B.1). This corresponds to the highest Rabi contrast reported in SiC and provides an achievable lower bound for initialization and readout errors combined. Reported coherences are for representative single defects.

For the strongly coupled nuclear spin experiments, Gaussian pulse shaping is used to perform spectrally narrow manipulation of the quantum registers. ^{13}C registers are also available[79], but occur with lower probability in both the natural and isotopic samples. For nuclear spin spectroscopy and control, randomized benchmarking and coherence measurements, square pulses were used with π pulse times ranging from 50 ns to 1 μs. Magnetic fields are applied with a large permanent magnet on a goniometer. Alignment at high field is achieved by reducing the mixing from off-axis magnetic fields, visible through the PLE magnitude after initializing the spin (a measure of cyclicity). In order to zero the magnetic field for kh divacancies, we utilize a three-axis electromagnet. Using a nearby c-axis kk defect as a magnetometer, the field is zeroed by reducing the splitting between the very narrow CW ODMR lines in the isotopically purified sample (<20 kHz).

B.1.2 Materials Growth

Natural 4H-SiC was obtained from Norstel AB (now ST Microelectronics) in the form of a 20 μm intrinsic epitaxial layer grown on 4 off-axis HPSI 4H-SiC. This layer contains $< 1 \times 10^{15}\ cm^{-3}\ V_c$. For the isotopically purified ("isotopic") sample, epitaxial 4H-SiC was CVD grown on a 4 degree off-axis n-type 4H-SiC substrate at a thickness of ∼90 μm using isotopically purified Si and C precursor gasses. The purity is estimated to be 99.85% ^{28}Si and 99.98% ^{12}C, which was confirmed by secondary ion mass spectroscopy (SIMS). C-V measurements show a slightly n-type behavior of this layer with a free carrier concentration

of $6 \times 10^{13} cm^3$. This roughly matches the measured concentration ($3.5 \times 10^{13} cm^{-3}$) of nitrogen through comparisons of the bound exciton lines. DLTS places the V_c concentration at the mid $10^{12} cm^{-3}$ range before irradiation.

In the naturally abundant material, single defects are created using a $110^{13} cm^{-2}$ dose of 2 MeV relativistic electrons. Subsequent annealing at 810 C in an Ar environment produces spatially isolated single VV^0. For the isotopically purified material, an electron dose of $1 \times 10^{13} cm - 2$ (Fig. 13.5) and $5 \times 10^{14} cm^{-2}$ (Fig. 13.1,13.2,13.3) are used. Despite the low impurity and defect content of the starting material, this means that the number of induced displacements[105] in the lattice after irradiation can be as high as $0.5 - 3\ cm^{-1} \times (dose) = (0.25 - 1.5) \times 10^{15}\ cm^{-3}$. These defects can be paramagnetic and most likely consists of V_C, V_{Si} and associated vacancy complexes. This is also a relatively common range even before irradiation in commercially available material. Upon annealing, divacancies are created along with other paramagnetic defects. Higher spin species or laser-induced scrambling of the charge states of these paramagnetic impurities may also increase the effect of impurities with respect to CCE.

Furthermore, the observed optical linewidth is significantly broadened by spectral diffusion. In this material, lines are in the 150-350 MHz range. We can use this broadening to estimate18 the trap density to be $3 \times 10^{14} - 3 \times 10^{15} cm^{-3}$ for the kk defect, which would be consistent with the observed Hahn echo times if these trap are assumed to be paramagnetic.

B.1.3 Calculations of Coherence Functions

Cluster-correlation expansion (CCE) calculations of the coherence function for the nuclear spins were carried out according to the method outlined by Yang and Liu[287] with the choice of parameters described by Seo et al.[102]. We apply the CCE up to second order under the assumption that the flip rate of each pair of electron spins is not impacted significantly by interactions with the spins outside a given pair. The total coherence function (L) can be factorized into contributions from electron and nuclear spins, respectively: $L(t) = L_{electron} \cdot$

$LL_{nuclear}$.

B.1.4 Calculations of Nuclear Memory Availability

In order to decide whether the nuclear spin at the lattice site i can be used as a memory, we evaluated the state fidelity of the electron spin state after a nuclear induced rotation. The fidelity can be inferred from the electron magnetization along the x-axis. Assuming that nuclei-nuclei interactions are neglegible, the expectation value of the electron magnetization along the x-axis at a given N and τ in the presence of a nucleus i can be expressed as

$$\tilde{M}_i = E\left(M|M_i \in M\right) = M_i \prod_{j \neq i} E\left(M_j\right) \tag{B.1}$$

where $M_i(M_j)$ is the conditional magnetization when only one nucleus (at lattice site $i(j)$) interacts with the electron, j runs over all other possible nuclear positions, and $E(M_j)$ is the expectation value of the conditional magnetization. A nucleus at lattice site j is considered to be useable as a memory unit if there exist at least one set of N and τ with $N2\tau$ smaller than a maximum gate time, such that the fidelity of the electron spin after rotation $\tilde{M}_i(N,\tau)$ is higher than a certain threshold F_{min}. The average number of nuclei i present at this lattice site is equal to the concentration of the spin-$\frac{1}{2}$ isotope c_i. The resulting total number of usable memory units is computed as the sum of c_i for all i that meet the fidelity criterion for at least one set of N, τ:

$$N_{\mathrm{mem}} = \sum_{i}^{F\left(\tilde{M}_i\right) \geq F_{\mathrm{min}}} c_i \tag{B.2}$$

B.1.5 Hyperfine Cutoff Value

A cutoff of $A_{\parallel} = 2\pi \cdot 60\ kHz$ is used in this work as a rough guideline for when hyperfine are low enough to act as optimal quantum memories. This corresponds to hyperfine values that were found to be ideal for communication protocols with the NV^{-} in diamond[179,

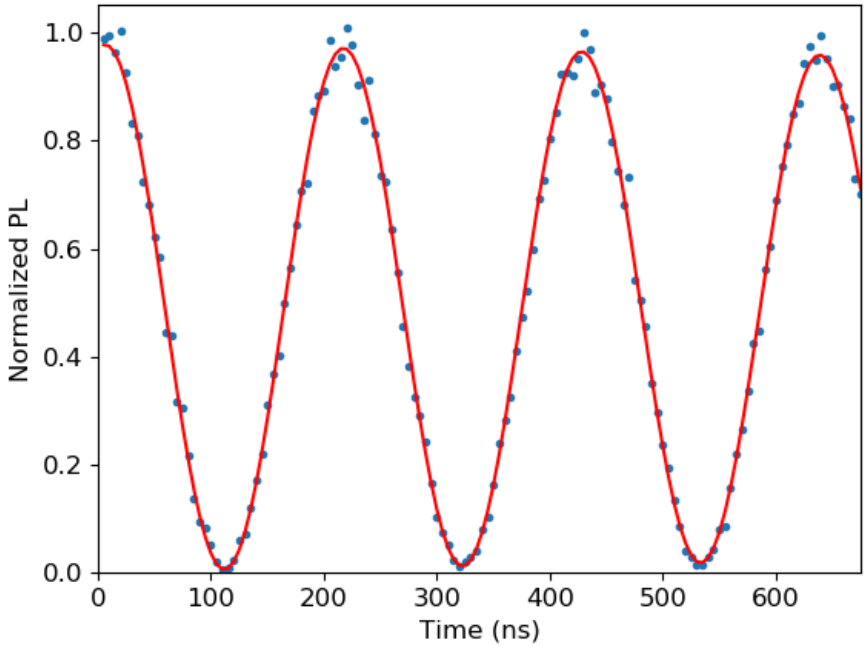

Figure B.1: **99% Rabi.** Rabi with $> 99\%$ contrast indicating that we can initialize, control and readout our electron spin qubit with less than 1% combined error.

180]. Coincidentally, this cutoff is also roughly the same order of magnitude as the ODMR linewidth we measure in isotopic samples (20 kHz) and provides an approximate limit for the lowest hyperfine spin which could be considered strongly coupled.

B.2 Supplementary Details

B.2.1 Probability to Have Strongly Coupled ^{29}Si Spins

When considering c-axis divacancy defects and only the 3 nearest sites[79], there are 12 possible ^{29}Si locations that result in a strongly coupled electron-nuclear system. The isotopic concentration of ^{29}Si is 4.685%. Thus, the probability of finding 0 or 1 strongly coupled ^{29}Si spins is:

$$P_0 = (1 - 0.04685)^{12}$$
$$P_1 = 12 \cdot (1 - 0.04685)^{11} \cdot 0.04685 \tag{B.3}$$

In order to evaluate the probability to find 2 strongly coupled ^{29}Si spins we need to ensure we do not count cases where the two ^{29}Si are at degenerate sites. Since there are two 3-fold degenerate cases and one 6-fold degenerate case, we have:

$$P_2 = (1 - 0.04685)^{10} \cdot 0.04685^2 \cdot (6 \cdot 3 \cdot 3) \tag{B.4}$$

Finally, for all three non-degenerate sites having exactly 1 ^{29}Si we have:

$$P_3 = (1 - 0.04685)^{9} \cdot 0.04685^3 \cdot (6 \cdot 3 \cdot 3) \tag{B.5}$$

Number of ^{29}Si	Probability
0	56.23%
1	33.16%
2	6.11%
3	0.36%

(B.6)

B.2.2 Initialization Fidelity of Strongly Couple Nuclear Spins

To determine the initialization fidelity, we use the fitted peak amplitudes in Fig. 13.1b, which correspond to the electron spin transitions at two different frequencies which depends on the nuclear spin state. We then simply use these peak amplitudes as the diagonal elements (populations) of a density matrix (with off-diagonal terms = 0). We then renormalize the elements such that the trace is 1 and then compare to the ideal target density matrix using the qutip.fidelity function which implements the following metric:

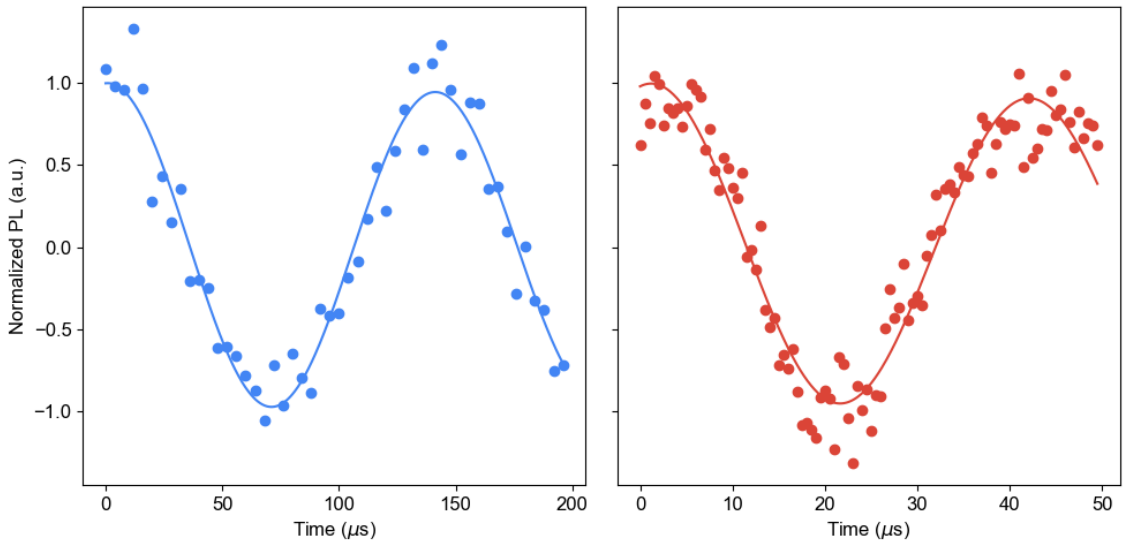

Figure B.2: **Two register control.** Independent control of the two nuclear registers in the strongly coupled 3-qubit system described in the main text. These correspond to a $C_{\pm 1}NOT_n$ rotation performed using a direct RF drive.

$$F(\rho, \sigma) = \sqrt{\mathrm{Tr}[\sqrt{\rho}\sigma\sqrt{\rho}]} \tag{B.7}$$

B.2.3 Independent Control of Nuclear Spins in the 3-qubit System

After finding a defect with 2 distinguishable strongly coupled nuclear spins, we demonstrate that we can control them independently by performing a nuclear Rabi oscillation on each of them. The results are shown in Fig. B.2.

B.2.4 Quantum State Tomography

To obtain the complete density matrix from our experiment we first need to perform the same experiment several time while swapping the readout sequence to probe the different terms of the density matrix[181]. Since we know that the density matrix is self-adjoint ($\rho_{ij=}\rho^*_{ji}$) we do not need to measure ρ_{ij} if we already know ρ_{ji}. Additionally, we know that the diagonal terms must be real and positive. Therefore, for a 4×4 density matrix we are left with 6 complex numbers (12 measurements) and 4 real numbers (4 measurements)

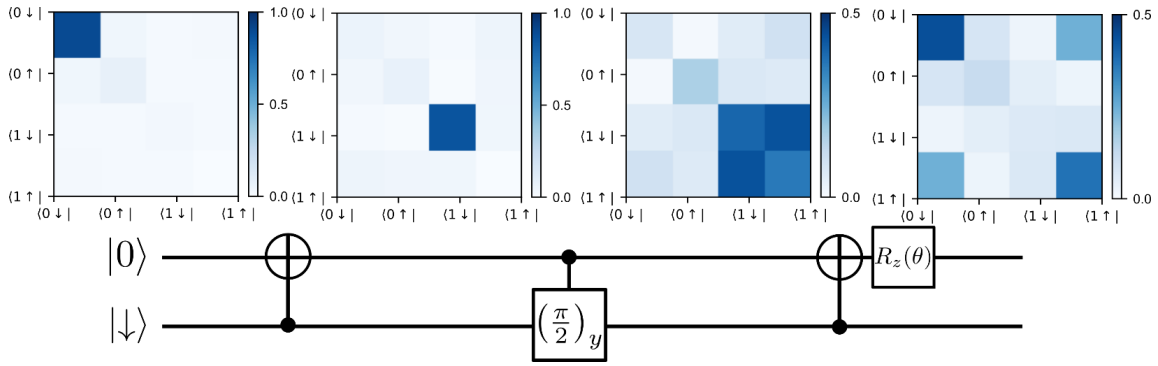

Figure B.3: **QST.** — Quantum state tomography showing the absolute value of the density matrix at every stage of the entanglement process shown in Fig. 13.1.

to be determined, which will require a total of 16 measurements. In addition, we record 1 value for a "zero" measurement (to subtract any systematic background) and 2 values that we can use to determine K (the brightness difference between the two electronic states in optical readout) by simply initializing the electron spin with a certain known fidelity (here we have used a conservative estimate of 90%). The off-diagonal terms are then simply obtained by normalizing the appropriate measurements by 2K. The diagonal terms can be found by solving the linear system composed by the 4 measurements. Note, that by using all 4 measurements we do not explicitly enforce that the trace should be one. Instead we simply we need to find the closest match of non-negative diagonal values such as to minimizes the square error and ensure a trace of 1. Thus we are essentially trying to fit an overdetermined set of linear equations.

B.2.5 Entangled State Fidelity

To create an entangled state, we use the quantum circuit shown in Fig. 13.1d and expanded in Fig. B.3. In this circuit, the last gate (Z-gate) is not explicit, but rather simply results from the fact that the state rotates under magnetic field in the standard rotating wave basis. We can show this rotation by varying the time delay between state preparation and readout (Fig. B.4). Therefore, to extract the true state fidelity, we can simply find the maximum fidelity with respect to a Z rotation angle (Fig. B.5). Doing so, we find a rotation angle of

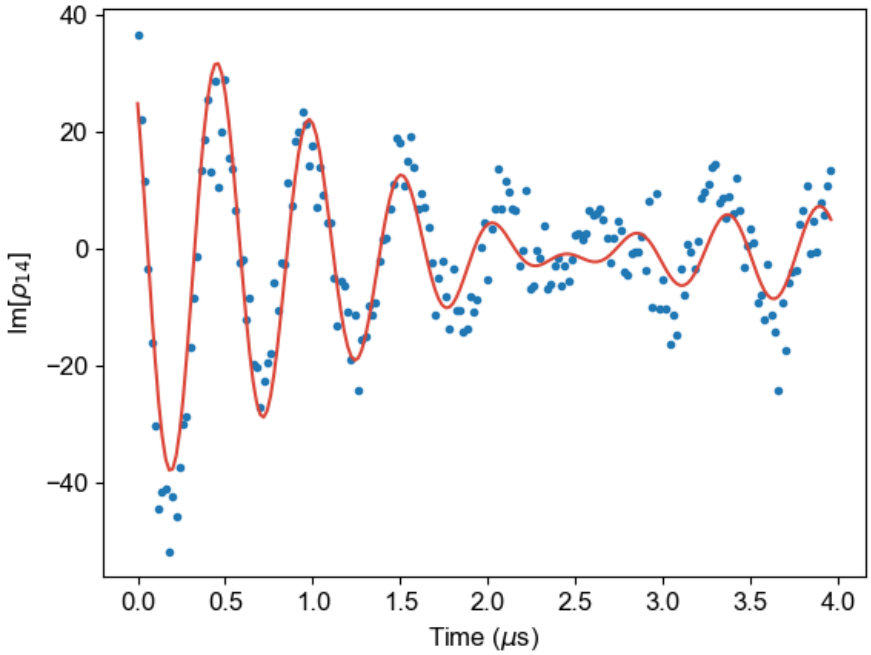

Figure B.4: **Entangled state oscillations.** Rotation that occurs as we increase the wait time before the state tomography.

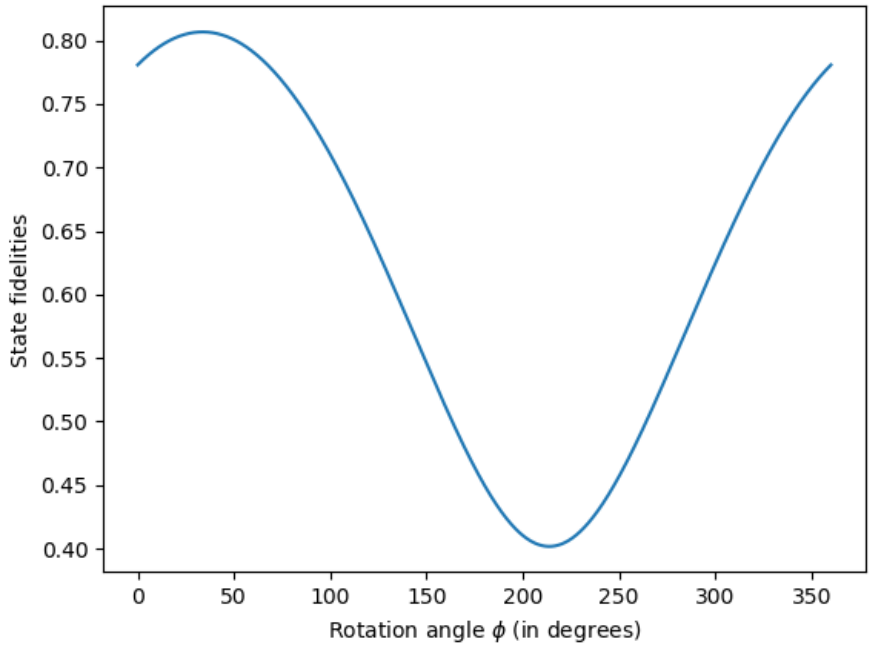

Figure B.5: **Entangled state fidelity as a function of assumed z-rotation**

32.1 degrees for the particular measurement delay in experiment, corresponding entangled state fidelity of 80.76% (as computed using the qutip.fidelity function[288]).

B.2.6 Positive Partial Transpose (PPT) Test

To confirm that we have an entangled state, we wish to check that the state corresponding to the density matrix is not separable. The Peres–Horodecki criterion (also known as the positive partial transpose (PPT) test) states that if $\rho^(T_A)$ has negative eigenvalues, then it cannot be separable. Applying this test to our density matrix we get one of the eigenvalue at -0.171 thus confirming a non-separable state

B.2.7 XY8 Pulse Sequence

For CPMG based control of the nuclear spins, we utilize a XY8-based sequence by alternating between X(I) and Y(Q) quadrature π pulses in the scheme:

$$\frac{\pi}{2}-(\tau-\pi_x-2\tau-\pi_y-2\tau-\pi_x-2\tau-\pi_y-2\tau-\pi_y-2\tau-\pi_x-2\tau-\pi_y-2\tau-\pi_x-\tau)^{N/8}-\tau-\frac{\pm\pi}{2} \tag{B.8}$$

With the spacing between the π pulses defined as 2τ, and the XY8 subsequence repeated N/8 times for total pulse number N. The $\pm\pi/2$ maps the coherence onto the $m_s = 0$ and $m_s = \pm 1$ basis for a differential measurement. The alternating control phases effectively corrects for pulse imperfections[289]. Our detection of weakly coupled nuclear spins involves varying the interpulse spacing and total pulse number.

B.2.8 Weakly Coupled 2-qubit Gates

Control of the weakly coupled nuclear spin is achieved using a sequence of successive π pulses spaced by $2\tau_k$ with[103].

$$\tau_k = \frac{\pi(2k-1)}{\omega_L + \omega} \tag{B.9}$$

where $\omega = \sqrt{\left(A_{\parallel} + \omega_L\right)^2 + A_{\perp}^2}$, ω_L is the Larmor frequency, $A_{\parallel}$ and $A_{\perp}$ are the hyperfine components and k is the dip order. At high magnetic field, this dynamical decoupling period rotates the nuclear spin around the $\pm x$ axis depending on the electronic spin state implementing an effective $C_eROT_{x,n}(\pm\theta)$. More specifically, for N/8 repetitions of the XY8 sequence, the nuclear spin rotates by[103].

$$\theta \approx \frac{N \cdot A_{\perp}}{\omega_L} + O\left(\left(\frac{A}{\omega_L}\right)^2\right) \tag{B.10}$$

We note that this constitute a fully entangling gate for $\theta = (2m-1)\pi/2$. Using single electron rotations we can transform a $U = C_eROT_{x,n}(\pm\pi/2)$ into a $CnNOTe$ like gate in the electron x-basis. This can be achieved for example using a sequence of

$$\frac{\pi_{e,x}}{2} - U - \frac{\pi_{e,y}}{2} \tag{B.11}$$

Additionally, when the resonance condition is not met, the dynamical decoupling sequence results in an unconditional z rotation of the nuclear spin. Combining conditional and unconditional rotations, full initialization and control of nuclear registers is possible

B.2.9 Control Fidelity of Weakly Coupled Nuclear Spin as a Function of τ Order (k)

In our nuclear spectroscopy (Fig. B.6), each nuclear spin results in a series of periodic dips in coherence at specific τ (with the space between π pulses of τ):

$$\tau_k \approx \frac{\pi(2k-1)}{\omega_L + \omega} \tag{B.12}$$

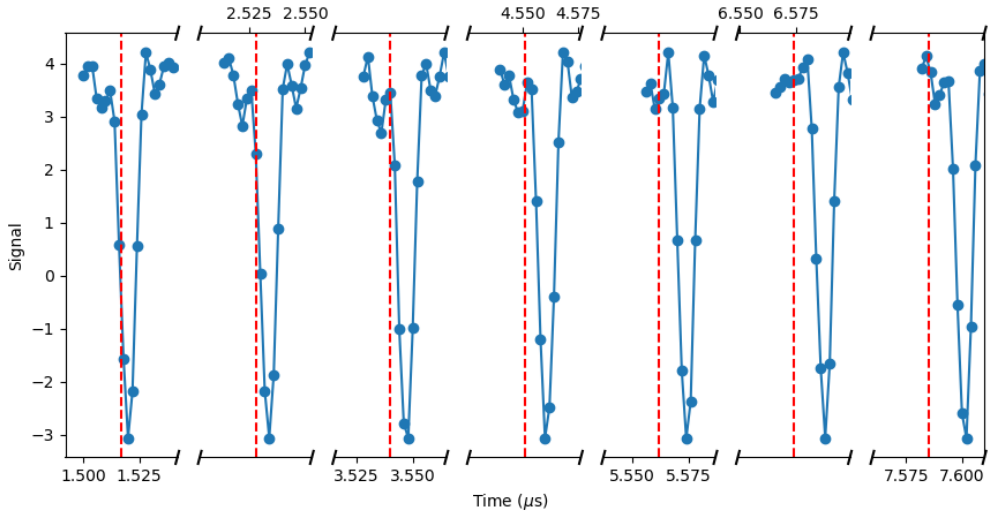

Figure B.6: **Nuclear spectroscopy.** Multiple order of the nuclear dips, with the red dotted line corresponding to the expected Larmor without a hyperfine (with the B field measured by the separation of the +1 and -1 electronic resonances)

Since every nuclear spin has its own frequency ω (due to the hyperfine), the dips caused by one nuclear spin becomes more isolated compared to dips caused by different nuclear spins. This allows for higher fidelity control of the nuclear spin at higher k, albeit by sacrificing gate speed. This is shown in Fig. B.7 and B.8 for the isolated nuclear spin in the main text.

B.2.10 Measurement of the Nuclear Spin Gyromagnetic Ratio

We perform CPMG NMR spectroscopy on the weakly coupled nuclear spin in the main text at two different magnetic fields. From the positions of the coherence dips we can extract the gyromagnetic ratio by calculating the frequency difference corresponding to the nuclear dip at two different values of B. We measure $|\gamma_n| \sim 8.50$ MHz/T (Figure B.9), identifying this nuclear spin to be a single ^{29}Si ($|\gamma_n| = 8.47$ MHz/T). This is expected since ^{29}Si is the most probable nuclear species available given the isotopic balance in the sample.

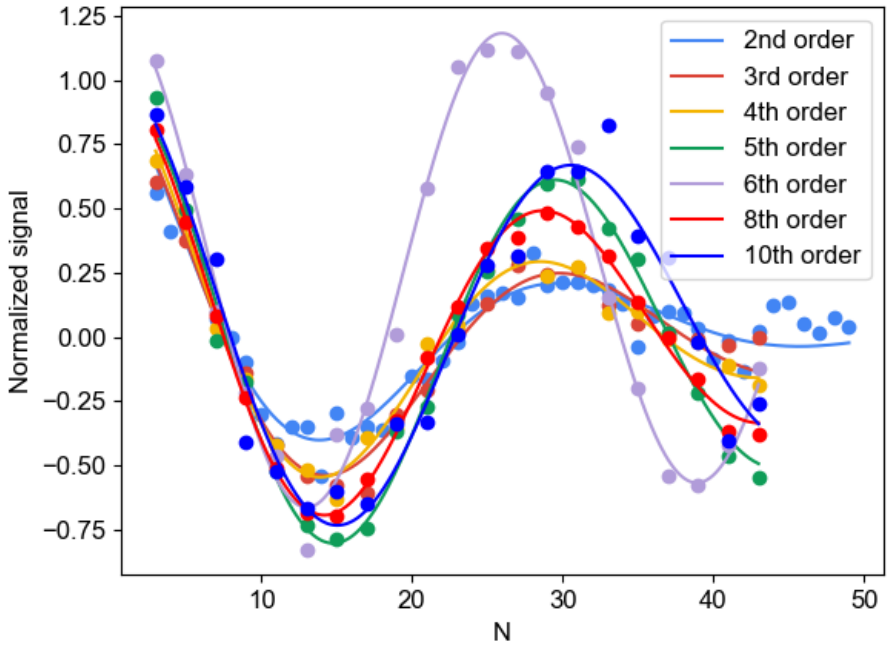

Figure B.7: **Nuclear oscillations obtained from different peak orders (k).**

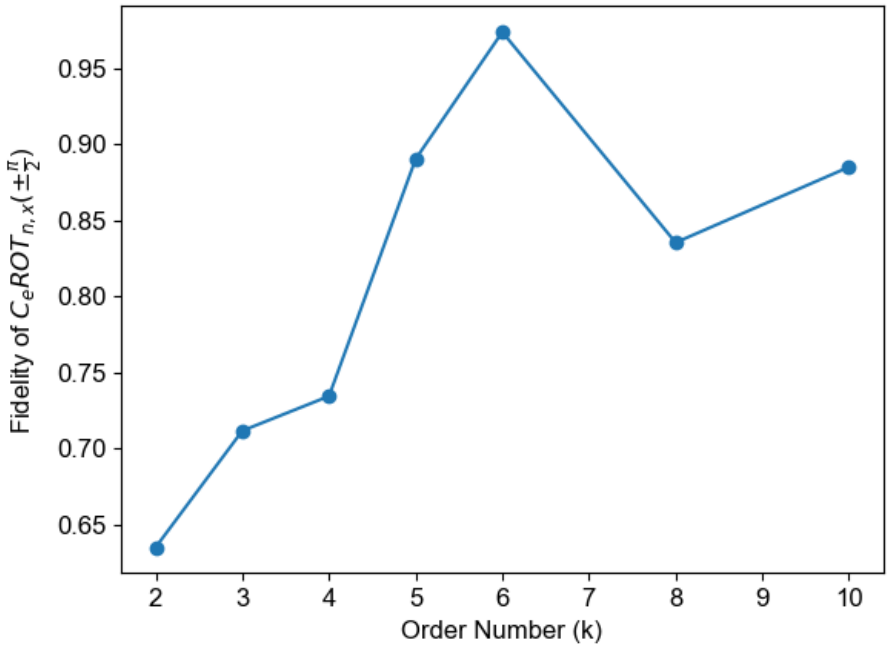

Figure B.8: **Fidelity of a conditional $\pi/2$ nuclear rotation as a function of order number.**

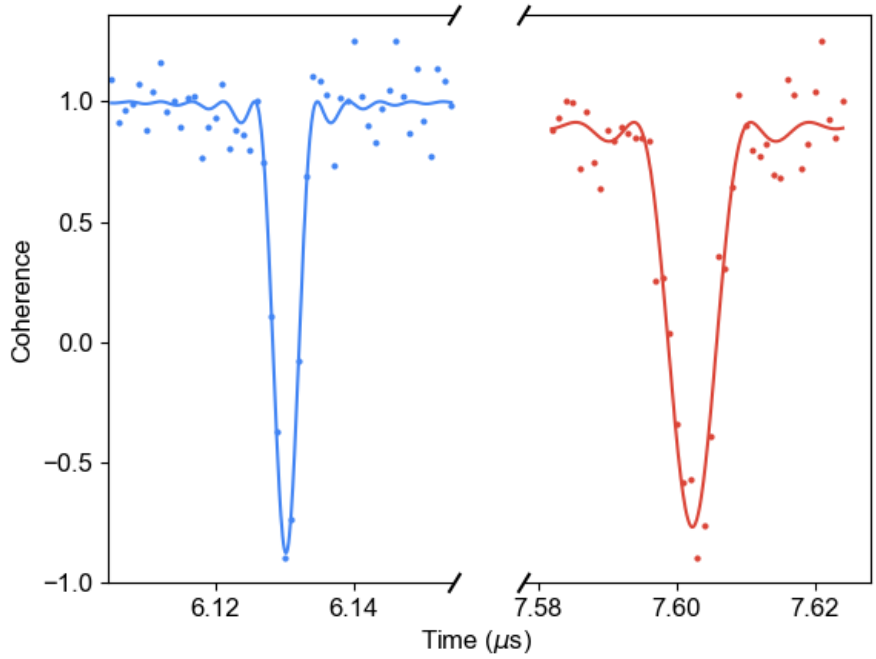

Figure B.9: **Gyromagnetic ratio check.** Checking $|\gamma_n|$ using the 8th order resonance at two different magnetic fields (58 mT in red and 72 mT in blue). Solid lines correspond to the fit.

B.2.11 Calculating the Hyperfine Values for Weakly Coupled Nuclear Spin

To calculate the hyperfine value ($A_{\parallel}$ and $A_{\perp}$) we use the following equations[290]:

$$A_{\parallel} = \frac{\omega_{+}^{2} - \omega_{-}^{2}}{4\omega_{L}} \tag{B.13}$$

Where $\omega_{\pm} = \frac{\pi \cdot (2k-1)}{2 \cdot \tau_{\pm}}$. $\tau_{\pm}$ are the coherence dip locations and k is the dip resonance order number. Additionally $\omega_L = B \cdot \gamma_{^{29}Si}$ is the Larmor frequency computed directly from the splitting of the $m_s = +1$ and $m_s = -1$ electron spin resonance lines. The perpendicular hyperfine is calculated from [103].

$$A_\perp = \sqrt{\frac{\left(A_\parallel + \omega_L\right)^2}{\left(\frac{N_\pi}{\pi}\right)^2 - 1}} \tag{B.14}$$

Where N_π is the number of pulses necessary to get a full π in the nuclear oscillations. In the limit of $\omega_L \gg A_\parallel$ and $N \gg \pi$ this simplifies to

$$A_\perp \approx \frac{\omega_L \pi}{N_\pi} \tag{B.15}$$

Note that these give the result in angular frequency (rad/sec) and we simply need to divide by 2π to get Hz. In our case, we calculate $A_\parallel \approx 2\pi \cdot 650\ Hz$ and $A_\perp \approx 2\pi \cdot 11.45 kHz$.

B.2.12 Locating Weakly Coupled Nuclear Spins

We assume that the hyperfine for distant nuclear spins is dominated by the dipole magnetic field of the electron which is oriented along z, with polar and azimuthal angles θ, ϕ:

$$\mathrm{B} = \frac{\mu_0}{4\pi r^3}|m|(3\hat{r}(\hat{z}\cdot\hat{r}) - \hat{z}) \tag{B.16}$$

The magnetic field at the nuclear spin is multiplied by the nuclear magnetic moment, and using the dipole moment of the electron $m = \gamma_e \hbar$ results in the hyperfine vector strength A (the elements of the hyperfine tensor along z):

$$\begin{gathered} \frac{A_0}{\hbar} = \frac{\mu_0 \gamma_n \gamma_e \hbar}{4\pi r^3} \\ \overrightarrow{\mathrm{A}} = A_0(3\hat{r}(\hat{z}\cdot\hat{r}) - \hat{z}) \end{gathered} \tag{B.17}$$

We can rewrite the radial unit vector and expand, using $(\hat{z}\cdot\hat{r}) = \cos(\theta)$

$$\overrightarrow{\mathrm{A}} = A_0(3\cos(\theta)(\cos(\phi)\sin(\theta)\hat{x} + \sin(\phi)\sin(\theta)\hat{y} + \cos(\theta)\hat{z}) - \hat{z}) \tag{B.18}$$

In particular we can break up the hyperfine in terms of those along z ($A_\parallel$) , and those

perpendicular ($A_\perp$)[291]

$$A_\perp = 3A_0 \cos(\theta)\sqrt{(\cos(\phi)\sin(\theta))^2 + (\sin(\phi)\sin(\theta))^2}$$
$$A_\perp = 3A_0 \cos(\theta)\sin(\theta) \tag{B.19}$$

And:

$$A_\parallel = A_0\left(3\cos(\theta)^2 - 1\right) \tag{B.20}$$

We can see that with these two equations, and by knowing the parallel and perpendicular hyperfine values we can locate our nuclear spin on a cone determined by θ at a distance r. ϕ is eliminated due to the symmetric nature of the dipole field. In our experiment, $|A_\perp| = 2\pi \cdot 11.45$ kHz, $A_\parallel = 2\pi \cdot 0.65$ kHz . We then solve for A_0 and θ, with $0 < \theta < \pi$ (spherical coordinates) and $A_0 < 0$ because the silicon gyromagnetic ratio is negative. Similarly, we know that our nuclear precession frequency increases (a measure of $A_\parallel$) with the use of $m_s = -1$ compared to $m_s = +1$. We know then that $A_\parallel > 0$[291]. With this, we get solutions at:

$$A_0 = 2\pi \cdot -8.273 \text{ kHz}$$
$$\theta = 56 \text{ \& } 124 \text{ degrees} \tag{B.21}$$

Solving for r using A_0, and using the gyromagnetic ratio for the silicon nuclei, r=1.24 nm. Measuring the sign of $A_\perp$ determines between the two possible polar angles, and the measuring the azimuthal angle is possible with similar techniques[291].

B.2.13 Electron Driven Nuclear Memory Decoherence

Besides obtaining a higher number of registers, weakly coupled nuclear spins are also desired because of their robustness to electronic spin manipulation. In particular, important protocols in quantum communication[44] requires one to store a state in the nuclear spin while manipulating the electron spin. While microwave manipulations are unitary and have

a deterministic time (which could presumably be accounted for[180]), the electron spin reinitialization or readout is inherently stochastic. Thus, this process (with a characteristic time related to the spin-flip rate and the ISC) can impart a random phase on the nuclear spin, thus causing the state to be dephase. This is due to the difference in nuclear precession frequency when the electron is in $m_s = 0$ or $m_s = \pm 1$ arising from the hyperfine interaction. For the NV^- center in diamond, one of every $\sim 10^3$ attempts produce entangled photons, with the Barret Kok scheme requiring $> 10^6$ attempts[246]. The nuclear memory therefore needs to withstand many thousands of entangling attempts, which involve reinitializing the electron spin. Using a model[246, 290] of the dephasing of weakly coupled nuclei caused by this process, we can get the fidelity of the nuclear state given N initializations of the electron.

$$F = \frac{1}{2} + \frac{1}{2^{N+1}} \left(1 + e^{-\frac{(\Delta\omega\tau)^2}{2}}\right)^N \tag{B.22}$$

Where $\Delta\omega = \omega_0 - \omega_{\pm 1} \cong 2\pi \times A_{\|}$, and τ is the average reinitialization time. We can see then that controlling nuclear spins with very small $A_{\|}$ is crucial to developing robust memories. The reinitialization time (τ) for the VV^0 system is expected to be faster because of a short ISC shelving times. Additionally, lower spin mixing[55] may make these memories particularly robust to manipulations of the electron[180]. Additionally, control errors on the electron plays a role in decoherence[180] of the nuclear spins, emphasizing the results in Fig. 13.5. Infidelity in the initialization of the electron similarly may limit the numbers of entanglement attempts. For the VV^0, we know that the initialization can be at least $> 99\%$ (Fig. B.1). However, both of these mechanisms decrease as $A_{\|}$ is reduced[180]. For these weakly coupled nuclei, T_2 decay is not the limiting factor for the number of entangling attempts. In experiment for the NV^- center, the memories are around 20 KHz [44, 180]. However, this is because more robust spins with less than 20 KHz are difficult to resolve in natural isotopic abundance in diamond. However, these memories are sufficient to survive $\sim$1000 entangling attempts as needed for the demonstration of entanglement purification [179, 180]. Moving to more weakly coupled registers through isotopic engineering may provide

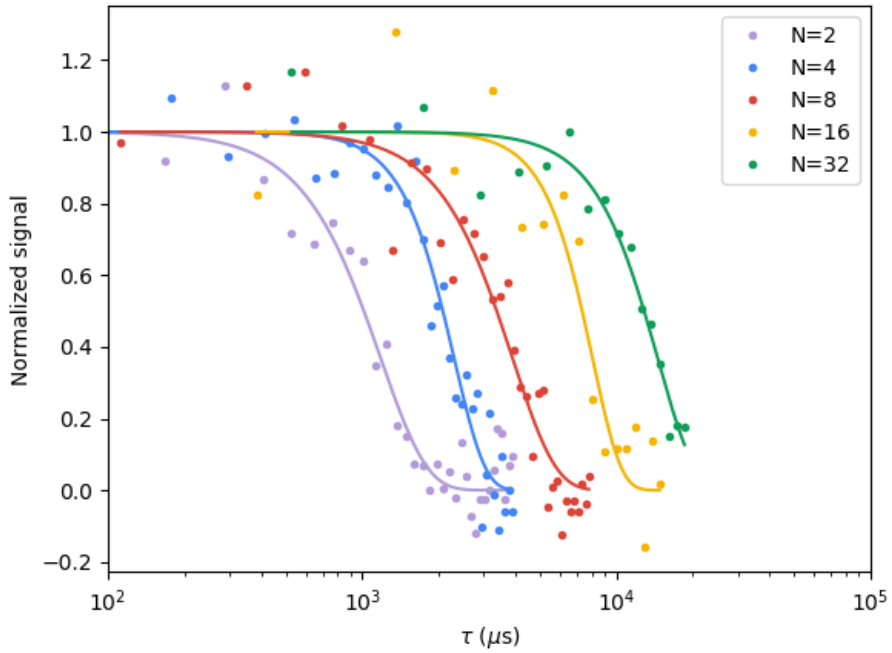

Figure B.10: **CPMG-N on a kk divacancy.** The time constant obtain from these traces are plotted in the main text (Fig. 13.4)

exponentially improved nuclear memories.

B.2.14 Coherence extension for the VV^0

In the main text, we demonstrate CPMG coherence extension on the kk divacancy (shown in Fig. B.10). This allow us to extend T_2^{DD} to 14.5 ms at N=32 with longer time being possible with more pulses. For completeness, we also performed CPMG coherence extension on a basal (kh) divacancy and obtained the results shown in Fig. B.11, extending the coherence to a maximum of T_2^{DD} ~3.5 ms with N=32. Further improvement on field alignment could potentially improve these coherences times. Additionally, charge depletion[6] could also help reduce paramagnetic traps from creating magnetic noise while charge switching.

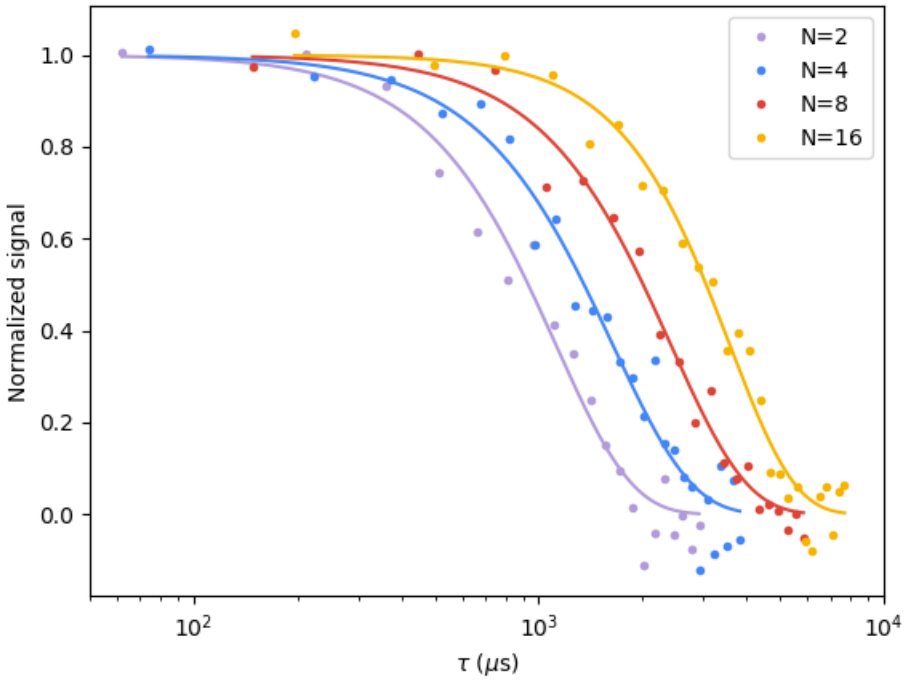

Figure B.11: **CPMG-N on a kh divacancy near B=0.** Only moderate coherence enhancement is observed.

B.2.15 T_1 Lower Bound

At low temperature, T_1 is predicted to be well in excess of a seconds in comparison to the NV center in diamond[292]. However, T_1 times for the divacancy in SiC at low temperature (5 K) have not been reported to date. Unfortunately, in practice, laser leakage through the AOM and other experimental imperfections can artificially lower T_1 which may affect coherences. To ensure we were not limited by such mechanisms we measured T_1 up to 500 ms. We see very little decay within this time scale, confirming that experiments were not limited by T_1 and that the relaxation times for divacancy defects in SiC at low temperatures can be extremely long.

B.2.16 Randomized Benchmarking

To put a lower bound on the gate fidelities we first select a set of Clifford gates to test. For our measurements, we selected the following set: $[I, x, y, x/2, y/2, -x/2, -y/2]$ Note that we

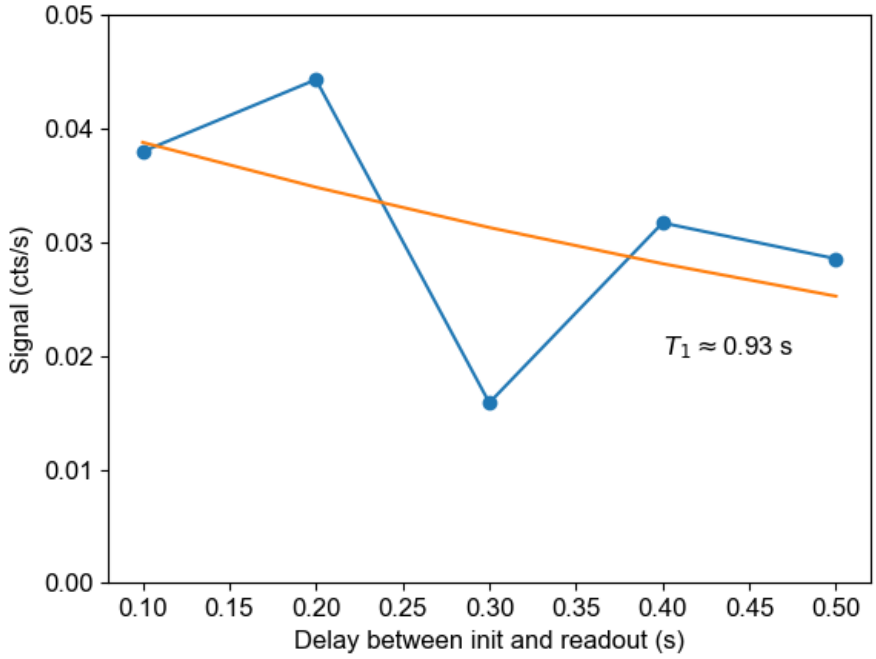

Figure B.12: T_1 **of a single** kk **defect in an isotopically purified sample.**

omitted the z, z/2 and –z/2 gates since these be have a simple instantaneous and error-free virtual implementation (i.e. change the frame of reference). Thus, including these would inflate the average gate fidelity. Additionally, we note that this set is complete in the sense that for every combination of N-1 randomly chosen gates in the set, we can find a single gate that will reverse the effect of that sequence. In practice we ensure that every gate has exactly the same length in time (200 ns). A x gate, for example would consist in [50 ns buffer]–[100 ns pulse]–[50 ns buffer] and a x/2 gate would be [75 ns buffer]-[50 ns pulse]-[75 ns buffer]. Once we have this universal set of gates, we can simply pick N-1 random gates, compute the matrix product of all of these and then we simply add a final gate which projects to $m_s = +1$ (seq1) or $m_s = 0$ (seq2). By taking the difference of seq1 and seq2 we get the randomized benchmarking signal for N gates. To avoid using only a single sequence, we repeat the process with 5 different randomized sequences for each N and average the results together. We then fit our results to $f(N) = A \cdot \alpha^N$N and extract the "Error per Clifford

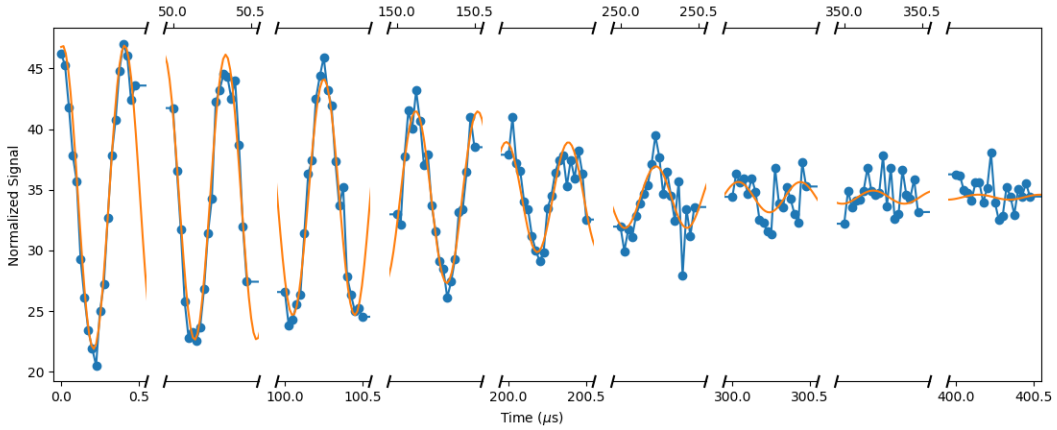

Figure B.13: **Continuous electron Rabi oscillation on shows Rabi $Q = 997 \pm 30$.**

Gate"[259] as:

$$r = 1/2(1 - \alpha) \tag{B.23}$$

This gives an error of 0.000156, or conversely a gate fidelity of 99.984%

B.2.17 Rabi Q

In the main text, we measure the single qubit gate fidelity using randomized benchmarking. Here we will use Rabi Q, a different (but related) metric, to confirm that gate fidelity number. In Fig. B.13, we see some slices of a continuous Rabi. We set the power such that the π time is ∼200 ns. We then globally fit the data to the following function:

$$y(t) = A \cdot e^{-\frac{t}{\gamma}} \cdot \cos\left(2\pi\left(\frac{t}{2T_\pi}\right) + \phi_i\right) \tag{B.24}$$

Where ϕ_i is different for each slices and allows us to account slight phase drift which are possibly due to heating at long times. From this fit we get $\gamma = 199 \pm 6\ \mu s$ and $T_\pi = 199.63 \pm 0.02\ ns$. This gives a Rabi oscillation quality factor $Q = \gamma/T_\pi = 997 \pm 30$

B.3 First-principles Calculations of the Coherence Function

B.3.1 System Hamiltonian

For a system consisting of central electron spin-1 and impurity spins-$\frac{1}{2}$ in an external magnetic field; the Hamiltonian is given by:

$$\widehat{H} = D\left(\hat{S}_z^2 - \frac{1}{3}S(S+1)\right) - \gamma_e B_z \hat{S}_z - \sum_i \gamma_n B_z \hat{I}_{iz} + \sum_i \boldsymbol{S}\boldsymbol{A}\boldsymbol{I}_i + \sum_{i\neq j} \boldsymbol{I}_i \boldsymbol{P} \boldsymbol{I}_j \tag{B.25}$$

where S is the central spin, S is the total spin quantum number of the central spin, and I_i are the bath (nuclear or electron) spins. The A tensor denotes the hyperfine interaction (spin dipole-dipole interaction) between the central spin and the bath nuclear (or electronic) spins. The P tensor denotes the spin dipole-dipole interaction between the spins belonging to the bath. We assume that the diagonal elements of the density matrix of the central electron do not change in time; hence the terms in the Hamiltonian containing $\hat{S}_x$ and $\hat{S}_y$ are negligible (secular approximation). Under this approximation, we can rewrite Eq. B.25 for the spin bath driven[287] by the $m_s = 0$ ($|0\rangle$ qubit state) or $m_s = -1$ ($|1\rangle$ qubit state) levels of the central electron spin as:

$$\begin{aligned}
\widehat{H}_0 &= -\gamma_n B_z \widehat{I}_z + \sum_{i,j} \vec{I}_i \boldsymbol{P} \vec{I}_j \\
\widehat{H}_1 &= -\sum_i \gamma_n B_z \hat{I}_{iz} - \sum_i \left[A_{zz}\widehat{S}_z\widehat{I}_z + A_{zx}\widehat{S}_z\widehat{I}_x + A_{zy}\widehat{S}_z\widehat{I}_y\right] + \sum_{i,j} \vec{I}_i \boldsymbol{P} \vec{I}_j
\end{aligned} \tag{B.26}$$

B.3.2 Hyperfine Tensor Calculations

Hyperfine tensors for nuclear spins were computed using Density Functional Theory (DFT)[293]. DFT calculations were performed with Quantum Espresso code[294] using PBE functional. A kinetic energy cutoff of 40 Ry was adopted. GIPAW pseudopotentials were used to model electron-ion interactions. We used a supercell with 1438 atoms with Gamma-point sampling of the Brillouin zone. GIPAW code is used to evaluate hyperfine tensors for all atoms within the supercell. For atoms outside the supercell, hyperfine tensors were estimated using dipolar-dipolar approximation. For the electron impurities the coupling tensors were computed using only dipolar-dipolar interactions, as exchange interactions between electrons are negligible at such distances.

B.3.3 Coherence Function

For the given delay between pulses (τ) and number of pulses (N), which determines the total time of the experiment $t = N \cdot 2\tau$, the coherence function of the qubit is given by:

$$L(t) = \frac{\mathrm{Tr}\left[\hat{\rho}(t)\hat{S}^{+}\right]}{\mathrm{Tr}\left[\hat{\rho}(0)\hat{S}^{+}\right]} \tag{B.27}$$

Where $\hat{\rho}$ is the density matrix of the qubit. If the qubit is prepared in $|+x\rangle = \frac{1}{\sqrt{2}}(|0\rangle + |1\rangle))$ state, the coherence function at time t is given by:

$$L(t) = \mathrm{Tr}\left[\widehat{U}_0\widehat{U}_1^{\dagger}\right] \tag{B.28}$$

With conditional propagators $\widehat{U}_0$ and $\widehat{U}_1$, which are defined differently for different experiments. For free induction decay (FID, n=0, t=τ):

$$\begin{aligned} \widehat{U}_0 &= \exp\left[-i\widehat{H}_0\tau\right] \\ U_1 &= \exp\left[-i\widehat{H}_1\tau\right] \end{aligned} \tag{B.29}$$

For Hahn-Echo experiment (N=1):

$$\begin{aligned}\widehat{U}_0 &= \exp\left[-i\widehat{H}_0\tau\right]\exp\left[-i\widehat{H}_1\tau\right] \\ \widehat{U}_1 &= \exp\left[-i\widehat{H}_1\tau\right]\exp\left[-i\widehat{H}_0\tau\right]\end{aligned} \tag{B.30}$$

For the experiments with number of pulses ≥ 2, the propagators are given by $\widehat{U}_0 = \widehat{V}_0^{N/2}$ and $\widehat{U}_1 = \widehat{V}_0^{N/2}$, where:

$$\begin{aligned}\hat{V}_0 &= \exp\left[-i\widehat{H}_0\tau\right]\exp\left[-i\widehat{H}_1 2\tau\right]\exp\left[-i\widehat{H}_0\tau\right] \\ \hat{V}_1 &= \exp\left[-i\widehat{H}_1\tau\right]\exp\left[-i\hat{H}_0 2\tau\right]\exp\left[-i\widehat{H}_1\tau\right]\end{aligned} \tag{B.31}$$

The coherence time is obtained by fitting the coherence function to the form $L(t) = exp[(t/T)^n]$, where T is the coherence time. We denote as T_2^* the coherence time T obtained for FID, and as T_2 the coherence time T obtained in Hahn-Echo experiments.

B.3.4 Cluster-Correlation Expansion

The coherence function $L(t)$ from (Eq. B.28) can be approximated as a product of cluster contributions using the cluster-correlation expansion (CCE) method:

$$L(t) \approx \prod_{C\subseteq\{1,2,\ldots N_C\}} \tilde{L}_C(\mathrm{t}) \tag{B.32}$$

Where $\tilde{L}_C$ is irreducible contribution of the cluster C, and N_c is the total number of clusters included in the expansion, which determines the order of approximation. For example, the notation CCE1 corresponds to accounting only for the contributions from isolated nuclear spins ($N_c = 1$), CCE2 corresponds to $N_c = 2$, and CCE3 corresponds to $N_c = 3$. The irreducible contributions are recursively computed as:

$$\tilde{L}_C(\mathrm{t}) = \frac{L_C(t)}{\prod_{C'\subseteq C}\tilde{L}_{C'}(\mathrm{t})} \tag{B.33}$$

Where $L_C(t)$ is the coherence function computed for bath, consisting only of cluster L_C

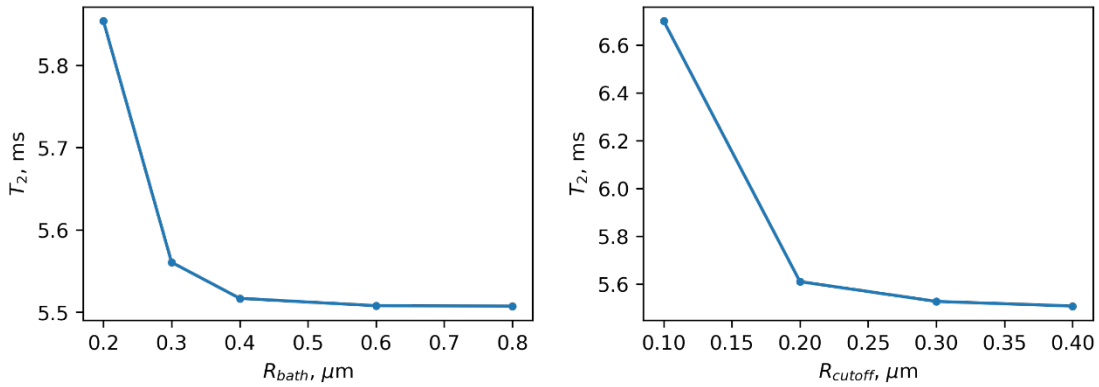

Figure B.14: **The convergence of the electron induced decoherence.** On the left the T_2 as a function of bath size, on the right – as a function of cutoff distance between electron spins to be considered a pair.

using (Eq. B.28).

B.3.5 Calculation Parameters

CCE calculations for nuclear spins were carried out according to [287] and convergence with respect to the order of the CCE was carefully checked in each case. The clusters were chosen according to the procedure described in [102]. In the case of electron spins, the strength of interactions between spins belonging to the bath is comparable to the coupling of the bath spins to the central spin, and the perturbative approach on which the cluster expansion is based upon is not justified. The break-down of the perturbative approach leads to CCE calculations of order 3 or higher to diverge[257]. We can however use an approximate description by assuming that CCE2 is sufficient to correctly estimate electron-electron interactions. This approximation likely yields underestimated coherence times at a given concentration of impurity electron spins, as in real systems the flip rate of electron pairs is reduced due to non-pair-wise interactions with other electrons. But at small electron spin concentration, high order effects are expected to be insignificant to determine the qualitative impact of electron spins on coherence times.

To compute the impact of the electron spins, we randomly placed the electron spins at

the distances between 0 - 2 μm from the qubit. Following a procedure to choose the clusters similar to the one used for nuclear spins, in the calculation of coherence functions we only included the pairs of electron spins with distance smaller than a given cutoff distance, and we only considered clusters of spins in a finite bath. Both the pair distance cutoff and the bath size were chosen to be large enough to obtain converge of the coherence function as shown in Fig. B.14.

Due to different space scale of the nuclear-electron and electron-electron interactions, the two baths (electron and nuclear) can be considered decoupled. Therefore, the total coherence function can be factorized into contributions from electron and nuclear spins, respectively:

$$L_t = L_{electron} L_{nuclear} \tag{B.34}$$

The coherence function was obtained by averaging over the results of 200 (1000) calculations for different configurations of electron or nuclear spins, in the presence of a magnetic field of 50 G (500 G). In the experimental measurement, the pulse bandwidth used to control the qubit state allows to simultaneously excite only a small subpopulation of the divacancies in the SiC sample. In this subpopulation, the energy splitting of the qubit levels does not deviate significantly from that of isolated divacancies. Hence, when computing the average coherence time to be compared with experiments, we need to exclude from the calculation the nuclear configurations whose hyperfine coupling would lead to significant deviation in energy splitting from that of an isolated divacancy. Therefore, only nuclear configurations with maximum parallel Hyperfine coupling <1 MHz were considered. However, we note that when including all the configurations, irrespective of their hyperfine coupling, we obtained very similar T_2 values and T_2^* values within 5-10%, for natural concentration.

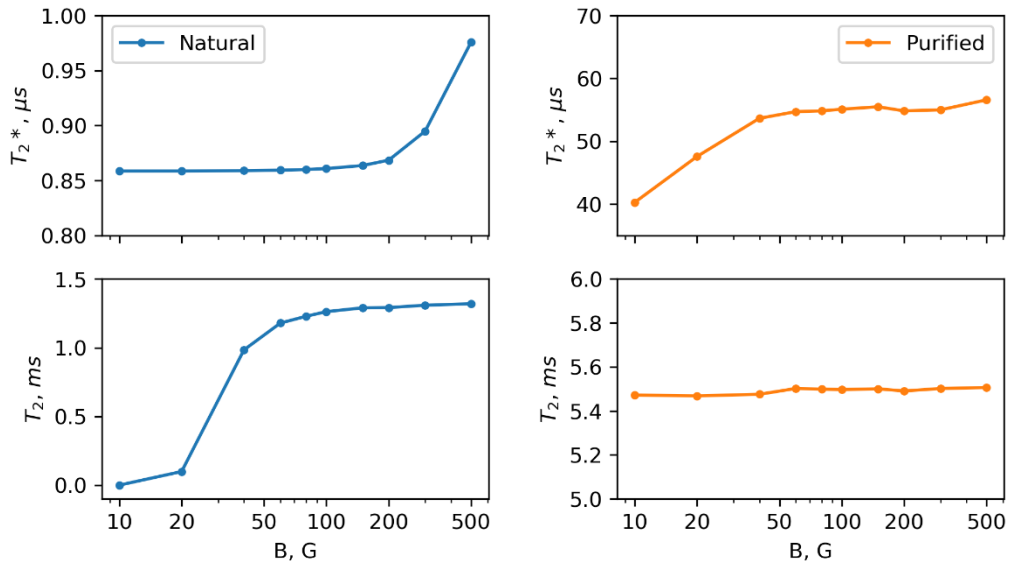

Figure B.15: **Coherence times as a function of magnetic field.** The coherence time T_2 of the natural material is shown on the left-hand side, and that of the isotopically purified material is on the right-hand side. The definitions of T_2 and T_2^* are given in the text.

B.3.6 Impact of the Magnetic Field

The computed values of T_2 and T_2^* for both isotopically purified and natural materials (with free electron concentration of $10^{15} cm^{-3}$) as a function of magnetic field is shown in Figure B.15. In both cases, the T_2^* is not significantly impacted by changes in the magnetic field, while T_2 is impacted: in particular in the natural material we observed a considerable increase in nuclei-limited coherence time. Instead, in the case of electron-limited decoherence, the effect of magnetic field in the range studied here (see Fig. B.15) is negligible.

B.4 Nuclear Memory Optimization

B.4.1 Conditional Magnetization

Using the secular approximations for a system of one electron and one nuclear spin, we can rewrite the Hamiltonian (Eq. B.25) as follows:

$$\widehat{H} = D\left(\hat{S}_z^2 - \frac{1}{3}S(S+1)\right) - \gamma_e B_z \widehat{S}_z - \gamma_n B_z \widehat{I}_z + A_{zz}\widehat{S}_z\widehat{I}_z + A_{zx}\widehat{S}_z\hat{I}_x + A_{zy}\widehat{S}_z\hat{I}_y \quad \text{(B.35)}$$

Using the notation for coupling parameters from [103] we can rewrite secular Hamiltonian (Eq. B.35) as:

$$\widehat{H} = D\left(\hat{S}_z^2 - \frac{1}{3}S(S+1)\right) - \gamma_e B_z \widehat{S}_z - \gamma_n B_z \widehat{I}_z + A_{\parallel}\widehat{S}_z\widehat{I}_z + A_{\perp}\widehat{S}_z\hat{I}_x \quad \text{(B.36)}$$

With $A = A_{zz}$, being parallel hyperfine coupling, and $B = \sqrt{A_{zx}^2 + A_{zy}^2}$ the perpendicular hyperfine coupling. The magnetization of the central electron spin along x-axis can be computed as the real part of the coherence function L:

$$M = \mathrm{Re}\, L(t) = \mathrm{Re}\,\mathrm{Tr}\left[\widehat{U}_0\widehat{U}_1^{\dagger}\right] \quad \text{(B.37)}$$

B.4.2 The Gate Fidelity

In order to understand how many nuclei on average can be used as memory units at a given nuclear spin concentration, we proceed as follows. A given nuclear spin i can be used as a memory unit if the state of the electron spin can be preserved, following a rotation induced by the nuclear spin. For an electron qubit initially prepared in the $|+x\rangle$ state, the fidelity function F measures how well its state is preserved:

$$F(|-x\rangle, \rho) = \langle -x|\rho|-x\rangle \quad \text{(B.38)}$$

where ρ is the density matrix of the qubit. If the fidelity of the qubit rotation induced by nucleus i is higher than a chosen threshold value, then the nucleus is considered a usable memory unit. The threshold value is chosen depending on the purpose of the memory unit, and typical values are in the range 0.9 - 0.99. The fidelity of the electron spin is related to

the electron magnetization M at given N, τ:

$$F_{N\tau}(|-x\rangle, \rho) = \sqrt{\frac{1}{2} - \frac{M}{2}} \tag{B.39}$$

At short time scales (compared to the decay of the coherence function), the interaction between different nuclei can be neglected. Then the electron spin magnetization can be written as a product of conditional magnetizations[103] given by the magnetization of the electron interacting with a single isolated nuclear spin. In other words, CCE1 is used to evaluate the electron magnetization. As a function of delay between pulses (2τ) and number of pulses (N) the magnetization is given by:

$$M(N, \tau) = \prod_i M_i(N, \tau) \tag{B.40}$$

To determine if a given nucleus i in the lattice is available as a memory unit, we consider the magnetization of the electron when the given nucleus is present. The expectation value of the magnetization when the nucleus i is present is:

$$\widetilde{M_i} = E\left(M | M_i \in M\right) = M_i \prod_{j \neq i} E\left(M_j\right) \tag{B.41}$$

Where j runs over all other possible nuclear positions. Then M_j is given as:

$$M_j = \begin{cases} M_j, & \text{if } \boldsymbol{j} \text{ is present} \\ 1, & \text{if } \boldsymbol{j} \text{ is not present} \end{cases} \tag{B.42}$$

At a given nuclear spin concentration c_j, the expectation value $E\left(M_j\right)$ is:

$$E\left(M_j\right) = 1 \cdot \left(1 - c_j\right) + M_j \cdot c_j \tag{B.43}$$

A given nucleus is considered usable as a memory register if the fidelity of electron spin after rotation at $\widetilde{M_i}$ is higher than a certain threshold F_{min}. The average number of nuclei

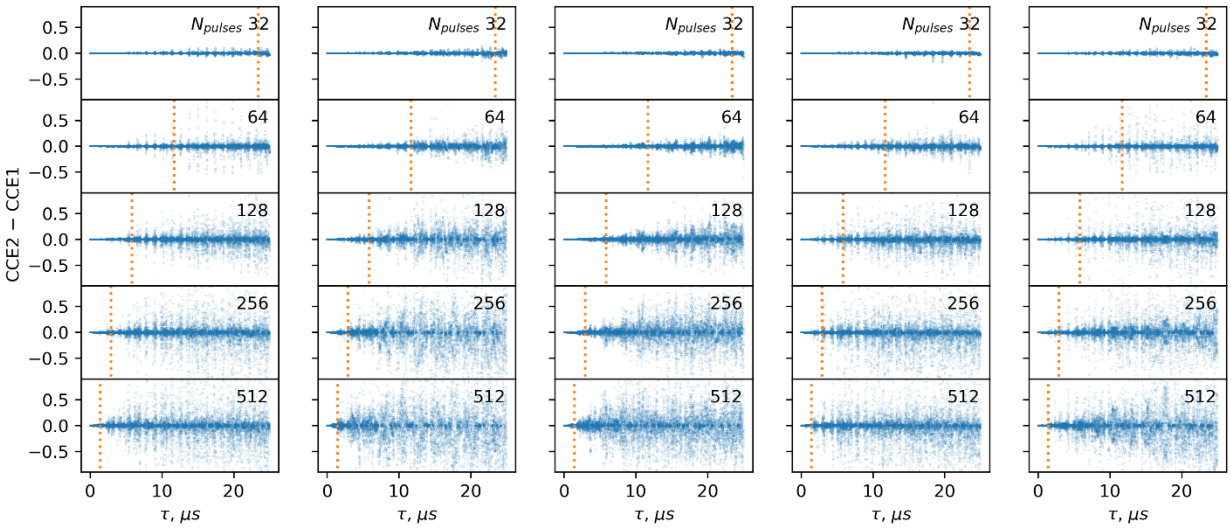

Figure B.16: **Difference in coherence function predicted by CCE2 and CCE1 calculations.** Blue dots show the difference between the coherence functions obtained from CCE1 and CCE2 calculations, and the orange line shows the total gate time of 1.5 ms for six different nuclear configurations at a natural concentration of nuclear spins.

i present at this lattice site, is equal to the concentration of the isotope c_i. Therefore, the total number of usable registers can be computed as the sum of c_i for all i that meets the fidelity criteria at least one set of N,τ:

$$N_{\text{mem}} = \sum_{i}^{F\left(\widetilde{M}_i\right) \geq F_{min}} c_i \tag{B.44}$$

B.4.3 Limitations of the Approach

The method adopted here assumes that the nuclei-nuclei interactions are negligible in determining the electron magnetization. The assumption can be verified by comparing coherence functions obtained at different orders of CCE for random nuclear configurations. A significant difference between the spectra obtained with the CCE1 and CCE2 approximations would indicate nonnegligible nuclei-nuclei interactions. Figure B.16 shows the difference between the results of CCE2 and CCE1 for 6 different nuclear spin configurations at natural concentration (c(^{29}Si) = 4.7%, c(^{13}C) = 1.1%). We can see that at long delay times

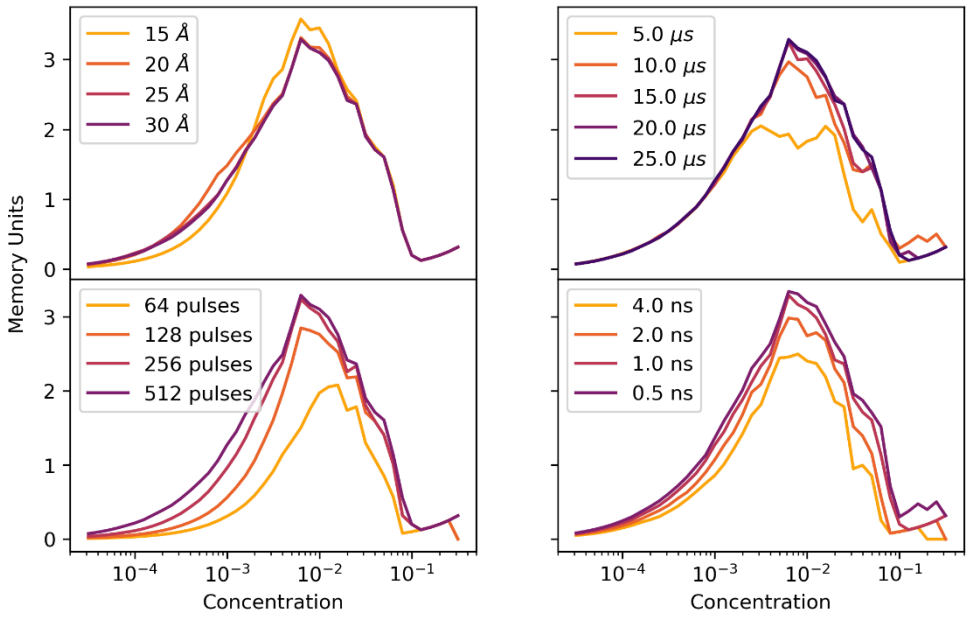

Figure B.17: **Convergence tests for the calculation of usable memory units.** Left to right, top to bottom: computed number of usable memory units as function of nuclear concentrations at a maximum gate time of 2 ms for varied bath size, maximum τ, number of pulses, and timestep. When parameters are not varied, default values of bath size = 30 $\mathring{A}$, maximum $\tau = 25$, number of pulses = 512, and timestep = 1 ns are used.

there are significant differences between coherence functions obtained with CCE2 and CCE1. The delay at which the deviations occur is inversely proportional to the number of pulses. Therefore, the maximum available gate time (equal to $N2\tau$) can be found from the value of the delay for a given number of pulses at which significant deviations occur. From the analysis of the CCE spectra for natural isotopic concentrations, the maximum gate time was established to be between 1-2 ms before significant deviations occur. This theoretical limit determines the maximum gate time, after which the fidelity of the rotation becomes limited by nuclear-nuclear interactions.

B.4.4 Convergence of the Results

Having established the theoretical maximum gate time, we checked the convergence of the number of memory units with respect to the size of the bath, timestep resolution, number of pulses, and the range of the delays between pulses. The convergence is shown in Figure B.17.

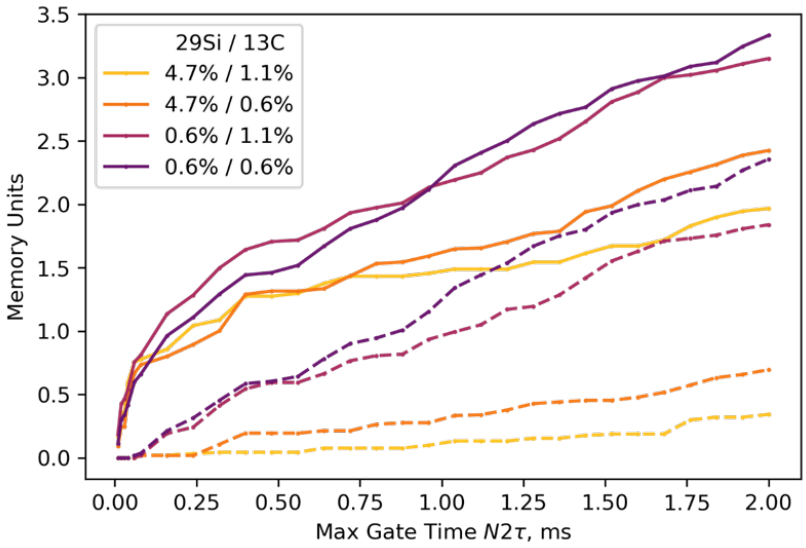

Figure B.18: **Number of usable memory units as a function of the gate time.** The different color of the lines corresponds to different isotopic concentration, indicated in the inset. Dotted lines shows number of memory units with parallel hyperfine terms below $2\pi \cdot 60$ kHz. Minimum fidelity is equal to 0.95.

It was found that the number of memory units at the magnetic field of 500 G is converged at bath size 30 Angstrom, maximum τ of 25 μs, timestep of 0.5 ns, number of pulses of 512, which were used in Fig. 13.4.

B.4.5 Number of Memory Units as a Function of Gate Time

The Figure B.18 shows shows the increase of an average number of memory units as a function of the maximum gate time. We can see that the total number is proportional to the square root of the gate time. Furthermore, the purification of Si leads to two-fold increase in the number of available memory units at long gate times, while the isotopic purification of carbon does not lead to any significant improvement.

It is interesting to note that the initial part of the curve corresponds to the nuclei with strong hyperfine coupling, and further increase in the number of usable nuclei include those with weak hyperfine coupling. The number of available memory units with weak hyperfine varies linearly with the maximum gate time within the chosen timescale.

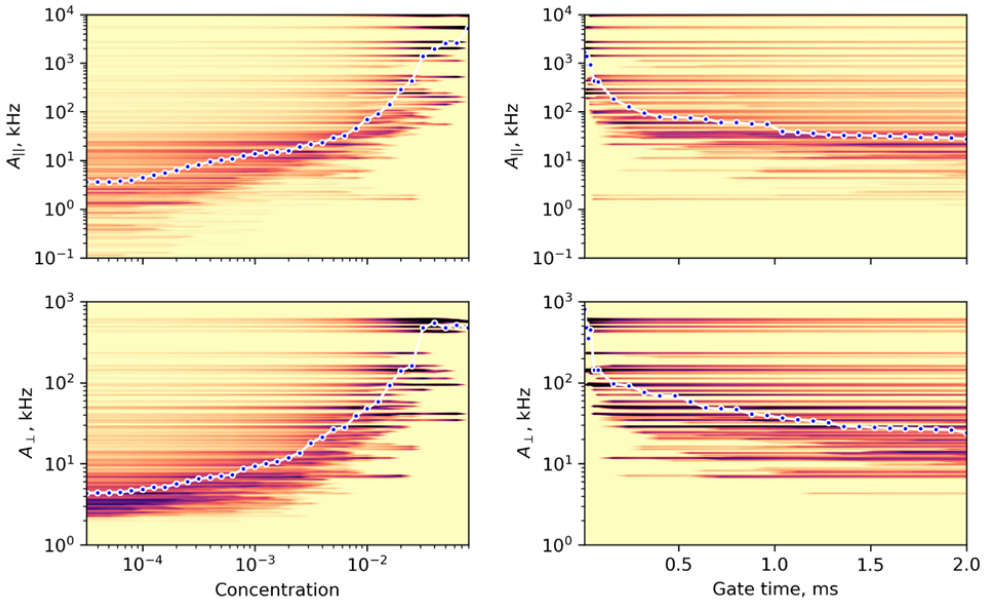

Figure B.19: **Distribution of the most plausible hyperfine values for memory units.** Color maps show the probability of memory units in the sample with given nuclear concentration and gate time to have corresponding hyperfine coupling. On the left, the distribution is shown as a function of the nuclear concentration at maximum gate time $N2\tau$ 1.5 ms, with minimum fidelity of 0.95. On the right, the distribution is shown as a function of maximum gate time with concentration of $c(^{29}Si) = c(^{13}C) = 0.63\%$, which was found to be optimal at minimum fidelity of 0.95. Blue circles show the median of hyperfine values at the given concentration or gate time.

B.4.6 Hyperfine Distribution

Figure B.19 shows the distribution of hyperfine couplings for memory units, available at different isotopic concentration/gate time. The gate time dependence further proves a point outlined above: usage of most of the nuclei with strong hyperfine coupling occurs at small timescales, and extended gate time allows one to access weakly coupled nuclei. Figure B.20 shows the distribution for different minimum fidelities. Interestingly, the shape of the distribution is the same, albeit shifted towards higher concentrations at lower F_{min}.

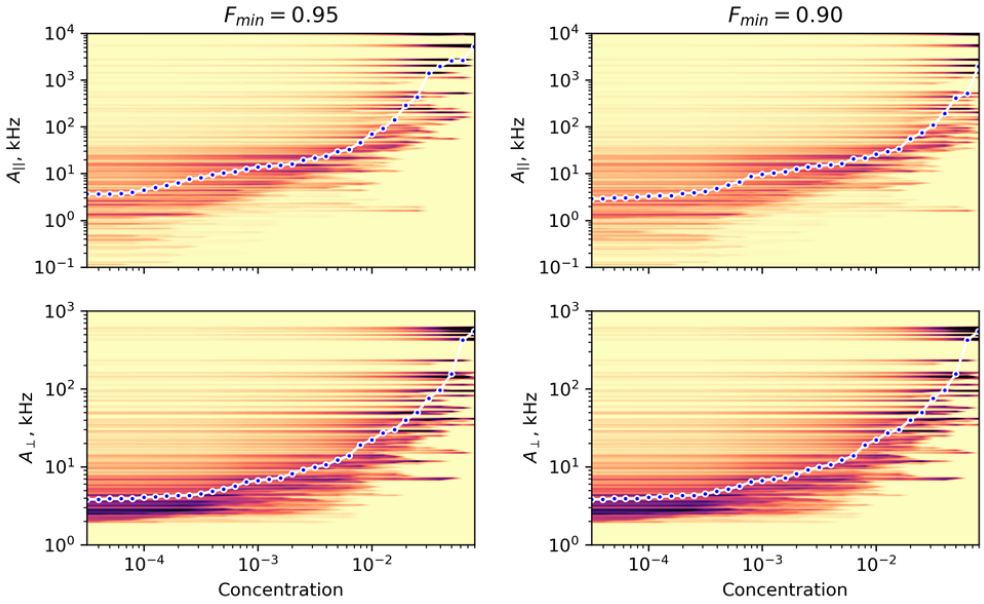

Figure B.20: **Most plausible hyperfine values for memory units at different fidelities.** Color corresponds to the probability that memory units in the sample with given nuclear concentration will have the corresponding hyperfine term. The maximum gate time $N2\tau$ 1.5 ms, On the left the minimum fidelity of 0.95 is shown, on the right F_{min}=0.90. Blue circles show the median of hyperfine values at the given concentration.

References

[1] Alexandre Bourassa, Christopher P. Anderson, Kevin C. Miao, Mykyta Onizhuk, He Ma, Alexander L. Crook, Hiroshi Abe, Jawad Ul-Hassan, Takeshi Ohshima, Nguyen T. Son, Giulia Galli, and David D. Awschalom. Entanglement and control of single quantum memories in isotopically engineered silicon carbide. may 2020.

[2] Nguyen T. Son, Christopher P. Anderson, Alexandre Bourassa, Kevin C. Miao, Charles Babin, Matthias Widmann, Matthias Niethammer, Jawad Ul Hassan, Naoya Morioka, Ivan G. Ivanov, Florian Kaiser, Joerg Wrachtrup, and David D. Awschalom. Developing silicon carbide for quantum spintronics. *Applied Physics Letters*, 116(19):190501, may 2020.

[3] Alexander L. Crook, Christopher P. Anderson, Kevin C. Miao, Alexandre Bourassa, Hope Lee, Sam L. Bayliss, David O. Bracher, Xingyu Zhang, Hiroshi Abe, Takeshi Ohshima, Evelyn L Hu, and David D. Awschalom. Purcell enhancement of a single silicon carbide color center with coherent spin control. *Nano Letters*, mar 2020.

[4] Gary Wolfowicz, Christopher P. Anderson, Berk Diler, Oleg G. Poluektov, F. Joseph Heremans, and David D. Awschalom. Vanadium spin qubits as telecom quantum emitters in silicon carbide. *Science Advances*, 6(18):eaaz1192, may 2020.

[5] Berk Diler, Samuel J. Whiteley, Christopher P. Anderson, Gary Wolfowicz, Marie E. Wesson, Edward S. Bielejec, F. Joseph Heremans, and David D. Awschalom. Coherent

control and high-fidelity readout of chromium ions in commercial silicon carbide. *npj Quantum Information*, 6(1):1–6, dec 2020.

[6] Christopher P. Anderson, Alexandre Bourassa, Kevin C. Miao, Gary Wolfowicz, Peter J. Mintun, Alexander L. Crook, Hiroshi Abe, Jawad Ul Hassan, Nguyen T. Son, Takeshi Ohshima, and David D. Awschalom. Electrical and optical control of single spins integrated in scalable semiconductor devices. *Science*, 366(6470):1225–1230, jun 2019.

[7] Kevin C. Miao, Alexandre Bourassa, Christopher P. Anderson, Samuel J. Whiteley, Alexander L. Crook, Sam L. Bayliss, Gary Wolfowicz, Gergő Thiering, Péter Udvarhelyi, Viktor Ivády, Hiroshi Abe, Takeshi Ohshima, Ádám Gali, and David D. Awschalom. Electrically driven optical interferometry with spins in silicon carbide. *Science Advances*, 5(11), 2019.

[8] Gary Wolfowicz, Christopher P. Anderson, Samuel J. Whiteley, and David D. Awschalom. Heterodyne detection of radio-frequency electric fields using point defects in silicon carbide. *Applied Physics Letters*, 115(4):043105, jul 2019.

[9] Samuel J. Whiteley, Gary Wolfowicz, Christopher P. Anderson, Alexandre Bourassa, He Ma, Meng Ye, Gerwin Koolstra, Kevin J. Satzinger, Martin V. Holt, F. Joseph Heremans, Andrew N. Cleland, David I. Schuster, Giulia Galli, and David D. Awschalom. Spin–phonon interactions in silicon carbide addressed by Gaussian acoustics. *Nature Physics*, 15(5):490–495, 2019.

[10] S. O. Hruszkewycz, S. Maddali, C. P. Anderson, W. Cha, K. C. Miao, M. J. Highland, A. Ulvestad, D. D. Awschalom, and F. J. Heremans. Strain annealing of SiC nanoparticles revealed through Bragg coherent diffraction imaging for quantum technologies. *Physical Review Materials*, 2(8), 2018.

[11] Gary Wolfowicz, Christopher P. Anderson, Andrew L. Yeats, Samuel J. Whiteley, Jens

Niklas, Oleg G. Poluektov, F. Joseph Heremans, and David D. Awschalom. Optical charge state control of spin defects in 4H-SiC. *Nature Communications*, 8(1), 2017.

[12] S O Hruszkewycz, W Cha, P Andrich, C P Anderson, A Ulvestad, R Harder, P H Fuoss, D. D. Awschalom, and F J Heremans. In situ study of annealing-induced strain relaxation in diamond nanoparticles using Bragg coherent diffraction imaging. *APL Materials*, 5(2), 2017.

[13] Abram L Falk, Bob B Buckley, Greg Calusine, William F Koehl, Viatcheslav V Dobrovitski, Alberto Politi, Christian a Zorman, Philip X-L Feng, and David D Awschalom. Polytype control of spin qubits in silicon carbide. *Nature communications*, 4(May):1819, jan 2013.

[14] Wikipedia contributors. Transistor — Wikipedia, the free encyclopedia, 2020. [Online; accessed 18-March-2020].

[15] Wikipedia contributors. Ibm 7030 stretch— Wikipedia, the free encyclopedia, 2020. [Online; accessed 18-March-2020].

[16] Wikibooks. Analogue electronics/pn junctions — wikibooks, the free textbook project, 2017. [Online; accessed 3-April-2020].

[17] Phillip Kaye, Raymond Laflamme, and Michele Mosca. *Silicon Carbide: Recent Major Advances (Advanced Texts in Physics) (v. 79)*. Springer.

[18] A. Einstein, B. Podolsky, and N. Rosen. Can quantum-mechanical description of physical reality be considered complete? *Physical Review*, 47(10):777–780, may 1935.

[19] Lov K. Grover. A fast quantum mechanical algorithm for database search. *Proceedings of the Annual ACM Symposium on Theory of Computing*, Part F129452:212–219, may 1996.

[20] P.W. Shor. Algorithms for quantum computation: discrete logarithms and factoring. pages 124–134. Institute of Electrical and Electronics Engineers (IEEE), dec 2002.

[21] Norman F. Ramsey. A molecular beam resonance method with separated oscillating fields. *Physical Review*, 78(6):695–699, jun 1950.

[22] C. L. Degen, F. Reinhard, and P. Cappellaro. Quantum sensing. *Reviews of Modern Physics*, 89(3):035002, jul 2017.

[23] E. L. Hahn. Spin echoes. *Physical Review*, 80(4):580–594, nov 1950.

[24] S. Meiboom and D. Gill. Modified spin-echo method for measuring nuclear relaxation times. *Review of Scientific Instruments*, 29(8):688–691, aug 1958.

[25] H. Y. Carr and E. M. Purcell. Effects of diffusion on free precession in nuclear magnetic resonance experiments. *Physical Review*, 94(3):630–638, may 1954.

[26] N. Bar-Gill, L. M. Pham, C. Belthangady, D. Le Sage, P. Cappellaro, J. R. Maze, M. D. Lukin, A. Yacoby, and R. Walsworth. Suppression of spin-bath dynamics for improved coherence of multi-spin-qubit systems. *Nature Communications*, 3(1):1–6, may 2012.

[27] T. Van Der Sar, Z. H. Wang, M. S. Blok, H. Bernien, T. H. Taminiau, D. M. Toyli, D. A. Lidar, D. D. Awschalom, R. Hanson, and V. V. Dobrovitski. Decoherence-protected quantum gates for a hybrid solid-state spin register. *Nature*, 484(7392):82–86, apr 2012.

[28] Manjin Zhong, Morgan P. Hedges, Rose L. Ahlefeldt, John G. Bartholomew, Sarah E. Beavan, Sven M. Wittig, Jevon J. Longdell, and Matthew J. Sellars. Optically addressable nuclear spins in a solid with a six-hour coherence time. *Nature*, 517(7533):177–180, jan 2015.

[29] Simone Schönbach.

[30] E. T. Jaynes and F. W. Cummings. Comparison of Quantum and Semiclassical Radiation Theories with Application to the Beam Maser. *Proceedings of the IEEE*, 51(1):89–109, 1963.

[31] Frank Arute, Kunal Arya, Ryan Babbush, Dave Bacon, Joseph C. Bardin, Rami Barends, Rupak Biswas, Sergio Boixo, Fernando G.S.L. Brandao, David A. Buell, Brian Burkett, Yu Chen, Zijun Chen, Ben Chiaro, Roberto Collins, William Courtney, Andrew Dunsworth, Edward Farhi, Brooks Foxen, Austin Fowler, Craig Gidney, Marissa Giustina, Rob Graff, Keith Guerin, Steve Habegger, Matthew P. Harrigan, Michael J. Hartmann, Alan Ho, Markus Hoffmann, Trent Huang, Travis S. Humble, Sergei V. Isakov, Evan Jeffrey, Zhang Jiang, Dvir Kafri, Kostyantyn Kechedzhi, Julian Kelly, Paul V. Klimov, Sergey Knysh, Alexander Korotkov, Fedor Kostritsa, David Landhuis, Mike Lindmark, Erik Lucero, Dmitry Lyakh, Salvatore Mandrà, Jarrod R. McClean, Matthew McEwen, Anthony Megrant, Xiao Mi, Kristel Michielsen, Masoud Mohseni, Josh Mutus, Ofer Naaman, Matthew Neeley, Charles Neill, Murphy Yuezhen Niu, Eric Ostby, Andre Petukhov, John C. Platt, Chris Quintana, Eleanor G. Rieffel, Pedram Roushan, Nicholas C. Rubin, Daniel Sank, Kevin J. Satzinger, Vadim Smelyanskiy, Kevin J. Sung, Matthew D. Trevithick, Amit Vainsencher, Benjamin Villalonga, Theodore White, Z. Jamie Yao, Ping Yeh, Adam Zalcman, Hartmut Neven, and John M. Martinis. Quantum supremacy using a programmable superconducting processor. *Nature*, 574(7779):505–510, oct 2019.

[32] Juan Yin, Yuan Cao, Yu Huai Li, Sheng Kai Liao, Liang Zhang, Ji Gang Ren, Wen Qi Cai, Wei Yue Liu, Bo Li, Hui Dai, Guang Bing Li, Qi Ming Lu, Yun Hong Gong, Yu Xu, Shuang Lin Li, Feng Zhi Li, Ya Yun Yin, Zi Qing Jiang, Ming Li, Jian Jun Jia, Ge Ren, Dong He, Yi Lin Zhou, Xiao Xiang Zhang, Na Wang, Xiang Chang, Zhen Cai Zhu, Nai Le Liu, Yu Ao Chen, Chao Yang Lu, Rong Shu, Cheng Zhi Peng, Jian Yu Wang, and Jian Wei Pan. Satellite-based entanglement distribution over 1200

kilometers. *Science*, 356(6343):1140–1144, 2017.

[33] David P. DiVincenzo. The physical implementation of quantum computation, sep 2000.

[34] Klaus Mølmer and Anders Sørensen. Multiparticle entanglement of hot trapped ions. *Physical Review Letters*, 82(9):1835–1838, mar 1999.

[35] J. I. Cirac and P. Zoller. Quantum computations with cold trapped ions. *Physical Review Letters*, 74(20):4091–4094, may 1995.

[36] C. Monroe, R. Raussendorf, A. Ruthven, K. R. Brown, P. Maunz, L. M. Duan, and J. Kim. Large-scale modular quantum-computer architecture with atomic memory and photonic interconnects. *Physical Review A - Atomic, Molecular, and Optical Physics*, 89(2):022317, feb 2014.

[37] R. B. Blakestad, C. Ospelkaus, A. P. Vandevender, J. M. Amini, J. Britton, D. Leibfried, and D. J. Wineland. High-fidelity transport of trapped-ion qubits through an X-junction trap array. *Physical Review Letters*, 102(15):153002, apr 2009.

[38] L. M. Duan, M. D. Lukin, J. I. Cirac, and P. Zoller. Long-distance quantum communication with atomic ensembles and linear optics. *Nature*, 414(6862):413–418, nov 2001.

[39] Yong Yu, Fei Ma, Xi Yu Luo, Bo Jing, Peng Fei Sun, Ren Zhou Fang, Chao Wei Yang, Hui Liu, Ming Yang Zheng, Xiu Ping Xie, Wei Jun Zhang, Li Xing You, Zhen Wang, Teng Yun Chen, Qiang Zhang, Xiao Hui Bao, and Jian Wei Pan. Entanglement of two quantum memories via fibres over dozens of kilometres. *Nature*, 578(7794):240–245, feb 2020.

[40] L J Stephenson, D P Nadlinger, B C Nichol, S An, P Drmota, T G Ballance, K Thirumalai, J F Goodwin, D M Lucas, and C J Ballance. High-rate, high-fidelity entanglement of qubits across an elementary quantum network. 110501:1–6, 2019.

[41] D. Hucul, I. V. Inlek, G. Vittorini, C. Crocker, S. Debnath, S. M. Clark, and C. Monroe. Modular entanglement of atomic qubits using photons and phonons. *Nature Physics*, 11(1):37–42, jan 2015.

[42] Aymeric Delteil, Zhe Sun, Wei Bo Gao, Emre Togan, Stefan Faelt, and Ataç Imamolu. Generation of heralded entanglement between distant hole spins. *Nature Physics*, 12(3):218–223, mar 2016.

[43] R. Stockill, M. J. Stanley, L. Huthmacher, E. Clarke, M. Hugues, A. J. Miller, C. Matthiesen, C. Le Gall, and M. Atatüre. Phase-Tuned Entangled State Generation between Distant Spin Qubits. *Physical Review Letters*, 119(1):010503, jul 2017.

[44] N. Kalb, A. A. Reiserer, P. C. Humphreys, J. J. W. Bakermans, S. J. Kamerling, N. H. Nickerson, S. C. Benjamin, D. J. Twitchen, M. Markham, and R. Hanson. Entanglement distillation between solid-state quantum network nodes. *Science*, 356(6341):928–932, 2017.

[45] B. E. Kane. A silicon-based nuclear spin quantum computer. *Nature*, 393(6681):133–137, may 1998.

[46] Juha T. Muhonen, Juan P. Dehollain, Arne Laucht, Fay E. Hudson, Rachpon Kalra, Takeharu Sekiguchi, Kohei M. Itoh, David N. Jamieson, Jeffrey C. McCallum, Andrew S. Dzurak, and Andrea Morello. Storing quantum information for 30 seconds in a nanoelectronic device. *Nature Nanotechnology*, 9(12):986–991, jan 2014.

[47] Arne Laucht, Juha T. Muhonen, Fahd A. Mohiyaddin, Rachpon Kalra, Juan P. Dehollain, Solomon Freer, Fay E. Hudson, Menno Veldhorst, Rajib Rahman, Gerhard Klimeck, Kohei M. Itoh, David N. Jamieson, Jeffrey C. McCallum, Andrew S. Dzurak, and Andrea Morello. Electrically controlling single-spin qubits in a continuous microwave field. *Science Advances*, 1(3):e1500022, apr 2015.

[48] Serwan Asaad, Vincent Mourik, Benjamin Joecker, Mark A. I. Johnson, Andrew D. Baczewski, Hannes R. Firgau, Mateusz T. Mądzik, Vivien Schmitt, Jarryd J. Pla, Fay E. Hudson, Kohei M. Itoh, Jeffrey C. McCallum, Andrew S. Dzurak, Arne Laucht, and Andrea Morello. Coherent electrical control of a single high-spin nucleus in silicon. *Nature*, 579(7798):205–209, mar 2020.

[49] Gershon Kurizki, Patrice Bertet, Yuimaru Kubo, Klaus Mølmer, David Petrosyan, Peter Rabl, and Jörg Schmiedmayer. Quantum technologies with hybrid systems. *Proceedings of the National Academy of Sciences*, 112(13):201419326, 2015.

[50] J. Brossel, S. Geschwind, and A. L. Schawlow. Optical detection of paramagnetic resonance in crystals at low temperatures. *Physical Review Letters*, 3(12):548–549, dec 1959.

[51] S. Geschwind, R. J. Collins, and A. L. Schawlow. Optical detection of paramagnetic resonance in an excited state of Cr3+ in Al2O3. *Physical Review Letters*, 3(12):545–548, dec 1959.

[52] Stefania Castelletto and Alberto Boretti. Silicon carbide color centers for quantum applications. *Journal of Physics: Photonics*, 2(2):022001, mar 2020.

[53] Z. Shang, A. Hashemi, Y. Berencén, H. P. Komsa, P. Erhart, A. V. Krasheninnikov, and G. V. Astakhov. Local vibrational modes of Si vacancy spin qubits in SiC. jan 2020.

[54] Roland Nagy, Matthias Niethammer, Matthias Widmann, Yu-Chen Chen, Péter Udvarhelyi, Cristian Bonato, Jawad Ul Hassan, Robin Karhu, Ivan G. Ivanov, Nguyen Tien Son, Jeronimo R. Maze, Takeshi Ohshima, Öney O. Soykal, Ádám Gali, Sang-Yun Lee, Florian Kaiser, and Jörg Wrachtrup. High-fidelity spin and optical control of single silicon-vacancy centres in silicon carbide. *Nature Communications*, 10(1):1954, 2019.

[55] David J. Christle, Paul V. Klimov, Charles F. de las Casas, Krisztián Szász, Viktor Ivády, Valdas Jokubavicius, Jawad Ul Hassan, Mikael Syväjärvi, William F. Koehl, Takeshi Ohshima, Nguyen T. Son, Erik Janzén, Ádám Gali, and David D. Awschalom. Isolated spin qubits in sic with a high-fidelity infrared spin-to-photon interface. *Phys. Rev. X*, 7:021046, Jun 2017.

[56] Viktor Ivády, Joel Davidsson, Nazar Delegan, Abram L. Falk, Paul V. Klimov, Samuel J. Whiteley, Stephan O. Hruszkewycz, Martin V. Holt, F. Joseph Heremans, Nguyen Tien Son, David D. Awschalom, Igor A. Abrikosov, and Adam Gali. Stabilization of point-defect spin qubits by quantum wells. *Nature Communications*, 10(1):1–8, dec 2019.

[57] Daniil M. Lukin, Constantin Dory, Melissa A. Guidry, Ki Youl Yang, Sattwik Deb Mishra, Rahul Trivedi, Marina Radulaski, Shuo Sun, Dries Vercruysse, Geun Ho Ahn, and Jelena Vučković. 4H-silicon-carbide-on-insulator for integrated quantum and nonlinear photonics. *Nature Photonics*, pages 1–5, dec 2019.

[58] L. J. Rogers, K. D. Jahnke, T. Teraji, L. Marseglia, C. Müller, B. Naydenov, H. Schauffert, C. Kranz, J. Isoya, L. P. McGuinness, and F. Jelezko. Multiple intrinsically identical single-photon emitters in the solid state. *Nature Communications*, 5(1):1–6, aug 2014.

[59] Jonathan M. Kindem, Andrei Ruskuc, John G. Bartholomew, Jake Rochman, Yan Qi Huan, and Andrei Faraon. Coherent control and single-shot readout of a rare-earth ion embedded in a nanophotonic cavity. jul 2019.

[60] Mouktik Raha, Songtao Chen, Christopher M. Phenicie, Salim Ourari, Alan M. Dibos, and Jeff D. Thompson. Optical quantum nondemolition measurement of a solid-state spin without a cycling transition. jul 2019.

[61] L. Gordon, A. Janotti, and C. G. Van De Walle. Defects as qubits in 3C- and 4H-SiC. *Physical Review B - Condensed Matter and Materials Physics*, 92(4):045208, jul 2015.

[62] Björn Magnusson, Nguyen Tien Son, András Csóré, Andreas Gällström, Takeshi Ohshima, Adam Gali, and Ivan G. Ivanov. Excitation properties of the divacancy in 4H -SiC. *Physical Review B*, 98(19), 2018.

[63] W. C. Mitchel, W. D. Mitchell, G. Landis, H. E. Smith, Wonwoo Lee, and M. E. Zvanut. Vanadium donor and acceptor levels in semi-insulating 4H - And 6H-SiC. *Journal of Applied Physics*, 101(1):013707, jan 2007.

[64] J. R. Weber, W. F. Koehl, J. B. Varley, A. Janotti, B. B. Buckley, C. G. Van De Walle, and D. D. Awschalom. Quantum computing with defects. *Proceedings of the National Academy of Sciences of the United States of America*, 107(19):8513–8518, may 2010.

[65] W. Shockley. Introduction to the first silicon carbide conference held in boston, April 2-3, 1958.

[66] B. W. Frazier. Report of an examination of crystals furnished by mr. e. g. acheson, president of the carborundum company. Technical Report p. 287, J. Franklin Inst., 1893.

[67] A. V. Los and M. S. Mazzola. Influence of carrier freeze-out on SiC Schottky junction admittance. *Journal of Electronic Materials*, 30(3):235–241, 2001.

[68] Natalie Briggs, Brian Bersch, Yuanxi Wang, Jue Jiang, Roland J. Koch, Nadire Nayir, Ke Wang, Marek Kolmer, Wonhee Ko, Ana De La Fuente Duran, Shruti Subramanian, Chengye Dong, Jeffrey Shallenberger, Mingming Fu, Qiang Zou, Ya-Wen Chuang, Zheng Gai, An-Ping Li, Aaron Bostwick, Chris Jozwiak, Cui-Zu Chang, Eli Rotenberg, Jun Zhu, Adri C. T. van Duin, Vincent Crespi, and Joshua A. Robinson. Atomically thin half-van der Waals metals enabled by confinement heteroepitaxy. *Nature Materials*, pages 1–7, mar 2020.

[69] Dillon Wong, Jairo Velasco, Long Ju, Juwon Lee, Salman Kahn, Hsin Zon Tsai, Chad Germany, Takashi Taniguchi, Kenji Watanabe, Alex Zettl, Feng Wang, and Michael F. Crommie. Characterization and manipulation of individual defects in insulating hexagonal boron nitride using scanning tunnelling microscopy. *Nature Nanotechnology*, 10(11):949–953, nov 2015.

[70] E. G. Acheson. Production of artificial crystalline carbonaceous materials, U.S. patent no. 17911, 1892.

[71] H. J. Round. A note on carborundum. *Electric. World*, (49), 1907.

[72] H. H. C. Dunwoody. Wireless telegraph system, U.S. patent no. 837,616, 1906.

[73] J. A. Lely. Darstellung von einkristallen von silicium carbid und beherrschung von art und menge der eingebauten verunreinigungen. *Berichte der Deutschen Keramischen Gesellschaft*, (32):229–236, 1955.

[74] Cree: History milestones.

[75] O. Kordina, A. Henry, J. P. Bergman, N. T. Son, W. M. Chen, C. Hallin, and E. Janzén. High quality 4H-SiC epitaxial layers grown by chemical vapor deposition. *Applied Physics Letters*, 66(11):1373–1375, mar 1995.

[76] Michel Bockstedte, Alexander Mattausch, and Oleg Pankratov. Ab initio study of the migration of intrinsic defects in 3C SiC. *Physical Review B - Condensed Matter and Materials Physics*, 68(20):205201, nov 2003.

[77] Rodrick Kuate Defo, Xingyu Zhang, David Bracher, Gunn Kim, Evelyn Hu, and Efthimios Kaxiras. Energetics and kinetics of vacancy defects in 4H -SiC. *Physical Review B*, 98(10):104103, sep 2018.

[78] E. Rauls, Th Frauenheim, A. Gali, and P. Deák. Theoretical study of vacancy diffusion

and vacancy-assisted clustering of antisites in SiC. *Physical Review B - Condensed Matter and Materials Physics*, 68(15):155208, oct 2003.

[79] N. T. Son, P. Carlsson, J Ul Hassan, E Janzén, T. Umeda, J. Isoya, A. Gali, M. Bockstedte, N. Morishita, T. Ohshima, H. Itoh, E Janze, T. Umeda, J. Isoya, A. Gali, M. Bockstedte, N. Morishita, T. Ohshima, H. Itoh, J. Ul Hassan, E. Janz??n, T. Umeda, J. Isoya, A. Gali, M. Bockstedte, N. Morishita, T. Ohshima, and H. Itoh. Divacancy in 4H-SiC. *Physical Review Letters*, 96(November):8–11, 2006.

[80] F. Joseph Heremans, Christopher G. Yale, and David D. Awschalom. Control of Spin Defects in Wide-Bandgap Semiconductors for Quantum Technologies. *Proceedings of the IEEE*, 104(10):2009–2023, oct 2016.

[81] N. T. Son, Z. Zolnai, and E. Janzén. Silicon vacancy related TV2a center in 4H-SiC. *Physical Review B - Condensed Matter and Materials Physics*, 68(20):205211, nov 2003.

[82] William F Koehl, Bob B Buckley, F Joseph Heremans, Greg Calusine, and David D Awschalom. Room temperature coherent control of defect spin qubits in silicon carbide. *Nature*, 479(7371):84–7, nov 2011.

[83] M. S. Dresselhaus, G. Dresselhaus, and A. (Ado) Jorio. *Group theory : application to the physics of condensed matter*. Springer-Verlag, 2010.

[84] Abram L. Falk, Paul V. Klimov, Viktor Ivády, Krisztián Szász, David J. Christle, WilliamF. Koehl, Ádám Gali, and David D. Awschalom. Optical Polarization of Nuclear Spins in Silicon Carbide. *Physical Review Letters*, 114(June):247603, 2015.

[85] M W Doherty, N B Manson, P Delaney, and L C L Hollenberg. The negatively charged nitrogen-vacancy centre in diamond: the electronic solution. *New Journal of Physics*, 13(2):025019, feb 2011.

[86] J. R. Maze, A. Gali, E. Togan, Y. Chu, A. Trifonov, E. Kaxiras, and M. D. Lukin. Properties of nitrogen-vacancy centers in diamond: The group theoretic approach. *New Journal of Physics*, 13, 2011.

[87] M. L. Goldman, A. Sipahigil, M. W. Doherty, N. Y. Yao, S. D. Bennett, M. Markham, D. J. Twitchen, N. B. Manson, A. Kubanek, and M. D. Lukin. Phonon-induced population dynamics and intersystem crossing in nitrogen-vacancy centers. *Physical Review Letters*, 114(14):145502, apr 2015.

[88] G. D. Fuchs, A. L. Falk, V. V. Dobrovitski, and D. D. Awschalom. Spin coherence during optical excitation of a single nitrogen-vacancy center in diamond. *Physical Review Letters*, 108(15):157602, apr 2012.

[89] D. M. Toyli, D. J. Christle, A. Alkauskas, B. B. Buckley, C. G. Van de Walle, and D. D. Awschalom. Measurement and control of single nitrogen-vacancy center spins above 600 K. *Physical Review X*, 2(3):031001, jul 2012.

[90] David J. Christle, Abram L. Falk, Paolo Andrich, Paul V. Klimov, Jawad Ul Hassan, Nguyen T. Son, Erik Janzén, Takeshi Ohshima, and David D. Awschalom. Isolated electron spins in silicon carbide with millisecond coherence times. *Nature Materials*, 14(2):160–163, 2015.

[91] Fei-Fei Yan, Jun-Feng Wang, Qiang Li, Ze-Di Cheng, Jin-Ming Cui, Wen-Zheng Liu, Jin-Shi Xu, Chuan-Feng Li, and Guang-Can Guo. Coherent Control of Defect Spins in Silicon Carbide above 550 K. *Physical Review Applied*, 10:44042, 2018.

[92] Matthias Widmann, Sang-Yun Lee, Torsten Rendler, Nguyen Tien Son, Helmut Fedder, Seoyoung Paik, Li-Ping Yang, Nan Zhao, Sen Yang, Ian Booker, Andrej Denisenko, Mohammad Jamali, S. Ali Momenzadeh, Ilja Gerhardt, Takeshi Ohshima, Adam Gali, Erik Janzén, and Jörg Wrachtrup. Coherent control of single spins in silicon carbide at room temperature. *Nature Materials*, 14(2):164–168, feb 2015.

[93] Ilya P. Radko, Mads Boll, Niels M. Israelsen, Nicole Raatz, Jan Meijer, Fedor Jelezko, Ulrik L. Andersen, and Alexander Huck. Determining the internal quantum efficiency of shallow-implanted nitrogen-vacancy defects in bulk diamond. *Optics Express*, 24(24):27715, nov 2016.

[94] Michel Bockstedte, Felix Schütz, Thomas Garratt, Viktor Ivády, and Adam Gali. Ab initio description of highly correlated states in defects for realizing quantum bits. *npj Quantum Materials*, 3(1):1–6, dec 2018.

[95] Joel Davidsson. Theoretical polarization of zero phonon lines in point defects. feb 2020.

[96] Péter Udvarhelyi, Gergő Thiering, Naoya Morioka, Charles Babin, Florian Kaiser, Daniil Lukin, Takeshi Ohshima, Jawad Ul-Hassan, Nguyen Tien Son, Jelena Vučković, Jörg Wrachtrup, and Adam Gali. Vibronic states and their effect on the temperature and strain dependence of silicon-vacancy qubits in 4H silicon carbide. 2020.

[97] M. W. Doherty, F. Dolde, H. Fedder, F. Jelezko, J. Wrachtrup, N. B. Manson, and L. C.L. Hollenberg. Theory of the ground-state spin of the NV - center in diamond. *Physical Review B - Condensed Matter and Materials Physics*, 85(20):205203, may 2012.

[98] P. V. Klimov, A. L. Falk, B. B. Buckley, and D. D. Awschalom. Electrically driven spin resonance in silicon carbide color centers. *Physical Review Letters*, 112(8), 2014.

[99] Abram L. Falk, Paul V. Klimov, Bob B. Buckley, Viktor Ivády, Igor A. Abrikosov, Greg Calusine, William F. Koehl, Ádám Gali, and David D. Awschalom. Electrically and mechanically tunable electron spins in silicon carbide color centers. *Physical Review Letters*, 112(18):187601, may 2014.

[100] A. Bienfait, J. J. Pla, Y. Kubo, X. Zhou, M. Stern, C. C. Lo, C. D. Weis, T. Schenkel,

D. Vion, D. Esteve, J. J.L. Morton, and P. Bertet. Controlling spin relaxation with a cavity. *Nature*, 531(7592):74–77, mar 2016.

[101] T. Astner, J. Gugler, A. Angerer, S. Wald, S. Putz, N. J. Mauser, M. Trupke, H. Sumiya, S. Onoda, J. Isoya, J. Schmiedmayer, P. Mohn, and J. Majer. Solid-state electron spin lifetime limited by phononic vacuum modes. *Nature Materials*, 17(4):313–317, apr 2018.

[102] Hosung Seo, Abram L. Falk, Paul V. Klimov, Kevin C. Miao, Giulia Galli, and David D. Awschalom. Quantum decoherence dynamics of divacancy spins in silicon carbide. *Nature Communications*, 7(1):1–9, sep 2016.

[103] T. H. Taminiau, J. J.T. Wagenaar, T. Van Der Sar, F. Jelezko, V. V. Dobrovitski, and R. Hanson. Detection and control of individual nuclear spins using a weakly coupled electron spin. *Physical Review Letters*, 109(13):137602, sep 2012.

[104] Zsolt Zolnai. *Irradiation-induced crystal defects in silicon carbide*. PhD thesis, Budapest University of Technology and Economics, 2005.

[105] A. A. Lebedev. *Radiation Effects in SiC*, volume 6. Materials research forum, 2017.

[106] Pavel Hazdra and Jan Vobecký. Radiation Defects Created in n -Type 4H-SiC by Electron Irradiation in the Energy Range of 1–10MeV. *physica status solidi (a)*, 216(17):1900312, sep 2019.

[107] C. Hemmingsson, N. T. Son, O. Kordina, E. Janzén, and J. L. Lindström. Capture cross sections of electron irradiation induced defects in 6H-SiC. *Journal of Applied Physics*, 84(2):704–708, jul 1998.

[108] Michel Bockstedte, Alexander Mattausch, and Oleg Pankratov. Ab initio study of the annealing of vacancies and interstitials in cubic SiC: Vacancy-interstitial recombination

and aggregation of carbon interstitials. *Physical Review B - Condensed Matter and Materials Physics*, 69(23):235202, jun 2004.

[109] Franziska C. Beyer. *Deep Levels in SiC*. PhD thesis, Linkoping University, 2011.

[110] P. Deák, A. Gali, and B. Aradi. Hydrogen in SiC. pages 57–88. Springer, Berlin, Heidelberg, 2004.

[111] W. E. Carlos, N. Y. Garces, E. R. Glaser, and M. A. Fanton. Annealing of multivacancy defects in 4H-SiC. *Physical Review B - Condensed Matter and Materials Physics*, 74(23):235201, dec 2006.

[112] F. Fuchs, B. Stender, M. Trupke, D. Simin, J. Pflaum, V. Dyakonov, and G. V. Astakhov. Engineering near-infrared single-photon emitters with optically active spins in ultrapure silicon carbide. *Nature Communications*, 6(1):1–7, jul 2015.

[113] W. Pfaff, B. J. Hensen, H. Bernien, S. B. Van Dam, M. S. Blok, T. H. Taminiau, M. J. Tiggelman, R. N. Schouten, M. Markham, D. J. Twitchen, and R. Hanson. Unconditional quantum teleportation between distant solid-state quantum bits. *Science*, 345(6196):532–535, 2014.

[114] B. MacHielse, S. Bogdanovic, S. Meesala, S. Gauthier, M. J. Burek, G. Joe, M. Chalupnik, Y. I. Sohn, J. Holzgrafe, R. E. Evans, C. Chia, H. Atikian, M. K. Bhaskar, D. D. Sukachev, L. Shao, S. Maity, M. D. Lukin, and M. Lončar. Quantum Interference of Electromechanically Stabilized Emitters in Nanophotonic Devices. *Physical Review X*, 9(3):031022, aug 2019.

[115] Daniil M. Lukin, Alexander D. White, Melissa A. Guidry, Rahul Trivedi, Naoya Morioka, Charles Babin, Jawad Ul Hassan, Nguyen Tien Son, Takeshi Ohshima, Praful K. Vasireddy, Mamdouh H. Nasr, Shuo Sun, Jean-Phillipe W. MacLean, Constantin Dory, Emilio A. Nanni, Jörg Wrachtrup, Florian Kaiser, and Jelena Vučković. Spec-

trally reconfigurable quantum emitters enabled by optimized fast modulation. (1), 2020.

[116] Charles F. De Las Casas, David J. Christle, Jawad Ul Hassan, Takeshi Ohshima, Nguyen T. Son, and David D. Awschalom. Stark tuning and electrical charge state control of single divacancies in silicon carbide. *Applied Physics Letters*, 111(26), 2017.

[117] Yiwen Chu and Mikhail D. Lukin. Quantum optics with nitrogen-vacancy centers in diamond. apr 2015.

[118] I. G. Ivanov, C. Hallin, A. Henry, O. Kordina, and E. Janzén. Nitrogen doping concentration as determined by photoluminescence in 4H- And 6H-SiC. *Journal of Applied Physics*, 80(6):3504–3508, sep 1996.

[119] Koutarou Kawahara, Xuan Thang Trinh, Nguyen Tien Son, Erik Janzén, Jun Suda, and Tsunenobu Kimoto. Quantitative comparison between Z1/2 center and carbon vacancy in 4H-SiC. *Journal of Applied Physics*, 115(14):143705, apr 2014.

[120] S. B. Van Dam, M. Walsh, M. J. Degen, E. Bersin, S. L. Mouradian, A. Galiullin, M. Ruf, M. Ijspeert, T. H. Taminiau, R. Hanson, and D. R. Englund. Optical coherence of diamond nitrogen-vacancy centers formed by ion implantation and annealing. *Physical Review B*, 99(16), 2019.

[121] Y. Chu, N. P. De Leon, B. J. Shields, B. Hausmann, R. Evans, E. Togan, M. J. Burek, M. Markham, A. Stacey, A. S. Zibrov, A. Yacoby, D. J. Twitchen, M. Loncar, H. Park, P. Maletinsky, and M. D. Lukin. Coherent optical transitions in implanted nitrogen vacancy centers. *Nano Letters*, 14(4):1982–1986, 2014.

[122] H. Bernien, B. Hensen, W. Pfaff, G. Koolstra, M. S. Blok, L. Robledo, T. H. Taminiau, M. Markham, D. J. Twitchen, L. Childress, and R. Hanson. Heralded entanglement between solid-state qubits separated by three metres. *Nature*, 497(7447):86–90, 2013.

[123] V. M. Acosta, C. Santori, A. Faraon, Z. Huang, K. M.C. Fu, A. Stacey, D. A. Simpson, K. Ganesan, S. Tomljenovic-Hanic, A. D. Greentree, S. Prawer, and R. G. Beausoleil. Dynamic stabilization of the optical resonances of single nitrogen-vacancy centers in diamond. *Physical Review Letters*, 108(20), 2012.

[124] Jan Isberg, Johan Hammersberg, Erik Johansson, Tobias Wikström, Daniel J. Twitchen, Andrew J. Whitehead, Steven E. Coe, and Geoffrey A. Scarsbrook. High carrier mobility in single-crystal plasma-deposited diamond. *Science*, 297(5587):1670–1672, sep 2002.

[125] Ph. Tamarat, T. Gaebel, J. R. Rabeau, M. Khan, A. D. Greentree, H. Wilson, L. C.L. Hollenberg, S. Prawer, P. Hemmer, F. Jelezko, and J. Wrachtrup. Stark shift control of single optical centers in diamond. *Physical Review Letters*, 97(8):083002, aug 2006.

[126] David Menichelli, Monica Scaringella, Francesco Moscatelli, Mara Bruzzi, and Roberta Nipoti. Characterization of energy levels related to impurities in epitaxial 4H-SiC ion implanted p+n junctions. *Diamond and Related Materials*, 16(1):6–11, jan 2007.

[127] N. Aslam, G. Waldherr, P. Neumann, F. Jelezko, and J. Wrachtrup. Photo-induced ionization dynamics of the nitrogen vacancy defect in diamond investigated by single-shot charge state detection. *New Journal of Physics*, 15, 2013.

[128] David A. Hopper, Joseph D. Lauigan, Tzu Yung Huang, and Lee C. Bassett. Real-Time Charge Initialization of Diamond Nitrogen-Vacancy Centers for Enhanced Spin Readout. *Physical Review Applied*, 13(2):024016, feb 2020.

[129] P. Siyushev, F. Kaiser, V. Jacques, I. Gerhardt, S. Bischof, H. Fedder, J. Dodson, M. Markham, D. Twitchen, F. Jelezko, and J. Wrachtrup. Monolithic diamond optics for single photon detection. *Applied Physics Letters*, 97(24):241902, dec 2010.

[130] Peter C. Humphreys, Norbert Kalb, Jaco P. J. Morits, Raymond N. Schouten, Raymond F. L. Vermeulen, Daniel J. Twitchen, Matthew Markham, and Ronald Han-

son. Deterministic delivery of remote entanglement on a quantum network. *Nature*, 558(7709):268–273, jun 2018.

[131] K. M. Lee, Le Si Dang, G. D. Watkins, and W. J. Choyke. Optically detected magnetic resonance study of SiC:Ti. *Physical Review B*, 32(4):2273–2284, aug 1985.

[132] Natasha Tabassum, Vasileios Nikas, Alex E. Kaloyeros, Vidya Kaushik, Edward Crawford, Mengbing Huang, Gallis, and Spyros. Engineered telecom emission and controlled positioning of Er3+ enabled by SiC nanophotonic structures, 2020.

[133] William F. Koehl, Berk Diler, Samuel J. Whiteley, Alexandre Bourassa, N. T. Son, Erik Janzén, and David D. Awschalom. Resonant optical spectroscopy and coherent control of C r4+ spin ensembles in SiC and GaN. *Physical Review B*, 95(3):035207, jan 2017.

[134] Charles H. Bennett, François Bessette, Gilles Brassard, Louis Salvail, and John Smolin. Experimental quantum cryptography. *Journal of Cryptology*, 5(1):3–28, jan 1992.

[135] Charles H. Bennett and Gilles Brassard. Quantum cryptography: Public key distribution and coin tossing. *Theoretical Computer Science*, 560(P1):7–11, dec 2014.

[136] Artur K. Ekert. Quantum cryptography based on Bellâs theorem. *Physical Review Letters*, 67(6):661–663, aug 1991.

[137] Stephanie Wehner, David Elkouss, and Ronald Hanson. Quantum internet: A vision for the road ahead, oct 2018.

[138] H. J. Kimble. The quantum internet, jun 2008.

[139] Sheng Kai Liao, Wen Qi Cai, Wei Yue Liu, Liang Zhang, Yang Li, Ji Gang Ren, Juan Yin, Qi Shen, Yuan Cao, Zheng Ping Li, Feng Zhi Li, Xia Wei Chen, Li Hua Sun, Jian Jun Jia, Jin Cai Wu, Xiao Jun Jiang, Jian Feng Wang, Yong Mei Huang, Qiang Wang, Yi Lin Zhou, Lei Deng, Tao Xi, Lu Ma, Tai Hu, Qiang Zhang, Yu Ao Chen,

Nai Le Liu, Xiang Bin Wang, Zhen Cai Zhu, Chao Yang Lu, Rong Shu, Cheng Zhi Peng, Jian Yu Wang, and Jian Wei Pan. Satellite-to-ground quantum key distribution. *Nature*, 549(7670):43–47, sep 2017.

[140] W. K. Wootters and W. H. Zurek. A single quantum cannot be cloned. *Nature*, 299(5886):802–803, 1982.

[141] Charles H. Bennett, Gilles Brassard, Claude Crépeau, Richard Jozsa, Asher Peres, and William K. Wootters. Teleporting an unknown quantum state via dual classical and Einstein-Podolsky-Rosen channels. *Physical Review Letters*, 70(13):1895–1899, mar 1993.

[142] Xiao Song Ma, Thomas Herbst, Thomas Scheidl, Daqing Wang, Sebastian Kropatschek, William Naylor, Bernhard Wittmann, Alexandra Mech, Johannes Kofler, Elena Anisimova, Vadim Makarov, Thomas Jennewein, Rupert Ursin, and Anton Zeilinger. Quantum teleportation over 143 kilometres using active feed-forward. *Nature*, 489(7415):269–273, sep 2012.

[143] Benjamin Kambs and Christoph Becher. Limitations on the indistinguishability of photons from remote solid state sources. *New Journal of Physics*, 20(11), 2018.

[144] T. Legero, T. Wilk, A. Kuhn, and G. Rempe. Time-resolved two-photon quantum interference. In *Applied Physics B: Lasers and Optics*, volume 77, pages 797–802. Springer, dec 2003.

[145] Katiúscia N Cassemiro, Kaisa Laiho, and Christine Silberhorn. Accessing the purity of a single photon by the width of the Hong–Ou–Mandel interference. *New Journal of Physics*, 12(11):113052, nov 2010.

[146] François Hénault. Quantum physics and the beam splitter mystery. In *The Nature of Light: What are Photons? VI*, volume 9570, page 95700Q, 2015.

[147] Ulf Leonhardt. Quantum physics of simple optical instruments. *Reports on Progress in Physics*, 66(7):1207–1249, 2003.

[148] Naoya Morioka, Charles Babin, Roland Nagy, Izel Gediz, Erik Hesselmeier, Di Liu, Matthew Joliffe, Matthias Niethammer, Durga Dasari, Vadim Vorobyov, Roman Kolesov, Rainer Stöhr, Jawad Ul-Hassan, Nguyen Tien Son, Takeshi Ohshima, Péter Udvarhelyi, Gergő Thiering, Adam Gali, Jörg Wrachtrup, and Florian Kaiser. Spin-controlled generation of indistinguishable and distinguishable photons from silicon vacancy centres in silicon carbide. 2020.

[149] Hannes Bernien, Lilian Childress, Lucio Robledo, Matthew Markham, Daniel Twitchen, and Ronald Hanson. Two-photon quantum interference from separate nitrogen vacancy centers in diamond. *Physical Review Letters*, 108(4), 2012.

[150] Sean D. Barrett and Pieter Kok. Efficient high-fidelity quantum computation using matter qubits and linear optics. *Physical Review A - Atomic, Molecular, and Optical Physics*, 71(6):060310, jun 2005.

[151] B. Hensen, H. Bernien, A. E. Dreaú, A. Reiserer, N. Kalb, M. S. Blok, J. Ruitenberg, R. F.L. Vermeulen, R. N. Schouten, C. Abellán, W. Amaya, V. Pruneri, M. W. Mitchell, M. Markham, D. J. Twitchen, D. Elkouss, S. Wehner, T. H. Taminiau, and R. Hanson. Loophole-free Bell inequality violation using electron spins separated by 1.3 kilometres. *Nature*, 526(7575):682–686, oct 2015.

[152] David D. Awschalom, Ronald Hanson, Jörg Wrachtrup, and Brian B. Zhou. Quantum technologies with optically interfaced solid-state spins. *Nature Photonics*, 12(9):516–527, 2018.

[153] Austin G. Fowler, David S. Wang, Charles D. Hill, Thaddeus D. Ladd, Rodney Van Meter, and Lloyd C.L. Hollenberg. Surface code quantum communication. *Physical Review Letters*, 104(18):180503, may 2010.

[154] Donovan Buterakos, Edwin Barnes, and Sophia E Economou. Deterministic generation of all-photonic quantum repeaters from solid-state emitters. *Physical Review X*, 7(4), 2017.

[155] Cody Jones, Danny Kim, Matthew T Rakher, Paul G Kwiat, and Thaddeus D Ladd. Design and analysis of communication protocols for quantum repeater networks. *New Journal of Physics*, 18(8):083015, aug 2016.

[156] Sophia E Economou and Pratibha Dev. Spin-photon entanglement interfaces in silicon carbide defect centers. *Nanotechnology*, 27(50), 2016.

[157] M. K. Bhaskar, R. Riedinger, B. Machielse, D. S. Levonian, C. T. Nguyen, E. N. Knall, H. Park, D. Englund, M. Lončar, D. D. Sukachev, and M. D. Lukin. Experimental demonstration of memory-enhanced quantum communication. *Nature*, 580(7801):60–64, apr 2020.

[158] Shuo Sun, Hyochul Kim, Zhouchen Luo, Glenn S. Solomon, and Edo Waks. A single-photon switch and transistor enabled by a solid-state quantum memory. *Science*, 361(6397):57–60, jul 2018.

[159] A. Sipahigil, R. E. Evans, D. D. Sukachev, M. J. Burek, J. Borregaard, M. K. Bhaskar, C. T. Nguyen, J. L. Pacheco, H. A. Atikian, C. Meuwly, R. M. Camacho, F. Jelezko, E. Bielejec, H. Park, M. Lončar, and M. D. Lukin. An integrated diamond nanophotonics platform for quantum-optical networks. *Science*, 354(6314):847–850, nov 2016.

[160] Sen Yang, Ya Wang, D. D.Bhaktavatsala Rao, Thai Hien Tran, Ali S. Momenzadeh, M. Markham, D. J. Twitchen, Ping Wang, Wen Yang, Rainer Stöhr, Philipp Neumann, Hideo Kosaka, and Jörg Wrachtrup. High-fidelity transfer and storage of photon states in a single nuclear spin. *Nature Photonics*, 10(8):507–511, aug 2016.

[161] S. Lloyd, M. S. Shahriar, J. H. Shapiro, and P. R. Hemmer. Long distance, uncondi-

tional teleportation of atomic states via complete bell state measurements. *Physical Review Letters*, 87(16):167903, sep 2001.

[162] Christoph Simon and William T.M. Irvine. Robust long-distance entanglement and a loophole-free bell test with ions and photons. *Physical Review Letters*, 91(11):110405, sep 2003.

[163] Kevin C. Chen, Eric Bersin, and Dirk Englund. A Polarization Encoded Photon-to-Spin Interface. apr 2020.

[164] Anaïs Dréau, Anna Tcheborateva, Aboubakr El Mahdaoui, Cristian Bonato, and Ronald Hanson. Quantum Frequency Conversion of Single Photons from a Nitrogen-Vacancy Center in Diamond to Telecommunication Wavelengths. *Physical Review Applied*, 9(6):064031, jun 2018.

[165] J. S. Pelc, C. Langrock, Q. Zhang, and M. M. Fejer. Influence of domain disorder on parametric noise in quasi-phase-matched quantum frequency converters. *Optics Letters*, 35(16):2804, aug 2010.

[166] Noel H. Wan, Tsung-Ju Lu, Kevin C. Chen, Michael P. Walsh, Matthew E. Trusheim, Lorenzo De Santis, Eric A. Bersin, Isaac B. Harris, Sara L. Mouradian, Ian R. Christen, Edward S. Bielejec, and Dirk Englund. Large-scale integration of near-indistinguishable artificial atoms in hybrid photonic circuits. nov 2019.

[167] Michael J. Burek, Charles Meuwly, Ruffin E. Evans, Mihir K. Bhaskar, Alp Sipahigil, Srujan Meesala, Bartholomeus MacHielse, Denis D. Sukachev, Christian T. Nguyen, Jose L. Pacheco, Edward Bielejec, Mikhail D. Lukin, and Marko Lončar. Fiber-coupled diamond quantum nanophotonic interface. *Physical Review Applied*, 8(2):024026, aug 2017.

[168] Stefan Bogdanović, Suzanne B. Van Dam, Cristian Bonato, Lisanne C. Coenen, Anne Marije J. Zwerver, Bas Hensen, Madelaine S.Z. Liddy, Thomas Fink, Andreas Reiserer,

Marko Lončar, and Ronald Hanson. Design and low-temperature characterization of a tunable microcavity for diamond-based quantum networks. *Applied Physics Letters*, 110(17):171103, apr 2017.

[169] Tzu Yung Huang, Richard R. Grote, Sander A. Mann, David A. Hopper, Annemarie L. Exarhos, Gerald G. Lopez, Garrett R. Kaighn, Erik C. Garnett, and Lee C. Bassett. A monolithic immersion metalens for imaging solid-state quantum emitters. *Nature Communications*, 10(1):1–8, dec 2019.

[170] Maximilian Ruf, Mark Ijspeert, Suzanne Van Dam, Nick De Jong, Hans Van Den Berg, Guus Evers, and Ronald Hanson. Optically Coherent Nitrogen-Vacancy Centers in Micrometer-Thin Etched Diamond Membranes. *Nano Letters*, 19(6):3987–3992, jun 2019.

[171] Francesco Pagliano, Yongjin Cho, Tian Xia, Frank Van Otten, Robert Johne, and Andrea Fiore. Dynamically controlling the emission of single excitons in photonic crystal cavities. *Nature Communications*, 5(1):1–6, dec 2014.

[172] Bharath Srivathsan, Gurpreet Kaur Gulati, Alessandro Cerè, Brenda Chng, and Christian Kurtsiefer. Reversing the temporal envelope of a heralded single photon using a cavity. *Physical Review Letters*, 113(16):163601, oct 2014.

[173] F. Kimiaee Asadi, S. C. Wein, and C. Simon. Long-distance quantum communication with single $ˆ{167}$Er ions. apr 2020.

[174] Lucio Robledo, Lilian Childress, Hannes Bernien, Bas Hensen, Paul F.A. Alkemade, and Ronald Hanson. High-fidelity projective read-out of a solid-state spin quantum register. *Nature*, 477(7366):574–578, 2011.

[175] P. C. Maurer, G. Kucsko, C. Latta, L. Jiang, N. Y. Yao, S. D. Bennett, F. Pastawski, D. Hunger, N. Chisholm, M. Markham, D. J. Twitchen, J. I. Cirac, and M. D.

Lukin. Room-Temperature Quantum Bit Memory Exceeding One Second. *Science*, 336(6086):1283–1286, jun 2012.

[176] Philipp Neumann, Johannes Beck, Matthias Steiner, Florian Rempp, Helmut Fedder, Philip R. Hemmer, Jörg Wrachtrup, and Fedor Jelezko. Single-shot readout of a single nuclear spin. *Science*, 329(5991):542–544, 2010.

[177] B. J. Shields, Q. P. Unterreithmeier, N. P. De Leon, H. Park, and M. D. Lukin. Efficient Readout of a Single Spin State in Diamond via Spin-to-Charge Conversion. *Physical Review Letters*, 114(13), 2015.

[178] David Hopper, Henry Shulevitz, and Lee Bassett. Spin Readout Techniques of the Nitrogen-Vacancy Center in Diamond. *Micromachines*, 9(9):437, aug 2018.

[179] Andreas Reiserer, Norbert Kalb, Machiel S. Blok, Koen J.M. van Bemmelen, Tim H. Taminiau, Ronald Hanson, Daniel J. Twitchen, and Matthew Markham. Robust quantum-network memory using decoherence-protected subspaces of nuclear spins. *Physical Review X*, 6(2):021040, jun 2016.

[180] N. Kalb, P. C. Humphreys, J. J. Slim, and R. Hanson. Dephasing mechanisms of diamond-based nuclear-spin memories for quantum networks. *Physical Review A*, 97(6):062330, jun 2018.

[181] Paul V. Klimov, Abram L. Falk, David J. Christle, Viatcheslav V. Dobrovitski, and David D. Awschalom. Quantum entanglement at ambient conditions in a macroscopic solid-state spin ensemble. *Science Advances*, 1(10), nov 2015.

[182] C. E. Bradley, J. Randall, M. H. Abobeih, R. C. Berrevoets, M. J. Degen, M. A. Bakker, M. Markham, D. J. Twitchen, and T. H. Taminiau. A ten-qubit solid-state spin register with quantum memory up to one minute. *Phys. Rev. X*, 9:031045, Sep 2019.

[183] T. H. Taminiau, J. Cramer, T. Van Der Sar, V. V. Dobrovitski, and R. Hanson. Universal control and error correction in multi-qubit spin registers in diamond. *Nature Nanotechnology*, 9(3):171–176, feb 2014.

[184] Bong-Shik Song, Takashi Asano, Seungwoo Jeon, Heungjoon Kim, Changxuan Chen, Dongyeon Daniel Kang, and Susumu Noda. Ultrahigh-Q photonic crystal nanocavities based on 4H silicon carbide. *Optica*, 6(8):991, aug 2019.

[185] Kenneth W. Lee, Donghun Lee, Preeti Ovartchaiyapong, Joaquin Minguzzi, Jero R. Maze, and Ania C. Bleszynski Jayich. Strain Coupling of a Mechanical Resonator to a Single Quantum Emitter in Diamond. *Physical Review Applied*, 6(3):034005, sep 2016.

[186] H. Y. Chen, E. R. MacQuarrie, and G. D. Fuchs. Orbital State Manipulation of a Diamond Nitrogen-Vacancy Center Using a Mechanical Resonator. *Physical Review Letters*, 120(16):167401, apr 2018.

[187] E. R. Macquarrie, M. Otten, S. K. Gray, and G. D. Fuchs. Cooling a mechanical resonator with nitrogen-vacancy centres using a room temperature excited state spin-strain interaction. *Nature Communications*, 8(1):1–10, feb 2017.

[188] Michael S.J. Barson, Phani Peddibhotla, Preeti Ovartchaiyapong, Kumaravelu Ganesan, Richard L. Taylor, Matthew Gebert, Zoe Mielens, Berndt Koslowski, David A. Simpson, Liam P. McGuinness, Jeffrey McCallum, Steven Prawer, Shinobu Onoda, Takeshi Ohshima, Ania C. Bleszynski Jayich, Fedor Jelezko, Neil B. Manson, and Marcus W. Doherty. Nanomechanical Sensing Using Spins in Diamond. *Nano Letters*, 17(3):1496–1503, mar 2017.

[189] Péter Udvarhelyi and Adam Gali. Ab Initio Spin-Strain Coupling Parameters of Divacancy Qubits in Silicon Carbide. *Physical Review Applied*, 10(5):054010, nov 2018.

[190] S. D Bennett, N. Y Yao, J. Otterbach, P. Zoller, P. Rabl, and M. D Lukin. Phonon-

Induced Spin-Spin Interactions in Diamond Nanostructures: Application to Spin Squeezing. *Physical Review Letters*, 110(15):156402, apr 2013.

[191] K. V. Kepesidis, S. D. Bennett, S. Portolan, M. D. Lukin, and P. Rabl. Phonon cooling and lasing with nitrogen-vacancy centers in diamond. *Physical Review B - Condensed Matter and Materials Physics*, 88:1–12, 2013.

[192] Ariana Beste, Decarlos E. Taylor, D. Andrew Golter, and Chih W. Lai. Charge state switching of the divacancy defect in 4H -SiC. *Physical Review B*, 98(21), 2018.

[193] G. Wolfowicz, S. J. Whiteley, and D. D. Awschalom. Electrometry by optical charge conversion of deep defects in 4H-SiC. *Proceedings of the National Academy of Sciences of the United States of America*, 115(31):7879–7883, 2018.

[194] F. Dolde, H. Fedder, M. W. Doherty, T. Nöbauer, F. Rempp, G. Balasubramanian, T. Wolf, F. Reinhard, L. C.L. Hollenberg, F. Jelezko, and J. Wrachtrup. Electric-field sensing using single diamond spins. *Nature Physics*, 7(6):459–463, 2011.

[195] Julia Michl, Jakob Steiner, Andrej Denisenko, André Bülau, André Zimmermann, Kazuo Nakamura, Hitoshi Sumiya, Shinobu Onoda, Philipp Neumann, Junichi Isoya, and Jörg Wrachtrup. Robust and Accurate Electric Field Sensing with Solid State Spin Ensembles. *Nano Letters*, 19(8):4904–4910, 2019.

[196] I. A. Chaikovskii, G. M. Shmelev, and A. I. German. AC Conductivity of Highly Inhomogeneous Semiconductors. *physica status solidi (b)*, 129(1):393–398, may 1985.

[197] C Bonato, M S Blok, H T Dinani, D W Berry, M L Markham, D J Twitchen, and R Hanson. Optimized quantum sensing with a single electron spin using real-time adaptive measurements. *Nature Nanotechnology*, 11(3):247–252, 2016.

[198] G. Waldherr, Y. Wang, S. Zaiser, M. Jamali, T. Schulte-Herbrüggen, H. Abe,

T. Ohshima, J. Isoya, J. F. Du, P. Neumann, and J. Wrachtrup. Quantum error correction in a solid-state hybrid spin register. *Nature*, 506(7487):204–207, 2014.

[199] Klaus D. Jöns, Katarina Stensson, Marcus Reindl, Marcin Swillo, Yongheng Huo, Val Zwiller, Armando Rastelli, Rinaldo Trotta, and Gunnar Björk. Two-photon interference from two blinking quantum emitters. *Physical Review B*, 96(7), 2017.

[200] Dolev Bluvstein, Zhiran Zhang, and Ania C.Bleszynski Jayich. Identifying and Mitigating Charge Instabilities in Shallow Diamond Nitrogen-Vacancy Centers. *Physical Review Letters*, 122(7), 2019.

[201] L. C. Bassett, F. J. Heremans, C. G. Yale, B. B. Buckley, and D. D. Awschalom. Electrical Tuning of Single Nitrogen-Vacancy Center Optical Transitions Enhanced by Photoinduced Fields. *Physical Review Letters*, 107(26):266403, 2011.

[202] Janik Wolters, Nikola Sadzak, Andreas W. Schell, Tim Schröder, and Oliver Benson. Measurement of the ultrafast spectral diffusion of the optical transition of nitrogen vacancy centers in nano-size diamond using correlation interferometry. *Physical Review Letters*, 110(2), 2013.

[203] T. Murai, T. Makino, H. Kato, M. Shimizu, T. Murooka, E. D. Herbschleb, Y. Doi, H. Morishita, M. Fujiwara, M. Hatano, S. Yamasaki, and N. Mizuochi. Engineering of Fermi level by nin diamond junction for control of charge states of NV centers. *Applied Physics Letters*, 112(11), 2018.

[204] K. Beha, A. Batalov, N. B. Manson, R. Bratschitsch, and A. Leitenstorfer. Optimum photoluminescence excitation and recharging cycle of single nitrogen-vacancy centers in ultrapure diamond. *Physical Review Letters*, 109(9), 2012.

[205] Benjamin Brunel, Carles Blanch, Vanni Petrolli, Antoine Delon, Romain Pierrat, and Giovanni Cappello. Structure and dynamics of multicellular assemblies measured by coherent light scattering. *New Journal of Physics*, 2017.

[206] Petr Siyushev, Milos Nesladek, Emilie Bourgeois, Michal Gulka, Jaroslav Hruby, Takashi Yamamoto, Michael Trupke, Tokuyuki Teraji, Junichi Isoya, and Fedor Jelezko. Photoelectrical imaging and coherent spin-state readout of single nitrogen-vacancy centers in diamond. *Science*, 363(6428):728–731, 2019.

[207] M. Kim, H. J. Mamin, M. H. Sherwood, K. Ohno, D. D. Awschalom, and D. Rugar. Decoherence of Near-Surface Nitrogen-Vacancy Centers Due to Electric Field Noise. *Physical Review Letters*, 115(8), 2015.

[208] M. S. Grinolds, M. Warner, K. De Greve, Y. Dovzhenko, L. Thiel, R. L. Walsworth, S. Hong, P. Maletinsky, and A. Yacoby. Subnanometre resolution in three-dimensional magnetic resonance imaging of individual dark spins. *Nature Nanotechnology*, 9(4):279–284, 2014.

[209] Matthias Pfender, Nabeel Aslam, Patrick Simon, Denis Antonov, Gergo Thiering, Sina Burk, Felipe Fávaro De Oliveira, Andrej Denisenko, Helmut Fedder, Jan Meijer, Jose A. Garrido, Adam Gali, Tokuyuki Teraji, Junichi Isoya, Marcus William Doherty, Audrius Alkauskas, Alejandro Gallo, Andreas Grüneis, Philipp Neumann, and Jörg Wrachtrup. Protecting a Diamond Quantum Memory by Charge State Control. *Nano Letters*, 17(10):5931–5937, 2017.

[210] Matthias Widmann, Matthias Niethammer, Takahiro Makino, Torsten Rendler, Stefan Lasse, Takeshi Ohshima, Jawad Ul Hassan, Nguyen Tien Son, Sang Yun Lee, and Jörg Wrachtrup. Bright single photon sources in lateral silicon carbide light emitting diodes. *Applied Physics Letters*, 112(23):231103, jun 2018.

[211] Matthias Niethammer, Matthias Widmann, Torsten Rendler, Naoya Morioka, Yu-Chen Chen, Rainer Stöhr, Jawad Ul Hassan, Shinobu Onoda, Takeshi Ohshima, Sang-Yun Lee, Amlan Mukherjee, Junichi Isoya, Nguyen Tien Son, and Jörg Wrachtrup. Coherent

electrical readout of defect spins in 4H-SiC by photo-ionization at ambient conditions. 2019.

[212] M. W. Doherty, C. A. Meriles, A. Alkauskas, H. Fedder, M. J. Sellars, and N. B. Manson. Towards a room-temperature spin quantum bus in diamond via electron photoionization, transport, and capture. *Physical Review X*, 6(4), 2016.

[213] Maki Shimizu, Toshiharu Makino, Takayuki Iwasaki, Kosuke Tahara, Hiromitsu Kato, Norikazu Mizuochi, Satoshi Yamasaki, and Mutsuko Hatano. Charge-state control of ensemble of nitrogen vacancy centers by n-i-n diamond junctions. *Applied Physics Express*, 11(3), 2018.

[214] Kenichi Ohno, F. Joseph Heremans, Lee C. Bassett, Bryan A. Myers, David M. Toyli, Ania C. Bleszynski Jayich, Christopher J. Palmstrøm, and David D. Awschalom. Engineering shallow spins in diamond with nitrogen delta-doping. *Applied Physics Letters*, 101(8), 2012.

[215] J Forneris, S. Ditalia Tchernij, P Traina, E Moreva, N Skukan, M. Jakšić, V Grilj, F. Bosia, E. Enrico, G. Amato, I. P. Degiovanni, B. Naydenov, F. Jelezko, M. Genovese, and P Olivero. Mapping the Local Spatial Charge in Defective Diamond by Means of N- v Sensors - A Self-Diagnostic Concept. *Physical Review Applied*, 10(1):1–15, 2018.

[216] Sören Wengerowsky, Siddarth Koduru Joshi, Fabian Steinlechner, Hannes Hübel, and Rupert Ursin. An entanglement-based wavelength-multiplexed quantum communication network. *Nature*, 564(7735):225–228, dec 2018.

[217] D. A. Broadway, N. Dontschuk, A. Tsai, S. E. Lillie, C. T.K. Lew, J. C. McCallum, B. C. Johnson, M. W. Doherty, A. Stacey, L. C.L. Hollenberg, and J. P. Tetienne. Spatial mapping of band bending in semiconductor devices using in situ quantum sensors. *Nature Electronics*, 1(9):502–507, 2018.

[218] A. N. Vamivakas, Y. Zhao, S. Fält, A. Badolato, J. M. Taylor, and M. Atatüre. Nanoscale Optical Electrometer. *Physical Review Letters*, 107(16):166802, oct 2011.

[219] Nicholas R. Jungwirth, Brian Calderon, Yanxin Ji, Michael G. Spencer, Michael E. Flatté, and Gregory D. Fuchs. Temperature Dependence of Wavelength Selectable Zero-Phonon Emission from Single Defects in Hexagonal Boron Nitride. *Nano Letters*, 16(10):6052–6057, oct 2016.

[220] Henri Thyrrestrup, Gabija Kirs, Hanna Le Jeannic, Tommaso Pregnolato, Liang Zhai, Laust Raahauge, Leonardo Midolo, Nir Rotenberg, Alisa Javadi, Diger Schott, Andreas D. Wieck, Arne Ludwig, Matthias C Lo, Immo So, Richard J. Warburton, Peter Lodahl, Gabija Kiršanskė, Hanna Le Jeannic, Tommaso Pregnolato, Liang Zhai, Laust Raahauge, Leonardo Midolo, Nir Rotenberg, Alisa Javadi, Rüdiger Schott, Andreas D. Wieck, Arne Ludwig, Matthias C. Löbl, Immo Söllner, Richard J. Warburton, and Peter Lodahl. Quantum Optics with Near-Lifetime-Limited Quantum-Dot Transitions in a Nanophotonic Waveguide. *Nano Lett*, 18(3):49, mar 2018.

[221] Matthias C. Löbl, Immo Söllner, Alisa Javadi, Tommaso Pregnolato, Rüdiger Schott, Leonardo Midolo, Andreas V. Kuhlmann, Søren Stobbe, Andreas D. Wieck, Peter Lodahl, Arne Ludwig, and Richard J. Warburton. Narrow optical linewidths and spin pumping on charge-tunable close-to-surface self-assembled quantum dots in an ultrathin diode. *Physical Review B*, 96(16), 2017.

[222] Chitraleema Chakraborty, Laura Kinnischtzke, Kenneth M. Goodfellow, Ryan Beams, and A. Nick Vamivakas. Voltage-controlled quantum light from an atomically thin semiconductor. *Nature Nanotechnology*, 10(6):507–511, 2015.

[223] C. Schreyvogel, V. Polyakov, R. Wunderlich, J. Meijer, and C. E. Nebel. Active charge state control of single NV centres in diamond by in-plane Al-Schottky junctions. *Scientific reports*, 5(1):12160, dec 2015.

[224] Hiromitsu Kato, Marco Wolfer, Christoph Schreyvogel, Michael Kunzer, Wolfgang Müller-Sebert, Harald Obloh, Satoshi Yamasaki, and Christoph Nebel. Tunable light emission from nitrogen-vacancy centers in single crystal diamond PIN diodes. *Applied Physics Letters*, 102(15), 2013.

[225] F. J. Heremans, G. D. Fuchs, C. F. Wang, R. Hanson, and D. D. Awschalom. Generation and transport of photoexcited electrons in single-crystal diamond. *Applied Physics Letters*, 94(15), 2009.

[226] D. A. Golter and C. W. Lai. Optical switching of defect charge states in 4H-SiC. *Scientific Reports*, 7(1):13406, dec 2017.

[227] Andreas V. Kuhlmann, Julien Houel, Arne Ludwig, Lukas Greuter, Dirk Reuter, Andreas D. Wieck, Martino Poggio, and Richard J. Warburton. Charge noise and spin noise in a semiconductor quantum device. *Nature Physics*, 9(9):570–575, 2013.

[228] Matthias Widmann, Matthias Niethammer, Dmitry Yu Fedyanin, Igor A. Khramtsov, Torsten Rendler, Ian D. Booker, Jawad Ul Hassan, Naoya Morioka, Yu Chen Chen, Ivan G. Ivanov, Nguyen Tien Son, Takeshi Ohshima, Michel Bockstedte, Adam Gali, Cristian Bonato, Sang Yun Lee, and Jörg Wrachtrup. Electrical Charge State Manipulation of Single Silicon Vacancies in a Silicon Carbide Quantum Optoelectronic Device. *Nano Letters*, 19(10):7173–7180, 2019.

[229] Michael E. Reimer and Catherine Cher. The quest for a perfect single-photon source, nov 2019.

[230] A. Lohrmann, N. Iwamoto, Z. Bodrog, S. Castelletto, T. Ohshima, T. J. Karle, A. Gali, S. Prawer, J. C. McCallum, and B. C. Johnson. Single-photon emitting diode in silicon carbide. *Nature Communications*, 6(1):1–7, jul 2015.

[231] A Lohrmann, B C Johnson, J C McCallum, and S Castelletto. A review on single

photon sources in silicon carbide. *Reports on Progress in Physics*, 80(3):034502, jan 2017.

[232] F. Fuchs, V. A. Soltamov, S. Väth, P. G. Baranov, E. N. Mokhov, G. V. Astakhov, and V. Dyakonov. Silicon carbide light-emitting diode as a prospective room temperature source for single photons. *Scientific Reports*, 3(1):1–4, apr 2013.

[233] T. Umeda, Y. Kagoyama, K. Tomita, Y. Abe, M. Sometani, M. Okamoto, S. Harada, and T. Hatakeyama. Electrically detected-magnetic-resonance identifications of defects at 4H-SiC(000 1)/SiO2 interfaces with wet oxidation. *Applied Physics Letters*, 115(15):151602, oct 2019.

[234] E. D. Herbschleb, H. Kato, Y. Maruyama, T. Danjo, T. Makino, S. Yamasaki, I. Ohki, K. Hayashi, H. Morishita, M. Fujiwara, and N. Mizuochi. Ultra-long coherence times amongst room-temperature solid-state spins. *Nature Communications*, 10(1):1–6, dec 2019.

[235] Felipe Fávaro De Oliveira, Denis Antonov, Ya Wang, Philipp Neumann, Seyed Ali Momenzadeh, Timo Häußermann, Alberto Pasquarelli, Andrej Denisenko, and Jörg Wrachtrup. Tailoring spin defects in diamond by lattice charging. *Nature Communications*, 8(1):1–8, may 2017.

[236] Tobias Lühmann, Roger John, Ralf Wunderlich, Jan Meijer, and Sébastien Pezzagna. Coulomb-driven single defect engineering for scalable qubits and spin sensors in diamond. *Nature Communications*, 10(1):1–9, dec 2019.

[237] Dávid Beke, Jan Valenta, Gyula Károlyházy, Sándor Lenk, Zsolt Czigány, Bence Gábor Márkus, Katalin Kamarás, Ferenc Simon, and Adam Gali. Room-Temperature Defect Qubits in Ultrasmall Nanocrystals. *The Journal of Physical Chemistry Letters*, pages 1675–1681, feb 2020.

[238] J. Stephen Hartman, Bob Berno, Paul Hazendonk, Christopher W. Kirby, Eric Ye, Josef Zwanziger, and Alex D. Bain. Nmr studies of nitrogen doping in the 4h polytype of silicon carbide: Site assignments and spinlattice relaxation. *The Journal of Physical Chemistry C*, 113(33):15024–15036, 2009.

[239] Peter Niedbalski, Qing Wang, Christopher Parish, Fatemeh Khashami, Andhika Kiswandhi, and Lloyd Lumata. Magnetic-Field-Dependent Lifetimes of Hyperpolarized 13C Spins at Cryogenic Temperature. *Journal of Physical Chemistry B*, 122(6):1898–1904, feb 2018.

[240] Cornelis J. Terblanche, Eduard C. Reynhardt, and Jan A. Van Wyk. 13C spin-lattice relaxation in natural diamond: Zeeman relaxation at 4.7 T and 300 K due to fixed paramagnetic nitrogen defects. *Solid State Nuclear Magnetic Resonance*, 20(1-2):1–22, aug 2001.

[241] Sebastian Zaiser, Torsten Rendler, Ingmar Jakobi, Thomas Wolf, Sang Yun Lee, Samuel Wagner, Ville Bergholm, Thomas Schulte-Herbrüggen, Philipp Neumann, and Jörg Wrachtrup. Enhancing quantum sensing sensitivity by a quantum memory. *Nature Communications*, 7(1):1–11, aug 2016.

[242] K. S. Cujia, J. M. Boss, K. Herb, J. Zopes, and C. L. Degen. Tracking the precession of single nuclear spins by weak measurements, jun 2019.

[243] T. K. Unden, D. Louzon, M. Zwolak, W. H. Zurek, and F. Jelezko. Revealing the Emergence of Classicality Using Nitrogen-Vacancy Centers. *Physical Review Letters*, 123(14):140402, oct 2019.

[244] Xing Rong, Jianpei Geng, Fazhan Shi, Ying Liu, Kebiao Xu, Wenchao Ma, Fei Kong, Zhen Jiang, Yang Wu, and Jiangfeng Du. Experimental fault-tolerant universal quantum gates with solid-state spins under ambient conditions. *Nature Communications*, 6(1):1–7, nov 2015.

[245] G. D. Fuchs, G. Burkard, P. V. Klimov, and D. D. Awschalom. A quantum memory intrinsic to single nitrogen-vacancy centres in diamond. *Nature Physics*, 7(10):789–793, oct 2011.

[246] Wolfgang Pfaff, Tim H. Taminiau, Lucio Robledo, Hannes Bernien, Matthew Markham, Daniel J. Twitchen, and Ronald Hanson. Demonstration of entanglement-by-measurement of solid-state qubits. *Nature Physics*, 9(1):29–33, 2013.

[247] M. V. Gurudev Dutt, L. Childress, L. Jiang, E. Togan, J. Maze, F. Jelezko, A. S. Zibrov, P. R. Hemmer, and M. D. Lukin. Quantum register based on individual electronic and nuclear spin qubits in diamond. *Science*, 316(5829):1312–1316, jun 2007.

[248] M. H. Abobeih, J. Randall, C. E. Bradley, H. P. Bartling, M. A. Bakker, M. J. Degen, M. Markham, D. J. Twitchen, and T. H. Taminiau. Atomic-scale imaging of a 27-nuclear-spin cluster using a quantum sensor. *Nature*, 576(7787):411–415, dec 2019.

[249] Nabeel Aslam, Matthias Pfender, Philipp Neumann, Rolf Reuter, Andrea Zappe, Felipe Fávaro De Oliveira, Andrej Denisenko, Hitoshi Sumiya, Shinobu Onoda, Junichi Isoya, and Jörg Wrachtrup. Nanoscale nuclear magnetic resonance with chemical resolution. *Science*, 357(6346):67–71, jul 2017.

[250] C. Müller, X. Kong, J. M. Cai, K. MelentijeviÄ, A. Stacey, M. Markham, D. Twitchen, J. Isoya, S. Pezzagna, J. Meijer, J. F. Du, M. B. Plenio, B. Naydenov, L. P. McGuinness, and F. Jelezko. Nuclear magnetic resonance spectroscopy with single spin sensitivity. *Nature Communications*, 5(1):1–6, aug 2014.

[251] Christopher P. Anderson Alexandre Bourassa Alexander L. Crook Gary Wolfowicz Hiroshi Abe Takeshi Ohshima David D. Awschalom Kevin C. Miao, Joseph P. Blanton. Universal coherence protection in a solid-state spin qubit. 2020.

[252] Erik Bauch, Connor A. Hart, Jennifer M. Schloss, Matthew J. Turner, John F. Barry, Pauli Kehayias, Swati Singh, and Ronald L. Walsworth. Ultralong Dephasing Times

in Solid-State Spin Ensembles via Quantum Control. *Physical Review X*, 8(3):031025, jul 2018.

[253] Toyofumi Ishikawa, Kai-Mei C Fu, Charles Santori, Victor M Acosta, Raymond G Beausoleil, Hideyuki Watanabe, Shinichi Shikata, and Kohei M Itoh. Optical and Spin Coherence Properties of Nitrogen-Vacancy Centers Placed in a 100 nm Thick Isotopically Purified Diamond Layer. *Nano Lett*, 12:34, 2012.

[254] A. A. Clerk, K. W. Lehnert, P. Bertet, J. R. Petta, and Y. Nakamura. Hybrid quantum systems with circuit quantum electrodynamics. *Nature Physics*, pages 1–11, mar 2020.

[255] P. Jamonneau, M. Lesik, J. P. Tetienne, I. Alvizu, L. Mayer, A. Dréau, S. Kosen, J. F. Roch, S. Pezzagna, J. Meijer, T. Teraji, Y. Kubo, P. Bertet, J. R. Maze, and V. Jacques. Competition between electric field and magnetic field noise in the decoherence of a single spin in diamond. *Physical Review B*, 93(2):024305, jan 2016.

[256] Gopalakrishnan Balasubramanian, Philipp Neumann, Daniel Twitchen, Matthew Markham, Roman Kolesov, Norikazu Mizuochi, Junichi Isoya, Jocelyn Achard, Johannes Beck, Julia Tissler, Vincent Jacques, Philip R Hemmer, Fedor Jelezko, and Jörg Wrachtrup. Ultralong spin coherence time in isotopically engineered diamond. *Nature materials*, 8(5):383–7, may 2009.

[257] Wayne M. Witzel, Malcolm S. Carroll, Aukasz Cywiński, and S. Das Sarma. Quantum decoherence of the central spin in a sparse system of dipolar coupled spins. *Physical Review B - Condensed Matter and Materials Physics*, 86(3):035452, jul 2012.

[258] C. H. Yang, K. W. Chan, R. Harper, W. Huang, T. Evans, J. C.C. Hwang, B. Hensen, A. Laucht, T. Tanttu, F. E. Hudson, S. T. Flammia, K. M. Itoh, A. Morello, S. D. Bartlett, and A. S. Dzurak. Silicon qubit fidelities approaching incoherent noise limits via pulse engineering. *Nature Electronics*, 2(4):151–158, apr 2019.

[259] Jun Yoneda, Kenta Takeda, Tomohiro Otsuka, Takashi Nakajima, Matthieu R. Delbecq, Giles Allison, Takumu Honda, Tetsuo Kodera, Shunri Oda, Yusuke Hoshi, Noritaka Usami, Kohei M. Itoh, and Seigo Tarucha. A quantum-dot spin qubit with coherence limited by charge noise and fidelity higher than 99.9%. *Nature Nanotechnology*, 13(2):102–106, feb 2018.

[260] E. Knill. Quantum computing with realistically noisy devices. *Nature*, 434(7029):39–44, mar 2005.

[261] M. Veldhorst, J. C.C. Hwang, C. H. Yang, A. W. Leenstra, B. De Ronde, J. P. Dehollain, J. T. Muhonen, F. E. Hudson, K. M. Itoh, A. Morello, and A. S. Dzurak. An addressable quantum dot qubit with fault-tolerant control-fidelity. *Nature Nanotechnology*, 9(12):981–985, jan 2014.

[262] Earl T. Campbell, Barbara M. Terhal, and Christophe Vuillot. Roads towards fault-tolerant universal quantum computation, sep 2017.

[263] Evan S. Petersen, A. M. Tyryshkin, J. J.L. Morton, E. Abe, S. Tojo, K. M. Itoh, M. L.W. Thewalt, and S. A. Lyon. Nuclear spin decoherence of neutral P 31 donors in silicon: Effect of environmental Si 29 nuclei. *Physical Review B*, 93(16):161202, apr 2016.

[264] R. Guichard, S. J. Balian, G. Wolfowicz, P. A. Mortemousque, and T. S. Monteiro. Decoherence of nuclear spins in the frozen core of an electron spin. *Physical Review B - Condensed Matter and Materials Physics*, 91(21):214303, jun 2015.

[265] Wenzheng Dong, F. A. Calderon-Vargas, and Sophia E. Economou. Precise high-fidelity electron-nuclear spin entangling gates in NV centers via hybrid dynamical decoupling sequences. 2020.

[266] Alexandra Oliveros, Anthony Guiseppi-Elie, and Stephen E. Saddow. Silicon carbide:

A versatile material for biosensor applications. *Biomedical Microdevices*, 15(2):353–368, apr 2013.

[267] Mark Oxborrow, Jonathan D. Breeze, and Neil M. Alford. Room-temperature solid-state maser. 488(7411):353–356, aug 2012.

[268] Jonathan D. Breeze, Enrico Salvadori, Juna Sathian, Neil Mc N. Alford, and Christopher W.M. Kay. Continuous-wave room-temperature diamond maser. *Nature*, 555(7697):493–496, mar 2018.

[269] M. Fischer, A. Sperlich, H. Kraus, T. Ohshima, G. V. Astakhov, and V. Dyakonov. Highly Efficient Optical Pumping of Spin Defects in Silicon Carbide for Stimulated Microwave Emission. *Physical Review Applied*, 9(5):054006, may 2018.

[270] Clai Owens, Aman LaChapelle, Brendan Saxberg, Brandon M. Anderson, Ruichao Ma, Jonathan Simon, and David I. Schuster. Quarter-flux Hofstadter lattice in a qubit-compatible microwave cavity array. *Physical Review A*, 97(1):013818, jan 2018.

[271] Jan Jeske, Jared H Cole, and Andrew D Greentree. Laser threshold magnetometry. *New Journal of Physics*, 18(1):013015, jan 2016.

[272] Luke Hacquebard and Lilian Childress. Charge-state dynamics during excitation and depletion of the nitrogen-vacancy center in diamond. *Physical Review A*, 97(6):063408, jun 2018.

[273] Shova D. Subedi, Vladimir V. Fedorov, Jeremy Peppers, Dmitry V. Martyshkin, Sergey B. Mirov, Linbo Shao, and Marko Loncar. Laser spectroscopic characterization of negatively charged nitrogen-vacancy (NV) centers in diamond . *Optical Materials Express*, 9(5):2076, may 2019.

[274] Sarath R, Lachlan J. Rogers, Xavier Vidal, Reece P. Roberts, Hiroshi Abe, Takeshi Ohshima, Takashi Yatsui, Andrew D. Greentree, Jan Jeske, and Thomas Volz. Ampli-

fication by stimulated emission of nitrogen vacancy centres in a diamond-loaded fiber cavity. dec 2019.

[275] K. J. Satzinger, Y. P. Zhong, H. S. Chang, G. A. Peairs, A. Bienfait, Ming Han Chou, A. Y. Cleland, C. R. Conner, Dumur, J. Grebel, I. Gutierrez, B. H. November, R. G. Povey, S. J. Whiteley, D. D. Awschalom, D. I. Schuster, and A. N. Cleland. Quantum control of surface acoustic-wave phonons, nov 2018.

[276] Ren Wei Zhou, Xue Chao Liu, Shi Yi Zhuo, Hong Ming Chen, Biao Shi, and Er Wei Shi. Divacancies induced ferromagnetism in 3C-SiC thin films. *Journal of Magnetism and Magnetic Materials*, 374:559–563, jan 2015.

[277] David M. Toyli, Christoph D. Weis, Gregory D. Fuchs, Thomas Schenkel, and David D. Awschalom. Chip-scale nanofabrication of single spins and spin arrays in diamond. *Nano Letters*, 10(8):3168–3172, 2010.

[278] M. E. (Mikhail Efimovich) Levinshtein, Sergey L. Rumyantsev, and Michael. Shur. *Properties of advanced semiconductor materials : GaN, AlN, InN, BN, SiC, SiGe*. Wiley, 2001.

[279] Josef Lutz, Heinrich Schlangenotto, Uwe Scheuermann, and Rik De Doncker. *Semiconductor power devices: Physics, characteristics, reliability*. Springer Berlin Heidelberg, 2011.

[280] Kevin G. Schädler, Carlotta Ciancico, Sofia Pazzagli, Pietro Lombardi, Adrian Bachtold, Costanza Toninelli, Antoine Reserbat-Plantey, and Frank H.L. Koppens. Electrical Control of Lifetime-Limited Quantum Emitters Using 2D Materials. *Nano Letters*, 19(6):3789–3795, 2019.

[281] Kai Mei C. Fu, Charles Santori, Paul E. Barclay, Lachlan J. Rogers, Neil B. Manson, and Raymond G. Beausoleil. Observation of the dynamic Jahn-Teller effect in

the excited states of nitrogen-vacancy centers in diamond. *Physical Review Letters*, 103(25):256404, dec 2009.

[282] Kay D. Jahnke, Alp Sipahigil, Jan M. Binder, Marcus W. Doherty, Mathias Metsch, Lachlan J. Rogers, Neil B. Manson, Mikhail D. Lukin, and Fedor Jelezko. Electron-phonon processes of the silicon-vacancy centre in diamond. *New Journal of Physics*, 17, 2015.

[283] Harishankar Jayakumar, Jacob Henshaw, Siddharth Dhomkar, Daniela Pagliero, Abdelghani Laraoui, Neil B. Manson, Remus Albu, Marcus W. Doherty, and Carlos A. Meriles. Optical patterning of trapped charge in nitrogen-doped diamond. *Nature Communications*, 7(1):1–8, aug 2016.

[284] C. J. Cochrane, P. M. Lenahan, and A. J. Lelis. Identification of a silicon vacancy as an important defect in 4H SiC metal oxide semiconducting field effect transistor using spin dependent recombination. *Applied Physics Letters*, 100(2), 2012.

[285] Sheldon M. Ross. *Introduction to probability and statistics for engineers and scientists*.

[286] A. Krtschil, H. Witte, M. Lisker, J. Christen, A. Krost, U. Birkle, S. Einfeldt, D. Hommel, F. Scholz, J. Off, and M. Stutzmann. Photoelectric properties of the 0.44 eV deep level-to-band transition in gallium nitride investigated by optical admittance spectroscopy. *Applied Physics Letters*, 77(4):546–548, jul 2000.

[287] Wen Yang and Ren Bao Liu. Quantum many-body theory of qubit decoherence in a finite-size spin bath. *Physical Review B - Condensed Matter and Materials Physics*, 78(8):085315, aug 2008.

[288] J. R. Johansson, P. D. Nation, and Franco Nori. QuTiP 2: A Python framework for the dynamics of open quantum systems. *Computer Physics Communications*, 184(4):1234–1240, apr 2013.

[289] Mustafa Ahmed Ali Ahmed, Gonzalo A. Álvarez, and Dieter Suter. Robustness of dynamical decoupling sequences. *Physical Review A - Atomic, Molecular, and Optical Physics*, 87(4):042309, apr 2013.

[290] M. S. Blok, N. Kalb, A. Reiserer, T. H. Taminiau, and R. Hanson. Towards quantum networks of single spins: Analysis of a quantum memory with an optical interface in diamond. *Faraday Discussions*, 184:173–182, 2015.

[291] J. Zopes, K. S. Cujia, K. Sasaki, J. M. Boss, K. M. Itoh, and C. L. Degen. Three-dimensional localization spectroscopy of individual nuclear spins with sub-Angstrom resolution. *Nature Communications*, 9(1):1–8, dec 2018.

[292] M. H. Abobeih, J. Cramer, M. A. Bakker, N. Kalb, M. Markham, D. J. Twitchen, and T. H. Taminiau. One-second coherence for a single electron spin coupled to a multi-qubit nuclear-spin environment. *Nature Communications*, 9(1):1–8, dec 2018.

[293] P Giannozzi, O Andreussi, T Brumme, O Bunau, M Buongiorno Nardelli, M Calandra, R Car, C Cavazzoni, D Ceresoli, M Cococcioni, N Colonna, I Carnimeo, A Dal Corso, S. De Gironcoli, P Delugas, R. A. Distasio, A Ferretti, A Floris, G Fratesi, G Fugallo, R Gebauer, U Gerstmann, F Giustino, T Gorni, J Jia, M Kawamura, H. Y. Ko, A Kokalj, E. Kücükbenli, M Lazzeri, M Marsili, N Marzari, F Mauri, N. L. Nguyen, H. V. Nguyen, A. Otero-De-La-Roza, L Paulatto, S Poncé, D Rocca, R Sabatini, B Santra, M Schlipf, A P Seitsonen, A Smogunov, I Timrov, T Thonhauser, P Umari, N Vast, X Wu, and S Baroni. Advanced capabilities for materials modelling with Quantum ESPRESSO. *Journal of Physics Condensed Matter*, 29(46):465901, nov 2017.

[294] Paolo Giannozzi, Stefano Baroni, Nicola Bonini, Matteo Calandra, Roberto Car, Carlo Cavazzoni, Davide Ceresoli, Guido L Chiarotti, Matteo Cococcioni, Ismaila Dabo, Andrea Dal Corso, Stefano de Gironcoli, Stefano Fabris, Guido Fratesi, Ralph Gebauer, Uwe Gerstmann, Christos Gougoussis, Anton Kokalj, Michele Lazzeri, Layla Martin-

Samos, Nicola Marzari, Francesco Mauri, Riccardo Mazzarello, Stefano Paolini, Alfredo Pasquarello, Lorenzo Paulatto, Carlo Sbraccia, Sandro Scandolo, Gabriele Sclauzero, Ari P Seitsonen, Alexander Smogunov, Paolo Umari, and Renata M Wentzcovitch. QUANTUM ESPRESSO: a modular and open-source software project for quantum simulations of materials. *Journal of Physics: Condensed Matter*, 21(39):395502, sep 2009.